Thermomechanical Behavior of Shape Memory Alloy Cables and Tubes

by

Benjamin Reedlunn

A dissertation submitted in partial fulfillment
of the requirements for the degree of
Doctor of Philosophy
(Mechanical Engineering)
in The University of Michigan
2012

Doctoral Committee:

Professor John A. Shaw, Co-Chair
Assistant Professor Samantha Hayes Daly, Co-Chair
Professor J. Wayne Jones
Associate Professor Diann Erbschloe Brei
Staff Researcher Nilesh Mankame, General Motors Corporation

Acknowledgments

Table of Contents

List of Tables

Table

List of Figures

List of Appendices

Appendix

Abstract

Shape memory alloys (SMAs) are well known for their substantial power density in shape memory mode and their large recoverable strains in superelastic mode. NiTi, the most popular SMA, has been studied extensively in pure tension, but studies of more complex structural forms and other deformation modes are rare in the published literature. Therefore, the first purpose of this research was to characterize and understand the superelastic thermomechanical behavior of one such structural form, cables (or wire ropes). The second purpose was to understand the superelastic tension, compression, and bending behavior of cylindrical NiTi tubes.

Cables made from SMA wires are relatively new and unexplored structural elements that combine many of the advantages of conventional cables with the unique properties of SMAs, leading to a number of potential applications. An extensive set of uniaxial tension experiments were performed on two SMA cable constructions, a 7×7 right regular lay, and a 1×27 alternating lay, to characterize their superelastic behavior in room temperature air. Details of the evolution of strain and temperature fields were captured by simultaneous stereo digital image correlation (DIC) and infrared imaging, respectively.

Different aspects of the SMA cable responses were considered. First, the nearly isothermal, yet quite different, superelastic responses of the two cable designs were examined. Second, selected subcomponents excised from the two cable constructions were studied to determine the individual contributions of the cables hierarchical construction. Third, the elongation rate sensitivity of the cables and their subcomponents were inspected to compare and quantify their thermomechanical coupling.

The tube experiments in the second part of this research should serve to calibrate and validate material models used to simulate SMA cables in the future. Tubes were studied instead of wires to avoid experimental difficulties, but even using tubes, custom built fixtures were required to avoid buckling during uniaxial compression and to avoid axial loads during large-rotation bending. Stereo DIC measurements during the tube experiments revealed that the material instability, which leads to propagating transformation fronts in pure tension, also leads to highly heterogeneous strain fields during bending.

Chapter 1

Introduction

1.1   Background on Shape Memory Alloys

Shape Memory Alloys (SMAs) are known for two unusual properties, the *shape memory effect* and *superelasticity*. In the shape memory effect, a SMA is first mechanically loaded such that it macroscopically appears to be plastically deformed. Then the material is heated above a critical transition temperature, which impressively causes the SMA to regain its original shape. Superelasticity involves mechanically loading the material while it is above the transition temperature. In this regime, a SMA can withstand large strains and fully recover upon unloading. The shape memory effect and superelasticity are employed in an ever growing number of applications.

The shape memory effect is primarily utilized to create actuators. A schematic of a typical actuator design is shown in Fig. 1.1a. A SMA wire, bias spring, and external spring

(a)   **(b)**
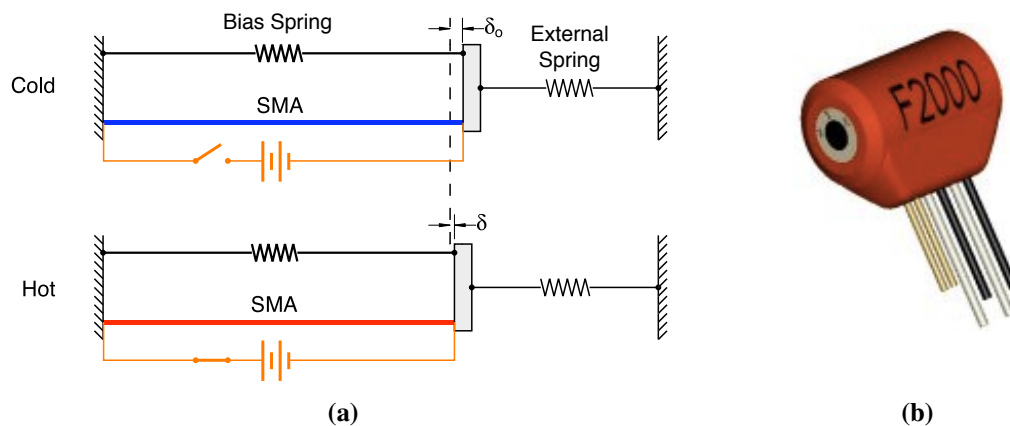
Figure 1.1   (a) A prototypical, multiple use, SMA actuator (adapted from [113]). (b) The Fran-gibolt™ is placed around a notched bolt, and then heated to fracture the bolt at the desired time.

are assembled together, which stretches the SMA wire from its reference configuration by δ_o. The external spring can be thought to represent a robotic limb, a mechanical latch, a part of a cuckoo clock, a morphing wing of a toy airplane, or many other products in need of movement [40]. Joule heating of the SMA causes it to contract and do useful work against the external spring. When the current is removed and the wire cools down, the bias spring and external spring stretch the wire back to δ_o. The bias spring allows the actuator to be used multiple times for any external spring stiffness, but some applications only use a SMA once, such as the Frangibolt™ in Fig. 1.1b [60]. The Frangibolt™ is compressed from its reference configuration to fit in between a bolt's head and its nut, or the surface the bolt is screwed into. At the desired time, the SMA is Joule heated, causing it to expand against the bolt head and nut. The expansion force eventually snaps the bolt in two at a pre-existing notch along the bolt shaft.

On the superelastic side, SMAs have numerous applications in the consumer, civil, and biomedical engineering sectors. In the consumer sector, superelastic SMAs are used for their bending compliance in eyeglass frames (see Fig. 1.2a), clothing, headphone headbands, and rugged cell phone antennas (see Fig. 1.2b) [56]. In civil engineering, SMAs are being explored for vibration damping of large structures, using the hysteresis in the superelastic stress-strain curve [20, 37]. Particular interest exists in biomedical engineering, where the strong trend towards minimally invasive surgery in medicine is often enabled by superelastic SMAs [39]. Self-expanding stents (see Fig. 1.2c) and stent grafts comprise the largest fraction of existing SMA biomedical applications. These devices are often laser cut from SMA tubes into a series of crowns and struts, which are locally bent to fit the stent inside a catheter. The catheter delivers the stent to the desired location in the body, where it expands (see Fig. 1.2d) and scaffolds the circumference of a tubular lumen. Other superelastic examples include catheter guidewires, inferior vena cava filters (see Fig. 1.2e), tissue ablation devices, retrieval baskets, birth control devices, endoscopes, intra-aortic balloon pumps, and biopsy forceps. In dentistry, superelastic SMAs are used as pretensioned orthodontic wires (see Fig. 1.2f) and root canal files (see Fig. 1.2g) that must bend to accommodate tortuous crevices [39, 84].

Most, if not all, of the applications mentioned use Nickel Titanium based alloys. Typically the composition is nearly equiatomic (50.0 to 50.8% at Ni), and it is known as NiTi, or by its commercial name, Nitinol. (Ternary alloys of NiTi, such as NiTiNb or NiTiHf [68], also do exist for specialized applications.) Polycrystalline NiTi-based alloys exhibit an energy density of 2.5×10^7 J/m^3, which is an order of magnitude higher than other active materials, such as piezoelectric, magnetostrictive, and ferromagnetic materials [65]. This potentially enables more compact structural designs than would otherwise be possible.
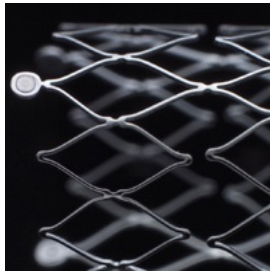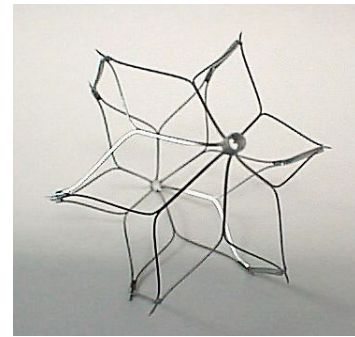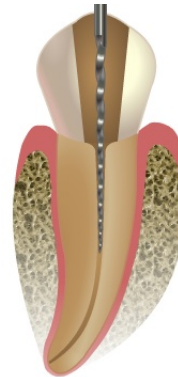
Figure 1.2 Selected superelastic SMA applications: (a) Eyeglass frame, (b) Cell phone antenna, (e) Inferior vena cava filter, (c) Stent, (d) Stent as it is deployed from a catheter, (f) Orthodontic archwire, (g) Root canal file.

Furthermore, NiTi's low cycle fatigue limit is between 5 and 8% strain, and the high cycle limit is near 2.5% strain. This flexibility, coupled with its excellent biocompatibility and corrosion resistance, has led to the wide adoption of NiTi as an implantable material in the medical device industry. There are a number of other SMAs shown in Fig. 1.3, but due to the properties mentioned, NiTi-based alloys have dominated the commercial market [104]. For these reasons, NiTi is the only SMA considered herein.

There are three primary crystallographic phases of interest in NiTi, as shown in Fig. 1.4: austenite (A), martensite (M), and R-phase (R). Austenite is a B2 cubic structure exhibiting high symmetry, which is thermodynamically stable at high temperatures and low stresses. Martensite is a B19' monoclinic structure, which is thermodynamically stable at low temperatures or high stresses. Due to the low symmetry of the M phase, it has 12 different lattice correspondent variants (LCV) [12], and can exist as thermal-M (twinned microstructure) or oriented-M (detwinned microstructure), as shown in the simplified schematic in Fig. 1.4. Taking a macroscopic view point, we will denote oriented-M due to tensile stresses as M^+, and oriented-M due to compressive stresses as M^-. Lastly, the R-phase is formed from a rhombohedral distortion of the austenite phase. Aside from affecting the electrical resistivity [27], the R-phase tends to play a relatively minor role in the behavior of SMAs due to its similarity to the austenite phase.

The differences between A and oriented-M are macroscopically visible and, accordingly, phase transformations between the two are responsible for the shape memory effect and superelasticity. Figure 1.5 depicts both the shape memory effect (⓪ to ⑤) and superelasticity (⑤ to ⑩) for a NiTi wire loaded in uniaxial tension. The plot axes are tensile stress σ, tensile strain ε, and temperature T of the wire. Let us first walk through the shape memory effect:

⓪-① The material starts as thermal-M. Loading to ① gives a non-linear response as M is reoriented into primarily detwinned M^+.
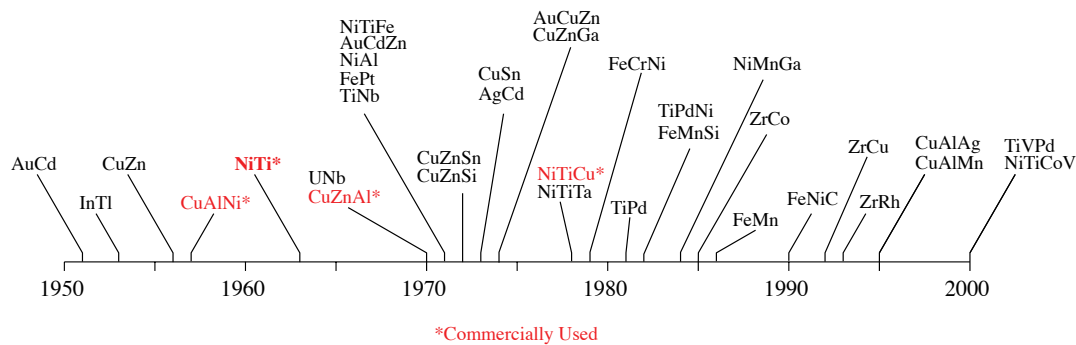
Figure 1.3 History of the discovery of important shape memory alloys. [104]

4
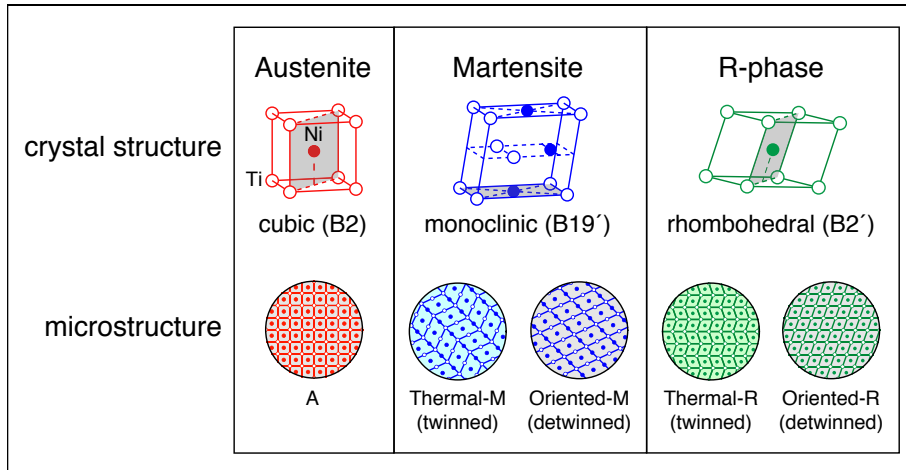
Figure 1.4 The three primary phases of NiTi. [108]

①-② Since all variants of martensite are energetically equivalent, unloading only causes elastic unloading of M^+, resulting in more than 4% residual strain.

②-⑤ Raising the temperature of the wire causes little change in the strain until ③, where it reaches a critical transformation temperature of -5°C for this particular wire. This temperature is known as the austenitic finish A_f temperature, because from ③ to ④ the wire transforms from M^+ to A, causing the wire to return to its original length. The strain remains static for further heating to ⑤.

If the wire were subsequently cooled back down, it would follow the line defined by $\sigma = 0$ MPa and $\varepsilon = 0\%$, and eventually revert back to thermal-M, completing a full shape memory cycle. Instead of cooling, however, the wire is strained superelastically:

⑤-⑦ Austenite is linear elastically loaded until the stress reaches a plateau at ⑥. As the material traverses the plateau martensite is *stress-induced*. By the end of the plateau the wire has transformed to M^+, and further straining to ⑦ causes an increase in stress. (Here, we have shown the microstructure as detwinned for simplicity. In reality, it is mostly pairs of twin-related LCVs, termed habit plane variants, of M at the end of the plateau. Detwinned M only occurs to a significant degree upon further loading above ⑦ [48].)

⑦-⑩ The wire unloads until ⑧, where M^+ is thermodynamically unstable at this low stress and high temperature. Consequently, after a nucleation peak (more on this later) the material returns to the A phase along the unloading plateau, closing the hysteresis loop at ⑨. Finally, the A phase elastically unloads to zero stress at ⑩.

5

Thus, when the temperature is greater than A_f, the wire is superelastic and can withstand more than 7% strain with negligible residual strain at zero load.

The superelastic response is quite sensitive to temperature, which has important practical implications. Figure 1.6a depicts a series of isothermal experiments on as-received wires, each at a different temperature [23][a]. Clearly the superelastic loading and unloading plateau heights σ_p trend with temperature, and they are plotted in Fig. 1.6b to create a quasi-phase diagram. The shaded areas indicate the stable phase. The phase in between the shaded areas depends on the loading path, so arrows designate which phase boundary is relevant for a given loading direction. The A to M^+ phase boundary has a steep linear slope of 6.7 MPa/°C. The Clausius-Clapeyron relation can reasonably predict this slope [107], but the important point here is just how sensitive this material is to temperature. Perhaps now it is clear why the majority of the superelastic applications mentioned above are designed to be implanted in the body or used in the operating room where the temperature is tightly controlled. Also, this temperature dependence plays a critical role in explaining the strain rate dependence of NiTi cables, as will be shown in Chapter 5.

Since its discovery, NiTi has been studied extensively and its behavior in uniaxial tensile loading is relatively well understood, but applications increasingly require more complex

---

[a]Several other experiments at lower temperatures were presented in [23], but they have been omitted to focus on the superelastic behavior.
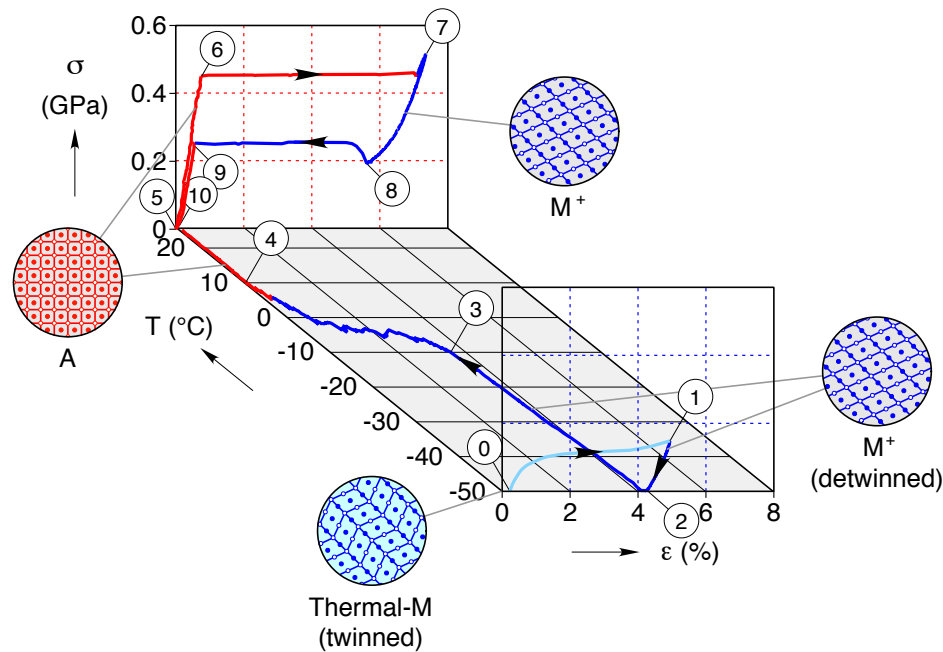
Figure 1.5 NiTi wire loaded in uniaxial tension to demonstrate the shape memory effect (0-5) and superelasticity (5-10) (adapted from [108]).
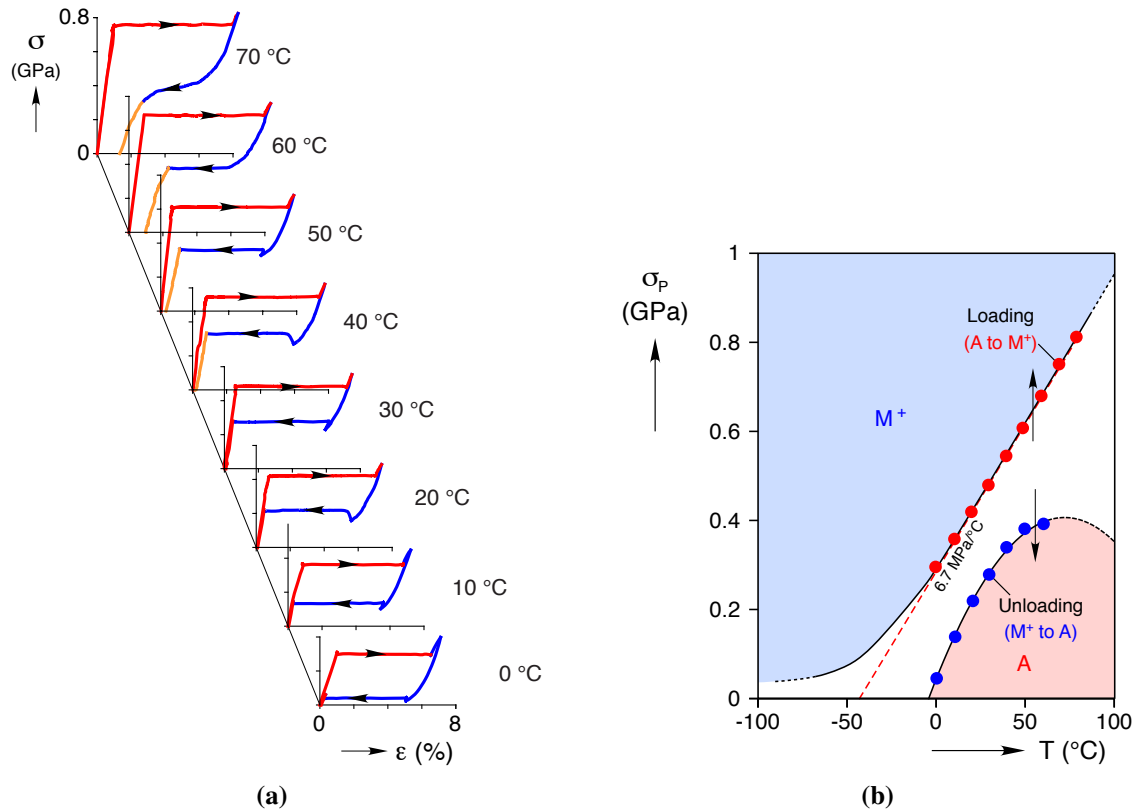
Figure 1.6 (a) NiTi wire loaded in uniaxial tension at several different temperatures demonstrating the temperature dependence of superelastic behavior, (b) Superelastic plateau stresses from (a) plotted in stress-temperature space to create a quasi-phase diagram (adapted from [108]).

structural forms, which subject the material to other deformation modes. The first purpose of this dissertation is to characterize and understand the thermomechanical behavior of one such structural form, cables (or wire rope). The second purpose is to consider how NiTi tubes, a more simple geometry than cables, perform in tension, compression, and bending deformation modes.

1.1.1 SMA Cable Background and Motivation

Conventional structural cables (or ropes) are composed of thin filaments of steel, natural or synthetic materials that are helically wound into strands, which in turn, are wound around a core. These have long been used as structural tension elements for a variety applications. For example, steel wire rope is used in civil engineering structures for power cables, bridge stays, and mine shafts; in marine and naval structures for salvage/recovery, towing, vessel mooring, yacht rigging and oil platforms; in aerospace structures for light aircraft control cables and astronaut tethering; and in recreation applications like cable cars and ski lifts.
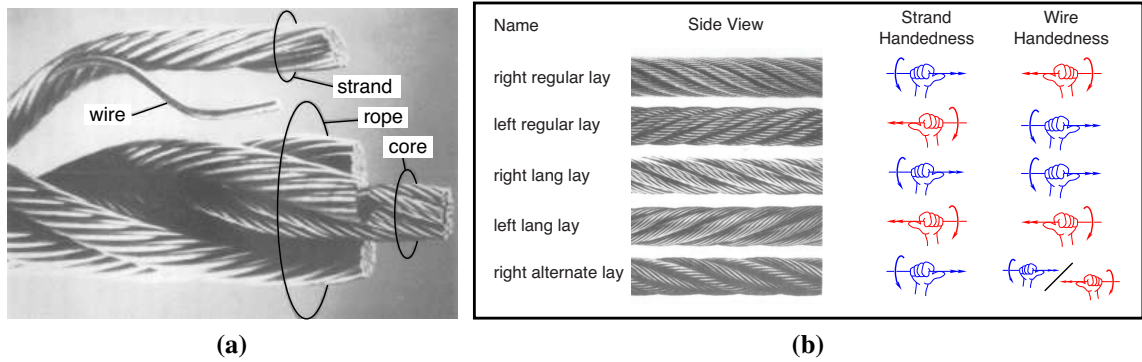
Figure 1.7 Typical wire rope (a) construction and (b) lays (adapted from [79] and [31]).

Wire cable is a built-up structure assembled in a hierarchical manner from thin wire elements (see Figure 1.7a). Several wires, not necessarily of the same diameter, are helically wrapped around a single wire to form a strand. Several strands are then laid helically around an axial core, which laterally supports the outer strands creating a nominally circular cross-section. Depending on the application, the axial core can be another strand, natural fibers, or a polymer. The chirality, or handedness, of the wires in a strand and of the strands in a rope can be laid in an opposite sense (regular lay) or same sense (lang lay), which affects the helix angle the wires make with the cable axis (Figure 1.7b) and the tension-torsion coupling of the overall cable response.

As a structural tension element, wire cable has many desirable qualities. It is relatively stiff in uniaxial tension and often has a large tensile strength, yet it is compliant in torsion and bending due to the large aspect ratio of the rope and the helical lays of elements within the cable. This compliance enables ease of handling and spooling. The numerous wires and strands support the tensile load in parallel, providing redundancy and more forgiving failure modes since the failure of one wire does not necessarily propagate to the failure of other wires, unlike fracture across a monolithic bar. The strand and rope cross-sections can be constructed in various geometric patterns, leading to considerable design flexibility with respect to axial stiffness, stored elastic energy, bending/twisting compliance, exterior smoothness, abrasion resistance, and redundancy.

SMA cables augment many of the advantages of conventional wire rope with the desirable properties of shape memory alloys. Compared to conventional steel cable, superelastic SMA cables can accommodate relatively large strains without permanent deformation. Under impact loading, steel cable is susceptible to "birdcaging", which is a bulbous-like permanent deformation mode that involves kinking of individual wire elements. This is caused by excessive compression (often resulting from a dynamic event), and usually leads

8

to scrapping of the cable [31]. SMA cables, on the other hand, would be relatively kink-resistant and transient overloading would be less likely to lead to permanent damage. The transformation plateaus in the superelastic behavior could be used to design cables that have inherent overload protection for adjacent structures and large energy absorption capabilities under impact loading. SMA cables can also replace the SMA wires and rods typically used in actuator applications. Wire and rod actuators have a fixed stroke per unit length, while SMA cables could be designed to increase the stroke per unit length at the expense of the axial load. In another example, Redmond *et. al.* [97] spooled shape memory wires to generate a large stroke actuator in a compact package. SMA cables enable either a more compact spooled actuator with the same force, or a larger force actuator with the same footprint.

The SMA wire rope construction itself may resolve some of the longstanding difficulties in the manufacturing of Nitinol devices and the scaling-up of simple structures to realize large-force SMA elements. Historically, joining Nitinol to itself or to adjacent materials to produce complex shapes has been difficult. This has required one to resort to specialized welding techniques, complex laser machining, or mechanical crimping to make attachments to other structures (although recent progress has been made on alternative joining techniques, see [51, 109]). Furthermore, as a monolithic material, Nitinol does not scale up easily for several reasons:

1. Properties of large-section bars are generally poorer than those of wires due to difficulties in controlling quench rates through the section during material processing and the impracticality of cold work procedures that have been optimized for SMA wire (although some recent improvements have been made by [34, 45, 85]).

2. Bars of Nitinol are quite expensive.

3. The thermal response time, due to the strong thermo-mechanical coupling, scales with the volume-to-surface ratio, leading to a sluggish response in large monolithic bars.

Thus, by leveraging the highly optimized manufacturing processes currently available for wire, the cable form results in a large-force SMA element with superior properties for less cost than a monolithic bar of comparable size.

SMA in cable form is a relatively new concept that has been implemented (or proposed) for only a few applications to date. In biomedical applications, small-scale stranded SMA wire is currently used where tight bend radii and high resistance to cyclic bending fatigue are needed. For example, small diameter superelastic strands are used for dental files due to NiTi's high hardness and the strand's ability to flex through tortuous cavities (see Fig. 1.2g).

Similarly, stranded SMA wire is used for vascular filters, snares, and guidewires for its ability to navigate the severe twists and turns of the vascular anatomy [46]. In fact, recent fatigue cracks in the electrodes (lead wires) of implanted heart devices [81] may make SMA cables an appealing alternative. In the consumer sector, superelastic SMA cables have also been used as cell phone antennas (see Fig. 1.2b) that can withstand extreme handling [46].

We note, however, a few (primarily applications oriented) publications do exist in the open literature where researchers have exploited certain features of SMA cables. Song *et. al.* [114] embedded pre-stretched martensitic SMA cables in concrete, and post-tensioned the cables via joule heating to put the concrete in compression. We expect that SMA cables could be used as reinforcements in other composites, where the rough exterior of the wire rope would help mitigate some long-standing debonding problems between the SMA and matrix material. In addition, SMA cables were investigated as actuation elements in a full-scale prototype of a variable area fan nozzle for the next generation of high bypass turbofan jet engines [8, 100]. Cables were used instead of wires or rod because of their bending flexibility in a convenient package. These same advantages have also prompted investigations into using SMA cables for vibration suppression.

SMAs are attractive for vibration damping compared to most metallic materials because of their high specific damping capacity. In addition, they can sustain large strains without plastic deformation, meaning they can actually apply a significant restoring force to a structure after it has been displaced [3]. These advantages and others have prompted volumes of scientific research into using large SMA elements for energy dissipation, especially in civil engineering [1, 35, 36, 38, 53, 78, 101, 123, 125].

Vibration damping and shock absorption are natural applications for SMA cables for many of the reasons previously mentioned. Compared with large monolithic bars, SMA cables (1) are less expensive, (2) consist of wires with superior properties, (3) have faster thermal response time due to greater surface area, (4) can be bent into compact configurations, (5) have enormous design flexibility, and (6) are more damage resistant. Vibration control of conventional cables is an active area of research, and several authors have done experiments, simulations, and prototypes of SMA damper mechanisms that can be attached to steel cables [72, 127]. A more elegant solution was investigated by Casciati *et. al.* [18]: they simply wrapped a single pre-strained 1 mm diameter SMA wire around a 10 mm diameter steel cable. Their best configuration consisted of wrapping the SMA wire 5 times around a 2.36 m length of cable, which roughly doubled the damping coefficient over the plain steel cable. In another example, Johnson *et. al.* [61] and Padgett *et. al.* [86] investigated the use of SMA cables as seismic restrainers for bridges. During earthquakes segments of a bridge can move relative to one another and become "unseated" from the structural piers they rest

on, so it has become common practice to tie bridge segments together or to the piers using steel restraining cables. As noted in [3], once a steel cable plastically deforms, the bridge segments are now free to move and unseat (as happened in the 1994 Northridge earthquake). Thus, steel cables are designed to operate in the elastic range, which means large forces get transmitted to adjacent structures. SMA cables overcome both of these problems with their damping capacity, force limiting plateaus, and large recoverable strains.

Besides the technological implications, SMA cables have scientifically interesting properties. Rich thermo-mechanical coupling and phase transformation-induced instabilities occur even in single uniaxially loaded SMA wires [19, 73, 110, 111, 116]. Built-up cables add multi-scale material-structural interactions, where contact conditions and latent heat interactions between adjacent wires can cause complex patterns of transformation kinetics. Many elaborate SMA constitutive models have been proposed in recent decades, but few have been validated against multi-axial experiments. The opportunity to investigate SMA behavior under complex stress states arising from inherent combined tension-torsion-bending is an additional scientific motivation to characterize SMA in wire rope form.

In summary, SMA cables have promise as high force actuators, thermal latches, and shock absorbing devices, all of which could be useful for a number of future infrastructure and transportation applications. They could be used as thermally-active structural members in a shape memory mode or as extremely resilient elements in a superelastic passive mode. Despite these advantages, we are not aware of any detailed characterization studies of SMA cables in the open literature, so we seek to begin filling that void here.

1.1.2   SMA Tube Background and Motivation

Each wire in a SMA cable undergoes varying degrees of tension, torsion, and bending. An attempt (in the future) to simulate the behavior of cables should start with a constitutive model that has been validated against careful experiments. Unfortunately, high quality experimental data in strain states other than uniaxial tension is rare in the published literature. To remedy this, we elected to perform tension, compression and bending experiments on cylindrical NiTi tubes.

Tubes were selected for these experiments rather than wires for several reasons. First, it is very difficult to avoid buckling a thin wire in a compression test. (For reference, the largest wire diameter in the SMA cables studied was 0.275 mm, whereas the tube outer diameter (OD) was 3.175 mm.) Second, creating a bending fixture capable of accurately measuring the small bending moment and large rotations of a thin wire is not a trivial task. Third, measuring the strain across the diameter of bent 0.275 mm wire using digital

image correlation (DIC)[b] is difficult, likely requiring a complex optical stereo microscope setup [103]. Fourth, wires in torsion have a significant strain gradient across the cross section, whereas thin walled tubes in torsion better approximate a state of pure shear. Fifth, it is relatively easy to flow fluid through the inner diameter of a tube to perform isothermal tests at temperatures other than room temperature. Torsion and non-room temperature tests are not discussed herein, but they are planned for the future, so it is prudent to select a geometry well suited for such experiments. Hence, while tubes may have slightly different properties than wires, they present a means to obtain conclusive data on these fundamental deformation modes and capture the overarching trends.

Aside from assisting in the development of a model to simulate SMA cables, collecting tension, compression, and bending data all on the same tubes has scientific value in itself. All of the superelastic applications listed above in Section 1.1 leverage superelasticity in bending mode to make highly deformable structures. Yet, despite the myriad of applications that employ superelastic SMA in bending, and despite the number of SMA bending models (we found 13) [5, 6, 11, 17, 33, 70, 88, 92, 94–96, 98, 122], few careful pure-bending experiments exist in the literature. Traditional 4-point bending fixtures operate under the assumption of small beam displacements and rotations, which are easily violated when used with slender SMA specimens. Under large displacements, undesirable axial loads tend to develop due to the support constraints. Also, curvature (κ) measurements are usually inferred from grip displacements or rotations. Measuring deformation from the grips is problematic with superelastic SMAs, since they frequently transform to martensite prematurely inside grips where stress concentrations exist which often masks the onset of transformation and/or causes slippage. In effect, the very bending compliance that makes SMAs attractive for applications also creates experimental difficulties.

Nevertheless, a few researchers have built custom devices to apply pure bending moments to SMA wires with negligible shear and axial load in the presence of large rotations and displacements. Berg [10] performed one of the first pure bending studies on SMA wires in the published literature. Berg's work is notable because he bent his specimens significantly further than in other studies, and he used an optical microscope to determine the coordinates of the bent wire centerline to measure the curvature, rather than relying on the grip rotation. In Berg's fixture the bending moment (M) was applied by hanging weights, resulting in a moment controlled experiment. In this control mode, unfortunately, the system has little control over the curvature when $dM/d\kappa$ is close to zero, so gaps exist in Berg's data

---

[b]DIC is a non-contact optical method used to measure full-field surface displacements of an object by tracking the specular pattern on the surface of a specimen [119]. An overview of the technique is provided in Section 2.1.

when this occurs. Furthermore, it is well known that the strain rate (especially in uniaxial tension) has a significant impact on the stress-strain response during the $A \rightarrow M$ and $M \rightarrow A$ transformation (see [19], for example). Consequently, the bending response depends on the curvature rate, but as Berg acknowledged, his fixture had little control over this quantity. In other work, Bundara *et. al.* [16] also constructed a custom pure bending fixture where the moment was applied to SMA wires by hanging weights. The moment curvature relation they measured was not as flat as Berg's, so they were able to capture more data points, but the strain rate still was not controlled. Rejzner *et. al.* [98] avoided this problem by building a displacement-controlled custom pure bending fixture that integrated directly into a load frame, but this design suffered from friction and imparted a small axial load on the specimen. The axial load was considered negligible by the authors and a friction correction was made, but their method was somewhat unclear to us. Furthermore both Bundara *et. al.* [16] and Rejzner *et. al.* [98] measured the curvature from the rotation of the grips, and bent their specimens roughly half as far as Berg, such that the outer fibers did not fully transform to martensite.

In this study, we sought to combine some of the best features of the previous studies and add new measurement capabilities. First, instead of wires, NiTi tubes with a larger outer diameter were used to permit large bending deformations without requiring an extremely small radius of curvature. Second, a custom pure bending fixture was built and integrated into a tensile testing machine, facilitating deformation controlled experiments under large displacements and rotations. Third, stereo DIC was used to capture the (sometimes) highly heterogenous strain field on the surface of the specimen, which has not been done before to our knowledge. DIC also allowed us to measure the curvature without having to resort to grip rotations. Fourth, unlike the previous investigations, the specimens were also characterized in uniaxial tension and compression to better understand the bending behavior and to use this uniaxial data to make a quantitative comparison to our bending data.

1.2 Organization & Goals

The remainder of this thesis is organized as follows.

Chapter 2 introduces the basic experimental setup used in the SMA cable study, while paying special attention to DIC. First, the fundamentals of DIC are reviewed, along with a number of practical suggestions to obtain high quality results. Second, the SMA cable experimental setup is described in detail, showing how we integrated infrared imagining, laser extensometry, and three dimensional DIC into a single tensile test. Finally, results

from a superelastic cycling experiment using the setup are examined. The primary intention of the chapter is to verify the experimental setup on a wire, whose tensile behavior is well understood, and to familiarize the reader with localized transformation phenomena.

Chapter 3 acquaints the reader with the two SMA cable designs tested: a more traditional 7×7 cable and a layered 1×27 cable. The chapter starts with the geometry of the designs and a characterization of the constituent NiTi wires using differential scanning calorimetry. Next is an initial comparison of the superelastic tensile responses of the two cables, followed by a more in depth look. Last is a discussion of the cycling performance of the straight core wires harvested from the center of the cables, and the cyclic performance of the cables themselves. The goal of this chapter is to characterize the superelastic tensile response of the cable designs.

Chapter 4 presents the superelastic responses of the subcomponents of the two designs. The core wire and core strand from the 7×7 design are considered first because their response is more straightforward in the context of typical superelastic behavior. The subcomponents of the 1×27 have more varied behavior, and consequently the DIC data and a subtraction analysis are used to understand the load and torque responses. This chapter aims to explore the behavior of the subcomponents to gain insight into the observations from Chapter 3.

Chapter 5 examines the superelastic responses of the two cables and all of their subcomponents over a range of elongation rates. The strong thermomechanical coupling inherent to SMAs has been studied in straight NiTi wires (see [19], for example), but it manifests in new ways in the hierarchical structure of a cable. Similar to the previous chapter, the components of the 7×7 cable are analyzed first, followed by the 1×27 components. The intention of the chapter is to characterize the response of the components at non-isothermal elongation rates, and explain why the rate sensitivity of each component is different.

Chapter 6 examines NiTi tubes in tension, compression, and pure bending. The goal of this chapter is to investigate if classical beam theory can predict the isothermal response of a superelastic NiTi tube in bending. The experimental setups for tension, compression, and bending of the tubes are different than that used in the cable experiments, so they are presented first. In the results section, we compare the superelastic mechanical responses and strain fields in tension and compression. This comparison then guides our investigation of the bending behavior.

Finally, Chapter 7 summarizes the results of the previous chapters and provides recommendations for future work.

Chapter 2

General Setup for Cable Experiments

In this Chapter we will discuss the general experimental setup used in the SMA cable experiments in Chapters 3-5. The focus of this chapter is on how to apply DIC measurement to the characterization of SMA wire. This is a powerful technique that gives the full-field strain *distribution* across a specimen, unlike conventional extensometry that gives a strain averaged over a single gage length. We will start with some background and fundamentals of DIC, describe the setup and specimen preparation, and then show results from a cyclic experiment on a superelastic wire.

2.1   Digital Image Correlation Fundamentals

Digital Image Correlation (DIC) is a non-contact optical method used to measure the full-field displacements on the surface of an object by tracking a nonuniform, random, pattern on the surface of a specimen. The technique is fast, robust, scalable, and provides an accurate method to determine the surface geometry, displacements, and strains of a deforming object. Below we provide a general overview, but see Sutton *et. al.* [119] and Daly [32] for further reading. DIC is particularly useful to quantify strain fields that are distinctly nonuniform, such as those arising from stress concentrations, and geometric or material heterogeneities/discontinuities. Note that standard DIC algorithms are not well suited to sharp strain or displacement discontinuities, such as kinks or cracks, but this is being overcome via new techniques [93, 99]. For our case of uniaxially-loaded SMA wire, large, but finite, strain gradients exist due to phase transformation.

The DIC method was first developed in the early 1980s by researchers at the University of South Carolina [90, 91, 120]. Initially, DIC was created to measure in-plane deformations of flat surfaces using a single camera (two-dimensional DIC). As the methodology developed and computing power grew over the years, the technique was improved and expanded to three-dimensional DIC in the late 1980s and early 1990s, using two or more synchronized cameras to track the three-dimensional position of points on non-planar objects (developed by McNeill, Luo, Faugeras, Chao, Sutton, and Helm, and others [42, 54, 74]). Both 2-D and

3-D DIC methods calculate surface displacements and their gradients, from which surface strains, velocities, accelerations, and strain rates can be calculated. Three dimensional DIC should not be confused with volumetric DIC, where displacements and other quantities *inside* the material are measured, often using X-ray tomography [9, 119], or confocal microscopy [44]. The basic principles behind the DIC method have no inherent length scale or time scale. Practical limitations on the use of DIC are imposed by the accuracy of measurement techniques at smaller length scales and high speeds, but substantial progress has been made in expanding the limits of DIC as better microscopy and high speed photography instrumentation have become available. Although 3-D DIC has obvious advantages, 2-D DIC remains a very useful and cost-effective tool to measure in-plane deformations of nominally planar samples.

The basic concept underlying DIC involves comparing two digitized images of a specimen surface, taken at different times, to obtain a quantitative, point-by-point mapping of the surface deformation. Commonly, a sequence of images is captured and correlated to obtain the evolution of the object's surface deformation with time. The surface deformation is obtained by optimizing a cross-correlation function to match the local grayscale intensity values of a reference image and a subsequent image of the deformed specimen. The reference image is usually taken to be the first image of the undeformed specimen. The total displacement and strain are then calculated between this first image and any later deformed configuration. Alternatively, to aid correlation, adjacent pairs of images in the sequence can be compared, and the reference image is updated in time to give incremental displacements and strains between it and the next image.

The specimen surface, either covered by a natural or an artificially applied pattern, is digitized into a spatial distribution of pixel intensities to apply a correlation function. The images are not compared pixel-by-pixel, but rather by matching local distributions of pixel intensity *subsets* between reference and deformed images. For simplicity, the following describes how 2-D DIC is performed. Summarizing sections of Chapter 5 in Sutton, *et al.* [119], the optimal match between subsets can be achieved by minimizing a chosen correlation function, S, such as the simple sum of squared differences criterion,

$$ S = \sum_{i=1}^{I} [G_i - F_i]^2 \,, \tag{2.1.1} $$

where $F_i = F(\mathbf{X}_i)$ represents the grayscale value at pixel i at position $\mathbf{X}_i = (X_i, Y_i)$ in the reference image, and $G_i = G(\mathbf{x}_i)$ represents the grayscale value at pixel i at position $\mathbf{x}_i = (x_i, y_i)$ in the deformed image. The summation ranges from the first ($i = 1$) to the last pixel ($i = I$) in the subset. Frequently this criterion is improved by adjusting for lighting

variations between the reference subset and current subset. If a subset moves between areas of different lighting intensities, say from an area of high illumination to shadow, the gray level values should scale uniformly. Thus, we can replace G with $b\,G$ in (2.1.1), where b is a scaling parameter. The optimum value of b can be found for each subset by minimizing S with respect to b, by calculating

$$\frac{\partial S}{\partial b} = 2 \sum_{i=1}^{I} [b\,G_i - F_i]\,G_i = 0,$$

$$\Rightarrow \quad b_{opt} = \frac{\sum_{i=1}^{I} F_i\,G_i}{\sum_{i=1}^{I} G_i^2}. \tag{2.1.2}$$

Substituting $b_{opt}\,G_i$ for G_i in (2.1.1), yields the normalized sum of squared differences,

$$S = \sum_{i=1}^{I} \left[\frac{\sum_{j=1}^{J} F_j\,G_j}{\sum_{j=1}^{J} G_j^2} G_i - F_i \right]^2. \tag{2.1.3}$$

At this point, it appears that a pixel in the reference image can be matched to a location in the current image only to within a pixel, however sub-pixel resolution is achieved by interpolating the gray level intensities of the subsets. Put another way, if the subset moves by 0.2 pixels, some of the pixels will remain nearly the same gray level intensity, but others near large gray level gradients will not. Using an interpolation scheme allows the matching algorithm to resolve this 0.2 pixel movement. Also instead of being restricted to summing over gray level intensities at exact pixel locations $\mathbf{x}_i$ in eq. (2.1.1), one can now sum over a list of optimally placed sample points across a subset.

The reader may also notice that, as described thus far, minimizing a chosen S will only produce accurate results for rigid body translation of the subset. Subset rotation and deformation are accounted for by introducing shape functions analogous to finite element shape functions. The most commonly used shape function assumes strains within the subset are uniform:

$$\mathbf{x}_i = \mathbf{x}(\mathbf{X}_i, \mathbf{p}) = \begin{pmatrix} p_0 \\ p_1 \end{pmatrix} + \begin{pmatrix} 1 + p_2 & p_3 \\ p_4 & 1 + p_5 \end{pmatrix} \mathbf{X}_i \tag{2.1.4}$$

where $\mathbf{p}$ is a vector of parameters $\{p_0, ..., p_5\}$. This allows us to write $S = S(\mathbf{p})$.

The optimal match between the reference subset and the current subset is found by minimizing S with respect to $\mathbf{p}$. The Newton-Raphson method is currently the preferred means to determine $\mathbf{p}$ (although the recent Levenburg-Marquardt nonlinear parameter estimation scheme also shows promise [118]). Once $\mathbf{p}$ is found for all subsets, strains can be calculated as a post-processing step. The components of the displacement $\mathbf{u} = \mathbf{x} - \mathbf{X}$ are

(u, v), which correspond to (p_0, p_1) for the shape functions of eq. (2.1.4). Instead of using the displacement gradients $(\frac{\partial u}{\partial X}, \frac{\partial u}{\partial Y}, \frac{\partial v}{\partial X}, \frac{\partial v}{\partial Y})$ that were calculated for each subset (p_2, p_3, p_4, p_5), the displacement gradients are typically recalculated from the displacements (u, v) at the center of each subset (a grid point). This way the displacement gradients at a point depend on the neighboring grid points, rather than relying entirely on the correlation analysis of one subset. From the gradients, the strain measure of choice can be calculated. Note that some degree of spatial smoothing is usually performed on the displacement gradients (and/or strains) to remove the noise amplified by taking derivatives of experimental data.

As shown in Fig. 2.1, 2D DIC only involves one camera, while 3D DIC involves two or more cameras at some stereo angle relative to one another. By imaging the specimen from multiple viewpoints at the same instant, 3D DIC can capture the 3D shape of the specimen surface and measure any out-of-plane motions that occur during the experiment. To measure both the initial shape and the deformation of an object, the relative positions and operating characteristics of the two cameras must be determined through a calibration procedure using a series of images of a grid with a known pattern. Once the calibration parameters of each camera and their relative orientation in space are determined, the specimen shape can be reconstructed using triangulation [103].

In general terms, the main parameters affecting the accuracy of the method are the following:

- *Specimen surface specularity.* Surfaces with random, fluctuating, gray-scale intensity distributions work best. Surfaces that have a matte color are much better that those that are highly polished/reflective. As a specimen moves during an experiment, the reflections on a polished surface can change, causing significant correlation errors. Also, surfaces with monotone (uniform) or very gradually varying surface intensities
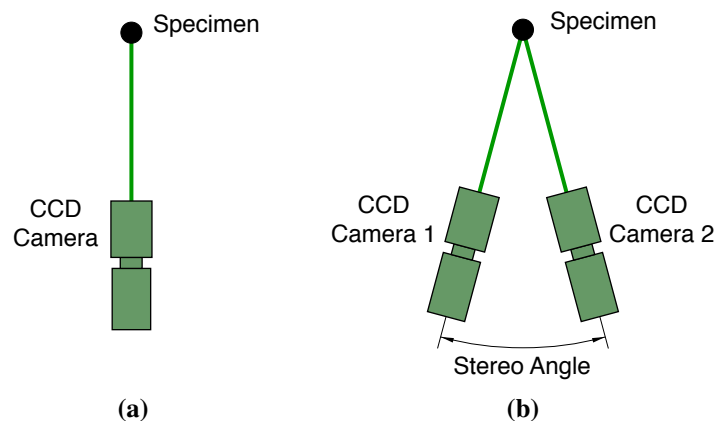
Figure 2.1 Schematics of typical camera orientation in (a) 2D DIC, and (b) 3D DIC.

may not work well. Consequently, unless the preexisting surface happens to be satisfactory, one must often artificially apply a speckle pattern using paint or some other high contrast medium.

- *Camera, lens, and environment.* The usual rules for good digital photography apply here. One must pay attention to illumination, field-of-view (FOV), and depth-of-field (DOF) throughout an experiment. Also, it is usually best to perform DIC with direct line-of-sight to the specimen surface. Intervening mirrors or other optics that refract light introduce optical aberrations in the images, so we discourage their use unless the distortions can be corrected prior to correlation.

- *Image spatial resolution versus speckle size.* Image quality can be improved by using a high pixel resolution charge coupled device (CCD) digital camera. Speckles should be large enough to encompass multiple pixels in an image (oversampled), but should not be so large that images cannot be correlated with the required spatial resolution. Saved images should be of a high-quality, uncompressed format, say bitmap or tiff (not jpeg).

- *Grayscale dynamic range.* A higher number of discrete gray levels (dynamic range) captured by the CCD camera and data acquisition system is generally better, but the usable dynamic range may be limited by illumination and the contrast of the surface pattern. A high bit A/D converter is advisable, and if needed, the CCD signal can be amplified to utilize the full dynamic range of the A/D converter. Color CCD cameras are not recommended, due to the way the CCDs are physically constructed, where the introduction of color introduces a non-monotonic intensity scale and reduces the effective dynamic range.

- *Frame rate.* The number of images taken must be sufficient to resolve the motion of the specimen. More images is better, provided one has sufficient storage capacity for them. One can always throw out images, if not needed during post-processing. If an insufficient number is taken, the relative displacements may be too large between sequential images, and the cross-correlation scheme may fail. This can sometimes be remedied by manually selecting an initial guess for the Newton-Raphson minimization of S described above, but this may be inconvenient.

- *Choice of interpolation function.* As mentioned previously, gray level intensity values and their derivatives between pixels are typically interpolated to reconstruct image intensity patterns prior to correlation. Higher order interpolation schemes increase

the accuracy. A dramatic error reduction is achieved when going from a linear to a cubic interpolation, with diminishing improvements for 5th-order and higher interpolation [102].

- *Out-of-plane displacements (2D DIC only).* 2D DIC is imaged by one camera oriented perpendicular to the specimen surface and is best used for a planar surface under primarily in-plane deformation. In practice, however, out-of-plane displacements are difficult to avoid. The error induced by out-of-plane motion can be minimized by either increasing the distance between the camera and the object when using a standard lens, by using a telecentric lens, or by estimating a functional form of the strain error from measurements of out-of-plane displacement at three points on the specimen [121]. A notable example where ignoring out-of-plane displacements can produce inaccurate measurements in the measurement of Young's modulus of steels is illustrated in Appendix A of [126].

- *Field-of-view (3D DIC only).* The same material points should be in view of multiple cameras, otherwise it is impossible to locate material points in 3D space. The curved surface of a cylindrical specimen, such as the wire in Fig. 2.1b, requires small stereo angles to achieve sufficient field-of-view (FOV) overlap. One must keep in mind, however, that out-of-plane measurement accuracy begins to suffer at stereo angles less than 10° [119], so the desire for FOV overlap can be taken too far.

When using 3D DIC, the camera-lens system must be optimized to balance depth-of-field (DOF) and FOV for the specific test under consideration. An insufficient DOF can cause pattern defocusing due to out-of-plane motion and introduce substantial error in the calculated displacement fields. The specimen must stay in the cameras FOV and stay in focus for the entire testing period. Assuming a fixed lens size, a reduction in aperture size will improve the DOF but will require an increase in object illumination. A reduction in aperture size may also cause light to diffract through the aperture causing an out of focus image. The DOF can also be increased by decreasing the focal length of a lens and holding the distance between the object and the lens fixed. On the other hand, if the FOV of the object is held fixed, which is often done when setting up DIC cameras, different focal length lenses will have comparable DOF [119].

Other sources of error can arise from poor pattern quality, poor specimen illumination, lens distortions, environmental disturbances, and complex testing environments (e.g. submerged specimens, high temperature testing). Sizeable error can also be introduced by the incorrect choice of speckle size and subset size. Sutton, *et al.* [119] recommend each speckle should fill a 3×3 pixel array in the image, as this gives near optimal spatial oversampling.

They also recommend that each subset contain at least 3×3 speckles to ensure reasonable matching accuracy. Typically linear shape functions are used (such as those of eq. (2.1.4)), so the selected subset must be small enough that the strain within the subset can be assumed constant yet large enough to encompass an area that has a statistically different pattern from the neighboring subsets. Computations show that if the gray level signal contains a dominant spatial frequency, the subset size should encompass at least half of this local wavelength in order to avoid mis-registration (i.e., aliasing) [64]. Using a combination of speckle oversampling, accurate interpolation between pixels and image quantization with at least 8 bits can produce displacement fields with an accuracy of ±0.02 pixels or better as shown in [102].

The accuracy of the DIC measurements is especially dependent on the quality of the surface pattern, and since the pattern is usually applied artificially, specimen preparation is worth discussing in some detail. This takes some practice to obtain good results. The speckle pattern must be sufficiently non-periodic, isotropic, and of high contrast to guarantee the uniqueness of the tracking signature for each subset. Prior work has shown that a smooth transition between black and white within a given speckle is preferable (as opposed to uniformly black speckles on a white background, which fortunately in practice is actually difficult to achieve) for accurate measurements, and the pixel-to-speckle ratio must be sufficiently large to enable oversampling [21, 102]. Of course, the pattern application should not alter the mechanical or chemical characteristics of the sample. The pattern should have minimal local areas of reflection, so the use of non-reflective matte paints and diffuse lighting is recommended. If there are persistent reflective or otherwise corrupted pixels in the image, then the user should consider removing these points from the correlation analysis.

Optimal pattern application methods vary, depending on the required magnification. For microscale measurements, high-quality patterns can readily be obtained by airbrushing. Airbrushes can be purchased with different nozzles depending on the desired size of the pattern, where a smaller nozzle diameter produces smaller paint droplets (speckles). The pattern is often applied by lightly coating the sample surface with a light paint, letting this dry, then spraying the coated specimen with a dark mist of paint. Reversing the sequence, first dark paint, then light paint works equally well. (More detailed suggestions for airbrushing will be provided in section 2.3.)

We now turn from general information about DIC to specifics about our specimen preparation, experimental setup, and the results of a cyclic shakedown test on a NiTi wire.

2.2 Cyclic Shakedown of Superelastic Wire

Cyclic shakedown of NiTi is an important aspect that SMA application engineers must often face for adaptive structures applications, since repeatable cyclic behavior is essential for the success of many devices. Usually, however, as-received NiTi wire exhibits significant changes in its response, including transformation stresses, recovery strains, and latent heat changes, when subjected to thermo-mechanical cycling. This can create difficulties for application engineers who wish to design devices, both for thermally-induced actuation and isothermal shape recovery (superelasticity). To cope with this, SMA wire is often "trained" prior to installation in the device to achieve a desired response through repetitive, carefully controlled thermo-mechanical cycles that are representative of expected operating conditions. The result is "shakedown" (or cyclic stabilization) to the desired material response (see, for example, [22, 57, 115]).

2.3 Specimen Preparation

The 0.762 mm diameter NiTi wire utilized in the cyclic shakedown experiment was obtained from Memry corporation (guide-BB30). Differential scanning calorimetry measured the A_f temperature as 13°C [19], indicating that the wire was in the A phase and superelastic at room temperature. This particular wire was selected instead of a core wire from a SMA cable design because wires from this very same lot # have been highly characterized. Much of the characterization is detailed in a series of papers [23–25, 108], where the wire is referred to as "SE wire". Here, we will also refer to it as SE wire when discussing the experimental results to prevent confusion with core wire results in future chapters.

To have an independent, confirmatory, measurement of the strain during the experiment and to control the strain amplitude during cycling, reflective tags were attached to the specimen to use a laser extensometer (LE). To get a reliable reading, the width of the laser tags must be at least 1.2 mm, which is beyond the diameter of the specimen, so tabs were made of epoxy on the back side of the specimen to affix the LE tags (see left hand image in Fig. 2.2). Care was taken to leave the front of the wire free of epoxy to permit DIC measurements. After the epoxy had cured, the specimen was first painted with a background coat of Golden Airbrush Titanium White (#8380), followed by a speckle coat of Golden Airbrush Carbon Black (#8040). These paints were chosen for their opacity, strong contrast, and good adhesion under large superelastic strains. They were both applied using an Iwata custom micron-B airbrush, which has the smallest nozzle in its class (0.18 mm). Through experimentation it was found that the smallest speckles were produced by pulling the air-
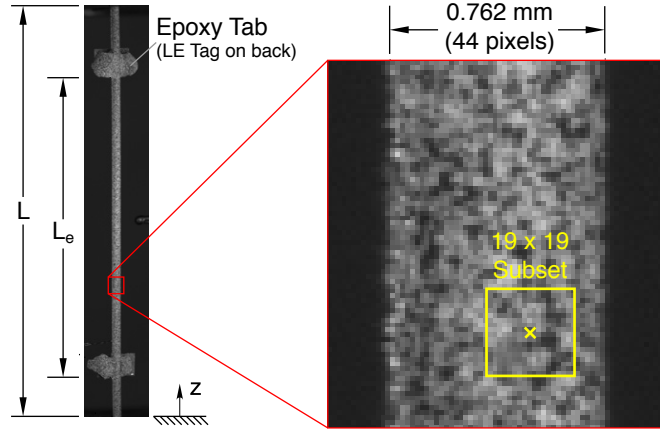
Figure 2.2 Superelastic specimen and speckle pattern

brush needle back as little as possible to allow paint to flow, and setting the air pressure as high as possible. This combination of a small opening for the paint and high pressure (340 kPa in our case) caused the paint to atomize upon exiting the airbrush. The airbrush was held about 50 mm away from the specimen during paint application. To quickly assess the resulting speckle pattern, we then took an image of the specimen using the cameras and field of view of our setup, and confirmed that speckles were approximately 3×3 pixels in size as recommended by Sutton, *et al.* [119]. A magnified view of the resulting image is shown as the inset of Fig. 2.2, showing 44 pixels across the wire diameter and a typical 19×19 subset used in the correlation analysis.

2.4   Experimental Setup

Before describing the experimental setup below, we would like to make clear that it was very similar to the setup used in the SMA cable experiments in Chapters 3-5, but a few differences do exist. These differences, such as reducing field of view of the DIC cameras and adding a torque cell, are detailed in section 3.2.

The front view of a typical imaging arrangement of a vertically oriented specimen is shown in Fig. 2.3a. An infrared camera (Inframetrics ThermCam SC1000 infrared imaging system with a 256×256 pixel array) measured the evolution of the specimen's axial temperature field, $T(z,t)$. The emissivity of the painted specimen was measured to be $\epsilon = 0.91$ (sufficiently close to the ideal emissivity of 1) by comparing the infrared temperature reading against a thermocouple. A container of ice water was placed about 0.6 m behind the specimen (see Fig. 2.3b) to provide background contrast in the infrared images. To avoid obscuring the specimen, the ice water was removed for the photo in Fig. 2.3a. In
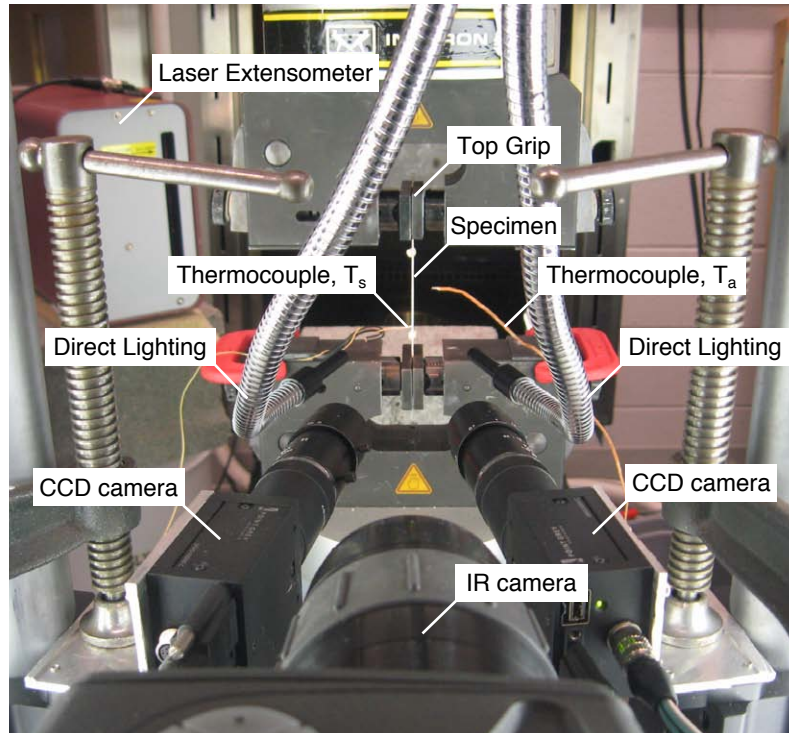
(a)
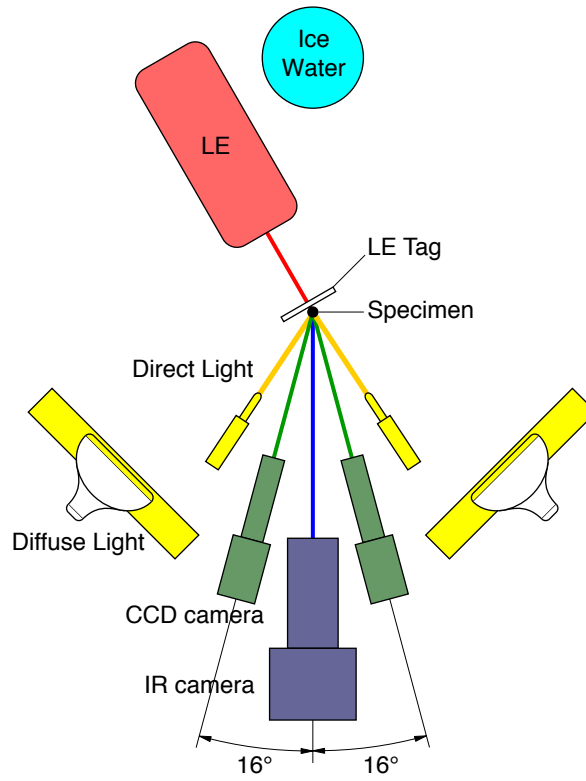
(b)

Figure 2.3   Experimental Setup: (a) photograph of front view, (b) schematic of top view.

addition to the infrared camera, two thermocouples measured the temperature of the air T_a and the specimen T_s during the experiment. A small amount of thermally conductive paste (Omegatherm 201) on the specimen thermocouple (located just above the lower LE tag) ensured good thermal contact with the specimen. To ensure that the specimen was surrounded in stagnant air and avoid any stray air currents, fine-meshed mosquito netting was draped over the entire experimental setup prior to each experiment.

The two optical cameras shown on either side of the IR camera are Pt. Grey Research Grasshoppers (GRAS-50S5M-C). Each is a rather compact camera with a 2448×2048 (3.45 μm square pixels) grayscale CCD. The manufacturer reports that the Grasshopper is capable of 14 bit grayscale resolution, but the effective (noise free) dynamic range was about 8 bits for our setup. We should mention that single lens reflex (SLR) digital cameras are not ideal for DIC because the quick movement of the mechanical mirror shutter system causes the camera body to shake slightly, as opposed to the electronic frame shutter utilized in the Grasshopper. Tamron CCTV 75 mm focal length lenses (as shown in Fig. 2.3a) were successfully used in the SMA cable experiments in Chapters 3-5, but here we used 75 mm Fujinon HF75SA lenses instead (not shown), which had a maximum aperture diameter of 41.6 mm (versus 19.2 mm for the Tamron lenses). This meant it was possible to rely on the diffuse fluorescent lights described below and use minimal direct lighting, which can cause glare.

The specimen was clamped between hardened steel plates within pneumatically-actuated grips resulting in an axial (z-direction) free length of $L = 36.96$ mm. It was loaded uniaxially in displacement control by an Instron 5585 electro-mechanical, lead-screw driven, load frame, where the lower grip was fixed and the upper grip displacement (δ) was controlled and measured by the load frame's high resolution optical encoder. An Instron 2525-816 500 N load cell monitored the resultant axial force (P). From the back side, an Electronic Instruments Research (model LE-05) laser extensometer (LE) measured the elongation (δ_e) between the laser tags affixed to a central gage section of initial length $L_e = 28.57$ mm. The upper grip displacement $\dot{\delta} = d\delta/dt$ was prescribed at a constant rate during loading ($\dot{\delta} > 0$) and unloading ($\dot{\delta} < 0$). Some disagreement between local and global strain measurements is typically unavoidable due to grip slippage as transformation fronts (localized strains) enter or exit the free length. Artifacts from grip slippage (typically unavoidable in such setups when transformation fronts, i.e. localized strains, entered or exited the free length) were eliminated by reporting the strains from the laser extensometer (δ_e/L_e) or DIC (ε) rather than the global strain (δ/L). The prescribed "global strain rate" was $\dot{\delta}/L = \pm 5 \times 10^{-4}$ s^{-1}, which should be emphasized again, is quite different than the "local strain rate" when transformation fronts are propagating.
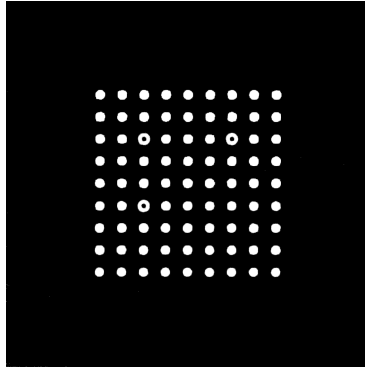
Figure 2.4 Vic-3D Calibration Grid

In setting up the cameras, many of the standard photography techniques were employed. Here is the procedure we used:

1. *Clean the lens and protective glass in front of the CCD.* If a certain area of a speckle pattern will not correlate, and there does not appear to be anything wrong with the focus, lighting, or the speckle pattern, then the problem may be dust on the lens or protective glass in front of the CCD. However, to correct this one must touch the cameras and destroy the calibration. So prior to camera placement in the setup, we held white paper in front of the camera, outside of the focal range, and slowly moved it around. The live camera images will appear as pure white if the lens and CCD protective glass are clean. If, however, gray smudges exist that do not move as the paper is moved, then the lens should be cleaned. If the smudges remain and they do not move when the lens is rotated inside its C-mount, then the source of the smudges is on the protective glass of the CCD, and blowing purified compressed air across the protective glass should correct the problem.

2. *Place and orient the cameras.* The cameras were placed on an optical table in front of the testing frame. In this setup, the bottom grip of the load frame was fixed and the top grip moved with the load frame crosshead, so we aligned the bottom of the FOV with the bottom of the specimen and included 13 % above the top of the specimen to allow for specimen elongation. The total FOV height was 45 mm, and the stereo angle between the cameras was 31.4°. In the SMA cable experiments we used 18-20°, a somewhat better FOV overlap between the cameras, but in this case the IR camera interfered with the bigger DIC camera lenses. At this point, the cameras were rigidly clamped down, and the data/power cables were tied down to the camera mounting posts.

3. *Focus the cameras and set the aperture.* To center the depth-of-field (DOF) across the

specimen, the aperture was initially fully opened to f/1.8 (41.67 mm diameter). This reduced the DOF to its minimum, making it easy to set the working distance and focus the camera on the specimen. The aperture was then closed back down to increase the DOF. Although the aperture could be closed down to f/22 (3.4 mm) to attain the maximum DOF, the image became noticeably blurry after f/8 (9.4 mm). Due to the especially small pixels of these cameras (3.45 μm), Airy circles from light diffracting through the small aperture were larger than a pixel, causing the blurriness. Close side-by-side comparison revealed that even an aperture of f/8 produced a slightly blurred image compared to f/5.6 (13.4 mm), so the aperture was set at f/5.6. From this point on, the cameras were not disturbed and equipment around the cameras was only touched carefully when necessary.

4. *Calibrate the camera orientations and positions.* A 3D DIC analysis requires the precise orientation of the cameras relative to one another. This is typically done by taking a number of images with both cameras of a known calibration grid in different positions and orientations. Only 5-10 images are required, but more are better to reduce the measurement uncertainty and quantify the effect of lens distortions. To calibrate the cameras without disturbing them, the specimen was removed from the grips, and the calibration grid shown in Fig. 2.4 was placed in view of the cameras. Having closed down the aperture meant less light was reaching the CCD, so the lighting and exposure time were adjusted to compensate. The calibration grid was attached to a three axis gimble and two micrometer stages, which were held in the top grip. Along with the movement of the crosshead, all six degrees of freedom were available to translate and rotate (approximately ±20º) the calibration grid to generate 40 different pairs of images of the calibration grid within various locations of the field-of-view.

5. *Set the lighting and exposure time.* With the well known temperature sensitivity of NiTi, special care must be taken to choose lighting sources that do not change the temperature of the specimen. Here we used fluorescent lights behind frosted translucent plastic (just out of view in Fig. 2.3a), similar to that of a light box, to produce a diffuse, flat light. In addition, flexible fiber optic lights (coming in from the top of Fig. 2.3a) with an adjustable light intensity were used to fine tune the illumination. The laser extensometer shown in Fig. 2.3 was placed behind the specimen to avoid shining the laser sheet on the front side of the specimen, which might interfere with optical and infrared images. In addition, care was taken to not shine the fiber optic lights directly at the laser extensometer, since that would affect the extensometer

27

reading. The camera exposure time was set at 20 ms using the camera control software, Vic-Snap [28]. Given sufficient light, it is usually better to minimize motion blur by selecting shorter exposure times. However, we have found exposure times less than 1 ms with the Grasshopper cameras produce noisy images. We believe that longer exposure times "integrate out" the noise in the light reaching the CCD sensor. Given this balance between motion blur and noise, our shutter time corresponds to 0.1 pixels or less of movement during the exposure. Finally, when selecting an exposure time/lighting combination, saturated pixels should be strictly avoided, since DIC performs its matching between the reference and deformed subsets using gray level gradients. If a collection of neighboring pixels are completely white, there is no gradient, and usually will cause the correlation routine to fail at that location.

6. *Perform a trial run.* Before running any experiment it is advisable to take a few images of the specimen while it is static, load these images into the DIC software, and run a quick correlation. This can help locate problem areas due to lighting glare, inadequate speckle pattern, etc. It can also give you a dry run, to test out your camera triggering system. Here, the cameras were triggered with a function generator using a 0.8 s period 0 to 5 V square wave. This same function generator signal was also sent to the data acquisition system that captured the load, laser extensometer, thermocouples, and crosshead displacement data to synchronize all measurements.

After the experiment, the DIC images were analyzed using the commercially-available Vic-3D software [29] across a region of interest (ROI), centered on the crown of the wire (2114×16 pixels). For the cables, each individual wire was assigned its own ROI. If one ROI was chosen for the entire cable FOV, then spurious strains would result due to wires moving past each other. The 3×3 rule (3×3 pixels per speckle with 3×3 speckles per subset) is a good guide to quickly assess speckle size, speckle spacing, and pixel subset size. In general, larger subsets lead to better correlation between the reference image and the deformed image, but subsets that are too large can result in "over-smoothing" of the strain fields. Vic-3D uses the same constant strain shape functions by eq. (2.1.4) as was used in Experiment 1. Thus, the choice of subset size is a tradeoff between the correlation strength and the desired spatial resolution of strain inhomogeneities to be resolved. Our 19×19 subset included roughly 3×3 speckles and corresponded to a dimensional region of about 0.33 mm $\times$ 0.33 mm (or $0.43d \times 0.43d$ in wire diameters). The analysis grid chosen was 1057×8 with 2×2 pixel spacing. The displacement of each grid point in 3D space was found by matching the deformed subsets to the reference subsets using Vic-3D's default cross correlation function, the normalized sum of squared differences eq. (2.1.3).

The displacement gradients were then used to calculate the engineering strain tensor ε. In this manner, a large amount of DIC data (roughly 25 gigabytes) was generated for each experiment.

Note that Vic-3D calculates the (total) strain by comparing the current deformed image against the reference (zero strain) image, instead of calculating the increment in strain comparing the current deformed image against the previous deformed image. The incremental method produces a better correlation between images, since for a smaller deformation increment the constant strain in the subset is a better assumption. However, the incremental method can lead to measurement error accumulation as an increasing number of images are compared. On occasions when automatic correlation fails in Vic-3D (such as when material leaves the FOV and later returns), the software allows the user to manually choose a "seed point" in the current image to help the software find a correlation match.

2.5   SE Wire Experimental Results

In this experiment, the wire was cycled 25 times in room temperature air (22 °C), under displacement control, at a global strain rate of $\dot{\delta}/L = \pm 5 \times 10^{-4}$ s^{-1}. For each cycle, the load frame stretched the specimen until $\delta_e/L_e = 7.5$ %, and then unloaded until $P/A_0 = 6.6$ MPa (a small load, just to keep the wire taut). The mechanical response shown in Fig. 2.5 exhibits typical superelastic shakedown behavior, where the upper plateau evolves downward in stress and the residual strain at near zero load ratchets forward in progressively smaller increments with cycling. In addition, the length of both plateaus decreases, the stress-strain response becomes more sigmoid-like in shape, and the magnitude of the hysteresis (area within the loop) diminishes. All these features are well known aspects of uniaxial NiTi wire behavior (see [57] for more details).

IR images and DIC images were taken at 1.25 frames/s during the experiment. Figure 2.6 shows an IR and a DIC snapshot at $t = 121$ s, corresponding to $\delta_e/L_e = 2.75$ % during the first-cycle upper plateau in Fig. 2.5. It shows a single $A \rightarrow M^+$ front propagating downward that is detected in the IR image as a local hot spot and in the DIC image as a near discontinuity in axial strain from 0.9 to 7.5 % (about 2 wire diameters in axial extent). To confirm the DIC measurements, we compared the extensometer measurement of strain δ_e/L_e against the average DIC strain between the extensometer tags $\bar{\varepsilon}_{zz}$. The two measurements track together nicely in Fig. 2.7.

Figure 2.8 shows contour plots of the axial strain field history, $\varepsilon_{zz}(z,t)$, and temperature field history, $T(z,t)$, during the first 5 cycles. In each plot the wire axial coordinate (z) is
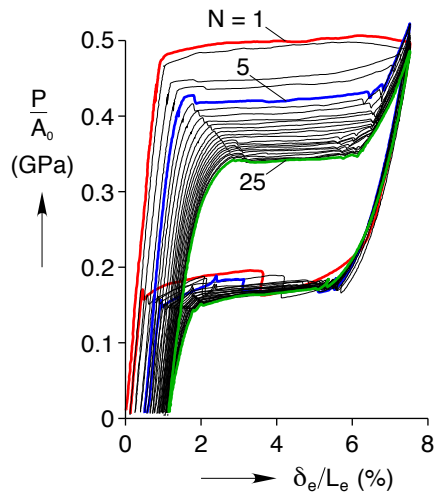
Figure 2.5 SE wire superelastic mechanical response to 25 load-unload cycles in room temperature air (22 °C).
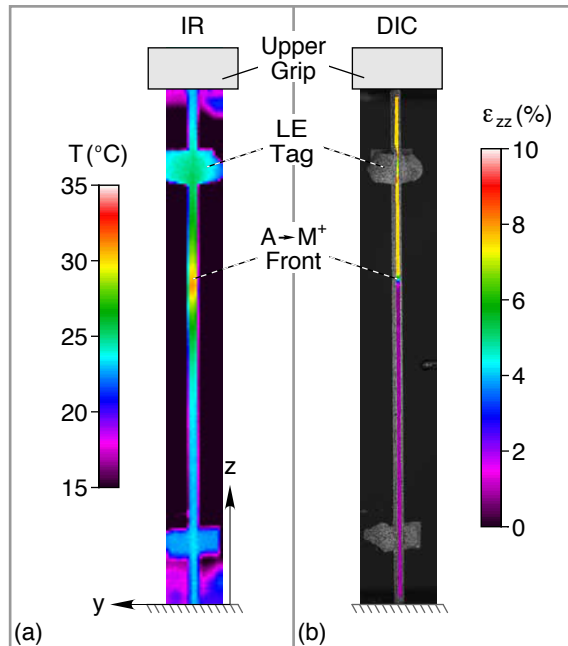
Figure 2.6 SE wire snapshots at $t = 121$ s of temperature (a) and axial strain (b) fields during first cycle loading ($A \rightarrow M^+$ propagation).

normalized by the initial free length (L), as shown on the left-hand vertical scale. The stress history is overlaid for reference, and its scale is the right-hand vertical axis. The axial strain contour plot was created by averaging the strain across the lateral (y) direction of the wire to create a 1-D axial profile from each DIC image. A selected sequence at 1.6 s intervals was then stacked side-by-side ($\approx$ 200 images per cycle) and synchronized with time (t) along the horizontal axis. 3D DIC provides a wealth of information, but here we are mostly
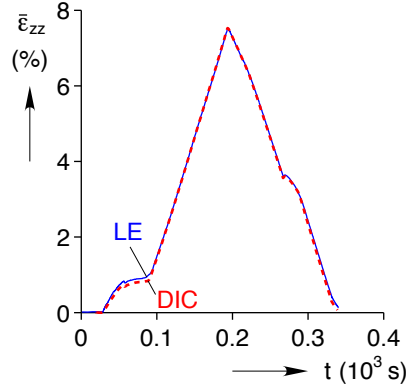
Figure 2.7 SE wire, cycle 1 comparison of the strain measured by the laser extensometer against the average DIC strain between the extensometer tags.

interested in axial strains. Plots of other strain components, such as lateral (ε_{yy}) and shear (ε_{zy}) strains show similar discontinuities where fronts exist, but are not shown here in the interest of space. The temperature contour plot was similarly created from the IR images at 1.6 s intervals ($\approx$ 200 images per cycle). Both fields are shown in the Eulerian frame (current configuration), so the top of the free length moves up during loading and down during unloading according to the upper grip displacement.

During the first cycle, the sharp transition between high strain and low strain regions in Fig. 2.8a clearly shows transformation fronts (locations of high strain gradient) traversing the specimen length. These fronts also manifest themselves as local temperature changes in the specimen, which can be seen in Fig. 2.8b, due to the exothermic ($A \rightarrow M^+$ during loading) and endothermic ($M^+ \rightarrow A$ during unloading) latent heat (enthalpy) exchanges with the environment. Since stagnant air is a relatively poor heat transfer medium, the $A \rightarrow M^+$ transformation creates self-heating and fronts show up as local hot spots (above room temperature); whereas, the $M^+ \rightarrow A$ transformation creates self-cooling and fronts show up as local cold spots (subambient temperatures). At this relatively slow loading rate, a single $A \rightarrow M^+$ transformation front starts at the top grip where there is a stress concentration due to clamping, and it propagates downward at nearly constant speed until $z/L = 0.1$ when the crosshead motion is reversed. The $A \rightarrow M^+$ strain jump is about $\Delta\varepsilon_{zz} = 7.5 - 0.9 = 6.6$ %. During unloading, this initial front remains static momentarily until the stress reaches the lower plateau, at which point it reverses direction, propagating upward until a new $M^+ \rightarrow A$ front starts from the top grip. These two fronts then propagate towards each other at about half the initial speed until they coalesce and annihilate each other at $z/L = 0.67$, at which point the end of the lower stress plateau is reached and further unloading occurs via a uniform strain field. The $M^+ \rightarrow A$ strain jump is about $\Delta\varepsilon_{zz} = 0.3 - 6.0 = -5.7$ %.

The magnitude of the slope of each strain discontinuity (front) in Fig. 2.8a is related

31
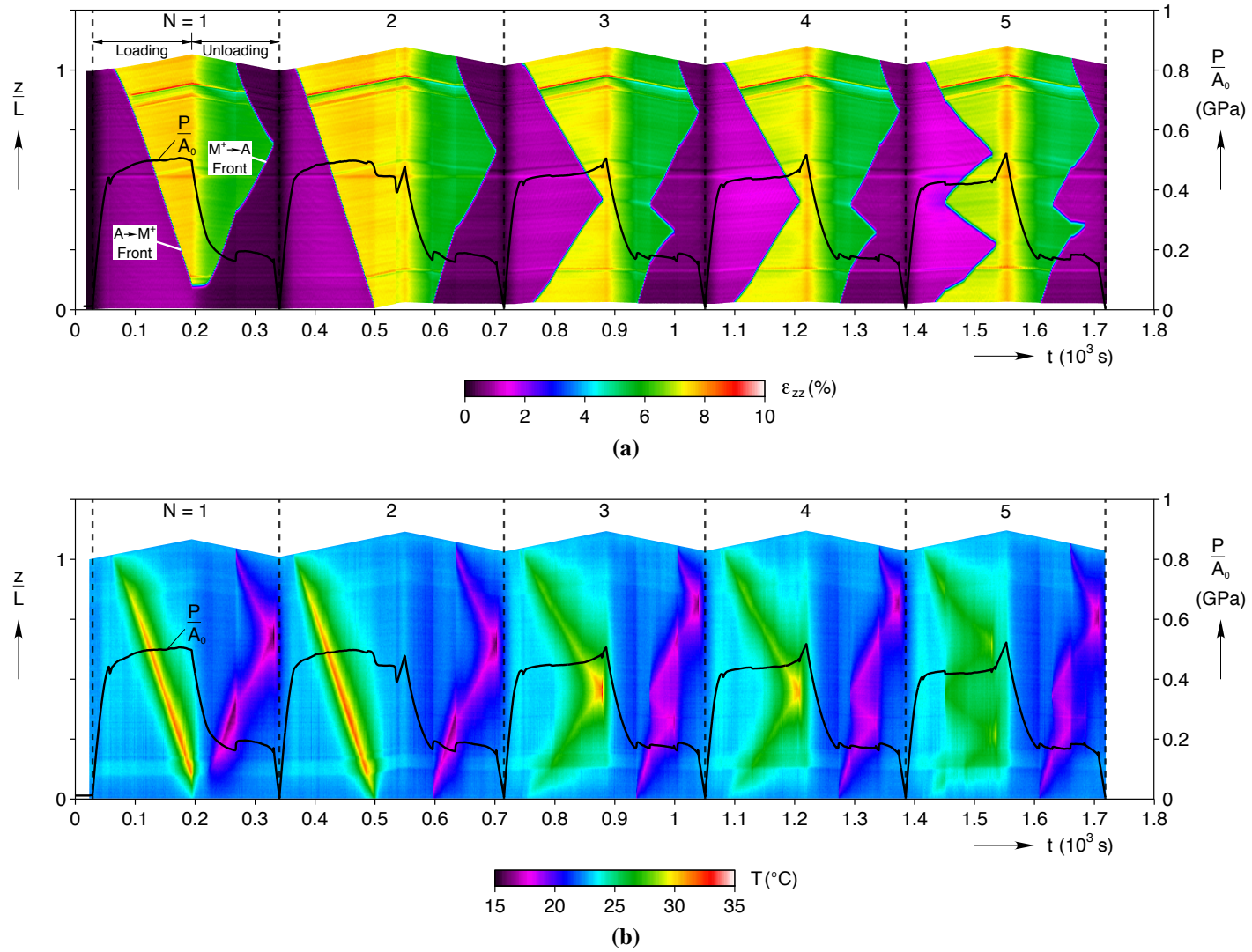
Figure 2.8   SE wire, cycles 1-5: (a) axial strain field history, (b) temperature field history.

to its front speed (c). As discussed in [110], transformation fronts tend to propagate at the same speed according to

$$c = \frac{\dot{\delta}}{n\,\Delta\varepsilon_{\mathrm{P}}}, \tag{2.5.1}$$

where $\dot{\delta}$ is the elongation rate, n is the number of fronts propagating, and $\Delta\varepsilon_{\mathrm{P}}$ is the strain jump across the stress plateau. Equation (2.5.1) is simply a statement of axial compatibility between the grips, written in rate form, for steady-state (equilibrium) conditions. As new fronts are generated (increasing n) they can slow down, since each front contributes to the prescribed the prescribed global elongation rate ($\dot{\delta}$). On the other hand, if the strain jump ($\Delta\varepsilon_{\mathrm{P}}$) decreases, as it does from cycle to cycle, the fronts speed up. In the absence of boundary effects or other inhomogeneities that would change the local temperature or stress conditions, all fronts tend to propagate at the same rate, since this minimizes the local self-heating (or self-cooling) in the specimen and is energetically favorable.

The axial strain field is useful to precisely locate fronts (compared to the temperature field that is more diffuse due to axial heat conduction) and to quantify strain jumps, but the temperature field is useful to explain the stress history. The thermo-mechanical coupling in NiTi is clearly illustrated in Fig. 2.9, where the stress closely follows the trends of the temperatures $T_{A \to M^+}$ and $T_{M^+ \to A}$, consistent with the Clausius-Clapeyron relation (eq. (1) in [25]), which predicts a linear relationship between transformation stress and temperature. These transformation front temperatures were simply found from the maximum and minimum temperatures in the gage section during front propagation.

Returning to Fig. 2.8a, one may notice three anomalies in the strain field history that exist during all cycles. Two of the anomalies are real disturbances in the strain field caused by the epoxy tabs for the laser tags at $z/L = 0.13$ and 0.86. The DIC strain measurements capture the fluctuations in strain caused by the constraint imposed by the epoxy mass and the slight stress concentration at these locations. The third anomaly consists of two slight horizontal streaks at about $z/L = 0.56$. The bottom streak does not follow the specimen displacement, while the upper streak does, which indicates a flaw in the CCD that affected both the deformed images and the reference image. This was confirmed by changing lenses and observing the same artifact on a new specimen. The bottom streak was in the exact same pixel location, verifying that the streaks are an artifact of the CCD imperfection and should be disregarded.

The transformation fronts in the second cycle propagate along similar paths as in the first cycle. The only significant difference is that the $A \to M^+$ front reaches the bottom of the gage length, where, as frequently happens, the lateral contraction at the front caused the wire to slip out of the bottom grip by a small amount. This slippage can be seen as a drop in the stress history as the front reaches the lower grip. It also created a rigid body
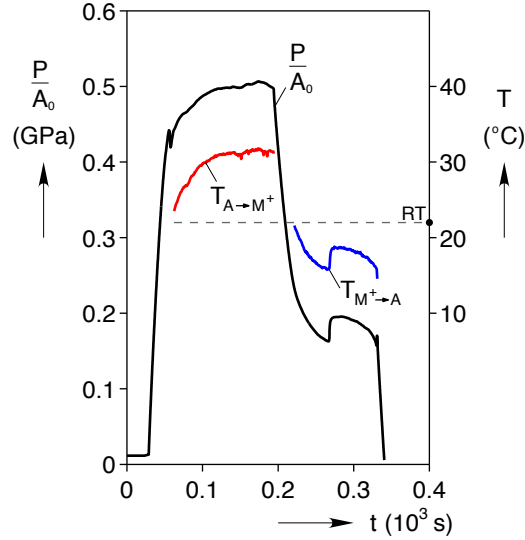
Figure 2.9   SE wire, cycle 1 stress and front temperature histories.

translation of the material points between $t = 500$ s and $t = 535$ s. Since sudden stress drops do occur due to localized phase transformation activity, it can often be difficult to determine whether load discontinuities are due to phase transformation or experimental problems. Here, DIC clearly identified this as an experimental problem, not the actual material response. The transformation did not reach the bottom grip during the first cycle but did during the second cycle. The reason was that the load frame was programmed to reverse the crosshead direction when $\delta_e/L_e > 7.5$ % (not the global strain). The average strain in the M^+ region reached $\varepsilon_{avg} = 7.53$ % (by DIC) in the first cycle, but only $\varepsilon_{avg} = 7.45$ % (by DIC) in the second cycle due to superelastic shakedown, so the crosshead proceeded further during this cycle before $\delta_e/L_e > 7.5$ %.

The remainder of the cycles exhibited typical superelastic shakedown and no further significant grip slippage occurred. As the cycle number (N) increases, we see an increasing number of fronts (Fig. 2.8a), probably due to accumulated defects in the wire that reduce the energy barriers for strain localization. One can see that the strains in the "austenite" (low strain) regions evolve to slightly increased strains, consistent with the small amount of residual strain accumulation (see again Fig. 2.5), which results in a decrease in strain jump across the fronts. With cycling the upper plateau moves downward in stress and its length (in time, or equivalently, $\Delta\varepsilon_P$) decreases. This means that transformation via front propagation is exhausted at earlier global strains, consistent with the somewhat higher front speeds according to eq. (2.5.1). Further transformation involves a nearly uniform strain field, and the stress rises steeply to its (nearly) same value at maximum elongation. This is the reason for the progressively larger stress "spikes" seen at the end of each loading increment.

34

Propagating fronts during later cycles are also accompanied by progressively less temperature deviations from room temperature than the first cycle, as shown in Fig. 2.8b. The stress history exhibits a number of small jumps and drops, each of which (except for the grip slippage problem at 500 s in cycle 2) is associated with by a change in front kinetics, in which fronts are created, annihilated, or change speed. By cycle 5 there are as many as four $A \rightarrow M^+$ fronts during loading and three $M^+ \rightarrow A$ fronts during unloading. A number of fronts even start and stop (see the unloading portion of cycle 5), apparently due to inhomogeneous defect accumulation in the wire that affects the local thermodynamic driving force for front propagation.

By cycle 25, as shown in Fig. 2.10a, there exist as many as eight fronts during loading and four fronts during unloading, with some again propagating in "fits and starts". The fronts in the IR images (Fig. 2.10b) are now quite faint, although still discernible upon close inspection. This occurs for two reasons: (1) the smaller strain jumps and residual strain accumulation indicate that local plasticity has locked-in micro pockets of residual martensite, such that a smaller fraction of the material within a given wire cross-section actually participates in the transformation to release or absorb latent heat, and (2) more fronts during the transformation effectively distribute the self-heating and self-cooling more evenly across the specimen. The persistence of only four fronts during unloading means the fronts must move relatively quickly to traverse the gage length, and self-cooling still decreases the specimen to as low as 18.4 °C. This causes the stress to steadily decrease during the $M^+ \rightarrow A$ transformation (unloading); whereas, the stress remains relatively constant during $A \rightarrow M^+$ transformation (loading) where the latent heat was distributed among twice as many (8) fronts.

The contour maps shown in Fig. 2.8 and Fig. 2.10 give a good overview of the thermomechanical behavior, but quantitative data can be somewhat difficult to see, so Fig. 2.11 shows selected strain profiles at 16 s intervals during the first load-unload cycle, all mapped back to the Lagrangian (reference) frame. The dashed arrows show the progression of profiles in time. Note that, as previously discussed, the sharp oscillations at $z/L = 0.13$ and 0.86 are due to the LE tags and the oscillation at $z/L = 0.56$ is the artifact due to the CCD imperfection.

Lastly, Fig. 2.12 shows a comparison of strain ε_{zz} profiles for cycles $N = 1, 5$, and 25 during loading at a selected strain level ($\delta_e/L_e = 4.5$ %) midway across the upper stress plateau. The three strain profiles correspond to times $t = 117.4$ s, 1462.2 s, and 7654.2 s, respectively. One can again see the number of fronts (strain jumps) increases and the magnitude of the strain jumps decreases with cycle number. Comparing cycles 1 and 25, the strain jump across a $A \rightarrow M^+$ transformation front during loading decreases from about $\Delta\varepsilon_{zz} = 6.6$ %
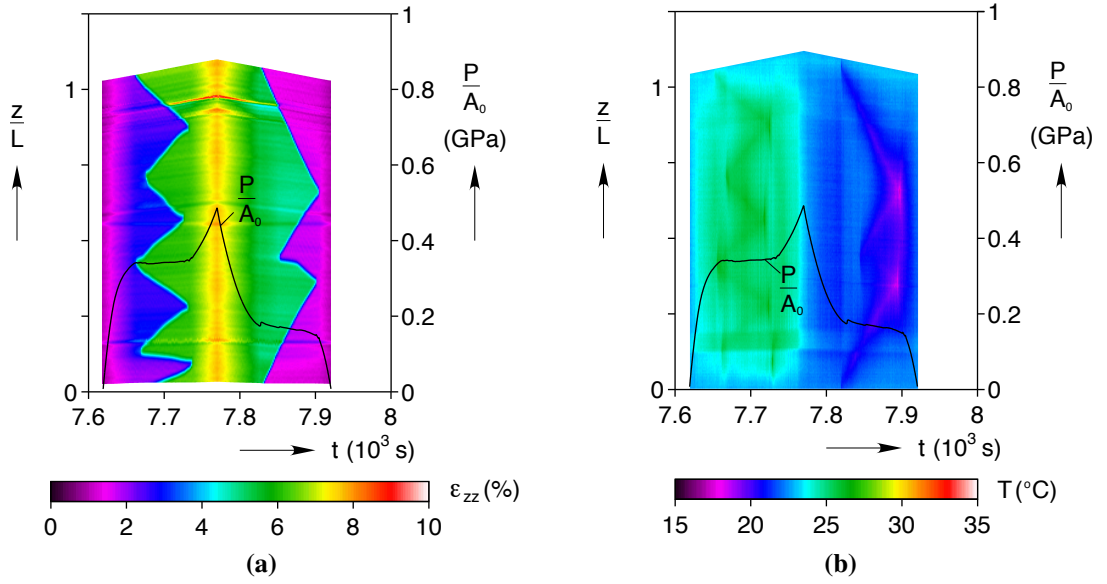
Figure 2.10 SE wire, cycle 25: (a) strain field history, (b) temperature field history.

to about 3.5 % (= 6.1 − 2.6 %), and the strain jump across a $M^+ \rightarrow A$ transformation front during unloading (not shown) changes from −5.7 % to about −3.5 % (= 1.5 − 5.0 %). The strain jump decrease is likely due to localized residual stresses, caused by plastic slip on previous cycles [82]. The residual stresses "lock in" pockets of martensite, which increases the macroscopic residual strain with each cycle and decreases both the loading and unloading strain jumps. We can also see non-linearity prior to and after the stress plateaus, indicating that the pockets of martensite and pockets of untransformed austenite cause macroscopically uniform transformation before and after the plateaus, further decreasing the strain jumps.

2.6   Summary & Conclusions

The wealth of quantitative information DIC provides on full-field surface deformations makes it an extremely useful tool in experimental mechanics. The basics of DIC were presented along with our recommendations for specimen preparation and experimental setup to achieve accurate measurements. Following this, we demonstrated an experiment where digital image correlation (DIC) and infrared (IR) imaging were used to quantify the nonuniform strain and temperature fields during superelastic cyclic loading. All observations were consistent with the known cyclic behavior of superelastic NiTi wire. (1) The mechanical response shook down with progressively shorter and lower transformation plateaus. (2) Transformation fronts in the temperature field history matched up with the axial strain field
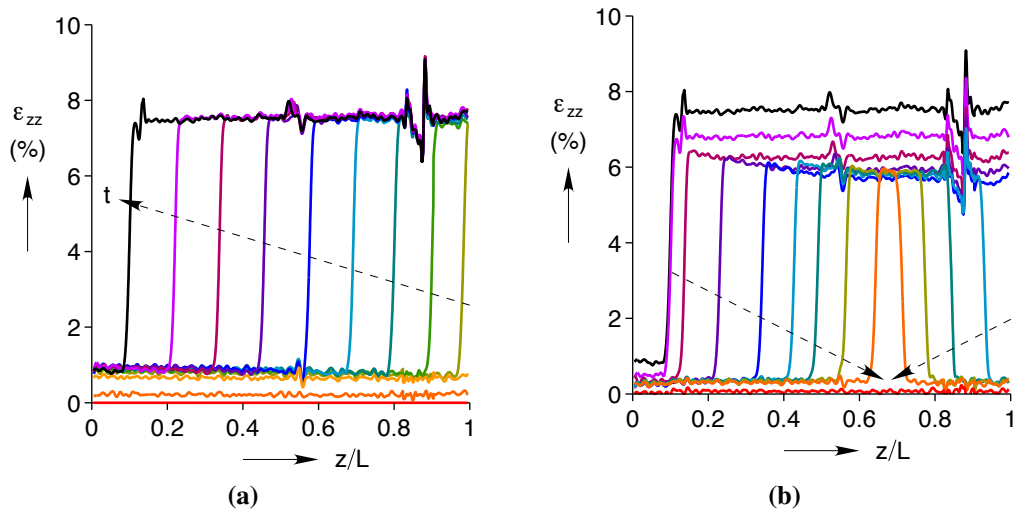
Figure 2.11 SE wire, cycle 1 axial strain profiles during (a) loading and (b) unloading. Shown in the reference frame.
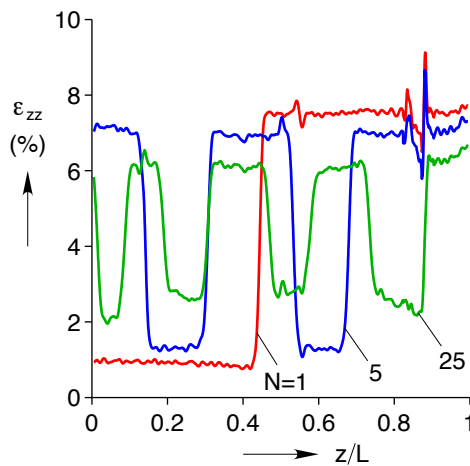
Figure 2.12 SE wire, axial strain profiles for cycles 1, 5, and 25 during loading at $\delta_e/L_e = 4.5\%$ (reference frame).

history. (3) Abrupt as well as gradual changes in the axial stress were traced back to fronts nucleating or thermally interacting. (4) Continued cycling produced greater numbers of fronts, each with a smaller strain jump across it and a smaller temperature excursion from the ambient temperature. Thus, the experimental setup was shown to be operating properly and well suited to measuring phenomena in superelastic NiTi wires in tension.

Chapter 3

Isothermal Cable Tension Experiments

This chapter introduces the two cable designs studied: a 7×7 right regular lay and a 1×27 alternating lay. The purpose is to familiarize the reader with the designs and show the significant differences in their isothermal tensile responses. Overall, the 7×7 construction has a mechanical response similar to that of straight wires with propagating transformation fronts and distinct stress plateaus during stress-induced transformations. The 1×27 construction, however, exhibits a more compliant and stable mechanical response, trading a decreased force for additional elongation, and does not exhibit transformation fronts due to the deeper helix angles of the layers.

The organization of this chapter is as follows. Section 3.1 describes the geometry of the two cable designs, material calorimetry, and specimen preparation. Section 3.2 lists modifications to the experimental setup detailed in section 2.4. Section 3.3 contains the experimental results, and Section 3.4 provides a summary of results and conclusions.

3.1   Specimens

Two NiTi cable designs were obtained from Fort Wayne Metals, Research Products Corp. (Fort Wayne, Indiana). Figure 3.1 shows annotated photographs of the 7×7×0.275 mm design (right regular lay), as well as a less conventional 1×27×0.226 mm cable made from slightly thinner wires. The identifier 7×7×0.275 mm indicates the number of strands, the number of wires in each strand, and the wire diameter, respectively. Fort Wayne Metals shape set the cable constructions by heat treating the specimens at roughly 500°Cfor a few minutes while the wires were mechanically constrained. As a result, the wires did not unravel if the cables were disassembled. Each experiment described in Section 3.3 and in the subsequent chapters was performed on a new specimen, as-received from the manufacturer.
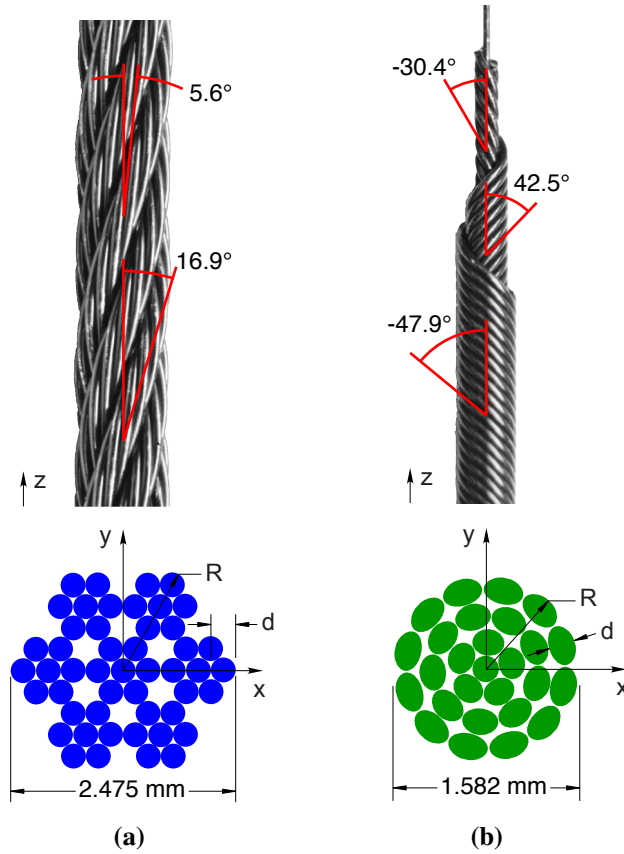
Figure 3.1   Two NiTi cable designs, showing cross-sections (lower schematics) and side views with dimensions (upper photographs): (a) 7×7×0.275 mm, (b) 1×27×0.226 mm.

3.1.1   Cable Geometry Details

Figure 3.1 shows cross-section schematics and side view photographs of the two cable designs, including the measured cable diameters and helix angles[a] (α_0) of individual wires to the cable's global axis (z-axis). We measured the reference helix pitch (p_0) and mean helix diameter (D_0, to the wire centerline) under a microscope with a micrometer translation stage to calculate the reference helix angle by $\alpha_0 = \tan^{-1}(\pi D_0/p_0)$. The pitch was measured by averaging the linear distance of at least seven helical turns, resulting in a more accurate measurement.

The first (7×7) cable design is a traditional right regular lay, where the six exterior strands are wound in a right-handed helix ($\alpha_0 = 16.9°$) around the core strand (Fig. 3.1a). Within an exterior strand, six wires are wound in a left-handed helix about the central helical wire, while the core strand has six wires wound in a right-handed helix ($\alpha_0 = 11.3°$, not

---

[a]Note that α_0 is measured here from the loading axis (z-axis), which is the complement of the angle conventionally used for helical springs (measured from a lateral axis.)

shown in Fig. 3.1a, but see Section 4.2) around the straight core wire ($\alpha_0 = 0°$). The angle of an exterior wire in an outer strand, however, varies with position ($5.6° \leq \alpha_0 \leq 28.2°$). The maximum misalignment of an exterior wire to the cable axis is at the point where the wire contacts the core strand.

The second (1×27) cable design is more tightly wound and was selected to provide a comparison with the previous design. Strictly speaking, it is a single layered strand, not a multi-strand cable, yet we will continue to call it a cable. The outer layers of the 1×27 were removed to reveal the alternating helices shown in Fig. 3.1b. The center core wire is straight ($\alpha_0 = 0°$). Progressing radially outward, the next three helical layers are composed of 5 wires at $\alpha_0 = -30.4°$, 9 wires at $\alpha_0 = 42.5°$, and 12 wires at $\alpha_0 = -47.9°$, respectively.

3.1.2 Material Calorimetry

The transformation temperatures of a wire from a 7×7×0.275 mm and a wire from a 1×27×0.226 mm were measured by a Perkin Elmer Pyris 1 differential scanning calorimeter (DSC) and a TA Instruments Q2000 DSC, respectively. The scan rate was ±10°C/min and Indium was used as a reference material to calibrate the temperature and heat flow. The masses of the specimens excised from the 7×7 and 1×27 cables were 30.93 mg and 18.48 mg, respectively, and specimens were prepared as outlined in Shaw *et. al.* [108]. As seen in the thermograms of Fig. 3.2, both materials exhibit a clear two step transformation from A to rhombohedral phase (R) and then $R \rightarrow M$ during cooling, as is common for commercial Nitinol. During heating, the 7×7 material (Fig. 3.2a) has overlapping $M \rightarrow R$ and $R \rightarrow A$ transformations creating a single peak, while the 1×27 (Fig. 3.2b) has partially
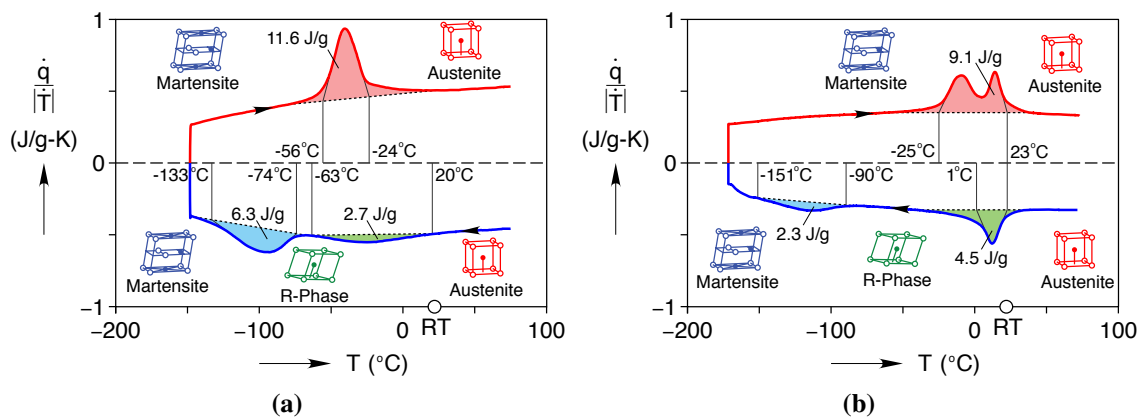
Figure 3.2 Differential scanning calorimetry thermogram of (a) 7×7 helical wire and (b) 1×27 core wire

separated $M \to R$ and $R \to A$ transformations. The austenite (A_s and A_f), martensite (M_s and M_f) and rhombohedral (R_s and R_f) transformation temperatures are indicated on the thermograms, as well as the corresponding specific enthalpies of transformation. The 7×7 material is clearly superelastic at room temperature since $A_f = -24$ °C. The double peak for the 1×27 during heating makes it somewhat less clear, but the mechanical response at room temperature (shown later in Fig. 3.4b) confirms that the material is indeed a superelastic alloy, and we estimate remains superelastic down to about 10°C.

3.1.3   Specimen Preparation

The specimen preparation for DIC and laser extensometer measurements was the same as detailed in Section 2.3. A typical speckle pattern is shown in Fig. 3.3b on a core wire extracted from a 1×27 cable. The magnified image is a portion of the actual image used for the DIC analysis and shows 47 pixels across the wire diameter along with a typical 19×19 subset used in the correlation analysis.

3.2   Cable Experimental Setup Modifications

The cable experiments used the same experimental setup as described in Section 2.4 with a few modifications:

- The cable specimens were clamped in the same manner as the SE wire in Chapter 2, but the axial (z-direction) free lengths were roughly $L = 75$ mm. (Values for specific experiments are listed in Table 3.1, Table 4.1, and Table 5.1.)

- In tests prior to the experiments, we found that a minimum of 35 pixels across a straight wire was needed to properly resolve the axial strain for DIC, so 47 pixels was selected to be conservative. A cable is made up of many individual wires, each of which must be analyzed independently. Hence, although the diameter of the cable was 1.58 mm or 2.48 mm, the DIC FOV was limited by the camera resolution and the diameter of the individual wires (0.226 mm or 0.275 mm) within the cables. And because the cable wires were roughly one third the diameter of the SE wire in Chapter 2, the DIC FOV was reduced from 45 mm to 15 mm. As shown in Fig. 3.1, 15 mm is only a fifth of the specimen gage length L. By contrast, the IR camera's FOV captured the entire specimen length, since it can measure the temperature of a wire only one pixel wide when calibrated and aligned properly. This difference in FOV is

41

emphasized in many of the forthcoming figures to assist the reader in interpreting the data.

- The DIC cameras were outfitted with Tamron CCTV 75 mm focal length lenses, as shown in Fig. 2.3a, rather than Fujinon HF75SA lenses. These smaller diameter lenses allowed the cameras to be placed close to the specimen with a smaller 18-20º stereo angle (better FOV overlap), without obstructing the view of the IR camera, as shown in Fig. 2.3a. The aperture diameters of the Tamron lenses were set to f/8 (9.4 mm) or f/6 (12.5 mm) depending on the depth of field required to keep the whole specimen in focus. The exposure time ranged from 50 ms for slow rate experiments ($\dot{\delta}/L \leq 10^{-4}$ s^{-1}) to 2.7 ms for higher rate experiments ($\dot{\delta}/L = 10^{-2}$ s^{-1}), which gave less than 0.1 pixel of specimen movement during the exposure.

- Once the DIC images were collected and analyzed, the Green-Lagrange strain $\boldsymbol{E}^{\mathrm{L}}$ was calculated, as opposed to the infinitesmal engineering strain ε. Line elements on the cable surfaces can undergo significant rotations, so it was important to chose a finite strain measure for the DIC data rather than ε. For infinitesimal strains and rotations $\boldsymbol{E}^{\mathrm{L}}$ and ε are equivalent, but here we have moderate strains ($\approx$ 4 % to 8 %), so a small difference exists. All mechanical responses are reported using the engineering strain measure by the LE ($\delta_{\mathrm{e}}/L_{\mathrm{e}}$). The difference between this and the averaged Green-Lagrange strain between the LE tags is $\bar{E}^{\mathrm{L}}_{zz} - \delta_{\mathrm{e}}/L_{\mathrm{e}} = 1/2\,(\delta_{\mathrm{e}}/L_{\mathrm{e}})^2 \approx 0.08$ % to 0.32 % strain, so the relative error is $\bar{E}^{\mathrm{L}}_{zz}/(\delta_{\mathrm{e}}/L_{\mathrm{e}}) - 1 = 1/2(\delta_{\mathrm{e}}/L_{\mathrm{e}}) \approx 2$ % to 4 %. This small difference is acceptable for our purposes, since $\boldsymbol{E}^{\mathrm{L}}$ fields are primarily intended to track strain localizations.

- The chiral architecture of a cable causes it to naturally unwind as it is stretched along its axis if one end is free to rotate. Here, however, the ends of the cable were rigidly clamped, preventing rotation about the z-axis, so a 2824 N-mm capacity torque cell (Futek TFF400) was added beneath the lower grip to measure the axial torque (M_z) in many of the experiments. In addition, the cables produced bigger axial loads (P) than the SE wire, so either 500 N (Instron model 2525-816) or a 5 kN (Instron model 2525-805) load cell was utilized, depending on the specimen size.

3.3 Experimental Results

Experimental results of the two cable designs are presented below in four subsections, an initial comparison of the mechanical response of the two cables subjected to a single
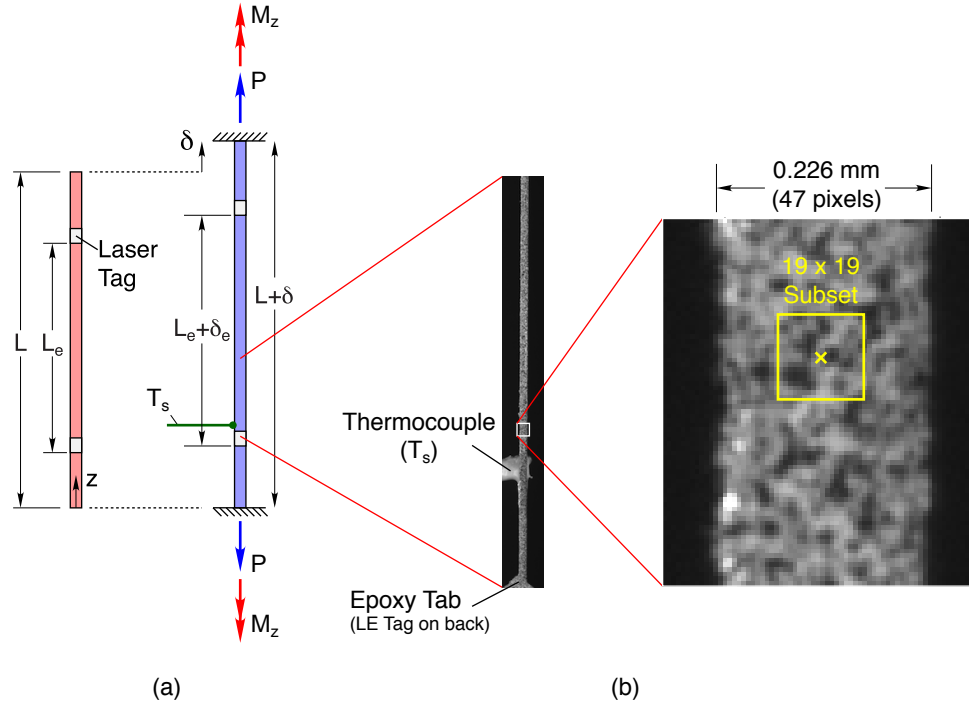
Figure 3.3 (a) Specimen schematic and free body diagram, (b) photograph of DIC field of view and close up of the speckle pattern on a 1×27 core wire.

load-unload superelastic cycle (Section 3.3.1), details of strain and temperature responses (Sections 3.3.2 and 3.3.3), and their multi-cycle shakedown behavior (Section 3.3.4). All these experiments were preformed at slow (nearly isothermal) elongation rates. Chapter 4 will present the slow-rate behavior of selected subcomponents of the two cables, and Chapter 5 will present a rate-sensitivity study of the cables and their subcomponents. A summary table of the experiments to be presented here is given in Table 3.1, showing the various specimens, dimensions, number of load-unload cycles N, and other experimental parameters. The experiment identifier starts with the type of specimen (C for cable, W for straight wire), then the cable/alloy type (1 for 7×7, 2 for 1×27), and then a lowercase letter appended for each experiment performed.

The average axial stress of each specimen is reported as P/A_0, where P is the tension force along the z-axis and $A_0 = n\pi d^2/4$ is a chosen reference area, based simply on the number of wires (n) in the specimen and the individual wire diameter (d). Note that this differs somewhat from the projected cross-sectional area of the wires (normal to the tensile axis), since cross-section normals of most wires are misaligned to the cable axis. Circular wire cross-sections become projected approximately as ellipses[b] in the overall cable's cross-

---

[b]The intersection of a helical wire with a plane z =constant is not quite an ellipse due to the wire curvature and its finite thickness, especially for tightly wound wires with small spring indices ($Ci \equiv r_i/r_w \simeq O(1)$, where r_i and r_w are the nominal helix radius and wire cross-section radius, respectively.)

Table 3.1 Experimental matrix and parameters

Specimen	Icon	D (mm)	Exp ID	Condition	L (mm)	L_e (mm)	N	$\dot{\delta}/L$ (s^{-1})
7×7×0.275 mm		2.475	C1a	dry	77.33	50.30	1	$\pm 2.5 \times 10^{-5}$
			C1b	lubricated	76.18	49.76	1	$\pm 2.5 \times 10^{-5}$
			C1c	dry	74.85	49.92	1	$\pm 1 \times 10^{-5}$
			C1d	dry	82.21	50.58	6	$\pm 1 \times 10^{-4}$
7×7 core wire		0.275	W1a	–	85.90	52.70	6	$\pm 1 \times 10^{-4}$
1×27×0.226 mm		1.582	C2a	dry	80.87	49.90	1	$\pm 1 \times 10^{-4}$
			C2b	lubricated	86.73	50.56	1	$\pm 1 \times 10^{-4}$
			C2c	dry	89.33	50.81	6	$\pm 1 \times 10^{-4}$
1×27 core wire		0.226	W2a	–	75.09	49.12	6	$\pm 1 \times 10^{-4}$

section. Nevertheless, the simple summation of wire cross-sections is a straightforward metric for reporting the macroscopic cable response and for later comparison with the response of a single straight wire.

The reaction torque, i.e., moment about the z-axis (M), generated by constraining the rotation of the specimen at the grips, is reported as MR/J_0, where R is the radius from the center of the specimen to the outermost point in the cross-section, and J_0 is a chosen reference torsion constant. One will recognize $\tau = MR/J_0$ as the classical formula for the maximum shear stress at the outer radius of a linearly elastic, straight, cylindrical rod subjected to twisting about its axis. Our torsion constant was selected simply as the polar moment of inertia of an idealized (fictitious) cross-section calculated by

$$J_0 = n\frac{\pi d^4}{32} + \sum_{i=1}^{n} \frac{\pi d^2}{4} r_i^2, \tag{3.3.1}$$

where the first term is the contribution of individual wires about their own axes and the second term is the sum of the parallel axis theorem contributions. Here, i is the index of the wire, r_i is the mean radius from the central z-axis of the specimen to the wire's centerline, and wire cross-sections are treated as circles rather than ellipses. Calculated values of A_0 and J_0/R are provided in Table 4.1 for both cables and their components. While the elementary theory does not strictly apply here, J_0 was chosen for simplicity to give a quick approximate sense of the average normal stress versus shear stress contributions in the different cable and strand designs.

3.3.1 Initial Comparison of the Two Cables

Figure 3.4a shows the average axial stress versus LE strain of four experiments performed on the two cable designs. For each cable design one specimen was as-received (dry, solid line) and one was lubricated (dashed line). To have a controlled comparison the cables were not painted with speckles for these experiments (so DIC was not performed), and each pair of dry/lubricated specimens was subjected to the same slow rate to avoid thermomechanical coupling effects in room temperature air ($\dot{\delta}/L = \pm 2.5 \times 10^{-5}$ s^{-1} for both 7×7 specimens and $\dot{\delta}/L = \pm 1 \times 10^{-4}$ s^{-1} for both 1×27 specimens). Prior to the experiments shown by dashed lines, 7×7 and 1×27 cable specimens were immersed in penetrating lubricant (Grignard TN-3, composed of a non-petroleum group of synthetic di-esters) for 1 minute. Following each experiment, the lubricated specimens were disassembled to confirm that the lubricant penetrated to the core.

Figure 3.4a addresses whether specimen lubrication has an appreciable effect on a cable's mechanical response, and the answer is no. The figure shows a near exact match[c] between the lubricated and dry responses, which suggests that static friction between the wires was quite high and prevented relative sliding of subcomponents. This is consistent with Costello [31], who devotes an entire chapter of his book on Wire Rope to argue that kinetic friction is a small effect in linear elastic cables. In the case of the single 1×27 strand, the argument is simple. If the entire strand is to stretch uniformly, the helical line of contact between the core wire and helical wires also stretches uniformly, so negligible relative motion exists between the core and helical wires. This indeed seems to be the case for the 1×27 cable, where the loading responses of the lubricated and dry specimens are virtually identical. The 7×7 cable has additional complications due to the motion of propagating fronts that may not be the same from wire to wire, as will be seen in Section 3.3.2. Nevertheless, the effect of lubrication is still barely noticeable, so further experiments were all performed on dry specimens.

For reference, Fig. 3.4b provides the uniaxial tension responses of the straight core wires that were removed from the respective cables. Both wires are superelastic at room temperature, but the mechanical responses are not identical. The 7×7 core wire has a larger loading plateau stress (526 MPa versus 481 MPa), a larger plateau strain (7.2 % versus 5.0 %, during loading), and a narrower stress hysteresis (238 MPa versus 260 MPa) compared to the 1×27 core wire. Also, the initial nonlinearity near 0.5 % during loading in the 1×27 core wire response is due to the R-phase [83], which is absent in the 7×7 core wire response at this temperature.

---

[c]While the loading responses of the 1×27 specimens match quite well, the unloading responses are different since unloading began at different maximum strains in the two experiments.
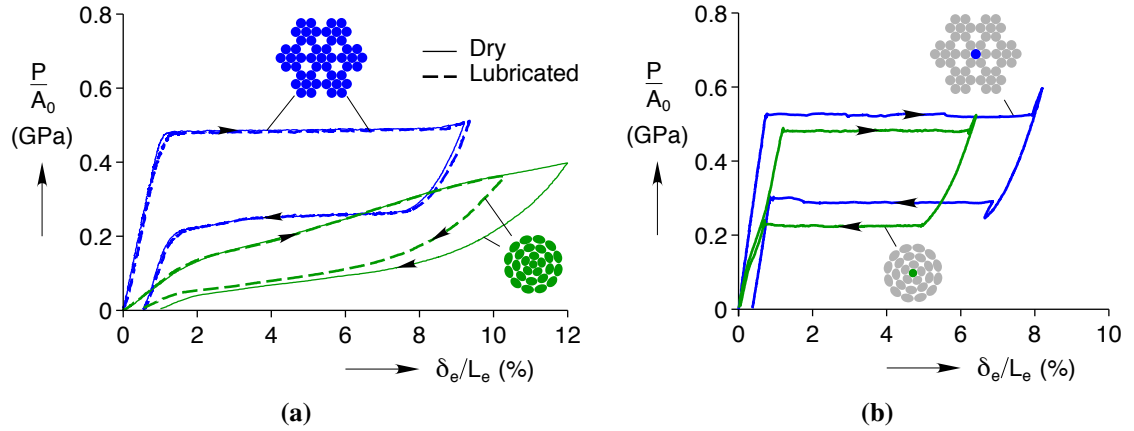
Figure 3.4 Room temperature superelastic tension responses: (a) comparison of 7×7 (Experiments C1a & C1b) and 1×27 (Experiments C2a & C2b) cables, also showing lubricated vs. dry cables, (b) responses of the straight core wires extracted from the two cables (first cycle of Experiments W1a & W2a).

Comparing the dry 7×7 cable response in Fig. 3.4a to that of its core wire in Fig. 3.4b, the cable response is similar to that of a single superelastic wire in pure tension, since the force has been divided by the cross sectional area of all 49 wires. It has distinct loading and unloading plateaus commonly found in NiTi wires, which suggest the presence of propagating transformation fronts. Although the cable was strained to $\delta_e/L_e = 9.3$ %, just beyond the loading plateau, most of this deformation was recovered with only 0.5 % residual strain remaining after unloading. The tensile load P was 1.42 kN (319 lbf) on the upper plateau. These characteristics should be encouraging for engineers wishing to leverage the excellent properties of SMA wire into a flexible, compact form that can withstand relatively large forces.

The 1×27 response, on the other hand, is significantly different from the typical uniaxial behavior of the SMA wires from which it is constructed. The 1×27 cable response is nonlinear with a slight knee near 2 % strain, but it has no obvious load plateau, i.e., it maintains a positive tangent modulus throughout loading-unloading. Also, no upturn in tangent modulus is seen, even by the maximum gage strain of $\delta_e/L_e = 12$ %. Here, a reduced axial force and a more compliant behavior has been traded for a larger recovery strain of about 11 %, with a final residual strain of about 1 %. In handling, the 1×27 specimen is also quite flexible in bending due to its larger helix angles that avoids direct tension/compression along the axis of the individual wires.

Thus, a wide range of cable behaviors can be achieved by simply varying the construction, which represents an opportunity for engineers to tailor the response to match the desired characteristics of specific applications. In particular, the 7×7 design might be desirable

where a high initial stiffness is needed, yet distinct load plateaus would be used to mitigate overload conditions or act as a mechanical switch. The 1×27 might be appropriate for those applications where a larger recoverable stroke and increased bending compliance are needed and/or a more stable axial response is desired.

The following two subsections present further details of the two cables' responses, one experiment on a 7×7 specimen at $\dot\delta/L = \pm 1 \times 10^{-5}$ s^{-1} (Experiment C1c), and one on a 1×27 specimen at $\dot\delta/L = \pm 1 \times 10^{-4}$ s^{-1} (Experiment C2a).

3.3.2   Details of the 7×7 Cable Response

Figure 3.5 shows the mechanical response during Experiment C1c on a 7×7 specimen, at a rate 2.5 times slower than that of Fig. 3.4. Figure 3.5a shows the mechanical response versus LE strain in terms of the normalized axial load (P/A_0, left axis) and normalized axial torque reaction (M_zR/J_0, right axis). Since it often helps in the interpretation of experimental data to not suppress the importance of time, Fig. 3.5b shows the time histories of average axial strains (upper plot) and the mechanical reactions (lower plot) against a common time axis. The upper plot shows the average strain derived from the grip displacement (δ/L, dashed line), which was controlled as a simple up-down ramp over the experiment duration
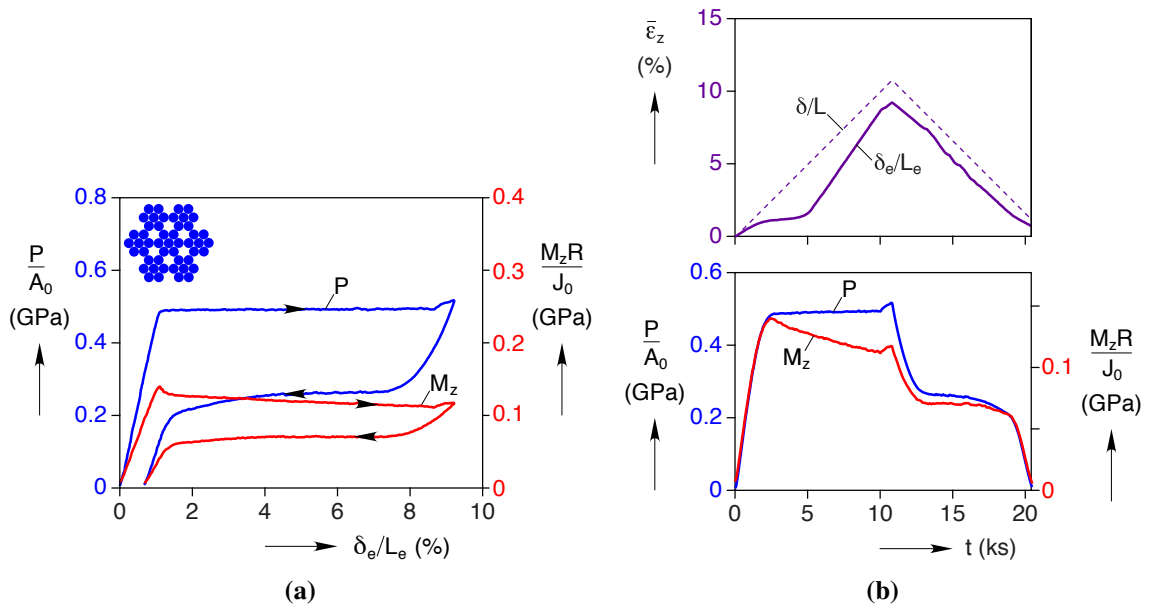
Figure 3.5   Experiment C1c on 7×7 cable ($L = 74.87$ mm, $L_e = 49.92$ mm) at $\dot\delta/L = \pm 1 \times 10^{-5}$ s^{-1}: (a) Normalized axial load (P/A_0, left axis) and axial torque (M_zR/J_0, right axis) versus LE strain, (b) Time histories of average axial strains from grips, δ/L, and laser extensometer, δ_e/L_e (upper plot), and normalized axial load and normalized torque (lower plot).

47

of 20.5 ks (5.7 hours). The evolution of the LE strain (δ_e/L_e, solid line) is also shown, which deviates from the δ/L for reasons discussed below. The lower plot in Fig. 3.5b shows the corresponding time histories of normalized load (P/A_0) and normalized axial torque (M_zR/J_0).

The axial load-LE strain response in Fig. 3.5a is quite similar to the previous one shown in Fig. 3.4, but now also shows the axial torque. The initial (austenite) axial load response of the 7×7 cable is nearly linear up to $\delta_e/L_e = 1.1$ % with a modulus of $E_A = 45.5$ GPa. The upper (loading) plateau stress is 493 MPa with a strain extent of 8.66 %. The lower (unloading) plateau stress is about 262 MPa, but the plateau is flat only between LE strains of 7.4 % to 5.3 % and the subsequent stress decreases gently until 1.5 % strain, the onset of the final linear elastic unload segment.

The torque response in Fig. 3.5a during loading is interesting. It initially exhibits a stiff linear branch with a slope of 13.5 GPa (shear stress/axial strain) up to $\delta_e/L_e = 1.1$ %. This is interrupted at the onset of the axial load plateau by a softening branch (while the axial load is flat). Once the axial load plateau is completed at $\delta_e/L_e = 8.66$ %, the torque turns upward again slightly. Note that what appears to be a "nucleation peak" in the torque response during loading near $\delta_e/L_e = 1.1$ %, is actually an artifact of plotting the response
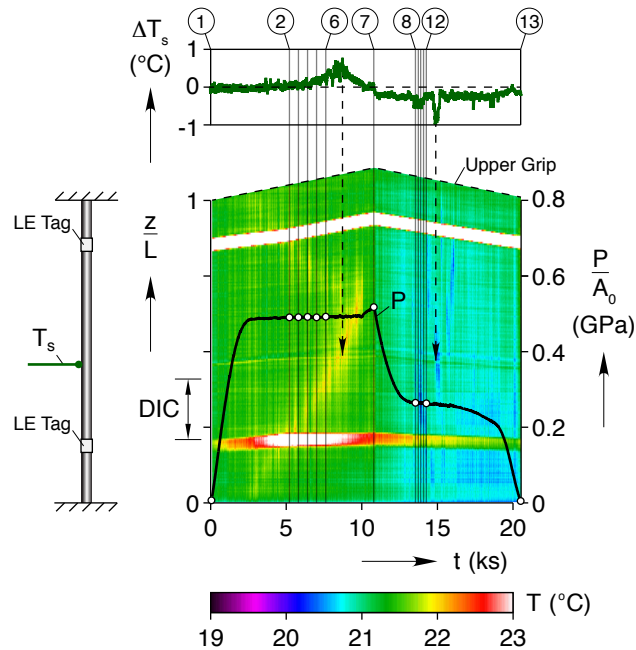
Figure 3.6 Experiment C1c (7×7 cable at $\dot{\delta}/L = \pm 1 \times 10^{-5}$ s^{-1}). Contour plot of axial temperature history from IR imaging with overlaid stress history (right-hand axis). The temperature change measured by the thermocouples ($\Delta T_s = T_s - T_a$) is shown above. Circled time labels above correspond to DIC strain images in Fig. 3.7. A scaled schematic of the specimen reference configuration is shown to the left.

against δ_e/L_e. As shown in the upper plot of Fig. 3.5b, the global strain ramps linearly with time, but at the onset of the loading plateau the LE strain history is relatively static then suddenly rises more steeply at 4.8 ks. As will be shown later, this is due to propagating fronts that first traverse the specimen outside the LE gage section then later enter the LE section. As seen in the lower plot of Fig. 3.5b, the "nucleation peak" disappears when the torque is plotted against the time, and the torque decreases almost linearly during the axial load plateau. The final residual strain is $\delta/L = 1.16$ % by the grip displacement, but is only $\delta_e/L_e = 0.71$ % by the LE measurement. The difference is likely due to grip slippage that occurred during the experiment, a common issue in tension experiments on straight SMA specimens (not dog-bone specimens) that exhibit strain localization. Thus, local extensometer measurements are a more accurate representation of the material response, even if they can be more difficult to interpret in the presence of localized strain fields. For this reason, we chose to use δ_e/L_e in Fig. 3.5a instead of δ/L.

The temperature field history, $T(z,t)$, from IR imaging of the 7×7 cable is plotted in Fig. 3.6, where the temperature legend spans a 4 °C window near room temperature ($T_a \approx 21$ °C). The contour plot was created by taking IR images at 5 s intervals, extracting a vertical temperature distribution along the crown of the specimen in each image, stacking the resulting sequence of one pixel wide slices side-by-side, and synchronizing them with time. Since the laser tags have a much lower emissivity than the painted specimen, they are clearly visible in Fig. 3.6 as the prominent, but artificial, horizontal streaks. The IR temperature reading is inaccurate there, but the tags do provide good markers for the movement of those locations. In addition, the slight horizontal streak in the temperature field history at $z/L = 0.46$ is due to the specimen thermocouple. Disregarding these locations, the overall kinetics of $A \rightarrow M^+$ transformation appear as two propagating hot spots, one from each grip, propagating inward and coalescing at $z/L = 0.68$ where the temperature reaches as high as 1.5 °C above ambient. Close inspection reveals that the fronts often appear to propagate in an alternating stop-start fashion, resulting in the vertical hot spot streaks in the contour plot. Each time the bottom front moves and heats up, the top front stops and cools down, and vice versa. During unloading, the kinetics of $M^+ \rightarrow A$ transformation are more diffuse without any clear fronts, just a few scattered local drops in temperature.

The topmost plot in Fig. 3.6 shows the time history of the temperature difference between the specimen and ambient thermocouples ($\Delta T_s \equiv T_s - T_a$). The noisy signal was due, in part, to the specimen thermocouple rubbing against the irregular surface of the cable as it deformed. Nevertheless, it recorded a small, but discernible, temperature peak near $t = 8.72$ ks of about 0.5 °C as $A \rightarrow M^+$ transformation occurred at the thermocouple location, and then a temperature drop of about -1 °C near $t = 14.89$ ks due to $M^+ \rightarrow A$
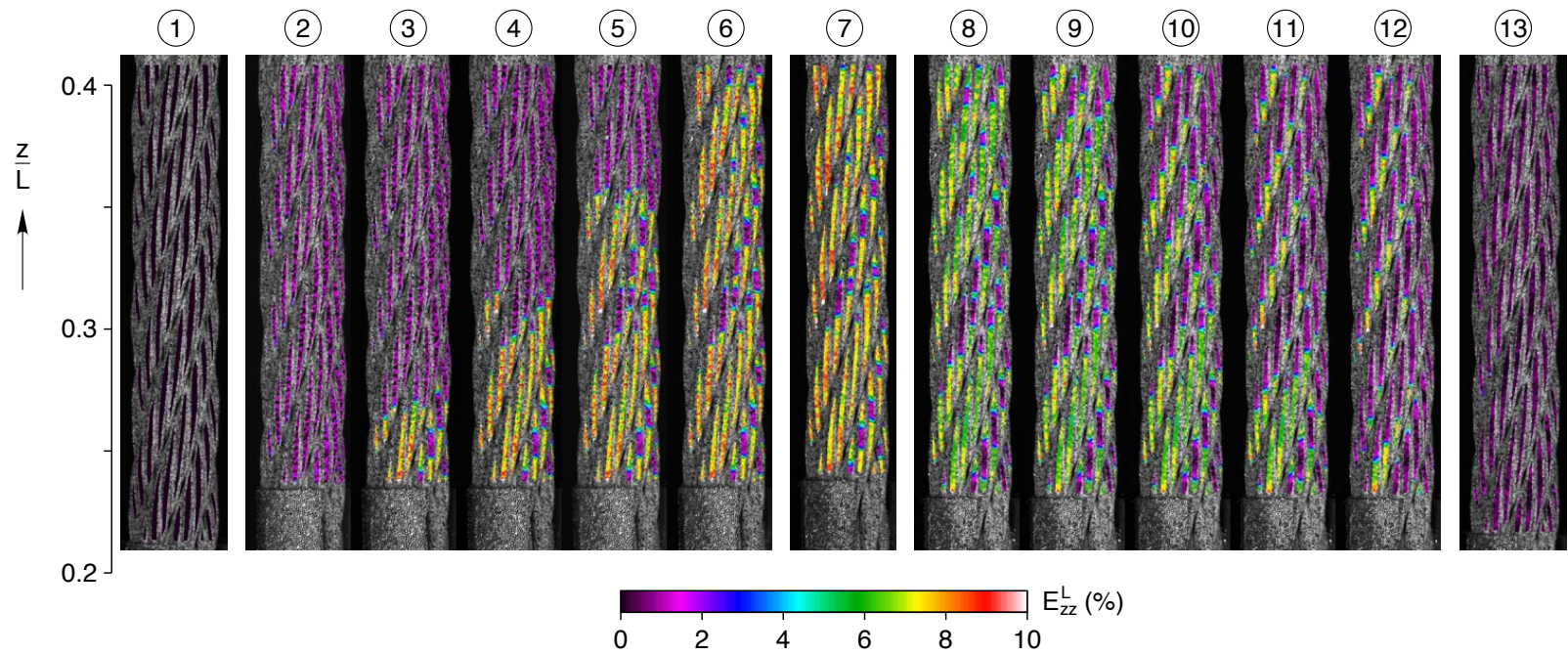
Figure 3.7 Experiment C1c (7×7 cable at $\dot{\delta}/L = \pm 1 \times 10^{-5}$ s^{-1}). Selected axial strain field images from DIC analysis. Circled image labels correspond to time labels in Fig. 3.6.

transformation. The vertical arrows in the contour plot show how the temperature peak/drop line up with instances when transformation activity was detected by the thermocouple.

The axial strain field, $E_{zz}^{L}(x, z; t)$, from the DIC analysis is shown in Fig. 3.7 at selected times, corresponding in Fig. 3.6 to the upper labels and the points overlaid on the stress history. The images were taken in a restricted FOV of the specimen as indicated in Fig. 3.6. At each time, the axial strain field was superimposed on a photograph of the cable in its current configuration, and colored according to the 0 to 10 % strain legend for E_{zz}^{L}. The lower LE tag, which was initially out of view in ①, appears as a gray band in the bottom of each strain field image from times ② to ⑬. Overall, the DIC sequence shows a macroscopic $A \rightarrow M^{+}$ front propagating upward from the bottom grip during loading (③ to ⑥ in the FOV) with a distinct strain discontinuity from about 1 % to 7.5 % strain, and then a more diffuse global front moving downward during unloading (⑨ to ⑫). Although not obvious in the few DIC images shown, a video of the complete set of 343 images (taken at 60 s intervals) during loading shows the global front move, then slow down, and then speed up again. This is consistent with the observation from the IR temperature field evolution that the fronts in the top half (out of the DIC FOV) and bottom half of the specimen often propagate in an alternating start-stop manner.

During unloading, the strain field images are more diffuse than during loading, which is consistent with the IR images. Note, the time interval between ⑧ to ⑫ during unloading is only 0.72 ks, compared to the time interval of 2.42 ks between ② to ⑥ during loading. As seen in the stress history of Fig. 3.6, this corresponds to the brief period where the axial load was constant. The front traversal is much quicker during unloading, indicating a generally smaller transformation strain across the $M^{+} \rightarrow A$ front. Further reverse transformation occurs in disparate regions and is accompanied by an overall decreasing axial stress history. Note that the fronts reach the grips well before the steep decrease in stress at $t = 19$ ks. Since most of the $M^{+} \rightarrow A$ transformation occurs in a rather uniform manner, little temperature change is detected in the IR images during unloading. All of this behavior is probably due to shakedown and residual pockets of "locked-in" martensite in the NiTi wires (to be discussed further in Section 3.3.4), which may explain why the $M^{+} \rightarrow A$ transformation required a decreasing load history.

Several other detailed observations are worth mentioning. The macroscopic front consists of fine features, first at the strand scale and then at the individual wire scale. The global front is jagged according to where fronts are located in the individual wires. These wire fronts tend to be staggered, which is reasonable since adjacent fronts would tend to amplify self-heating and would be energetically unfavorable. In other words, individual wire fronts tend to "repel" each other thermally, yet the steep local strain gradient along an individual

51

wire's axis tends to encourage further transformation there. Next, note that some of the individual wires in the cable do not transform after the global front has passed through the region. As the outer six strands of the cable stretch, they can also reduce their helix angles to accommodate a given global axial strain, while the core strand must simply stretch, making the tensile strains in the core wires greater for the same global axial strain. The overall morphology of transformation must maintain global axial strain compatibility between the rigid grips, yet high friction between the components within the cable section also tends to enforce local axial strain compatibility between components. One can imagine that the radial compressive stresses are likely quite large between the outer helical strands and the core strand, since if unsupported the helical strands would contract radially inward (as for a simple tension coil spring). Thus, the likely reason the wires in the exterior strands do not fully transform is to maintain axial compatibility with the core strand.

Once the loading plateau is exhausted ($t = 10.0$ to 10.8 ks), these low strain (austenite) regions shrink slightly (images ⑥ to ⑦). As will be seen in Section 4.2, the end of the core strand plateau corresponds to the upturn in stress at the end of the 7×7 cable plateau. At this point the outer strands have not yet fully exhausted their loading plateaus. Only when the core strand begins to uniformly strain again after the termination of its plateau do the pockets of austenite in the exterior strands begin to disappear.

Another interesting observation, which is clearer in the full video than the few still images here, is that a given cross-section of the cable rotates about the z-axis (ϕ_z, in a positive right-hand sense) until ②, but once the front passes the rotation reverses direction until ⑦. A cable made of conventional stable material, restrained from rotation at the grips, would not exhibit this behavior. The rotation evolution of our 7×7 cable in the DIC FOV is shown in Fig. 3.8. We measured the rotation of the cable by first fitting a cylinder to the
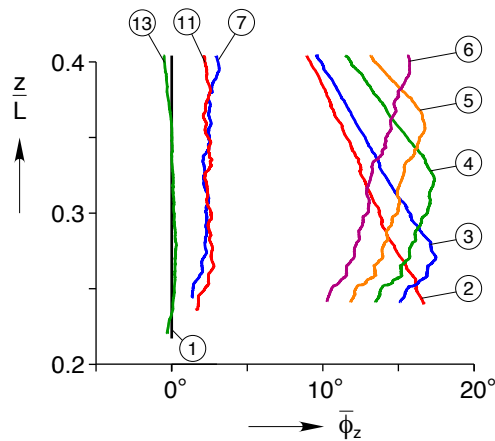
Figure 3.8 Experiment C1c: Rotation profiles of the 7×7 cable about the z-axis in the DIC region.

DIC data points to determine the precise location of the z-axis for a cylindrical coordinate system. Then the rotation angle, $\phi_z(\theta, z)$, was found by subtracting the current angle of each material point from the angle at zero axial load, and then averaging across the cable diameter to obtain an average angle, $\bar{\phi}_z(z)$, for each cross section. Whenever the strain field is relatively uniform, such as between time $t = 0.02$ ks (①) and $t = 2.5$ ks (just prior to $A \rightarrow M^+$ transformation) and ⑦ to ⑬ (unloading), the cable rotation is relatively constant along the length and is less than 4°. However, as the macroscopic front traversed the DIC FOV, ② to ⑥, there exists a kink in the rotation profile with a propagating peak (reaching as high as 17.5° in ③), whose location corresponds to the position of the global front. Clearly, the $A \rightarrow M^+$ transformation front causes the cable to twist to accommodate localized deformation. Upon subsequent unloading where localized deformation was less prevalent, the rotation at ⑦ is about 2.3°, and there is little change between ⑦ to ⑪. After final unloading at ⑬ the rotation is essentially zero again.

3.3.3 Details of the 1×27 Cable Response

We now turn to Experiment C2a performed on a 1×27 cable specimen at $\dot{\delta}/L = \pm 1 \times 10^{-4}$ s^{-1}. The mechanical response is shown in Fig. 3.9a in terms of the axial load and axial torque versus LE strain. The axial load response is the one shown previously in Fig. 3.4 (dry). The axial torque response (added here) has a larger relative magnitude compared to the axial load than for the 7×7 cable, due to the much larger helix angles of the wires (despite the alternating lays in the construction). It is negative according to the right-hand sign convention adopted in Fig. 3.3a, and it exhibits an interesting multi-step behavior with a knee at about 2 % strain and another knee at about 8 % strain during loading. These undulations will be shown in Section 4.3 to be due to transformation activity in the individual layers of the cross-section occurring at different times.

Histories of the specimen thermocouple, the average axial strains, axial load, and torque are shown in Fig. 3.9b. In this case, the grip and LE strain histories match more closely than for the 7×7 cable, still indicating a small amount of grip slippage, but no evidence of localized transformation since the LE strain traces constant-rate ramps. The specimen thermocouple measured a rise in temperature of about 0.5 °C during loading after the first knee in the axial load/torque, and then about −0.5 °C during unloading. This is about the same temperature changes as seen in the previous experiment on the 7×7 cable, despite the 10× faster rate. Clearly, the 1×27 cable is less rate-sensitive. Briefly, this is due to several factors, including the lack of propagating transformation fronts, the deeper helix angles in the construction, and the somewhat more slender aspect ratio. These will be discussed
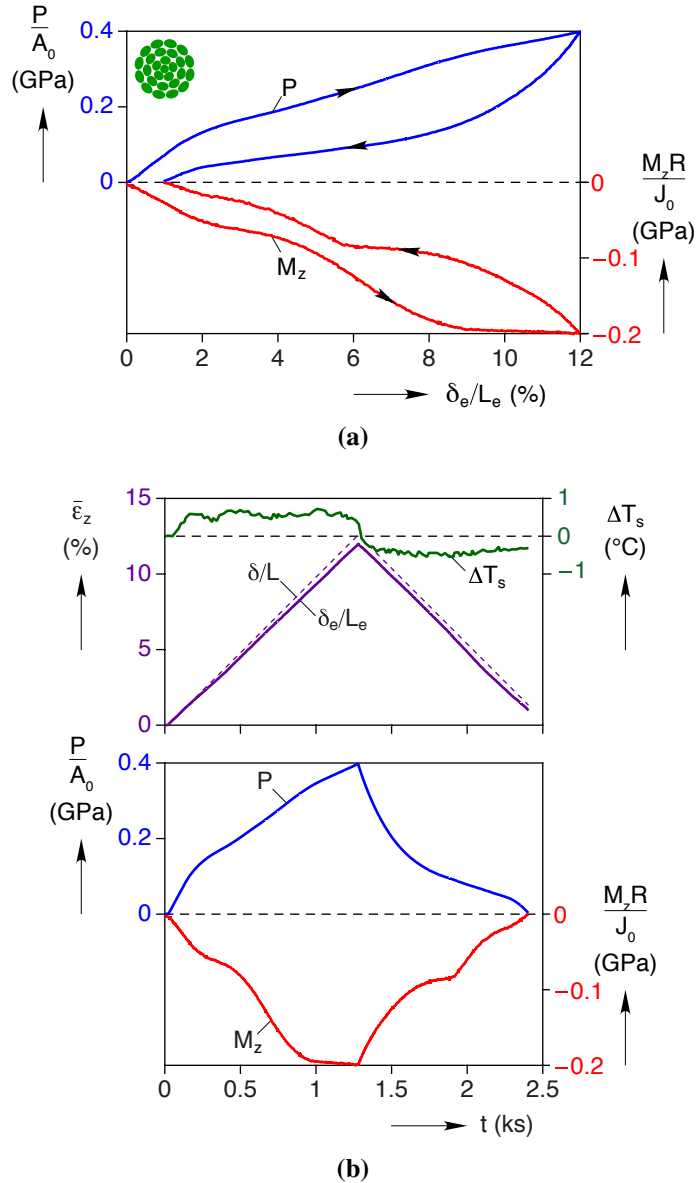
Figure 3.9 Experiment C2a (1×27 cable at $\dot{\delta}/L = \pm 1 \times 10^{-4}$ s^{-1}): (a) Axial load (P, left axes) and axial torque (M, right axes) versus LE strain, (b) Time histories of average axial strains and specimen temperature change (upper plot), and axial load and torque (lower plot).

further in Chapter 5.

3.3.4 Cyclic Shakedown Responses

Most SMAs exhibit an evolution of their thermo-mechanical response during their first thermo-mechanical cycles. This process is called *shakedown* if the response asymptotically approaches a limit cycle. Since repeatable cyclic behavior is often essential for the success

of an SMA device, cyclic shakedown is an important aspect to characterize. In practice, the material may be subjected to 'training' to achieve a repeatable limit-cycle behavior, which additionally may be used to induce a two-way shape memory effect. The degree and cyclic rate of shakedown are strongly dependent on the particular training procedure used and have obvious implications for durability and fatigue life. Despite intense interest in the literature (e.g. [13, 26, 41, 63]), a comprehensive map of the influence of possible training procedures does not yet exist even for monolithic SMAs, due to the large variety of loading parameters (temperature, strain, stress) and their path dependence. Accordingly, the purpose of this section is to preliminarily explore the different cyclic responses of the two cable designs.

Before presenting the cyclic responses of the full cables and attempting a comparison, the early shakedown responses of the straight core wires, extracted from the two cables, is shown to establish the base material differences. The responses to six cycles for each core wire are shown in Fig. 3.10. The force-elongation responses for the 7×7 and 1×27 core wires are shown respectively in Fig. 3.10a (Experiment W1a) and Fig. 3.10c (Experiment W2a), each subjected to six load-unload cycles taken to a maximum strain just beyond its load plateau. The corresponding stress and specimen temperature histories are shown in Figs. 3.10b and 3.10d.

Focus first on Fig. 3.10a, which shows the evolution of the superelastic response of the 7×7×0.275 mm core wire for six cycles to a maximum LE strain of 8.15 %. The cyclic response shows how the superelastic response progresses from one that has distinct plateaus (first cycle, $N = 1$) to one that has a more sigmoid-like shape (last cycle, $N = 6$). During this process, the upper plateau moves downward in stress and the lower plateau moves downward to a lesser degree, until a flat plateau is no longer discernible during either $A \rightarrow M^+$ or $M^+ \rightarrow A$. The length of both plateaus decrease and eventually develop a positive tangent modulus, while the strain and temperature fields tend to become more uniform (although not shown here). As cycling proceeds, the magnitude of the hysteresis (area within the loop) diminishes. The residual strain, upon each unloading to zero axial load, evolves forward in strain (ratchets) with progressively smaller increments after cycle 2. Interestingly, the increment of residual strain accumulation after cycle 2 is actually larger than after cycle 1, but decreases monotonically thereafter. The final residual strain after cycle 6 is 2.74 %. This is only one specific example, relevant to the study at hand, and more cycles would be required to truly reach a limit cycle behavior.

Figure 3.10b shows the axial stress history, again showing how the plateaus disappear with cycling. The figure also shows the specimen temperature changes as measured by a thermocouple placed near the bottom laser tag. The temperature excursions are about ±0.6 °C during cycles 1 and 2 and are relatively sharp in time ($\approx$ 150 s duration), indicating
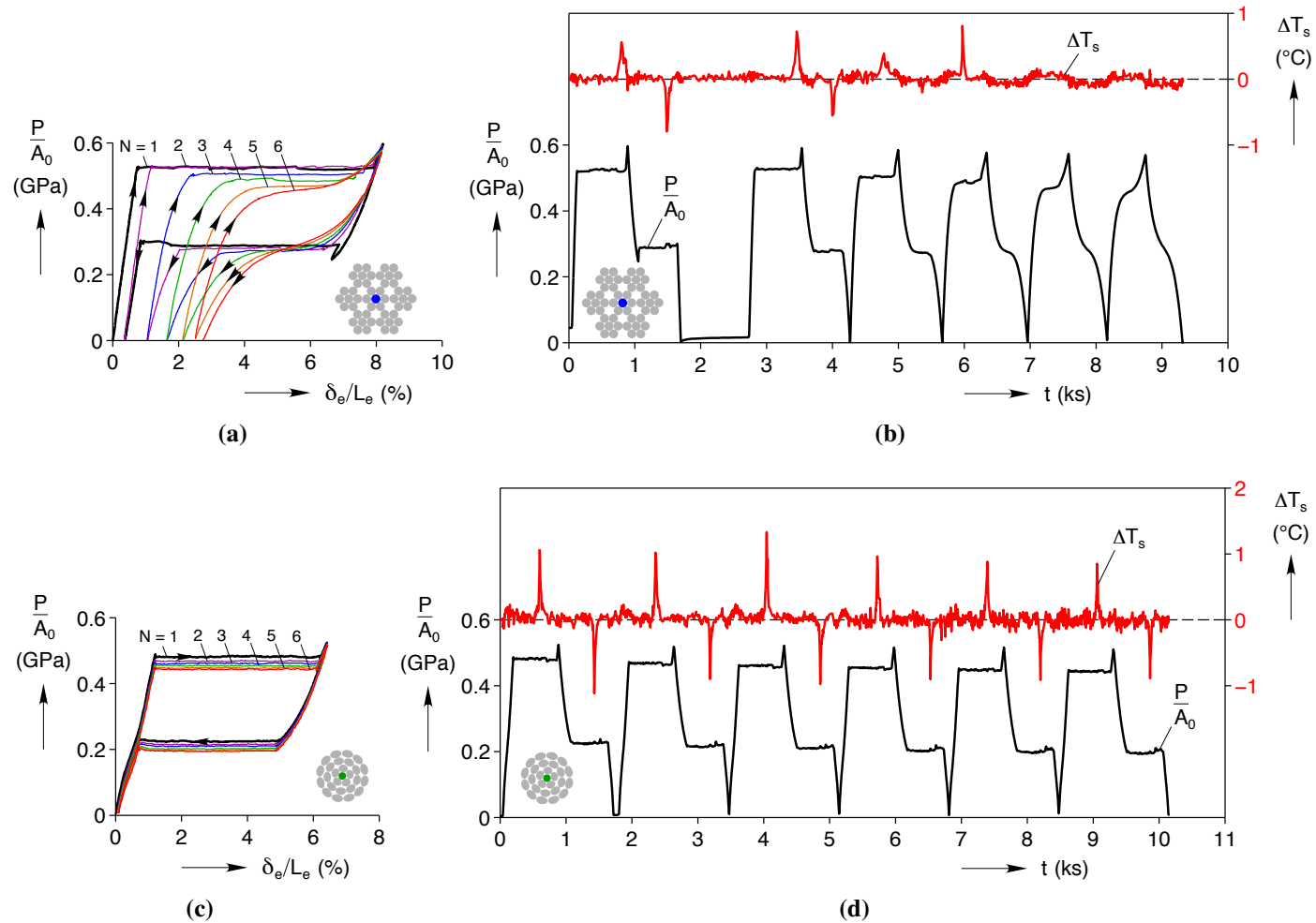
Figure 3.10 Superelastic cyclic responses (Experiments W1a and W2a) at $\dot{\delta}/L = \pm 1 \times 10^{-4}$ s^{-1} of the straight core wires extracted from the two cables: (a) 7×7 core wire force-elongation response (W1a), (b) 7×7 core wire stress and temperature histories (W1a), (c) 1×27 core wire force-elongation response (W2a), (d) 1×27 core wire stress and temperature histories (W2a).

localized transformation as transformation fronts pass the thermocouple location. A final sharp peak is measured during cycle 4 at 6 ks, which is due to a new nucleation event. Subsequently, however, the temperature changes become progressively rounded and diminished in magnitude to roughly ±0.1 °C by cycle 6, indicating more diffuse transformations. This change in temperature behavior corresponds to the disappearance of the stress plateaus.

By contrast, Fig. 3.10c shows a less severe shakedown in the mechanical response of the 1×27 core wire, where the stress plateaus remain over the six cycles but just shift downward somewhat in each (about −35 MPa in total). The residual strain even after cycle 6 is only 0.1 %, and the superelastic loop remains nearly closed. Figure 3.10d shows that, unlike the 7×7 core wire, the temporal spikes in specimen temperature exist for all six cycles. Both this feature and the flatness of the stress plateaus indicate that $A \leftrightarrow M^+$ transformations still involve propagating fronts.

Clearly the alloys are not identical, which is unfortunate for a direct comparison between the two cables. We suspect processing variables for the two cable constructions were different, leading to the different material properties. As shown in the DSC thermograms of Fig. 3.2, we estimate that the 1×27 wire is superelastic above 10°C, while the 7×7 wire is superelastic above -24°C. This difference causes the 1×27 wire to have a −45 MPa lower initial $A \rightarrow M^+$ transformation stress and a −64 MPa lower initial $M^+ \rightarrow A$ transformation stress. Because the plateau strain is also smaller for the 1×27 wire, the maximum strain during cycling was less (6.41 % vs. 8.19 %). Generally speaking, the cyclic rate of shakedown (if ever reached) is quite sensitive to the transformation stress, and thus the specimen temperature according to the Clausius-Clapeyron relation, and indirectly sensitive to the maximum strain, especially if taken well beyond the initial loading plateau. Had we taken the 1×27 wire to the same maximum strain as the 7×7 wire, which would have been well into the post-plateau regime, the shakedown would have been more severe.

Figure 3.11 presents the cyclic behavior of the full 7×7 cable, again in room temperature air, but at a rate of $\dot{\delta}/L = \pm 1 \times 10^{-4}$ s^{-1} for this longer experiment. Each cycle was taken to $\delta_e/L_e = 10.37$ % before being unloaded as shown in Fig. 3.11a. The cable's mechanical response is qualitatively similar to the uniaxially loaded core wire (Fig. 3.10a). In the first cycle of the 7×7 cable, after the initial stiff, nearly linear, mechanical response, there exist the usual distinct plateaus during loading ($A \rightarrow M^+$ transformation) and unloading ($M^+ \rightarrow A$ transformation). The subsequent cycles exhibit the typical superelastic shakedown response for NiTi when stress-induced transformation requires a large stress (over 500 MPa in this case). Similar to the core wire response, the mechanical response becomes more sigmoid-like as cycling proceeds, and the magnitude of the hysteresis (area within the loop) diminishes. At the same time, the strain at zero stress increases, but in successively
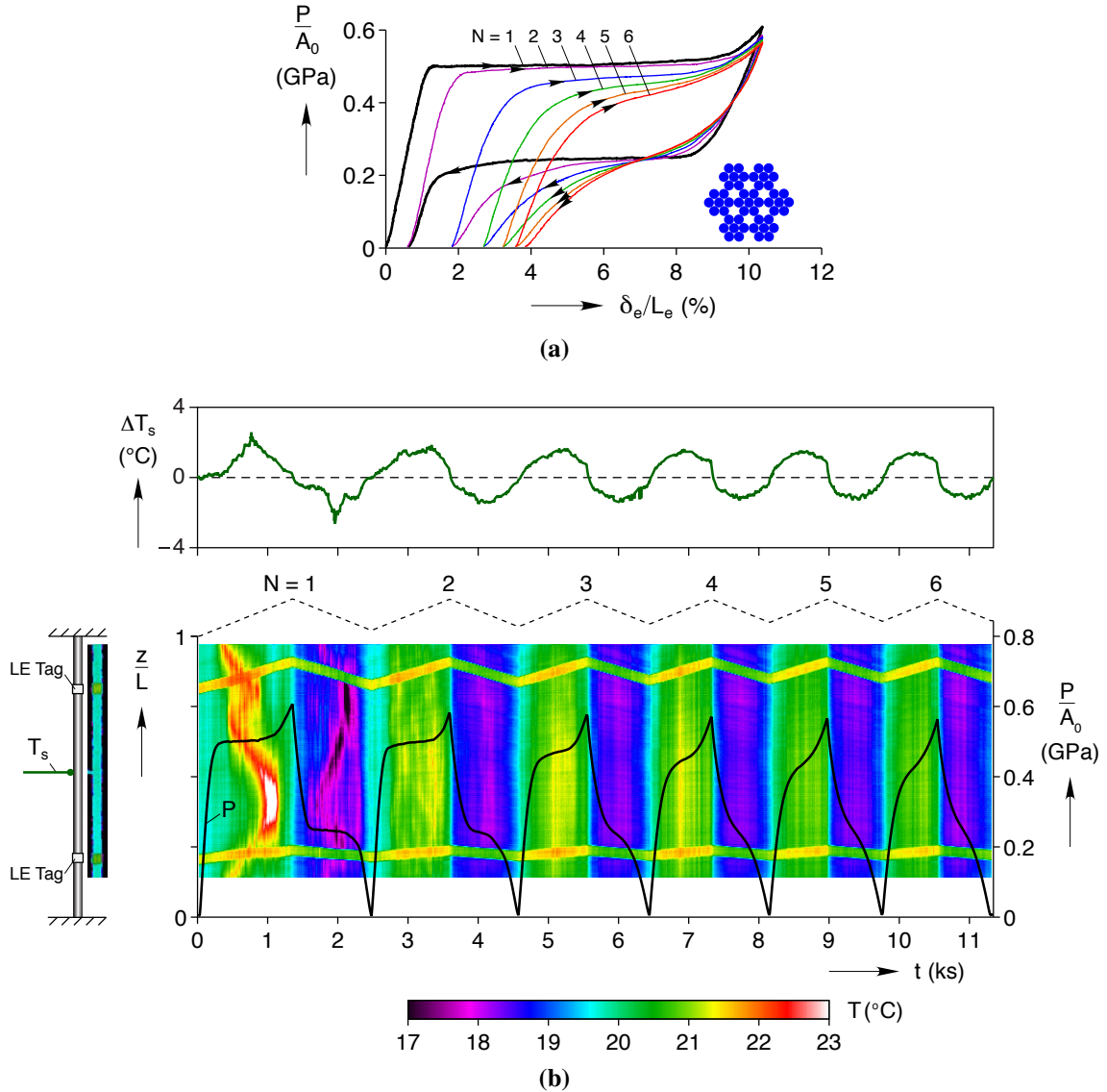
Figure 3.11 Experiment C1d (6 cycles of a 7×7 specimen at $\dot{\delta}/L = \pm 1 \times 10^{-4}$ s^{-1}): (a) mechanical response (b) histories of IR temperature profile and stress (lower plot), and specimen thermocouple (upper plot).

smaller increments for each cycle (again after cycle 2). Comparing cycle 1 and 6 of the 7×7 cable, the incremental changes with cycles are qualitatively similar to that of the core wire (Fig. 3.10a), but the changes are larger for the cable specimen.

Along with these mechanical changes, we see cyclic evolution of the specimen thermocouple readings of the 7×7 cable in Fig. 3.11b. The 7×7 cable follows the same general trend as seen previously in Fig. 3.10b for its core wire, but quantitative differences exist. First, the temperature peaks during the first cycle occur over about 1000 s, indicating that the transformation is more diffuse than in the core wire. Second, magnitudes of the temperature

excursion are larger in the cable for the same global strain rate (note the difference in the axis scaling). In cycle 1, the temperature excursions are ±2.5 °C, which fades to ±1.4 °C by cycle 6. This occurs, despite the more diffuse transformation in the cable compared to the wire, due to the cable's larger thermal inertia. The influence of specimen size (thermal inertia) and cable construction on strain rate sensitivity are investigated further in Chapter 5.

Next, observe the 7×7 cable IR contour plot (Fig. 3.11b), where the color legend spans 6 °C about ambient room temperature (20 °C). The FOV of the IR camera in this experiment included most, but not all, of the free length. During the first cycle, as expected from the flat loading and unloading plateaus, the temperature field shows transformation fronts traversing the specimen gage length (again ignore the LE tag locations). One front nucleates at the top grip and another front nucleates at the bottom grip, due to the stress concentrations there. Once the temperature of the initial two fronts rises by about 2.2 °C, another pair of fronts nucleate at $z/L = 0.7$. The top two fronts, one from the top grip the other from the $z/L = 0.7$ nucleation, coalesce at $z/L = 0.8$, at which point a very small drop in the load exists at $t = 0.85$ ks. This leaves only the bottom two fronts, which speed up to comply with the global strain rate $\dot{\delta}/L = \pm 1 \times 10^{-4}$ s^{-1}, thereby raising the exothermic heat release rate. As these fronts propagate and approach each other, they thermally interact, locally raising the temperature to 24.7 °C, above the limit of the temperature scale in the figure, until they coalesce at $z/L = 0.4$. The rise in temperature is accompanied by 22 MPa increase in propagation stress. After the fronts coalesce, the specimen temperature does not immediately return to room temperature (light blue). Instead, the specimen remains above ambient by about 1 °C. Notice, in fact, near the upper edge of the IR FOV that had cooled to room temperature, but heats up again when the axial load takes its upturn after the plateau. During this time, a vertical green band is observed across the entire FOV, which is likely due to the regions of austenite shown in images ③-⑦ of Fig. 3.7, which were left behind by the global front, finally transforming to martensite. We do not have DIC data for this experiment to prove the point, but given that the uniform heating occurs between $\delta_e/L_e = 8.8$ % and 10.2 %, and the remnant regions of austenite started to transform at $\delta_e/L_e = 8.7$ % in the isothermal DIC experiment, we are confident this is the case. During the unloading plateau, two fronts emanate from the final coalescent site during loading, and close inspection reveals evidence of transformation activity near the other coalescent site as well (cool spots near $z/L = 0.75$ at $t = 1.6$ ks). Reverse nucleations at the site of $A \rightarrow M^+$ front coalescences are commonly observed in uniaxially loaded wires [19], so the observation here is not surprising. The two $M^+ \rightarrow A$ fronts from $z/L = 0.4$ propagate outward until they meet fronts emanating from the grips at $z/L = 0.25$ and 0.8, and the temperature drops low off-sc ale (black) in those regions. After these four $M^+ \rightarrow A$ fronts

coalesce, and some further transformation occurs scattered along the gage length, reverse transformation completes and the specimen returns to zero load.

The second cycle in Fig. 3.11a still has relatively flat loading and unloading plateaus, and as such, localized transformation activity can be seen in Fig. 3.11b. However, it is difficult to discern any clear propagations like those seen in the first cycle. Transformation fronts most likely exist in individual wires or groups of wires, yet transformation seems to be nucleating at several locations with relatively little room for propagation. Cycles 3-6 have a more sigmoid shape in Fig. 3.11a, and the temperature field exhibits nearly uniform heating and cooling. Therefore, if transformation fronts exist in the individual wires at all, they are quite diffuse by cycle 6.

The final experiment (C2c) of this chapter is shown in Fig. 3.12, where the 1×27 cable was subjected to six load-unload cycles at $\dot{\delta}/L = \pm 1 \times 10^{-4}$ s^{-1}, but the maximum strain was larger (δ_e/L_e = 12.5 %). Figure 3.12a shows the evolution of the mechanical response, but the qualitative shape of the response does not change much with cycling. As mentioned previously, while the response is certainly nonlinear, it never has a distinct plateau even in its first cycle, only gentle undulations. The residual strain only ratcheted to δ_e/L_e = 2.0 % and a limit cycle (complete shakedown) has been nearly reached cycle 6. By contrast, despite being cycled to a smaller maximum strain (δ_e/L_e = 10.3 %), the 7×7 cable residual strain reached 4 % by cycle 6. Furthermore, the shape of the 7×7 cable mechanical response in cycle 6 is very different from cycle 1, and the response would certainly continue to evolve after cycle 6, unlike the 1×27 cable.

Figure 3.12b shows the corresponding IR temperature field, specimen thermocouple temperature, and overlaid stress history. The IR field plot does show exothermic temperature changes during each loading and endothermic temperature changes during unloading, but the temperature profiles are rather uniform at any given time (at least in the central FOV of the IR camera). No propagating transformation fronts are detected, even in the first cycle. Likewise, the thermocouple measures step-like temperature changes in time, up or down depending on the sign of the elongation rate, $\dot{\delta}$. Over the six cycles, the temperature deviations from ambient during loading and unloading (about ±1.5 °C) do not change significantly, as opposed to the 7×7 design whose temperature deviations became smaller with each successive cycle.

As a final comparison, certain features of the cyclic mechanical responses of the two cables are compared in Fig. 3.13. Characteristic stresses at the onset and termination of the plateaus, or knees, in the response curves are shown in Fig. 3.13a and 3.13b for the respective cables. The insets in the figures show the constructions used to extract these stresses from the mechanical response (final cycle response shown) in a systematic way. For
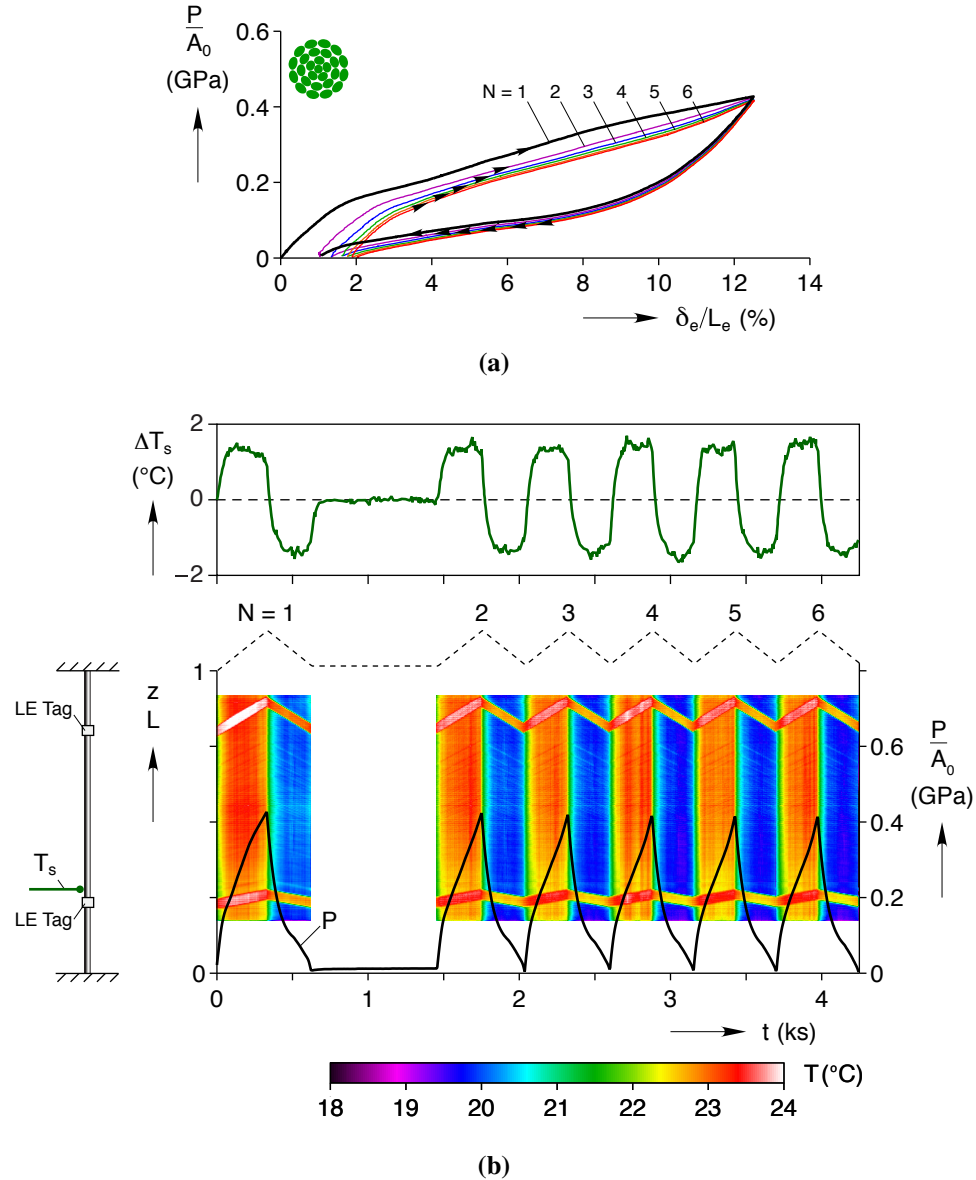
Figure 3.12 Experiment C2c (6 cycles of a 1×27 cable at $\dot{\delta}/L = \pm 4 \times 10^{-4}$ s^{-1}): (a) mechanical response, (b) histories of IR temperature profile and stress (lower plot), and specimen thermocouple (upper plot).

the 7×7 cable, Fig. 3.13a shows that stresses at the onset/termination of the $A \rightarrow M^+$ plateau generally decrease with cycles, but diverge from each other as the response curve becomes more sigmoid-like. The stresses during the $M^+ \rightarrow A$ plateau also diverge from each other, but the onset of the knee moves upward in stress while the reverse knee near the termination of $M^+ \rightarrow A$ transformation moves downward. The average of these two values remains relatively constant with cycling. The cyclic trends in each value are relatively monotonic, and the dotted lines are single-exponential fits of the data (for $N \geq 2$) as discussed further
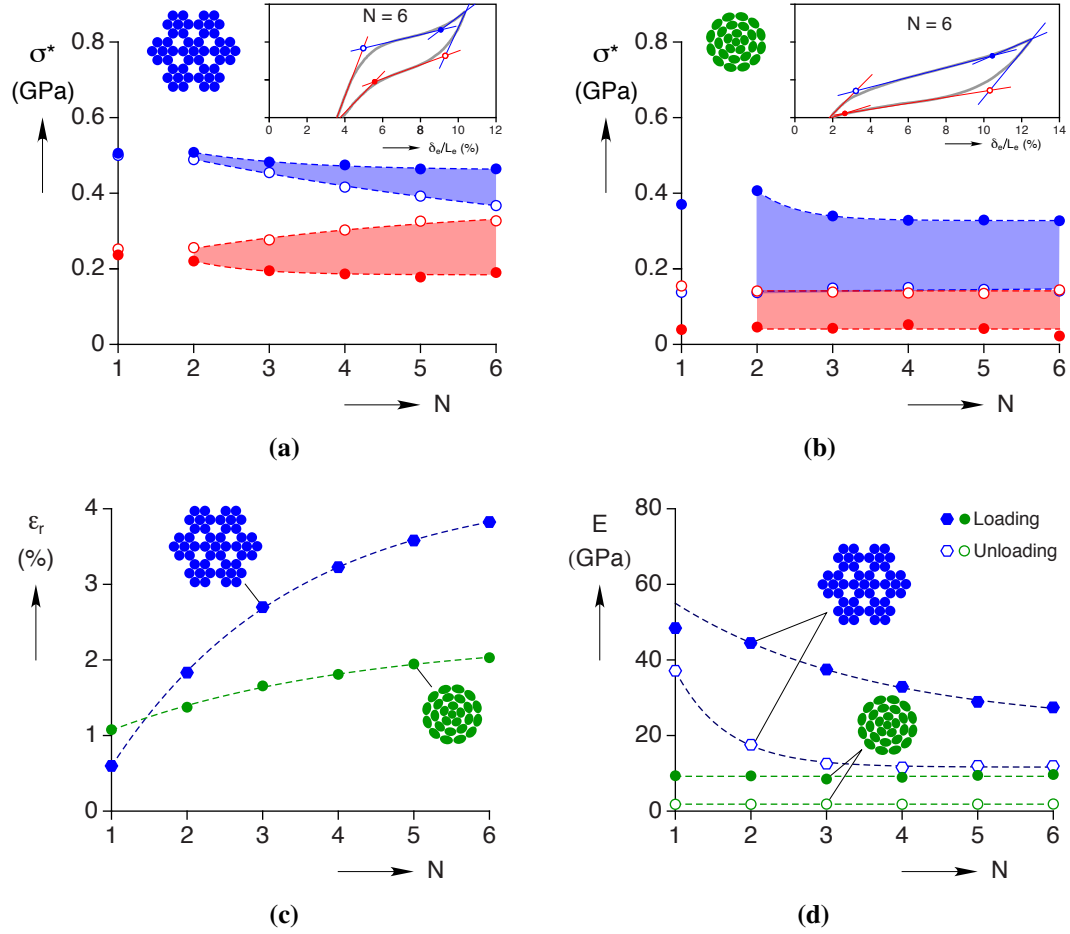
Figure 3.13 Comparison of cycle responses of the 7×7 cable and 1×27 cable (dashed lines are single-exponential fits): (a) Characteristic $A \leftrightarrow M^+$ stresses for the 7×7 cable, (b) Characteristic $A \leftrightarrow M^+$ stresses for the 1×27 cable, (c) Residual strain versus cycle, (d) Initial loading modulus (closed symbols) and final unloading modulus (open symbols) versus cycle.

below. The trends in the characteristic stresses for the 1×27 cable in Fig. 3.13b are less dramatic. The first knee in the curve ($A \rightarrow M^+$ onset) quickly converges to an asymptotic value by about cycle 3. The other three characteristic stresses change very little over the six cycles.

Figure 3.13c plots the residual strains upon complete unloading after each cycle, and Fig. 3.13d plots the initial and final elastic moduli for each cycle. The dashed lines are three-parameter exponential fits of the form $a(N) = a^\infty \left[1 - \exp\left(-\frac{N-N_0}{\tau_a}\right) \right]$, where a is either ε_r or E. In both cases, the fits nicely capture the trends of the data, at least for these few cycles. Figure 3.13c clearly shows the more extreme evolution of the residual strain for the 7×7 cable with a predicted asymptotic value of about 4.3 % strain, compared to the 1×27 cable which has a predicted asymptotic value of about 2.3 % strain. Interestingly, the data

62

fits in Fig. 3.13c do not extrapolate to the origin as one might expect, again showing that the first cycle is somewhat of an outlier in the overall cyclic trends in the mechanical response (as it was for the straight wire). Likewise, the trends in Fig. 3.13d show a significantly reduced elastic modulus for the 7×7 cable, but very little change in elastic modulus for the 1×27 cable.

The exponential-like behavior (starting with the second cycle) in all these features suggests that their evolution may be governed by a Maxwellian "rate" equation. For example, suppose the characteristic stresses are each governed by the first-order differential equation

$$\frac{d\sigma}{dN} = -\frac{\sigma}{\tau},$$ (3.3.2)

where τ is a "time-constant" in terms of the number of full transformation cycles the material experiences. This has the exponential solution

$$\Delta\sigma(N) = \Delta\sigma_\infty \left[1 - \exp\left(-\frac{N}{\tau} \right) \right],$$ (3.3.3)

where $\Delta\sigma(N)$ is the change in the transformation stress from its initial value, and $\Delta\sigma_\infty$ is the asymptotic (shaken down) change after a sufficiently large number of cycles. We suspect the cyclic "rate-constant" (τ) during shakedown is determined more by the material and the temperature at which the experiment was run, than by the construction of the cable. The amount of shakedown ($\Delta\sigma_\infty$), however, is probably a strong function of the cable construction, since it influences the distribution and multi-axiality of the local stress state in the wires.

Of course, the maximum strains between the two experiments are different, so a direct comparison here is difficult. Furthermore, as shown previously in Fig. 3.10, the two cable designs were constructed from somewhat different NiTi alloys so it is not possible to quantitatively determine how much of the difference in shakedown behavior is due to the cable design versus differences in material properties. We leave for later the challenging modeling task of connecting a cable design's shakedown behavior back to the constitutive behavior of its individual wires. Nevertheless, given the enhanced compliance of the 1×27 components and lack of propagating transformation fronts (in all but perhaps the single core wire), the cable construction certainly plays a significant role.

Overall, the data suggests the 1×27 cable may have better ultimate (many cycle) fatigue performance, durability, and overall cyclic repeatability. Of course, this comes at the cost of a significantly reduced stiffness and less dramatic transitions between elastic and phase transformation regions, if those are desired. Thus, the question of which cable design is

favored depends on the intended application. It should be apparent by now that many other possible constructions could be investigated to obtain behaviors in between, or drastically different, from those shown here.

3.4   Summary & Conclusions

The room temperature, nearly isothermal tensile responses of the 7×7×0.275 mm cable and 1×27×0.226 mm cable were characterized. Both cable design responses were relatively unaffected by lubrication, indicating high friction between the subcomponents. Overall, the mechanical responses of the 7×7 cable and the straight core wire extracted from it were quite similar, indicating the 7×7 cable behaves similar to that of 49 straight wires loaded in parallel. The behavior of the 1×27 cable was considerably different due to the larger helix angles involved in its construction. Thus, the 7×7 cable may be ideal for those engineers wishing to have the excellent properties of superelastic wires in a high force, compact package, while the 1×27 cable trades off force for a larger recoverable strain, exhibits more stable structural response with a positive tangent modulus, and less severe shakedown characteristics. Both cables had an interesting non-monotonic torque reaction during the tension experiments, yet the relative magnitude was more significant in the 1×27 cable.

Simultaneous infrared thermography and digital image correlation were used during the experiments on the two designs to investigate local strain and temperature field variations. The 7×7 cable clearly exhibited propagating phase transformation fronts that behaved in a similar manner to the fronts in its straight core wire. Some interesting features were observed, however, in the propagation of fronts between adjacent wires in the cable and some incomplete propagation in some of the outermost wires. Stress-induced phase transformation activity was detected in the temperature fields of the 1×27, but no propagating transformation fronts were observed. This made the 1×27 specimen less sensitive to latent heat-induced temperature changes, allowing relatively isothermal experiments to be performed at faster elongation rates than for the 7×7 cable. The range of responses for the two cable designs seems to indicate significant future opportunities to tailor the structural behavior of SMA cables to their intended applications by designing the construction and layups.

Chapter 4

Cable Subcomponent Responses

Chapter 3 presented the fundamental, slow-rate (nearly isothermal) responses of two cable designs at room temperature. In this chapter, the uniaxial tension responses of components of the same two Nitinol cable constructions (7×7 right regular lay, and 1×27 alternating lay) are explored. These constructions were disassembled and selected components were subjected to quasi-static tensile experiments to study the contributions of the individual components of the cables' hierarchical construction. Also, it is worthwhile to characterize the components for the simple reason that, in certain applications, they might also be cable designs in their own right. In Section 4.2, we show further details of propagating transformation fronts in the straight core wire and the core strand of the 7×7 design. In Section 4.3 the 1×27 component responses help explain the tensile compliance, lack of localized self heating, and the "stair-step" torque response seen previously in the full cable.

4.1 Specimens and Experimental Setup

The 7×7×0.275 mm and 1×27×0.226 mm cable designs and their selected components are shown in Table 4.1. All specimens came from the same two cable lots as the specimens of Chapter 3, and, where necessary, the cables were disassembled to extract their individual components for testing. The specimen preparation for stereo DIC and laser extensometry was the same as presented in Chapter 2.

The same experimental setup as that used in Chapter 3 was utilized for the experiments discussed below. As before, all experiments were performed on as received (dry) specimens in room temperature air under elongation control at constant, slow ramp rates ($\dot{\delta}/L$). Specimens were clamped at their ends to enforce a zero rotation boundary condition. The conjugate axial reaction torque was measured using a torque cell underneath the bottom grip. In certain cases, stereo DIC was performed to measure the strain field evolution (in a restricted field of view) and infrared (IR) imaging was performed to measure the temperature field transients. Mechanical responses are presented in terms of the normalized axial load (P/A_0, axial force per reference area) and normalized axial torque (MR/J_0, axial moment

Table 4.1 Specimen components from two cable designs and experimental and geometric parameters

Cable	Specimen	Icon	A_0 (mm^2)	J_0/R (mm^3)	Exp ID	L (mm)	L_e (mm)	$\dot{\delta}/L$ (s^{-1})
7×7	core wire		0.059	4.083×10^{-3}	W1b	76.04	49.55	$\pm 1 \times 10^{-5}$
	1×7 core strand		0.416	7.486×10^{-2}	S1a	75.93	50.17	$\pm 1 \times 10^{-5}$
	7×7 cable		2.910	1.547×10^{0}	C1c	74.85	49.92	$\pm 1 \times 10^{-5}$
1×27	core wire		0.040	2.266×10^{-3}	W2b	74.67	49.05	$\pm 1 \times 10^{-4}$
	1×6 core strand		0.241	3.475×10^{-2}	S2a	75.05	49.70	$\pm 1 \times 10^{-4}$
	1×15 multi-layer		0.602	1.555×10^{-1}	M2a	75.09	49.88	$\pm 1 \times 10^{-4}$
	1×27 cable		1.083	3.947×10^{-1}	C2d	75.21	49.21	$\pm 1 \times 10^{-4}$

times outer radius per reference torsion constant). The chosen reference area and reference torsion constant are those defined in Section 3.3, but calculated for the component being examined (values provided in Table 4.1). Responses are generally plotted either against the laser extensometer (LE) gage strain (δ_e/L_e) or time (t). In the following, Sections 4.2 and 4.3 present the experimental results and analysis of the component responses for the two cable types, 7×7 and 1×27.

4.2 Isothermal Responses of 7×7 Cable Components

Before presenting the experimental results, it is worthwhile to take a closer look at the geometry of the 7×7 cable construction. As shown in Fig. 4.1, the 7×7 cable construction includes one core strand and six outer helical strands. Each strand, in turn, is composed of a central wire and six outer wires wound about it. Based on their geometry, the wires can be classified into four groups (A, B, C, D) as indicated in Fig. 4.1a. The dashed lines are projections of the trajectories of each wire type as it extends along the cable axis (z-axis),
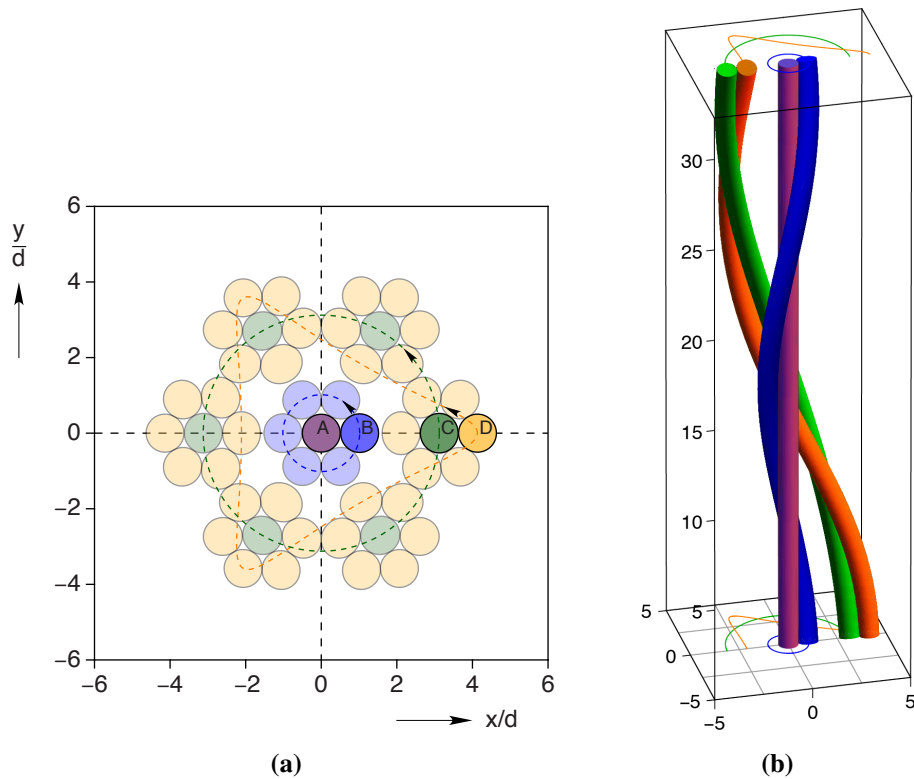
Figure 4.1 7×7×0.275 mm cable geometry: (a) cross-section ($z = 0$) with dimensions normalized by the wire diameter (d). (b) isometric view of the four wire types (A, B, C, D) in (a).

67

Table 4.2 Geometric parameters of the four wire types in the 7×7 cable: reference helix angle (α_0), normalized mean helix radius (r_0/d), and normalized pitch (p_0/d).

Wire type	Number of wires	α_0	r_0/d	p_0/d
A	1	0°	0	NA
B	6	11.3°	1	31.6
C	6	16.9°	3	62.2
D	36	5.6° to 28.2°	varies	20.7 and 62.2

and an isometric view of each wire type is shown in Fig. 4.1b. Geometric parameters for each wire type in the 7×7 cable construction are provided in Table 4.2. Wire A is the single straight core wire that runs along the centerline of the cable (z-axis). Wire type B is one of six helical wires wound in a right-hand sense around Wire A. Wires types A and B comprise the 1×7 core strand. Wires types C and D comprise the six outer helical strands. Wire C is one of six central wires of the outer helical strands, and it traverses a simple right-hand helix about the core strand. Wire D is the most prevalent wire type (36 of the 49 wires). It traverses a second-order helix, wrapping three left-hand turns about wire C for each right-hand turn of wire C about the z-axis. Two values for p_0 are given in Table 4.2 for wire D. The first ($p_0/d = 20.7$) is the pitch of wire D about wire C, while the second ($p_0/d = 62.2$) is the same pitch as wire C. The angle to the global cable axis in wire D varies from about 6° at its outermost point in the cable to about 28° (by calculation) at its innermost point adjacent to the core strand. These values should be treated as approximate, since the geometry has been idealized somewhat by assuming integer values of r_0/d. This is not strictly correct geometrically if one accounts for curvature effects on the projected wire sections, which can be seen upon close inspection of the true projections in Fig. 4.1a where wires of different types do not quite touch. The drawing process used to make the cable, however, likely did not preserve this exact geometry either, as wires settled/deformed against one another.
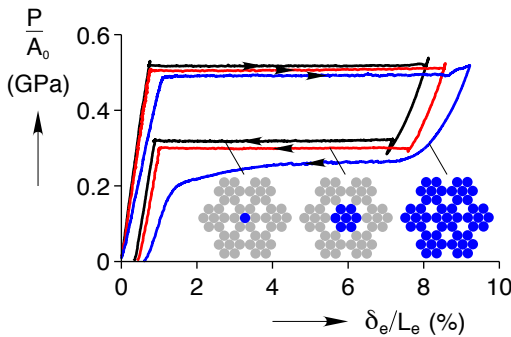
Figure 4.2 Comparison of isothermal mechanical responses ($\dot{\delta}/L = \pm 1 \times 10^{-5} \text{ s}^{-1}$) of the 7×7-×0.275 mm core wire (Exp. W1b), core strand (Exp. S1a), and full cable (Exp. C1c).

Two components, a core wire and a core strand, were harvested from the as-received 7×7×0.275 mm cable. Figure 4.2 overlays the isothermal ($\dot{\delta}/L = \pm 1 \times 10^{-5}$ s^{-1}) mechanical responses of the three components of the cable: (1) the 0.275 mm diameter straight core wire, (2) the 1×7×0.275 mm core strand, and (3) the full 7×7×0.275 mm cable. All three responses exhibit qualitatively similar force-elongation responses, when normalized by the individual reference cross-sectional areas to give an average stress measure. Some quantitative differences exist, however, and it should be noted that each specimen was taken to a slightly different maximum strain (8.12 %, 8.57 %, and 9.21 %), where unloading commenced just after the termination of the upper load plateau. Overall, there exists a monotonic progression in the response curves, from the core wire, to the 1×7 core strand, to the full 7×7 cable. The transformation load plateaus move downward slightly, the unload plateaus move downward to a greater extent, and the extent of the plateau strains increase somewhat. The responses of the core wire and core strand are quite similar, with nearly identical initial elastic modulus (prior to $A \rightarrow M^+$) and both exhibiting distinct load plateaus during both $A \rightarrow M^+$ (loading) and $M^+ \rightarrow A$ (unloading) transformations. This is not surprising, since its straight core wire contributed 1/7 of A_0 and the other six outer wires have relatively small helix angles (11.6º) to the loading axis. This means that all wires are loaded predominantly in direct tension, with only a very small bending and torsion contribution. The full 7×7 cable has a load plateau during $A \rightarrow M^+$, but a less distinct one during $M^+ \rightarrow A$, as well a larger stress hysteresis overall. Also, the initial (and final) elastic modulus is noticeably less than for the other two components. The 7×7 cable response (Experiment C1c) was analyzed in detail in Section 3.3.2, so below we focus on the responses of the core wire and the 1×7 strand.

Focusing on the core wire response of Fig. 4.2, the experiment was essentially isothermal at this extremely low loading rate. Within the noise of the specimen thermocouple ($\approx \pm 0.1$ °C) and the sensitivity of the IR camera ($\approx \pm 0.1$ °C), no measurable temperature changes occurred. The force-elongation curve has an initial linear elastic segment during elastic straining of austenite, followed by a quite flat load (engineering stress) plateau ($A \rightarrow M^+$ transformation) during loading, and then an abrupt (but short) upturn after this plateau. Initial unloading has a nonlinear response with a positive but monotonically decreasing tangent modulus, which is interrupted by a $M^+ \rightarrow A$ localization event outside the LE gage length, so the LE strain records a momentary increase in strain and the force rises to comply with global compatibility between the grips (see the inverted peak at the onset of the lower plateau). Further reverse $M^+ \rightarrow A$ transformation during unloading occurs along the lower load plateau, and, once the lower load plateau is exhausted, the wire unloads again along a steep linear elastic segment to zero load. We certainly recognize that all of

these features, and many of those described in the next paragraph, have been shown and explained before in the tensile response of superelastic NiTi wires [19, 58, 73, 110, 116]. The DIC measurements here provide a clearer and more quantitative view of the localized strain fields, and we review the localized strain field evolution below to provide a reference point for the subsequent more complex cable behavior.

The flatness of the load plateaus indicates instabilities during the $A \leftrightarrow M^+$ transformations, where deformation has localized, and this is confirmed by the axial DIC strain contours shown in Fig. 4.3. The figure shows a contour plot of the axial strain field history, $E_{zz}^{\mathrm{L}}(z, t)$ where the wire axial coordinate (z) is normalized by the initial free length (L), as shown on the left-hand vertical scale in a limited field of view spanning $z/L = 0.2$ to 0.4 (our CCD cameras lacked sufficient resolution to perform DIC on the entire gage length). In a similar manner to that used previously in Chapter 2 for the IR temperature contour plots, the axial strain contour plot here was created by averaging the axial strain across the lateral (x) direction of the wire to create a 1-D axial profile from each DIC image. A sequence of images at 40 s intervals was then stacked side-by-side (405 images) and synchronized with time (t) along the horizontal axis. The strain field is shown in the Eulerian frame (current configuration), so the bottom of the DIC analysis area moves up during loading and down during unloading as new material points appear in the FOV (for which we do not have their reference position). The axial stress history is overlaid for reference, and its scale is the right-hand vertical axis.

The sharp transition between high strain and low strain regions in Fig. 4.3 clearly shows a transformation front (a strain discontinuity) traversing the specimen length from top to bottom during the loading stress plateau ($A \rightarrow M^+$) and then from bottom to top during the unloading stress plateau ($M^+ \rightarrow A$). These strain discontinuities separate nearly homogeneous regions of low (A) and high (M^+) strain. The slight striations in the strain field also allow one to observe the displacement of material points in time, and a clear kink in the displacement field is seen across each propagating front. The DIC measurements show that the front is not actually a strain discontinuity, but instead a region of high strain gradient (macroscopic neck) with an axial extent of about $\Delta z^* = 0.27$ mm (about one wire diameter). This makes sense considering that compatibility of radial displacements must be enforced between a given cross-section and its neighbor. The relevant length-scale is, therefore, the wire diameter.

The speed of each front is nearly constant, measured as 0.0108 mm/s during $A \rightarrow M^+$ and 0.0121 mm/s during $M^+ \rightarrow A$. As mentioned in Chapter 2, the speed of front motion
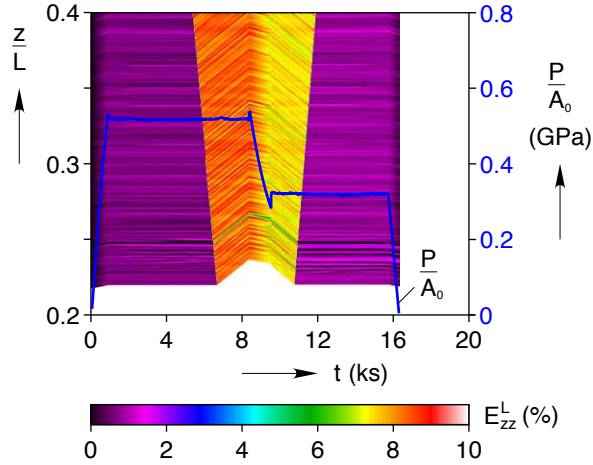
Figure 4.3 Experiment W1b. DIC axial strain field and stress history of the core wire from the 7×7×0.275 mm cable ($\dot{\delta}/L = \pm 1 \times 10^{-5}$ s^{-1}).

can be predicted for steady-state conditions as

$$c = \frac{\dot{\delta}}{n\Delta\varepsilon_P}, \tag{4.2.1}$$

where $\dot{\delta}$ is the prescribed elongation rate, n is the number of propagating fronts, and $\Delta\varepsilon_P$ is the strain jump across a front (idealized as a discontinuity). The equation is valid for isothermal transformation (constant strain jump) and all fronts moving at the same speed, which tends to be true to minimize temperature excursions. Note that the length of the wire specimen (L) does not appear in eq. (4.2.1), so the front speed is independent of specimen length. This means specimens of different lengths for the same global strain rate ($\dot{\delta}/L$) will have different front speeds and potentially behave differently. For a single moving front ($n = 1$), the predicted front speeds from this equation are $c = 0.0104$ mm/s during $A \rightarrow M^+$ and 0.0121 mm/s during $M^+ \rightarrow A$, where we used the strains at the onset and termination of the stress plateaus in Fig. 4.2 to find the respective strain jumps, $\Delta\varepsilon_P = 7.32$ % and -6.28 %. The predicted speeds agree well with the measured ones, indicating (despite our limited FOV) that a single constant-speed $A \rightarrow M^+$ front traversed the entire specimen from top to bottom during loading, and then a single $M^+ \rightarrow A$ front traversed the entire specimen from bottom to top during unloading. Based on the observed front motion here and our experience from IR imaging in many other similar experiments, the $M^+ \rightarrow A$ nucleation event at the onset of the unloading stress plateau probably occurred quite close to the bottom grip, which momentarily created two diverging fronts, but the lowermost one immediately reached the grip leaving only a single upward moving front. Furthermore, since we measured the axial extent of the front Δz^*, we can also estimate the local strain rate as a front transits a given

material point, using eq. (4.2.1),

$$\dot{\varepsilon} \approx \frac{\Delta \varepsilon_{\mathrm{P}}}{\Delta t} = \left(\frac{L}{n \, \Delta z^*}\right)\frac{\dot{\delta}}{L}, \tag{4.2.2}$$

where $\Delta t = \Delta z^*/c$ is the time interval for front passage. Thus, compared to the global strain rate ($\dot{\delta}/L$) the local strain rate ($\dot{\varepsilon}$) is amplified by the factor in parentheses. For the case of a single moving front, $L/\Delta z^* = 282$ for our specimen, which is why even for thin wire, the experiment must be performed at an extremely slow global strain rate ($\dot{\delta}/L = 1 \times 10^{-5}$ s^{-1}) to achieve isothermal conditions in stagnant air. Aside from the important influence of the ambient medium, what constitutes a sufficiently slow rate clearly depends on the length of specimen. This is a common pitfall in our experience, counter to the usual expectations for material testing. One must be aware, that when transformations occur via propagating fronts, longer SMA specimens are more rate-sensitive than shorter ones for the same global strain rate.

The second component of the 7×7×0.275 mm cable hierarchy to be addressed is the 1×7×0.275 mm strand. The similarity of the core strand mechanical response to that of its core wire can be attributed to the shallow helix angle ($\alpha_0 = 11.6^{\circ}$) of the wires to the tensile axis, but some quantitative differences exist. The end of the core strand plateau increases from $\delta_{\mathrm{e}}/L_{\mathrm{e}} = 8.04\%$ to 8.55%, at the cost of a small decrease in loading plateau stress from 517 MPa to 506 MPa. Assuming purely tensile loading in each wire at 517 MPa, a rough calculation to account for the six helical wires is 517 MPa $(1 + 6\cos 11.3^{\circ})/7 = 508$ MPa, which agrees reasonably well to the measured value. In addition, a small torque was measured for the core strand, but it was well under 1 % of the torque cell capacity (2824 N-mm), so the measurement was not sufficiently accurate to generate a meaningful torque-response curve. Based on a similar calculation as above, the estimated torque was probably near 6×0.275 mm $\times$ 0.0594 mm$^2 \times 517$ MPa $\sin 11.3^{\circ} \approx 10$ N-mm.

Figure 4.4 shows the temperature field by IR imaging and the specimen thermocouple (Fig. 4.4a) and several DIC axial strain images (Fig. 4.4b) during the experiment. The specimen thermocouple history (top plot of Fig. 4.4a), while somewhat noisy in this small temperature range, does show a small 0.25 °C transient above ambient during the loading plateau between ⑤ and ⑥ and then a small -0.25 °C transient below ambient during the unloading plateau near ⑪. In this case, the somewhat increased diameter of the core strand (3× the core wire) and the thermal scaling (increased volume/exterior surface area) allowed infrared imaging to be performed. The noise makes the front difficult to see, but the IR contour plot in Fig. 4.4a does show a single $A \rightarrow M^+$ front traversing the specimen downward during loading, and a single $M^+ \rightarrow A$ front traversing the specimen upward during

unloading (the same as for the single core wire experiment). The contour plot in Fig. 4.4a was generated in the same fashion as that of Fig. 4.3, except temperature is the field variable, and the entire gage length is visible. At this slow loading rate, the relevant temperature changes are quite small and are somewhat masked by the clutter of other artifacts. The core strand is only 1 pixel wide as viewed by the 256×256 IR sensor. It was not perfectly aligned, especially above and below the LE gage length, so incident infrared radiation was split between two pixels in these areas, making the temperature measurement inaccurate at the specimen ends. In addition, during unloading the LE gage length is about 1°C warmer than during loading, due to a small temperature increase in our laboratory (T_a) over the five hour experiment. (Cleaner IR contour plots can be found at higher rates, as in Fig. 3.11b and subsequently in Chapter 5.) Nevertheless, close inspection does show a slight warm spot moving downward at constant rate during the loading plateau, and then a slight cool spot moving upward during the unloading plateau. Dashed white lines have been overlaid in Fig. 4.4a to highlight these locations. These intersect the specimen thermocouple location and times when the ±0.25 °C transients occur.

The circled numbers above the specimen thermocouple history and the points overlaid on the stress history in Fig. 4.4a correspond to the DIC axial strain images of Fig. 4.4b. The DIC images have the axial surface strains overlaid on black and white images of the specimen. As in Chapter 3, the DIC FOV corresponds to the lower third of the LE gage length. We can now clearly see the global transformation front that was identified in Fig. 4.4a. As expected from the IR contour plot, the $A \rightarrow M^+$ front enters the DIC FOV between image ② and ③, and by image ⑦ has exited the FOV. In addition, it is now apparent that the macroscopic front is comprised of staggered fronts in the individual wires that revolve around the tensile axis during overall propagation. Upon close inspection we also found that fronts in individual wires never pass one another as they propagate. For example, examine the staggered pattern of fronts at $z/L = 0.37$ in image ③. The same wire is found one pitch below (a single turn of its helix) by counting down the strand by six wires to $z/L = 0.25$. Accordingly, we see the same staggered pattern of fronts at $z/L = 0.25$ in image ⑥. The same can be done with the staggered fronts during unloading. This staggering is similar to what was observed in the 7×7 cable in Section 3.3.2, and the explanation is the same. Staggered fronts distribute the individual heat sources, thereby minimizing temperature deviations from ambient and any consequent axial stress changes. They remain clustered within about one strand diameter, however, to minimize incompatibility within a given cross-section that would be severe if one wire front greatly outpaced the others.

Although the core wire, core strand, and full cable have similar mechanical responses, slight differences in their thermal behavior at this slow strain rate of $\dot{\delta}/L = \pm 1 \times 10^{-5}$ s^{-1}
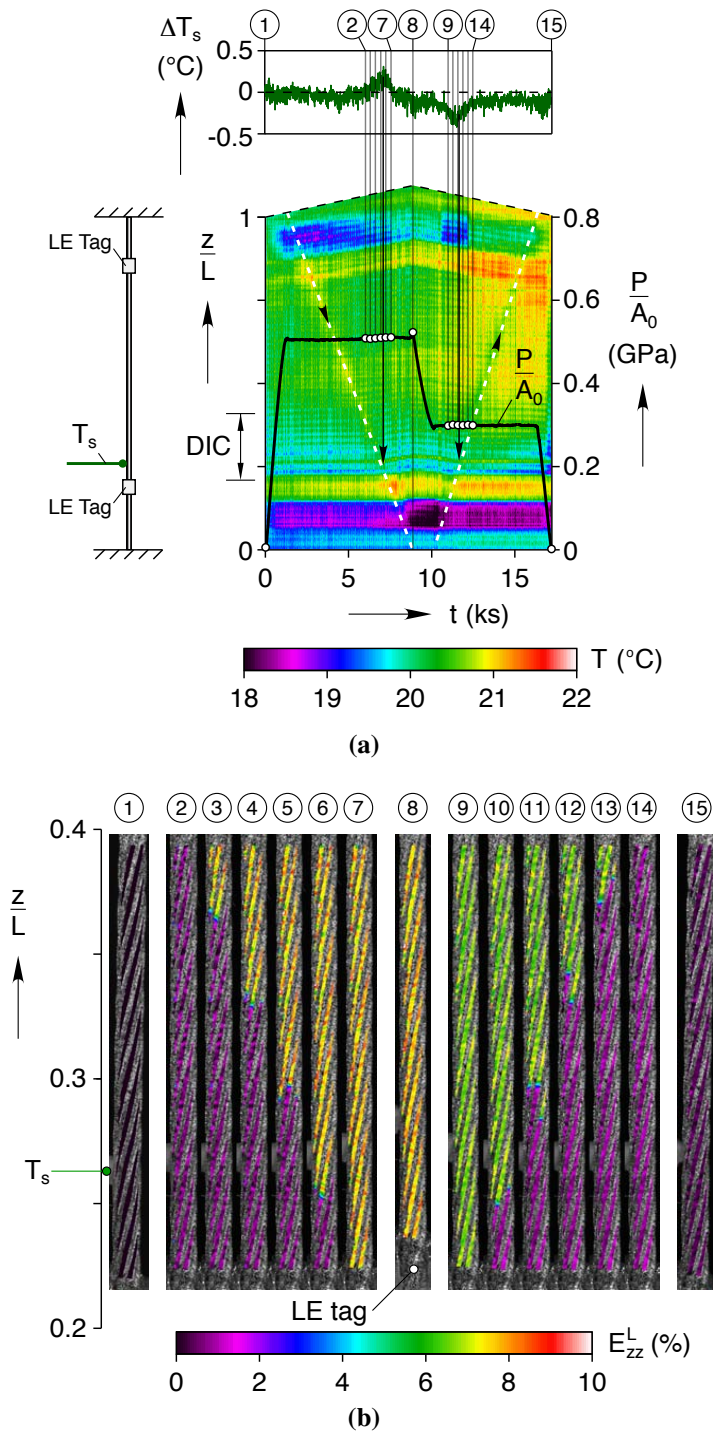
Figure 4.4 Experiment S1a (1×7 strand at $\dot{\delta}/L = \pm 1 \times 10^{-5}\ \text{s}^{-1}$): (a) Contour plot of IR temperature field and overlaid stress history (right hand axis). Evolution of the specimen thermocouple history is shown above ($\Delta T_s = T_s - T_a$), (b) Selected axial strain field images from DIC analysis where image labels correspond to circled numbers in (a).

are harbingers of large differences in their mechanical response at higher strain rates. In the single core wire, the temperature excursions as the front passed by the type-K thermocouple were less than the inherent noise in the thermocouple used (±0.1 °C). Yet the temperature excursions were about ±0.25 °C for the core strand (see Fig. 4.4a) and ±0.75 °C for the full cable (see Fig. 3.6) for the same strain rate. This shows that enthalpy changes are dissipated less quickly in the larger diameter core strand and cable, but probably not as slow as in monolithic rods of the same diameters.

4.3 Isothermal Responses of 1×27 Components

We now turn to the 1×27 cable, whose response is significantly different from wires loaded in parallel, due to the deeper helix angle of its layers. Figure 4.5 shows a cross-section of cable ($z = 0$), which again has four wire types (labelled A, B, C, D), but in this case wires B, C, and D are all simple (first-order) helices in a left/right/left-hand lay as shown in Fig. 4.5b. The helix angles range from $-47.9°$ to $42.5°$ as shown in Table 4.3 along with other dimensions. These values can be treated as faithfully accurate to the exact idealized geometry shown in Fig. 4.5a, where unlike the 7×7 cable, the different wire types fit together to radially touch exactly one diameter apart. Again, however, the drawing process used in the cable's fabrication likely disturbed this geometry somewhat by wire settling and Hertzian
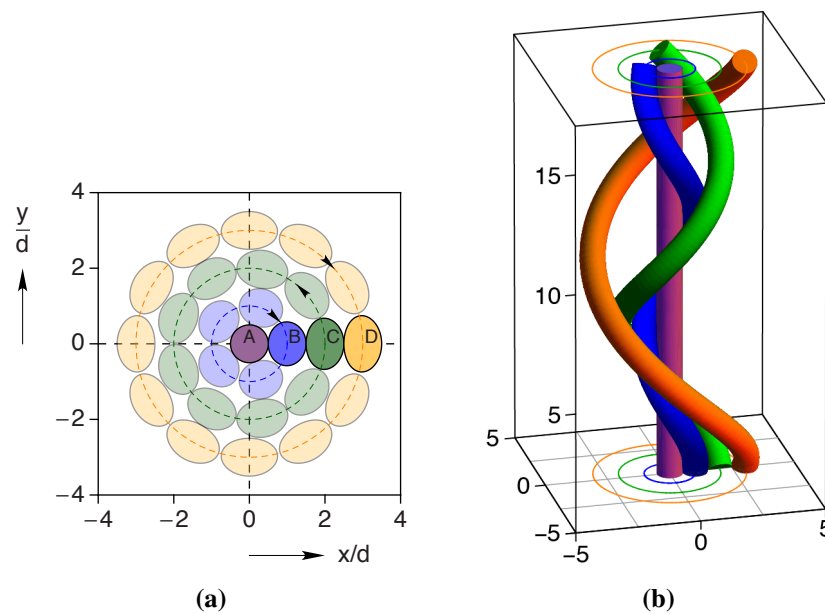
Figure 4.5 1×27×0.226 mm cable geometry: (a) cross-section ($z = 0$) with dimensions normalized by the wire diameter (d). (b) isometric view of the four wire types (A, B, C, D) in (a).

contact deformation.

4.3.1 Measured Responses

The large values of α_0 lead to increased axial and bending compliance of the overall cable. Rather than pulling these specimens to the end of a loading plateau (which may not clearly exist), an incremental loading was performed for each of the 1×27 components. The incremental loading program generally consisted of cycles out to successively greater maximum strains of $\delta_e/L_e = \{7, 10, 20, 30, 40\}$ %. Some experiments were halted when the specimen failed, and in others the test was stopped short of failure in order to disassemble and inspect the specimen. These experiments are presented below in section 4.3.1, starting with the core wire and progressing to successively larger components. Infrared and DIC data was collected during all the experiments, but the available DIC results are deferred until section 4.3.2 where the observations can be properly explained using the deduced responses of the layers.

For the core wire as shown in Fig. 4.6, one cycle was performed to $\delta_e/L_e = 6.3\%$ prior to cycling to 7%, then 10%, and failure occurred during cycle 4 loading. The first cycle to $\delta_e/L_e = 6.3\%$ was to capture the fundamental tensile response of the wire without introducing appreciable plasticity. The small amount of non-linearity in the curve prior to the loading plateau is due to rhombohedral phase (R-phase), as mentioned in Section 3.3.1. The second cycle shows a small amount of shakedown in that the loading plateau is slightly lower (-12 MPa) than that for cycle 1, and since the maximum strain was beyond the initial load plateau, the unloading plateau during cycle 2 is lower by a greater amount (-32 MPa). Cycle 3 shows a further, but small (-12 MPa), reduction in the stress at the loading plateau,
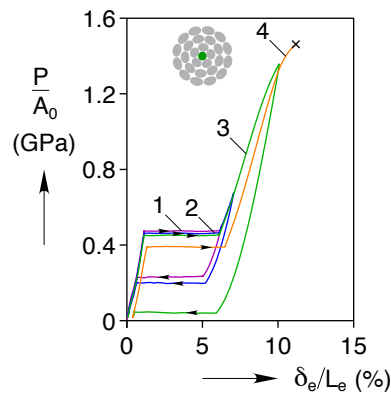
Figure 4.6 Experiment W2b. Mechanical response of core wire from 1×27 cable subjected to incremental cycles at $\dot{\delta}/L = \pm 1 \times 10^{-4}$ s^{-1}.

76

Table 4.3 Geometric parameters of the four wire types in the 1×27 cable: reference helix angle (α_0), normalized mean helix radius (r_0/d), and normalized pitch (p_0/d).

Wire type	Number of wires	α_0	r_0/d	p_0/d
A	1	0º	0	NA
B	5	-30.4º	1	10.7
C	9	42.5º	2	13.7
D	12	-47.9º	3	17.0

and since it was taken well into the post-plateau regime, the unloading plateau is greatly lowered to only 42 MPa. Cycle 4 shows a significantly reduced loading plateau from the previous cycle (by −61 MPa), and no unloading response was measured since the wire broke at the grips at 11.2% (1.46 GPa). Note that all cycles exhibited a propagating transformation front, very similar to that shown in Fig. 4.3, during each load plateau.

The force-elongation and torque-elongation response of the 1×6 core strand is shown in Fig. 4.7a. Despite the substantial helix angle ($\alpha_0 = -30.4$º) of the five helical wires, the overall shape of axial load response still looks quite similar to the core wire in uniaxial tension, but differences do exist. The loading modulus during cycle 1 is roughly 21 GPa, compared to 41 GPa in the core wire, neglecting the slight R-phase nonlinearity in both responses. The loading plateau onset and height are at $\delta_e/L_e = 2.2$ % and $P/A_0 = 374$ MPa, versus 1.1 % and 475 MPa in the core wire. Interestingly, the plateaus of both components terminate at $\delta_e/L_e = 6.0$ %. The 1×6 shakedown behavior in cycle 2 and 3 is similar to the core wire, with large stresses depressing the unloading plateaus more than the loading plateaus. Finally, in cycle 3 the core strand fails at $\delta_e/L_e = 16.4$ % (1.14 GPa), an additional 5.2 % beyond the core wire.

It is also helpful to compare the 1×6 strand stress to the 1×7 strand, even if the wires are different NiTi alloys. Note that the type-B wires in the 1×6 have a greater helix angle and thus experience more torsion and bending. Tellingly, the same calculation used to explain the slight reduction in 1×7 core strand plateau height, compared to the 7×7 core wire, does quite poorly on the 1×6: $475 \text{ MPa} (1 + 5\cos(-30.4º))/6 = 421$ MPa. This calculation ignores the contribution of shear loads, yet it still significantly over predicts the 1×6 plateau height. A possible explanation for the reduced plateau is the local torsion and bending on each type B wire reduced the wire's average tensile stress from its uniaxial plateau height, as has been observed in tension-torsion testing of NiTi tubes [117]. Alternatively, the reduced plateau may also be due an interaction with the core wire, as explored in Section 5.3.1.

The 1×6 torque in 4.7a roughly follows the axial load, except it is negative due to the left hand lay of layer B. The two responses deviate slightly between $\delta_e/L_e = 6.0$ % and 8.0 %,
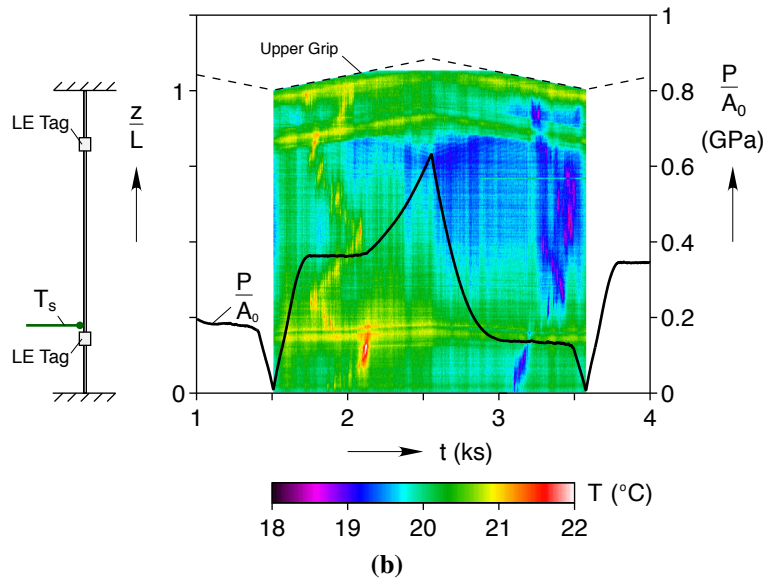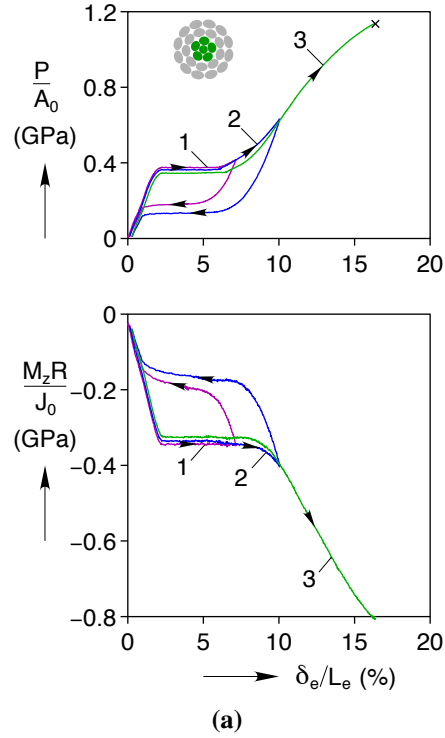
Figure 4.7 Experiment S2a ($1{\times}6$ strand at $\dot{\delta}/L = \pm 1 \times 10^{-4}\ s^{-1}$): (a) Mechanical response for three successively larger cycles. (b) Contour plot of IR temperature field and overlaid stress history during the 2nd cycle.

where the axial load stiffens and the torque remains relatively flat. As we will show below, this is because the core wire contributes to the axial load, but it does not affect the torque.

The IR temperature field and stress history for cycle 2 of experiment are displayed in Fig. 4.7b. Temperature blooms of about 1 to 2 °C from ambient (T_a = 20.4 °C) are

seen along the specimen during the loading and unloading plateaus. Cycles 1 and 3 exhibit similar behavior, so they are not shown. As before, the temperature readings at the LE tags are inaccurate and can be disregarded. The pattern of blooms look somewhat like diffuse transformation fronts propagating along the specimen gage length, but this is only at the length scale of the IR measurements. The DIC strain fields gave a magnified view of the blooms and revealed that they are, in fact, strain localizations initiated at stress concentrations. The localizations appear quickly causing the small local temperature rise seen in Fig. 4.7b, but they do not sweep through the specimen like a propagating transformation front. Unfortunately, the DIC results for this particular experiment were lost in a hard drive failure prior to publication so the data cannot be displayed, but similar strain fields were observed in experiment S2b in Chapter 5 (see Fig. 5.12). We defer a more thorough explanation of the observations until that experiment is discussed, but the stress concentrations causing the localizations can be explored now.

Although invisible to the naked eye, the scanning electron microscope images in Fig. 4.8 unveiled the source of the stress concentrations. The core wire has a helical line indentation, while the 1×6 strand and 1×15 multilayer strand have small dimples in systematic patterns on their surfaces. These surface indentations are due to the cable forming process, where the alternating layers are tightly wound around each other, creating large contact stresses, and then shape set, freezing the indentation in place. In addition, the 1×6 has large divots of missing material (see Fig. 4.8b), creating more severe stress concentration sites for the strain localizations.

(a) (b) (c)
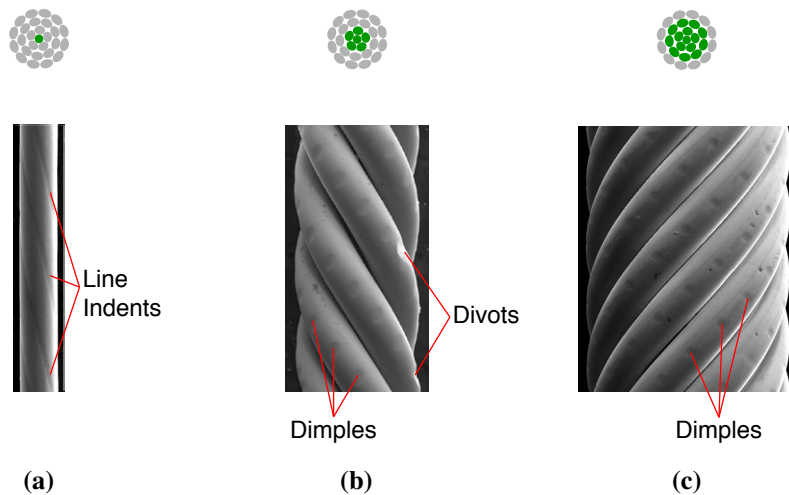
Figure 4.8 SEM images of (a) 1×27 core wire, (b) 1×6 core strand, and (c) 1×15 multi-layer strand, showing Hertzian line indents, dimples, and a few divots resulting from contact of outer layers previously removed.
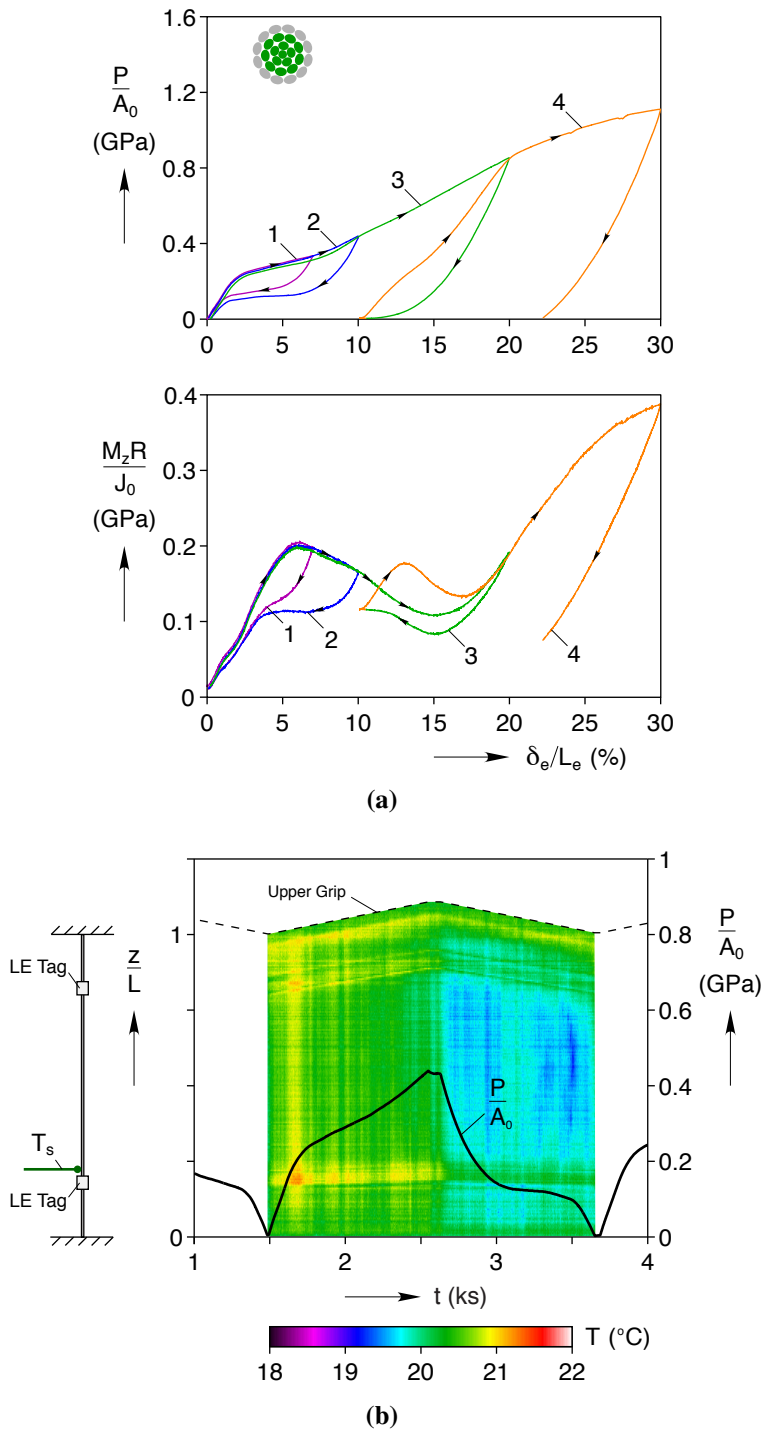
Figure 4.9 Experiment M2a (1×15 strand at $\dot{\delta}/L = \pm 1 \times 10^{-4}$ s^{-1}): (a) Mechanical response during four cycles, each to a successively larger strain. (b) Contour plot of IR temperature field and overlaid stress history during the 2nd cycle.

The force-elongation and torque-elongation response of the 1×15 multi-layer strand (experiment M2a) is shown in Fig. 4.9a. The deep helix angle ($\alpha_0 = 42.5$) and large helix radius ($r_0 = 2\,d$) of the 9 layer C wires clearly have modified the behavior so that the axial load, compared to the 1×6, bears little resemblance to the core wire. Cycles 1 and 2 have an initial loading modulus of only 12.4 GPa, they do not exhibit loading and unloading plateaus, and the transitions between elastic and phase transformation regions are rounded. After being loaded to $\delta_e/L_e = 20.0\%$ for cycle 3, one might have expected the cable to linearly unload to about 15% residual strain. Instead, the curve is quite nonlinear and the strain returned to 10.1% before reaching zero axial load. This suggests that the layer C wires of the 1×15 underwent a $M \rightarrow A$ transformation, while the less compliant wires had experienced significant plasticity and thus prevented full strain recovery. Loading on the fourth cycle also shows non-linear, hysteretic, behavior associated with phase transformation until reaching the maximum load of cycle 3. Two small load drops occur at $\delta_e/L_e = 24.1\%$ and 27.4 % prior to unloading on cycle 4. The extensometer strain rate $\dot{\delta}_e/L_e$ slowed during these load drops, and none of the wires in this cable broke, as discussed below, indicating that the load drops are due to the grips slipping at these high loads. A fifth cycle beyond $\delta_e/L_e = 30\%$ was not performed to preserve an intact 1×15 strand, but in two other experiments at higher elongation rates (Exp M2b and M2c in Chapter 5) the 1×15 specimens broke at $\delta_e/L_e = 29.3\%$ and 26.8 %.

The 1×15 torque is strikingly non-monotonic and path dependent. Cycles 1 and 2 both exhibit wavy responses up to the local maximum at $\delta_e/L_e = 6.0\%$ (205 MPa on cycle 1), and upon unloading they both return to nearly zero torque. From the local maximum in cycle 3, the normalized torque drops to a local minimum of 108 MPa at $\delta_e/L_e = 15.1\%$ before increasing again to 191 MPa. Cycle 3 unloading drops to another local minimum of 84 MPa and then rises to 117 MPa to complete unloading to zero axial load. Cycle 4 has an up-down-up shape during loading that looks like a smaller, shifted, version of the cycle 3 loading response. Surprisingly, the local maximum of 177 MPa during cycle 4 actually exceeds the loading path set by cycle 3 until rejoining it at $\delta_e/L_e = 20\%$. After unloading, cycle 4 concludes with a smaller torque than cycle 3, but still non-zero (75 MPa).

The intriguing torque response of the 1×15 is due in part to the alternating handedness of the layers. In the 1×6 we observed a negative torque, but the torque switches sign in the 1×15 because each of the 9, right-hand laid, layer C wires has twice the moment arm of the 5, left-hand laid, layer B wires. This alternating handedness has little effect on the axial load P since $\cos(-\alpha_0) = \cos(\alpha_0)$, yet the handedness strongly affects M_z since $\sin(-\alpha_0) = -\sin(\alpha_0)$. For instance, during loading there are changes in the torque tangent modulus at $\delta_e/L_e = 2.2\%$ and 6.0 %, yet there are no corresponding changes in the axial

load tangent modulus.

The torque response beyond $\delta_e/L_e = 10$ % is difficult to precisely interpret since plasticity and phase transformation intermingle. We can, however, make a few observations. First, note that after cycles 1 and 2 the axial load and torque both return to zero, but after cycles 3 and 4 only the axial load returns to zero. This is because of the layered construction of the 1×15. At zero total load, the load from each layer must sum to zero, but the torque is only zero at the same δ_e/L_e by chance or if all the layers generate zero torque. Second, we can postulate that the bizarre behavior starting with the local minimum at $\delta_e/L_e = 15.1$ is due to the stiff layer B wires plastically deforming while the compliant layer C wires remain superelastic. The rise in torque after $\delta_e/L_e = 15.1$ could be layer B plastically deforming causing its negative torque to diminish in comparison to layer C's positive torque. By extension, the cycle 3 unloading and cycle 4 loading torque may be higher than otherwise due to the lessened influence of layer B.

Figure 4.9b depicts the temperature field and axial stress history for the second cycle. On the whole, the specimen uniformly heats up by 0.5°C during loading and cools down by -0.5°C during unloading, with no evidence of localized transformation. There is some evidence of early transformation around $t = 1.7$ ks, but it is also uniform. (The small stress relaxation at 2.55 ks occurred while the load frame was being reprogrammed to return to zero load.) Thus, the 1×15 has the same spatially uniform temperature fields as we saw in Chapter 3 for the full 1×27 cable (see Fig. 3.12b).

The mechanical response of the complete 1×27 cable is in Fig. 4.10, showing many of the same trends as the 1×15. The axial load response is quite similar, including the non-linear unloading curve on cycle 3. As to be expected, though, the layer D wires reduced the initial axial load modulus to 8.8 GPa and permitted a fifth cycle to $\delta_e/L_e = 40$ %. Although the specimen did not break on cycle 5, another 1×27 cable pulled at a higher strain rate (Exp. C2f in Chapter 5) did break at $\delta_e/L_e = 39.2$ %. Again, the 7 small load drops during loading on cycle 4 and cycle 5 all correlate with drops in $\dot{\delta}_e/L_e$, suggesting that the drops are due to grip slippage. Also similar to the 1×15, the torque remains non-monotonic and switches sign due to the addition of another layer with a helix angle of opposite sign.

As can be seen for all four components tested in Figs. 4.6, 4.7a, 4.9a, and 4.10, despite the incremental cycling, an outer loading envelope exists for each mechanical response during $A \rightarrow M^+$ transformation and beyond to the plasticity (slip) dominated regime. The axial load and reaction torque return to nearly the same global stress value upon reloading to the previous cycle's maximum δ_e/L_e. As a quick comparison, these outer envelope are plotted together in Fig. 4.11. It shows the progression in the force-elongation responses, becoming generally more compliant and ductile as each layer (B, C, D) is added. Each
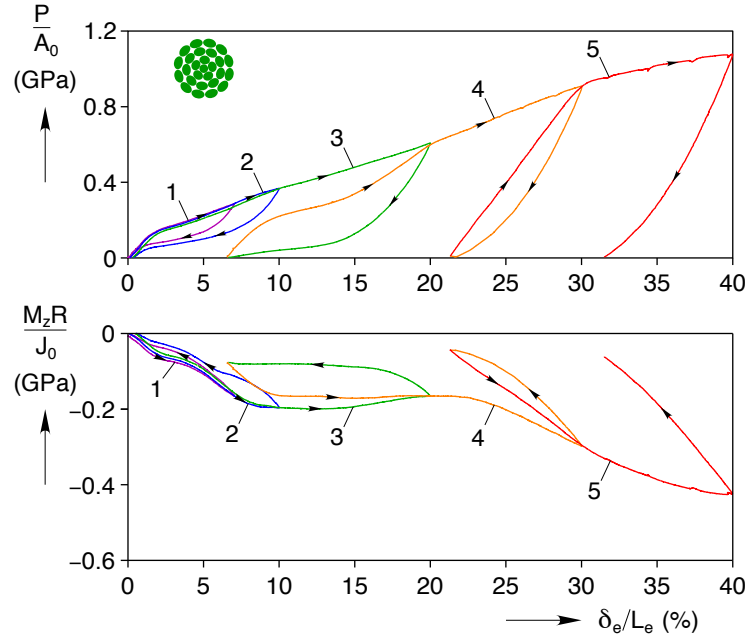
Figure 4.10 Experiment C2d. Mechanical response ($\dot{\delta}/L = \pm 1 \times 10^{-4} \text{ s}^{-1}$) of 1×27 cable subjected to five cycles, each to a successively larger strain.

successive layer has a deeper angle (α_0) and thus, just like any common coil spring, force is traded for greater maximum displacement. Also, the force responses progress from ones that have clear load plateaus (core wire and 1×6 strand) to ones that are nonlinear but maintain a positive tangent modulus (1×15 strand and 1×27 cable).

We should mention that our grips were simple flat knurled plates that clamped the specimens at their ends with significant radial pressure, so a severe stress concentration exists there. For the particular experiments in Fig. 4.11, the 0.226 mm core wire and 1×6 broke near the grips at the maximum strain shown, while the 1×15 and 1×27 did not break. As previously mentioned, however, in other experiments the 1×15 and 1×27 broke at the grips within 1 % strain of the maximum strains shown in Fig. 4.11. Of course, cables are customarily terminated by loops/crimps that are designed to minimize stress concentrations in engineering practice, so the failures here were due to the severe boundary conditions used and should not be interpreted quantitatively as expected ductility values. The qualitative trends, however, between the four components are representative, i.e., one can expect larger failure strains as more layers are added and the overall compliance is enhanced.

From the evolution of stiffnesses in Fig. 4.11, one might have expected the less ductile inner layers to fail, or perhaps slip, inside the outer layers during the experiments. To investigate whether the inner layers failed, a 1×15 (Exp. M2a), and 1×27 (Exp. C2d) specimen were disassembled and it was found that all wires were fully intact. Rather than
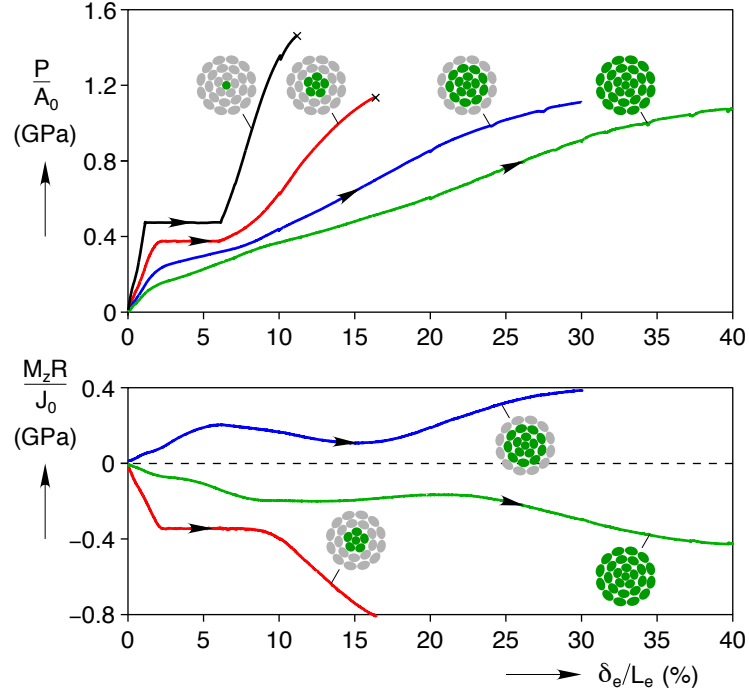
Figure 4.11 Comparison of mechanical responses of 1×27 components (Exp. W2b, S2a, M2a, and C2d). Only the outer loading portions of the multiple incremental cycles of Figs. 4.6, 4.7a, 4.9a, and 4.10 shown.

disassemble the failed 1×6 specimen from experiment S2a, an unbroken 1×6 specimen (Exp. S2b in Chapter 5) was disassembled instead. The S2b specimen was stretched to a maximum strain of $\delta_e/L_e = 13$ %, which is beyond the core wire failure strain in experiment W2b (11.2 %), yet all 6 wires were intact upon disassembly. This still leaves the possibility of inner layers slipping within outer layers. Prior to the experiments, the specimens were cut to length using an abrasive cut-off wheel, which made all the wires at each end flush with one another. After the experiment, but prior to disassembly, the ends were inspected under an optical microscope, and the wires at each end remained flush with one another within one wire diameter. Furthermore, a 305 mm long 1×15 with welded ends was tensile tested ($L = 269$ mm, and $L_e = 50.31$ mm) to $\delta_e/L_e = 10\%$. Afterwards the strand was torn apart to confirm that the core wire was still attached to the weld. The mechanical response of the welded-end 1×15 was the same as the outer envelope defined by cycles 1 and 2 in Fig. 4.9a. Thus, all signs indicate that the inner layers did not appreciably slip in the experiments described above.

The lack of wire failure or evidence of slipping in experiments S2b, M2a, and C2d may be surprising so we offer a few observations and explanations. First, the responses in Fig. 4.11 are quite smooth without any load drops large enough to indicate failure of a

sub-layer prior to the failure of the entire component. Second, each outer layer shields the inner layers from the stress concentrations at the grips that caused the observed failures in the 1×6, 1×15, and 1×27 components. Third, as a strand is stretched, the outer layers radially tighten on the inner layers, impeding slip, and causing the inner layers to elongate in the axial direction.

Returning to Fig. 4.11, the progression in the torque responses, are less monotonic than the axial load. The 1×6 strand has a relatively large, negative (due to the left-hand lay of layer B) torque reaction with a clear moment plateau. Adding layer C (right-hand lay) in the 1×15 strand causes the torque reaction to switch sign and to progress in an up-down-up manner with axial elongation. Adding layer D (left-hand lay) in the full 1×27 cable causes the torque to switch back to a negative sign and has an up-down-up character, but at a reduced torque magnitude for the same axial strain as the previous case. Each layer that is added not only has a deeper helix angle, but has more wires and a bigger moment arm than the previous layer, so that outer layer tends to dominate the torque response of the assembly. The alternating handedness also serves to keep the normalized torque relatively small in the full 1×27 cable despite the large helix angles. On the other hand, the outer layers do not completely overwhelm the inner layer torque responses. The "stair step" changes to the 1×27 torque response from $\delta_e/L_e = 0$ % to 10 %, for instance, seem to coincide with changes in the torque of inner layers. This observation leads to the concept of subtracting one component's mechanical response from the next bigger component, leaving the response of the outer layer for that component

4.3.2   Deduced Responses of the Layers

In this section, the response of each layer of wires in the 1×27 is deduced by subtracting the directly measured responses of section 4.3.1 from one another. For example, the deduced layer B response is calculated by subtracting the core wire response from the 1×6 response. Clearly this analysis method must be used with caution, since we are inferring the response of each outer layer, rather than directly measuring it, but there are a number of observations below that strongly support this technique.

The most straightforward method to perform a subtraction would be to subtract the axial load and torque of, say, the core wire from the 1×6 at the same global strain δ/L. However the local strains caused by the grips on the 1×6 are different than on the core wire, and one or both of the specimens may have slipped in the grips, so we subtracted the axial load and torque at the same LE strain δ_e/L_e to eliminate these effects. This subtraction makes two notable assumptions. (1) It assumes that any interactions between the various layers do not
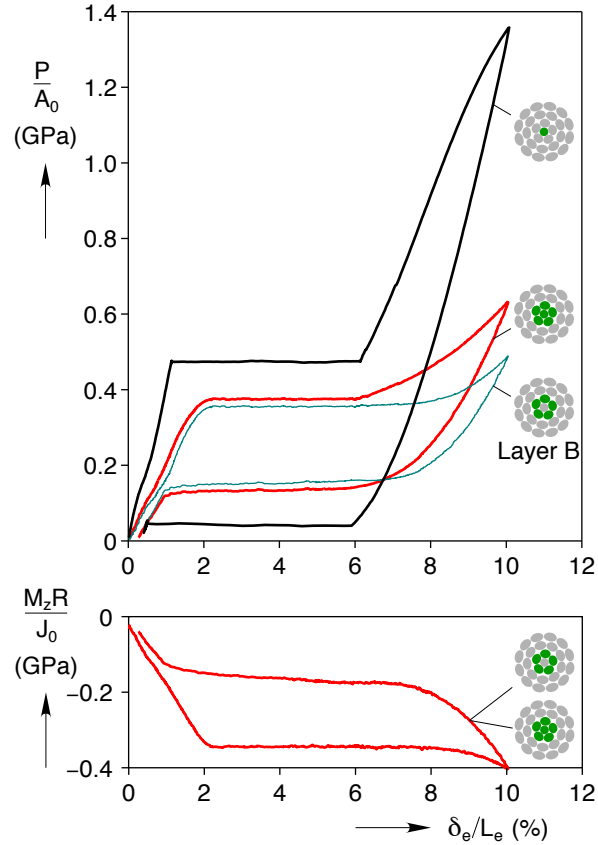
Figure 4.12 Mechanical responses (bold lines) from the 1×27 core wire (Exp. W2b) and the 1×6 (Exp. S2a), then subtracted to produce the deduced response of layer B (thin line).

affect the axial load or torque response. (2) It assumes that the layers do not slip relative to one another, or if there is local slipping, this averages to zero along the 50 mm distance between the two LE tags.

First we subtract the core wire from the 1×6 strand. In Fig. 4.6 and Fig. 4.7a each cycle on the core wire and 1×6 were shown. To keep Fig. 4.12 legible, only the outer envelope of cycles 1, 2 and 3 of experiment (Exp. W2b) on the core wire, and the outer envelope of cycles 1 and 2 on the 1×6 strand (Exp. S2a) are shown and subtracted. This represents the isothermal response that would be observed if the specimens were simply elongated to $\delta_e/L_e = 10$ % and back to zero load. Recall the observation that the 1×6 axial load and torque do not always follow one another. This discrepancy is shown clearly in Fig. 4.12, where the 1×6 axial load P increases at $\delta_e/L_e = 6.0$ %, but the torque M_z does not increase until about $\delta_e/L_e = 8$ %. According to the core wire stress-strain curve, at $\delta_e/L_e = 6$ % there is a sharp change in the core wire tangent modulus when it reaches the martensite modulus. When the core wire mechanical response is subtracted from the 1×6 response, the axial load tangent modulus increase at $\delta_e/L_e = 6$ % is postponed to 8 %. Now the presumed layer B
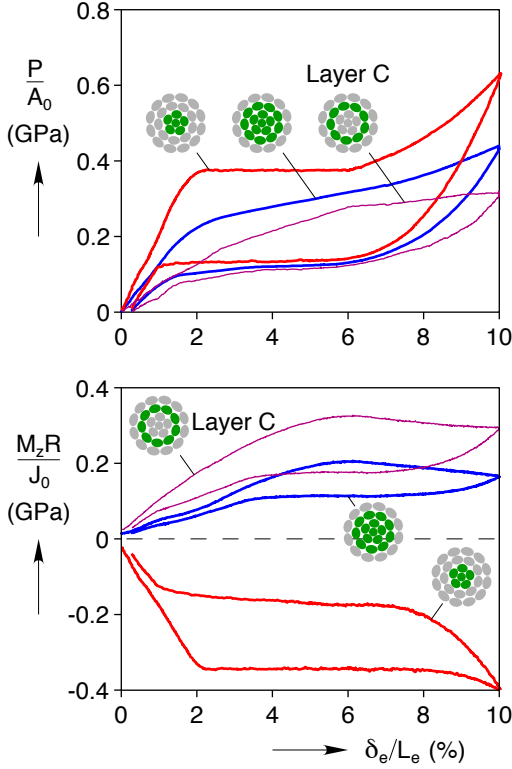
Figure 4.13 Mechanical responses (bold lines) from the 1×6 core strand (Exp. S2a) and the 1×15 (Exp. M2a), then subtracted to produce the deduced response of layer C (thin line).

axial load response follows the normalized torque curve nicely.

The subtraction of the 1×6 from the 1×15 sheds light on both the mechanical response and the DIC results, so prior to discussing the subtraction, we must alert the reader to a DIC coordinate system change. In previous DIC strain field images, the zz component of strain was overlaid on the image of the specimen because the helix angles on the surface of the 7×7 components were relatively small. The 1×27 components, however, have larger helix angles, so the coordinate system was oriented along the wires in the reference (undeformed) image as closely as possible. Vic-3D does not permit full three-dimensional curvilinear coordinate systems, but it does wrap the coordinate system around the surface of the specimen [30]. To envision the coordinate system used, consider a cylinder with a plane sliced though it at an angle α_0. The intersection of the plane and the cylinder is an ellipse. Here we report the component of strain along the ellipse, which does not follow the path of a helix exactly, but it is a close approximation. Despite this small difference, the color bar in Fig. 4.14b is labeled as E_{tt}^{L} to indicate that the colors correspond to the strain component tangent to the helix.

Figure 4.13 depicts the subtraction of the 1×6 strand (Exp. S2a) axial load and torque from the 1×15 multi-layer strand (M2a) to look at the deduced behavior of layer C. As
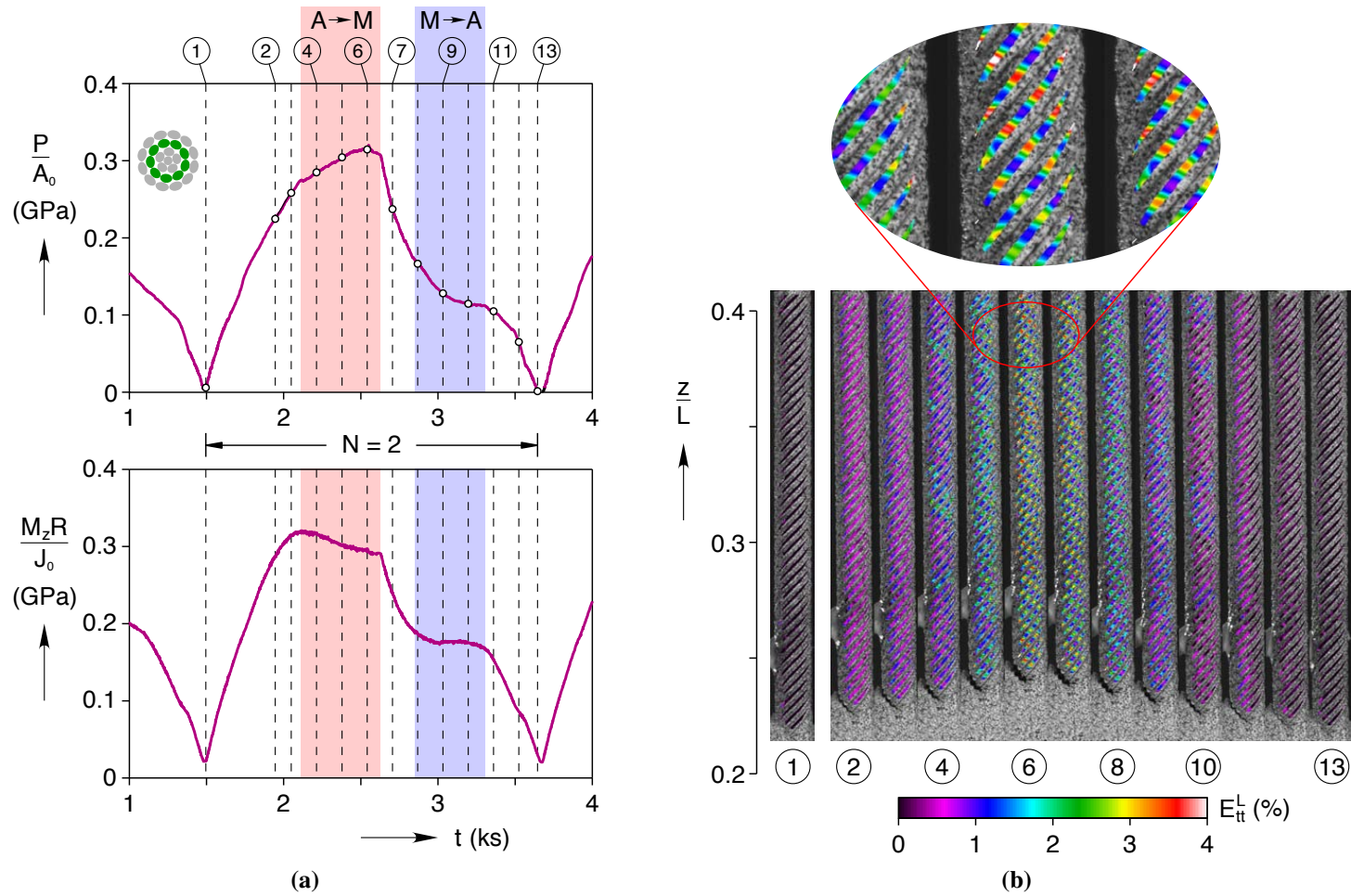
Figure 4.14 (a) Deduced layer C axial load and torque history during the 2nd cycle (generated by subtracting the 1×6 (Exp. S2a) from the 1×15 (Exp. M2a) at the same values of δ_e/L_e). (b) 1×15 tangential strain field images (Exp. M2a), where circled time labels in (a) correspond to image labels in (b).

before, only the outer loop of cycle 1 and 2 of both components are shown and subtracted. Figure 4.14a, however, depicts cycle 2 ($\delta_e/L_e = 0.1\%$ to 10%), since the presumed axial load and torque of layer C are plotted against time. Note that, even though both the 1×6 and 1×15 responses were subtracted to deduce the layer C response, the time t on the x-axis is the time for the 1×15 experiment. The circled time labels in Fig. 4.14a correspond to the strain field images in Fig. 4.14b, which are the 1×15 DIC results (Exp. M2a). Several confusing aspects of the 1×15 results are removed by this subtraction. First, during loading below $\delta_e/L_e = 6\%$, the 1×15 torque has a slightly wavy character, but the inferred torque of layer C is much more smooth. Second, the 1×15 torque has a local maximum at $\delta_e/L_e = 6\%$ during loading, yet the axial load tangent modulus is constant. After the subtraction, layer C's axial stress and normalized torque tangent moduli both change together at $\delta_e/L_e = 6\%$. This simultaneous tangent modulus change is shown more clearly in Figure 4.14a. Third, it was previously difficult to correlate the appearance and disappearance of strain localizations with changes in the axial load response of the 1×15 multi-layer strand. The changes the layer C tangent moduli, however, are associated with changes in the strain field.

- The strain field first begins to have local areas of strain above $E_{tt}^L = 1\%$ between image ③ and ④, right when both the axial load and torque tangent moduli change at $\delta_e/L_e = 6.0\%$.

- During unloading between ⑥ and ⑧ the magnitude of the localized strains decrease, but their spatial size stays relatively constant.

- Just before ⑨ at $\delta_e/L_e = 6.6\ \%$ the axial load and torque moduli change and in ⑨ we see some of the localizations starting to disappear.

- Between ⑩ and ⑪ ($\delta_e/L_e = 3.7\ \%$) the moduli change again as the last of the localized strain regions disappear.

Thus, these tangent moduli changes in the presumed layer C response denote the beginning of the $A \rightarrow M$ transformation during loading. During unloading, they denote the beginning and end of the $M \rightarrow A$ transformation.

As shown in the magnified image at the top of Fig. 4.14b the localized strains on the surface of the 1×15 appear in a striated pattern. These striations were not visible in the temperature field (Fig. 4.9b) because they slowly appear and disappear (like any stress concentration) distributing the heat exchanges over time, and because the IR sensor does not have sufficient spatial resolution to pick up such fine features. The pattern of striations matches the dimples in Fig. 4.8c, leading us to conclude that the striations are caused by the dimple stress concentrations. As expected, the helix angle of the striations is roughly -50°
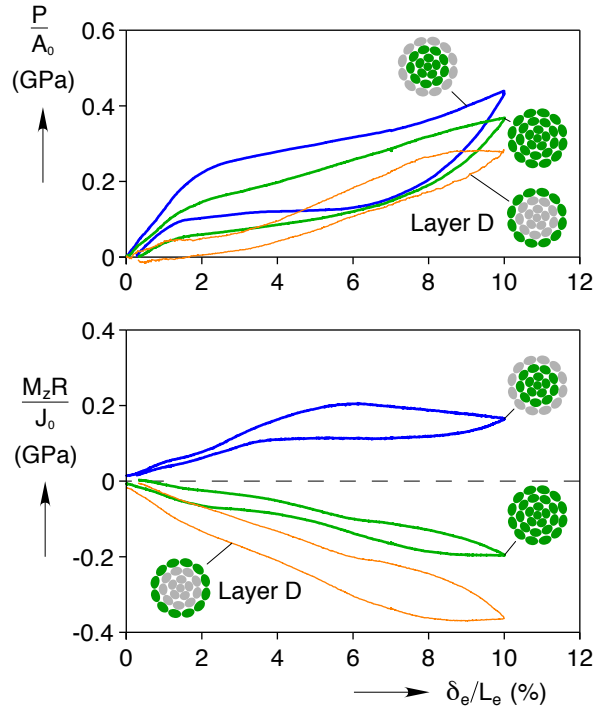
Figure 4.15 Mechanical responses (bold lines) from the 1×15 multi-layer strand (Exp. C2d) and the 1×27 cable (Exp. C2d), then subtracted to produce the deduced response of layer D (thin line).

in image ⑥, which matches the stress free $-47.9°$ helix angle of layer D if one allows for some deformation.

The 1×27 response in Fig. 4.17a has a similar shape to the 1×15, and as such the analysis of layer D is similar to layer C. Similar plots of the subtraction, response histories, and strain fields are shown in Fig. 4.15, Fig. 4.16a, and Fig. 4.16b. During loading, layer D's axial load is non-linear between roughly $\delta_e/L_e = 1.1$ % and 4.0 %. Similar non-linearities appear in layers B and C as well, although they become more pronounced with greater helix angles and helix diameters. Given that the qualitative shape of the non-linearity is quite similar to the non-linearity in layer A, the core wire (Exp. W2b herein, and Exp. W2a in Chapter 3), it is likely due to the R-phase. Next, similar to layer C, observe that "stair step" behavior of the 1×27 torque is removed when the 1×15 is subtracted. There still is a slight "stair step" left in the torque response, but this appears to be the same R-phase non-linearity manifesting itself in the torque response. When the elongation reaches $\delta_e/L_e = 8.8$ % both the axial load and torque tangent moduli change together. As expected from the layer C analysis, although the 1×27 axial load response did not suggest any significant changes in the strain field at $\delta_e/L_e = 8.8$ %, the layer D responses tell a different story.

• Between ③ and ④ the layer D tangent moduli changes coincide with the first strain

90
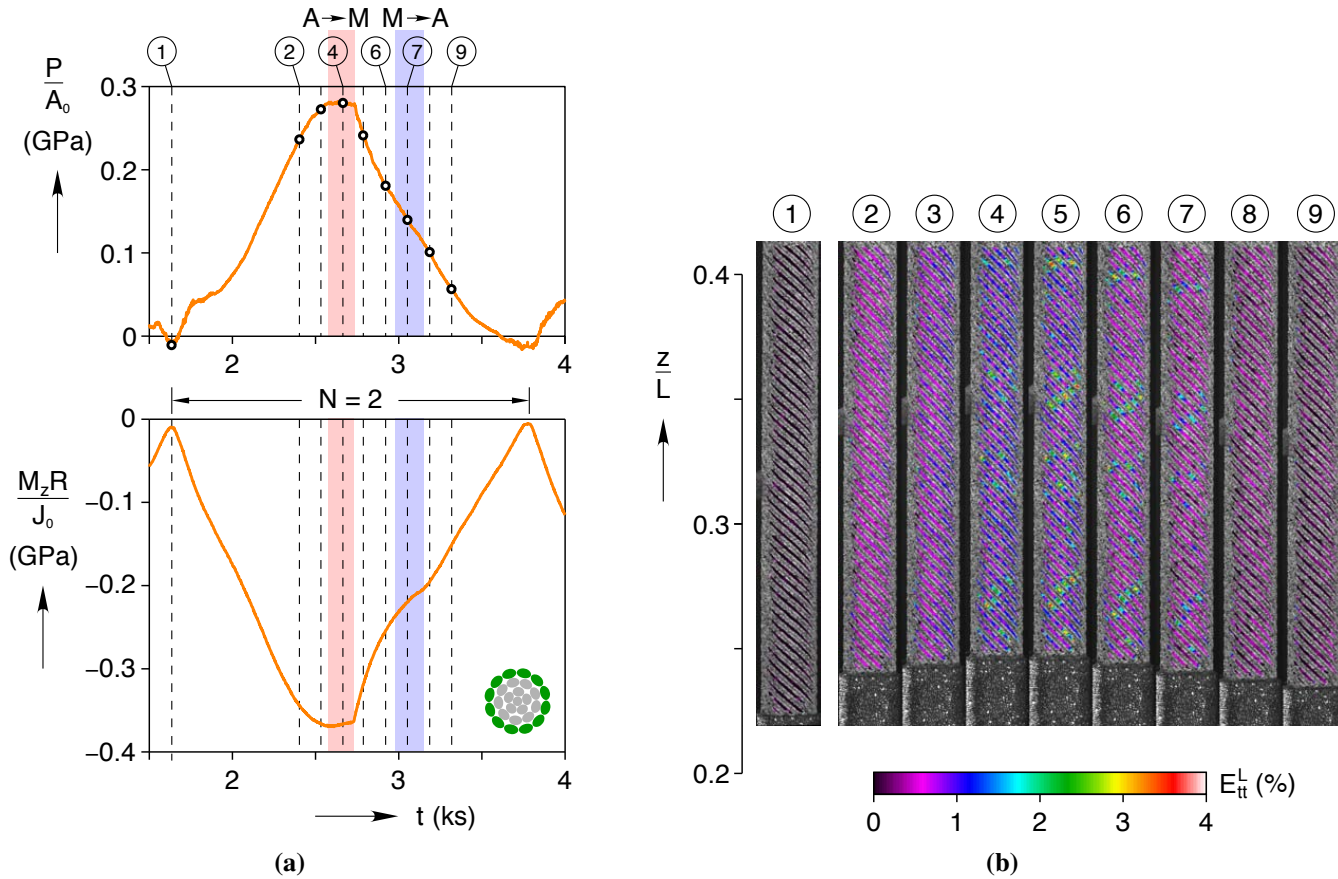
Figure 4.16 (a) Deduced layer D axial load and torque history during the 2nd cycle (generated by subtracting the 1×15 (Exp. M2a) from the 1×27 (Exp. C2d) at the same values of δ_e/L_e). (b) 1×27 tangential strain field images (Exp. C2d), where circled time labels in (a) correspond to image labels in (b).

localizations in Fig. 4.16b. After the start of layer D's $A \rightarrow M$ transformation, the elongation only reaches $\delta_e/L_e = 10.0$ %, which explains why the 1×27 strain field only has a few localizations.

- During unloading from ⑤ to ⑥ the strain localizations reduce in magnitude, but remain roughly the same size.

- From ⑥ and ⑦ the strain localizations start to disappear. The tangent modulus changes are quite muted, so it is difficult to say how well this correlates with the mechanical response, but we estimate the $M \rightarrow A$ transformation in layer D begins at $\delta_e/L_e = 7.6$ %.

- Then end of transformation is more distinct at $\delta_e/L_e = 6.0$ %, and by image ⑧ we see no localizations.

Upon further unloading, layer D's presumed axial load is slightly negative, reaching a minimum of -7.7 N. These negative loads do not make physical sense and should be disregarded. They are likely due to small sample-to-sample variation or a stack-up of measurement errors (-7.7 N is less than 0.2 % of the load cell's 5 kN capacity) exacerbated by subtracting small experimentally measured values. Despite this small error, layer D's presumed response agrees well the DIC strain field images and remains a valuable tool to understand the behavior of the 1×27 cable.

To conclude this section we directly compare the four 1×27 component responses in Fig. 4.17a and the deduced responses of the three helical layers in Fig. 4.17b. Note the nearly full recovery of the 1×6, 1×15, and 1×27 after being strained to 10%, even though the uniaxial loading plateau for the core wire terminates at a relatively modest $\delta_e/L_e = 6$%. The broad range of behaviors are an excellent demonstration of how tailorable SMA cables are. Considering that a single alloy of NiTi wire can be made to respond in many different ways by varying the construction, far more can surely be done by varying the alloy composition of the components.
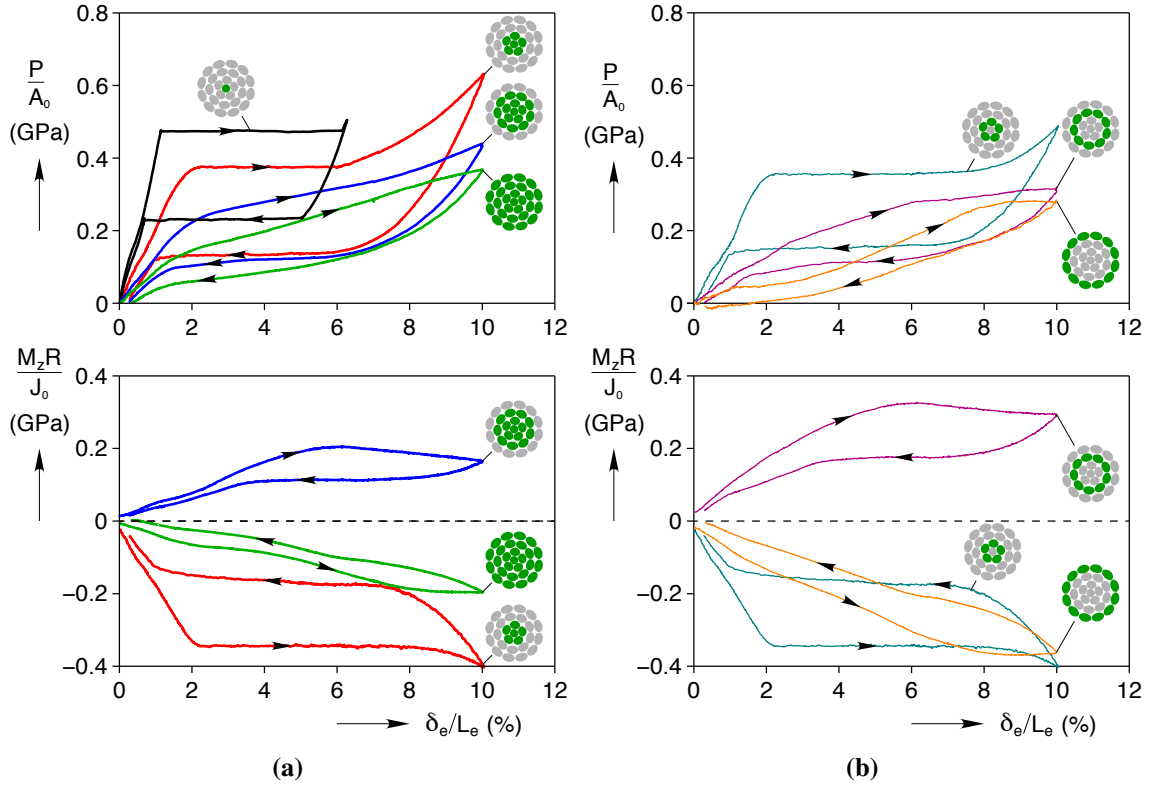
Figure 4.17 1×27 components' mechanical responses at $\dot{\delta}/L = 1 \times 10^{-4}$ s^{-1}: (a) Outer loop of the 1st cycle of the core wire (Exp. W2b), and outer loop of the 1st and 2nd cycles on the 1×6 (Exp. S2a), 1×15 (Exp. M2a), and 1×27 (Exp. C2d). (b) The deduced mechanical responses of layer B, layer C, and layer D.

4.4 Summary & Conclusions

In Chapter 3 we introduced the 7×7×0.275 mm and 1×27×0.226 mm designs. Here in Chapter 4, the cables were dissected to examine the behavior of the sub-components. The significant conclusions are as follows:

1. The 7×7 core stand and full cable had similar isothermal mechanical responses to the straight core wire. This similarity is largely due to the small helix angles in the design, which causes the wires to be predominately in tension. As such, all three components exhibited propagating transformation fronts.

2. SMA cables are highly tailorable, as illustrated by the wide range of mechanical responses from each of the 1×27 components. For example, for the core wire, 1×6, 1×15, and 1×27 the axial stress secant modulus at $\delta_e/L_e = 2\%$ strain was 23.7, 18.4, 11.1, and 7.3 GPa, respectively, while the strain at failure (at the grips) was 11.2%,

16.4%, 29.3%, and 39.2%, respectively. Similar to a spring, one can trade force for displacement.

3. To further analyze the 1×27 cable, the mechanical responses of the various components were subtracted from one another. This led to several observations:

    (a) Subtraction provides a means to obtain a reasonable estimate of the mechanical behavior of each layer of the 1×27 cable, in the absence of a direct measurement.

    (b) Unlike the 7×7 cable and core strand, which have clear transformation plateaus, the responses of the 1×15 and 1×27 made it difficult to discern when transformation began for each layer. By comparing changes in the *subtracted* response tangent moduli with the DIC derived strain fields, it became possible to detect the start and end of transformation in the outer layer of the 1×15, and 1×27, respectively.

    (c) The "stair-step" behavior of the 1×15 and 1×27 torque, which was first observed in Chapter 3, was traced back to the layered construction of the cable. Each layer has a different helix angle, and thus each layer produces a significantly different torque response. And because transformation is triggered at different global axial strains for each layer, the combined response has a "stair-step" quality to it.

4. Despite the fact that localized transformation fronts were observed in the core wire, fronts were not detected in the other 1×27 components. However, localized transformation was detected in the strain field at indents on the surfaces of wires. As might be expected from a stress concentration, these localizations slowly grew and faded with the global strain on the specimen. Also, because there were many indents along the specimen, the localizations were spread out. These two observations, explains why the temperature field of the 1×27 specimen from Chapter 3 was uniform, giving the impression of homogeneous transformation.

By characterizing the isothermal performance of the 7×7 and 1×27 components, we have constructed a more complete understanding of the cable designs. We are now equipped to move forward and study the elongation rate sensitivity of the cables, as well as their components, in Chapter 5.

Chapter 5

Cable Elongation Rate Sensitivity Experiments

The previous two chapters focused on the fundamental, slow-rate (nearly isothermal) responses of the 7×7 and 1×27 designs. It is known, however, that superelastic behavior is highly sensitive to how quickly the SMA is loaded (especially if loaded in tension) [19], and many SMA cable applications require non-isothermal elongation rates, particularly those in vibration dampening and shock absorption (see Section 1.1.1). In this chapter, elongation rates ranging from 10^{-5} s^{-1} to 10^{-2} s^{-1} were applied to each cable and each of its subcomponents. Due to the strong thermomechanical coupling inherent to SMAs and the varied construction of each cable component, a wide range of mechanical responses were observed. These observations are analyzed and explained with the help of simultaneous digital image correlation and infrared thermography.

5.1 Experimental Scope

An extensive experimental study will be presented in Sections 5.2 and 5.3 for the respective cable designs, and the scope of the experimental program and parameters are provided in Table 5.1. The study includes elongation rates over four decades in the range $\dot{\delta}/L = 10^{-5}$ s^{-1} to 10^{-2} s^{-1} for the seven selected components (three from the 7×7 and four from the 1×27 cable) studied in Chapter 4. The specimens were taken from the same 7×7×0.275 mm right regular lay and 1×27×0.226 mm alternating lay cables described in Section 3.1. The experimental setup was the same as that detailed in Section 3.2. Measurements included the axial load, axial torque, elongation, strain field (by DIC), and temperature field (by infrared imaging and thermocouples). All experiments were performed in stagnant room temperature air, under elongation control ramps. The free length of most specimens was about 75 mm. All specimens had clamped end conditions, and each experiment was performed on a new specimen from the same cable lot.

For the 7×7 cable, experiments were performed on the core wire, core strand (1×7), and

the full 7×7 cable at four different elongation rates: $\dot{\delta}/L = \pm10^{-5}$ s^{-1}, $\pm10^{-4}$ s^{-1}, $\pm10^{-3}$ s^{-1}, and $\pm10^{-2}$ s^{-1}. The 1×27 cable and its components (except for the core wire) were characterized at three different elongation rates: $\dot{\delta}/L = \pm10^{-4}$ s^{-1}, $\pm10^{-3}$ s^{-1}, $\pm10^{-2}$ s^{-1}. As will be shown, the 1×27 was less rate sensitive than the 7×7, so the slowest rate of $\pm10^{-5}$ s^{-1} was unnecessary.

5.2 Experimental Results of 7×7 Components

Experimental results of the three selected components of the 7×7×0.275 mm cable are presented below, progressing upward through the hierarchy from the core wire, to the 1×7 core strand, to the full cable. Each component was subjected to a single load-unload cycle at four global elongation rates, starting at the very slow rate $\dot{\delta}/L = \pm1 \times 10^{-5}$ s^{-1} and progressing to faster rates in 10× intervals.

5.2.1 Core Wire

The core wire (of both cable designs) is simply a straight wire, for which the elongation-rate sensitivity has been shown before [19, 110]. We include these experiments on the 7×7 core wire primarily for completeness and to enable a direct comparison to the other components, but the addition of DIC measurements of the strain field for the first time (that we are aware of) also allows a clearer and more quantitative view of strain localization than before. This was especially helpful at high loading rates where numerous and tightly spaced strain localizations occurred.
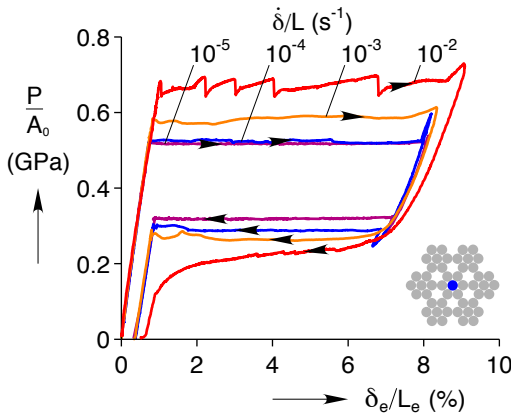
Figure 5.1 7×7×0.275 mm core wire mechanical response at four different elongation rates (Experiments W1b, W1a, W1c, and W1d).

Table 5.1 Specimen components from two cable designs and experimental and geometric parameters

Cable	Specimen	Icon	A_0 (mm^2)	J_0/R (mm^3)	Exp ID	L (mm)	L_e (mm)	$\dot{\delta}/L$ (s^{-1})
7×7	core wire		0.059	4.083×10^{-3}	W1b	76.04	49.55	$\pm 1 \times 10^{-5}$
					W1a	85.90	52.70	$\pm 1 \times 10^{-4}$
					W1c	75.92	50.38	$\pm 1 \times 10^{-3}$
					W1d	74.51	49.15	$\pm 1 \times 10^{-2}$
	1×7 core strand		0.416	7.486×10^{-2}	S1a	75.93	50.17	$\pm 1 \times 10^{-5}$
					S1b	74.71	50.05	$\pm 1 \times 10^{-4}$
					S1c	74.71	50.32	$\pm 1 \times 10^{-3}$
					S1d	75.00	49.86	$\pm 1 \times 10^{-2}$
	7×7 cable		2.910	1.547×10^{0}	C1c	74.85	49.92	$\pm 1 \times 10^{-5}$
					C1d	82.21	50.58	$\pm 1 \times 10^{-4}$
					C1e	74.66	50.25	$\pm 1 \times 10^{-3}$
					C1f	78.28	49.19	$\pm 1 \times 10^{-2}$
1×27	core wire		0.040	2.266×10^{-3}	W2b	74.67	49.05	$\pm 1 \times 10^{-4}$
	1×6 core strand		0.241	3.475×10^{-2}	S2a	75.05	49.70	$\pm 1 \times 10^{-4}$
					S2b	74.97	49.74	$\pm 1 \times 10^{-3}$
					S2c	74.93	49.36	$\pm 1 \times 10^{-2}$
	1×15 multi-layer		0.602	1.555×10^{-1}	M2a	75.09	49.88	$\pm 1 \times 10^{-4}$
					M2b	75.19	50.16	$\pm 1 \times 10^{-3}$
					M2c	75.05	49.58	$\pm 1 \times 10^{-2}$
	1×27 cable		1.083	3.947×10^{-1}	C2d	75.21	49.21	$\pm 1 \times 10^{-4}$
					C2e	75.18	49.45	$\pm 1 \times 10^{-3}$
					C2f	75.14	49.38	$\pm 1 \times 10^{-2}$

A summary of the uniaxial tension responses at the four rates is shown in Fig. 5.1. The maximum strain for each experiment was chosen such that the apparent loading plateau for that rate was exhausted before reversing the elongation-rate for unloading. The 7×7 core wire response at $\dot{\delta}/L = \pm 1 \times 10^{-5}$ s^{-1} is clearly the fundamental response of the wire, i.e. isothermal and quasi-static (taking 272 minutes to complete). The response shows the least stress hysteresis of the four experiments, and the load plateaus during $A \rightarrow M^+$ (loading, 517 MPa) and $M^+ \rightarrow A$ (unloading, 320 MPa) are truly flat. The strain at the end of the loading plateau is $\delta_e/L_e = 8.04$ %, and the length of the loading plateau is 7.32 % strain. The extent of the unloading plateau is 6.36 % strain.

The response at $\pm 10^{-4}$ s^{-1} is nearly identical to $\pm 10^{-5}$ s^{-1} during loading, but it is 32 MPa lower than the fundamental response during unloading. This is likely due to the somewhat larger maximum strain for this experiment resulting in a maximum stress 58 MPa above that reached in the $\pm 10^{-5}$ s^{-1} experiment. So for this length of wire, $\dot{\delta}/L = \pm 1 \times 10^{-4}$ s^{-1} can still reasonably be called nearly isothermal.

At $\dot{\delta}/L = \pm 1 \times 10^{-3}$ s^{-1} we begin to see rate effects, where the plateau stresses have shifted from the fundamental response by about 71 MPa during loading and -55 MPa below the fundamental response (the maximum stress reached during the experiment was quite close to that of the $\dot{\delta}/L = \pm 1 \times 10^{-4}$ s^{-1} experiment). These shifts, as well as other details, in the stress evolution are explained by the temperature field evolution shown in Fig. 5.2. (See Section 3.3.2 for a description of temperature field history plots.) The temperature field history shows two transformation fronts propagating along the specimen during loading and unloading. During loading, $A \rightarrow M^+$ fronts nucleated in the grips and then traveled
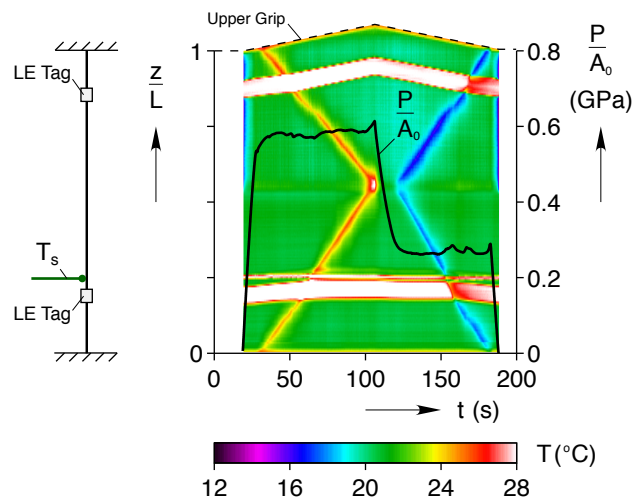
Figure 5.2 Experiment W1c. Temperature field history and stress history of a 7×7×0.275 mm core wire at $\dot{\delta}/L = \pm 1 \times 10^{-3}$ s^{-1}.

along the gage length at steady speed, causing a temperature rise at the fronts of about 4.5 °C that remained relatively constant for most of their traversal. Consequently, the stress remains constant as well. Small drops in stress at $t = 47.9$ s, 52.9 s, 59.3 s and $t = 66.2$ s are caused by the two fronts passing underneath the LE tags. Later, as the fronts coalesce at $z/L = 0.56$, they thermally interact, which raises the local temperature slightly, and we see a small increase in stress. During the unloading plateau, small (but more noticeable) increases in stress are once again caused by the fronts passing the LE tags. One may also notice that the top half of the temperature field history generally looks slightly cooler compared to the bottom half, but this is an artifact of IR imaging of a very slender wire. The wire has a cylindrical surface and is only one pixel wide in the IR sensor, so IR imaging was challenging. While we aligned the sensor array as precisely as possible, any slight misalignment affected the absolute temperature reading. The changes in temperature (to this baseline), however, we believe are reasonably accurate to within 0.5 °C. DIC data was also collected for this experiment but is not shown here since only one front is visible in the DIC FOV similar to that shown previously in Fig. 4.3.

Returning to Fig. 5.1, the response at $\dot{\delta}/L = \pm 1 \times 10^{-2}$ s^{-1} is quite different from the previous three. The upper plateau is higher by roughly another 80 MPa over the previous experiment and is quite jagged. The unloading plateau is no longer flat, having a gentle nonlinear curve that maintains a positive tangent modulus (slope) and occurs at a lower stress than before. Note that the residual strain of the previous experiments was nearly the same (about 0.4 %), but now a larger residual strain is measured (about 0.5 %) due to the higher stress (and strain) reached during loading.

While this is the highest rate studied, the reader should recognize that this is not fast in the usual dynamics sense where physical inertia dominates the response. For example, loading from 0 to 10 % strain takes a full ten seconds. By contrast, a longitudinal elastic wave propagates at $\sqrt{E/\rho} \approx 3300$ m/s for NiTi, which takes only about 23 μs to transit a 75 mm long specimen, so a large separation of time scales exists between our experiments and inertial dynamics. Instead, "thermal inertia" is responsible for the response changes we see here, where latent heat exchanges with the environment take place at a much slower time scale. The prescribed elongation rate determines the global rate of latent heat release ($A \rightarrow M^+$) or absorption ($M^+ \rightarrow A$), and if the ambient medium cannot keep up with this demand the specimen temperature rises above ambient temperature or falls below it. The transformation stress is, in turn, coupled to the specimen temperature by the Clausius-Clapeyron relation for $d\sigma/dT$, typically about 7 MPa/°C in superelastic NiTi alloys [23]. Thus, thermal inertia sets the relevant time scale for "dynamics" at these loading rates.

The cause of the jagged response at $\dot{\delta}/L = \pm 1 \times 10^{-2}$ s^{-1} in Fig. 5.1 during $A \rightarrow M^+$
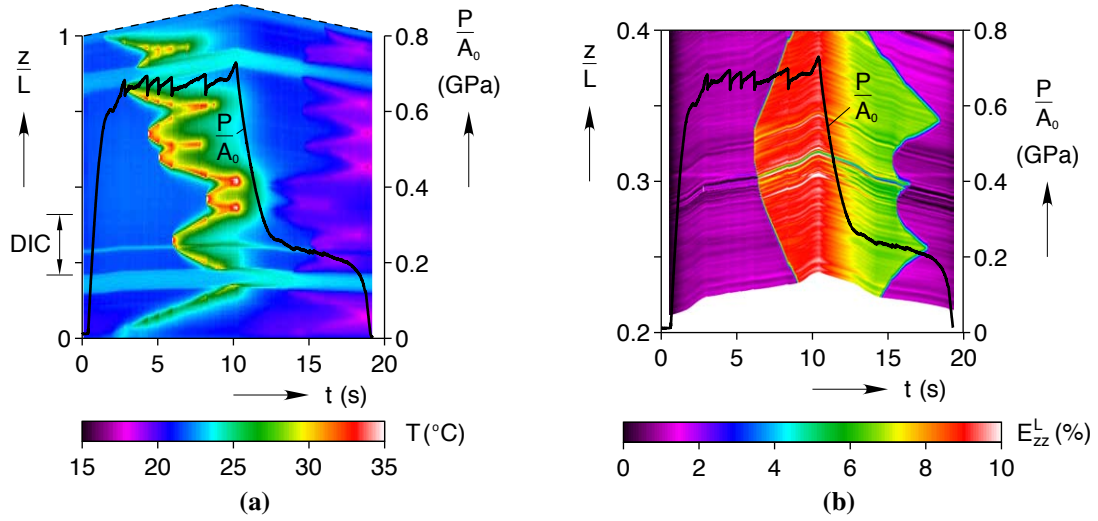
Figure 5.3 Experiment W1d. $7 \times 7 \times 0.275$ mm core wire at $\dot{\delta}/L = \pm 1 \times 10^{-2}$ s^{-1}: (a) temperature field history with stress history, (b) axial strain field history with stress history.

transformation is shown in the temperature field history of Fig. 5.3a. As $A \to M^+$ fronts propagate, they heat up so much that it becomes thermodynamically favorable to nucleate new fronts in a colder location of the gage length [106]. Looking closely at Fig. 5.3a, one can see each front heating up as it propagates and then drop in temperature when a new front nucleates elsewhere. Thus, the small drops in stress on the loading plateau are due to sudden martensite (M) localization (not experimental artifacts, like grip slippage). Every stress drop can be correlated in time with a nucleation event.

One of these $A \to M^+$ localizations can be seen in the DIC strain field history in Fig. 5.3b at $z/L = 0.32$. (See Section 4.2 in Chapter 4 for a description of strain field history plots.) Note that the slight streaks in the strain field and temperature field history, which start at $z/L = 0.28$ and move up and down with the specimen, are caused by the specimen thermocouple (T_s). The thermocouple was placed on the back of the specimen to avoid obscuring the speckle pattern from the optical cameras, but a small amount of thermal paste got on the speckle pattern during the specimen preparation. This gave a poor correlation in that small location in the DIC post-processing, so the strains should be disregarded there. Accounting for these artifacts, the strain profiles are nearly piecewise constant at each time instant, and transformation fronts are clearly seen as near discontinuities in the local strain. Although DIC only provided a limited FOV, the location of fronts and their motion can be tracked with greater precision than with IR imaging. This is because the IR sensor has less spatial resolution than DIC, and axial conduction along the wire tends to smear out the "kink" in the temperature profile.

The $A \to M^+$ nucleation in Fig. 5.3b occurs between two strain field images taken at

40 ms time intervals and the high strain region is 1.7 mm long by the time it is first detected. As seen by the near vertical stress drop, occurring over roughly 10 ms, this was a truly dynamic event (and with acute hearing, one can hear an audible "click" when it occurs). The abrupt stress drop is due to a finite region of high strain (axial inclusion) that suddenly appears, during which the overall prescribed elongation has not changed, so the material elsewhere along the gage length must unload elastically to compensate. Similarly, when a pair of converging fronts get close enough they are observed to "snap" together as the strain field de-localizes, and another stress drop is measured. However, this is often masked by the counter-acting thermal transient due to the doubling of the latent heat source/sink as a pair of fronts approach one another. See, for example, the hot spots in Fig. 5.3a near $t = 10$ s at $z/L = 0.43$ and 0.52 where the temperature has locally risen off-scale, in excess of $\Delta T = 15$ °C.

During unloading, numerous $M^+ \rightarrow A$ localizations occur, first near the middle of the specimen (although a lower front also appears from the lower grip at about the same time) and later elsewhere along the gage length. As fronts propagate, the self-cooling of the specimen intensifies, despite the proliferation of many fronts by the end of $M^+ \rightarrow A$ transformation ($\Delta T \approx -3$ °C). All of the nucleation sites for $M^+ \rightarrow A$ fronts can be traced back to $A \rightarrow M^+$ coalescent sites during loading. Here, each $M^+ \rightarrow A$ localization event is accompanied by a stress rise, although they are much smaller than during loading. The stress rise is due to low strain regions suddenly appearing, where the remainder of the material must reload somewhat to compensate for the prescribed global elongation.
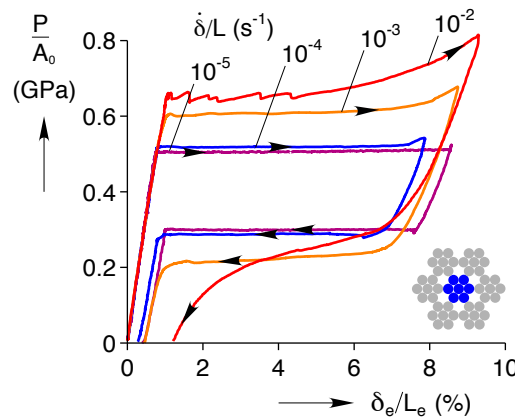
Figure 5.4 1×7×0.275 mm mechanical response at four different elongation rates (Experiments S1a, S1b, S1c, and S1d)

5.2.2 1×7 Core Strand

Next, we turn to the elongation rate sensitivity of the 1×7 core strand (see Fig. 5.4). Much of the same trends are seen in the 1×7 responses as was seen for the core wire. The mechanical responses at $\dot{\delta}/L = \pm 1 \times 10^{-5}$ s^{-1} and $\dot{\delta}/L = \pm 1 \times 10^{-4}$ s^{-1} are similar, both with flat stress plateaus. The response at $\dot{\delta}/L = \pm 1 \times 10^{-3}$ s^{-1} has a significantly larger stress hysteresis, but still has relatively flat plateaus. The response at $\dot{\delta}/L = \pm 1 \times 10^{-2}$ s^{-1} has a still larger stress hysteresis, a jagged response during loading, and a nonlinear path with no discernible plateau during unloading. Quantitative differences, however, do exist for the 1×7 core strand, and a few features are new.

As mentioned in Chapter 4, compared to the core wire, the fundamental response of the 1×7 core strand at $\dot{\delta}/L = \pm 1 \times 10^{-5}$ s^{-1} during loading has a longer plateau (terminating at $\delta_e/L_e = 8.55$ % versus 8.04 %), and the loading plateau stress is slightly lower (517 MPa versus 506 MPa). Curiously, one may notice that the length of the loading plateau at $\dot{\delta}/L = \pm 1 \times 10^{-4}$ s^{-1} is less than that of the response at $\dot{\delta}/L = \pm 1 \times 10^{-5}$ s^{-1}. The experiment at $\dot{\delta}/L = \pm 1 \times 10^{-4}$ s^{-1} was actually performed before we performed the slower one, so when the apparent stress plateau ended at $\delta_e/L_e = 7.4$ % with an upturn in the response, we believed localized transformation had ended and so unloading commenced soon thereafter. We discovered later that the post-plateau upturn in the response was actually due to two converging $A \rightarrow M^+$ fronts that began to thermally interact, and unloading had begun prematurely. We mention this to explain the apparent non-monotonic trends in the length of the $A \rightarrow M^+$ plateaus in Fig. 5.4. It also highlights a good example of how even a seasoned experimentalist can get caught and why it is important to be aware of the thermal origins of an SMA's rate sensitivity.

The increased rate sensitivity of the core strand compared with the core wire becomes more apparent at $\dot{\delta}/L = \pm 1 \times 10^{-3}$ s^{-1}. The core strand loading plateau and unloading plateaus are offset from the fundamental plateaus by 103 MPa and -76 MPa, respectively. The magnitude of these offsets are 45 % and 38 % larger than the offsets measured for the core wire at the same rate. The rise in the 1×7 stress late in the loading plateau at about $\delta_e/L_e = 6.5$ % is also larger than that measured in the core wire. The temperature field history during loading at $\dot{\delta}/L = \pm 1 \times 10^{-3}$ s^{-1} is shown in Fig. 5.5, which is qualitatively similar to the core wire at the same elongation rate (compare to Fig. 5.2). $A \rightarrow M^+$ fronts propagate inward from the top and bottom grips, and coalesce near the middle of the gage length. Overall, the temperature of each front increases monotonically as it travels, with one exception. When a front crosses the LE tag, the measured temperature rise drops momentarily for two reasons: (1) IR imaging is less accurate at the tag locations that have a lower emissivity than the rest of the painted specimen, and (2) the epoxy/tag provides a heat
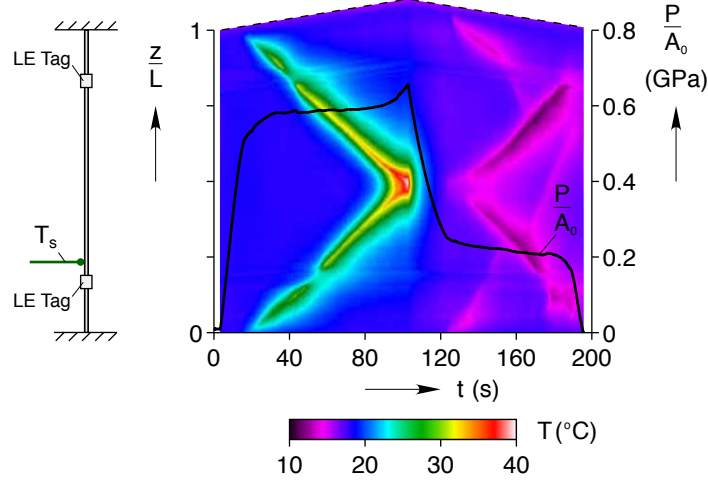
Figure 5.5 Experiment S1c. 1×7×0.275 mm temperature field and stress history at $\dot{\delta}/L = \pm 1 \times 10^{-3}$ s^{-1}.

sink for latent heat. Upon close inspection one can see that the front speeds up slightly in this region and the stress drops ever so slightly, so the reduced temperature there is, in part, a real effect. Late in the front traversals they thermally interact, raising the stress accordingly, and when the fronts finally coalesce the temperature is risen high off scale ($\Delta T > 20$ °C). Furthermore, one can see that it takes several seconds (during the initial unloading segment) for the temperature field to return to ambient.

The primary difference from the core wire response is the magnitude of the temperature excursions, roughly twice as large. This is due to the larger thermal inertia of the 1×7 specimen. As mentioned before, the ratio of specimen volume (V) over the surface area exposed to ambient air (S) is the relevant length-scale for the governing heat equation, which can easily be shown if we approximate the specimen as a thin solid cylinder whose Biot number is much less than 1. The 1-D heat equation for this scenario is

$$-\frac{\partial Q_Z}{\partial Z} - \frac{P_0}{A_0} Q_R = \rho_0 \frac{\partial e}{\partial t}, \tag{5.2.1}$$

where Q_Z is the axial heat flux, Z is the axial coordinate, P_0 is the perimeter (circumference) of the cylinder, Q_R is the radial heat flux, and ρ_0 is the density, all in the reference configuration. The specific internal energy is e. The radial heat flux allows the cylinder to shed or absorb heat to the surrounding environment, and its coefficient P_0/A_0 is the only portion of eqn. (5.2.1) that scales with the diameter of the cylinder. The inverse $A_0/P_0 = V/S$ is the thermal inertia, which is clearly larger for the core strand than the core wire. Thus, all other things being equal, it is not surprising that the 1×7 specimen is more rate-sensitive than the core wire.

The unloading response in Fig. 5.5 is rather interesting. It shows two "primary" $M^+ \rightarrow A$ fronts (cold spots, $\Delta T \approx -10\,°C$) emanating from the middle of the specimen (where fronts had coalesced during loading), but also shows other "secondary" fronts originating at the upper and lower grips. We conclude these are fronts in the core wire that appear as the finer "ghost" fronts in the IR image. Interestingly, these seem to propagate independently to the primary fronts in the outer helical wires. The bottom secondary front reaches $z/L = 0.3$, pauses to let the lower primary front pass by (without any temperature excursion that would be associated with fronts coalescing), and then later proceeds upward. Likewise, the upper secondary front may have included the outer wires, based on the intensity and width in the IR image, stalled when it reached the upper LE tag but a finer front (presumably in the core wire) continued at greater speed. Later, this front stops when it intersects the upper primary front (again with no evidence of front coalescence). The notion that the core wire can deform independently of the helical wires is a somewhat unsettling, since it would indicate sliding between the core wire and the six helical wires, contrary to our previous assertion that cross-sections prefer to deform together. Obviously, this may not always be true, but this is the only experiment where this type of multi-front behavior was observed. The DIC strain field images during unloading (not shown because they are nearly identical to images ⑨ through ⑭ in Fig. 4.4b) only show the lower primary front in the outer helical wires in the FOV $0.2 \leq z/L \leq 0.4$. This does show the usefulness of IR imaging that not only explains the fluctuations in the mechanical response, but also shows what may be happening inside a multi-layer structural element like this one.

To conclude our discussion of the 1×7 core strand, we again compare the core strand response to the core wire response, but at the highest elongation rate of $\dot{\delta}/L = \pm 1 \times 10^{-2}\ \mathrm{s}^{-1}$. Note that the temperature scale ranges from 10°C to 50 °C in Fig. 5.6a, as opposed to the 15 °C to 35 °C range for the core wire in Fig. 5.3a. Like the core wire, all the stress drops line up with the $A \rightarrow M$ nucleations shown in the temperature field, and one nucleation at $z/L = 0.35$ is visible in the strain field. As the fronts begin to coalesce after $t = 6.5$ s the stress rises by 168 MPa before the end of loading, which is more than twice the rise seen in the core wire, due to the increased thermal inertia of the core strand. The strain field image taken at the end of loading (image ⑦) reveals that some material did not transform even after being strained $\delta_e/L_e = 0.75\ \%$ beyond the end of the isothermal plateau. This is because the length of the plateau increases somewhat with temperature and stress, at least up to stresses where significant plasticity starts to diminish the plateau length [23, 25]. It is interesting that these residual regions of austenite did not serve as starting points for $M^+ \rightarrow A$ transformation fronts. Instead, $M^+ \rightarrow A$ fronts gradually initiate nearby and then propagate to the residual austenite. It is possible that reverse transformation did initiate
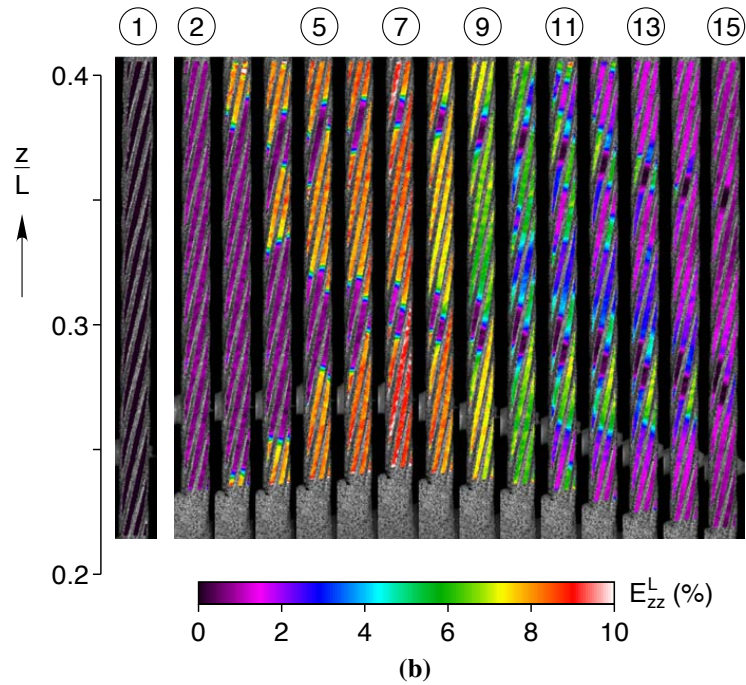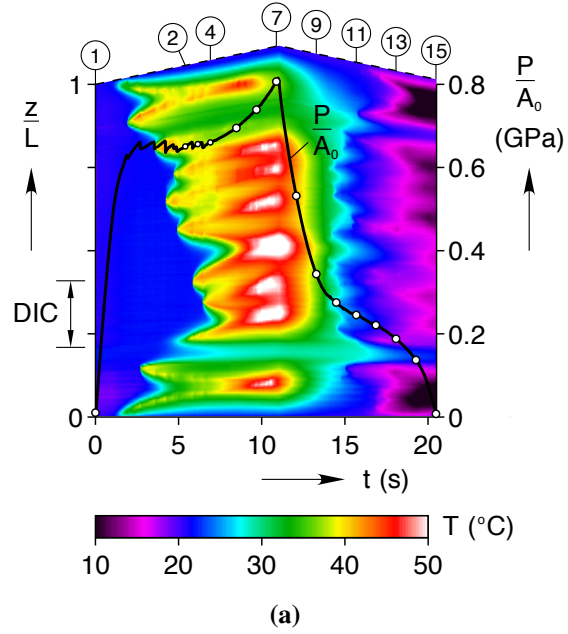
Figure 5.6 Experiment S1d. 1×7 core strand at $\dot{\delta}/L = 1 \times 10^{-2}$ s^{-1}: (a) temperature field history and stress history, (b) axial strain field images (circled numbers in (a) correspond to image labels in (b)).

at these locations in the core wire, which caused local temperature decreases that briefly suppressed transformation in the outer wires. At zero load, the residual austenite regions reach $E_{zz}^L = 0$ %, while material points in the rest of the strand in the DIC FOV have a permanent strain, unloading to only $E_{zz}^L \approx 1.2$ %.
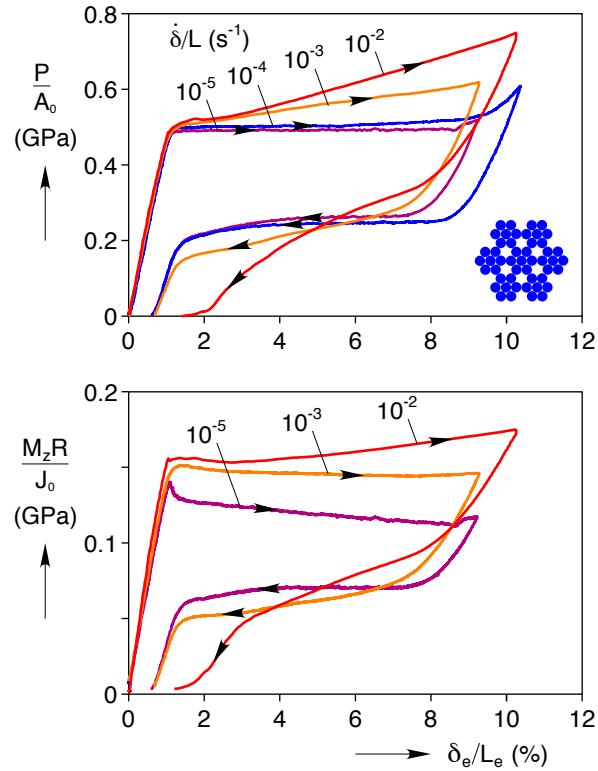
Figure 5.7 7×7×0.275 mm mechanical response at four different elongation rates. (Exp. C1c, C1d, C1e, and C1f)

5.2.3   7×7 Cable

Until this point, the 1×7 core strand and the 7×7 cable have performed qualitatively similar to wires loaded in parallel. At non-isothermal elongation rates, however, the 7×7
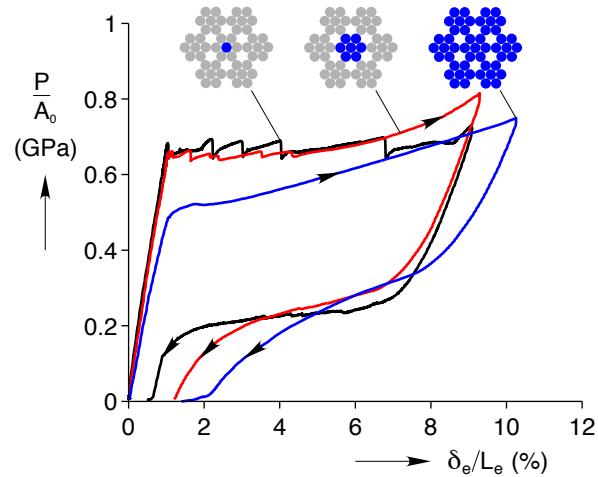
Figure 5.8 7×7core wire (Exp. W1d), core strand (Exp. S1d), and cable (Exp. C1f) mechanical response at $\dot{\delta}/L = 1 \times 10^{-2}$ s^{-1}.

cable's response is substantially different than the core wire and the 1×7 core strand. Figure 5.7 shows the mechanical response of the 7×7 cable at four different elongation rates. The normalized torque at $\dot{\delta}/L = \pm 1 \times 10^{-4}$ s^{-1} is missing because the experiment was performed before we integrated a torque cell into our setup, but the torque response was likely similar to that of the experiment at $\dot{\delta}/L = \pm 1 \times 10^{-5}$ s^{-1}. First, instead of offset plateaus with greater elongation-rate, the axial stress (and normalized torque) tangent modulus increases substantially and becomes nearly constant during most of the mid to late portion of $A \rightarrow M^+$ transformation. Second, except for the minor stress drop just after the initial knee in the axial response at the highest rate, no further stress drops (jaggedness) are measured at any of the elongation rates performed. Figure 5.8 provides a comparison of the axial load responses of the three components of the 7×7 at the highest elongation rate. This shows a substantially different response of the 7×7 cable compared to its core strand and core wire, despite their similar isothermal responses (see again Fig. 4.2 for the mechanical responses of the three components at $\dot{\delta}/L = \pm 1 \times 10^{-5}$ s^{-1}). As discussed below, the causes of this behavior can be understood by analyzing the 7×7 temperature and strain fields.

The temperature field history and strain field images at $\dot{\delta}/L = \pm 1 \times 10^{-2}$ s^{-1} are shown respectively in Fig. 5.9 and Fig. 5.10. The corresponding plots at $\dot{\delta}/L = \pm 1 \times 10^{-3}$ s^{-1} look very similar, so they are not shown here. No distinct macroscopic fronts are observed in Fig. 5.9, contrary to the previous 7×7 temperature field histories presented (Fig. 3.6 and Fig. 3.11b). The specimen steadily and uniformly heats up during loading to reach 54 °C at the maximum load (at $\dot{\delta}/L = \pm \times 10^{-3}$ s^{-1} the temperature reached 36 °C), and cools back down to room temperature during unloading. Note that since there was no pause
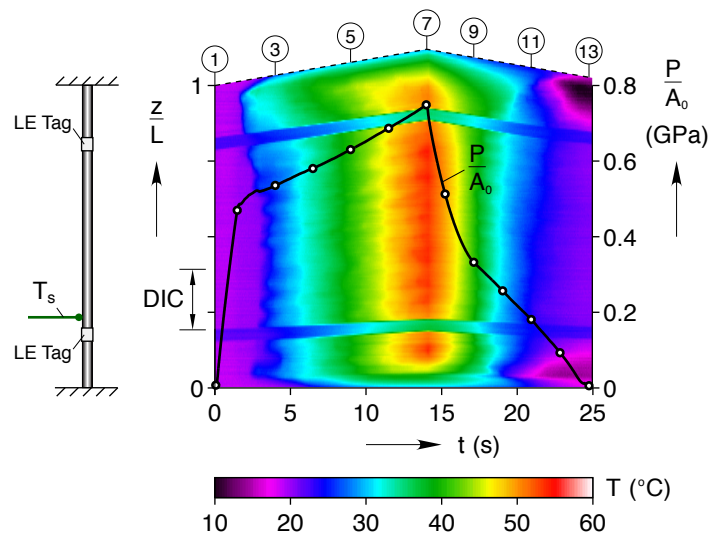
Figure 5.9 Experiment C1f. Temperature field history and stress history of 7×7 cable at $\dot{\delta}/L = 1 \times 10^{-2}$ s^{-1}. Circled time labels correspond to strain field image labels in 5.10.

107

between loading and unloading, most of the reverse transformation took place at elevated, but decreasing, temperature. Accordingly, in comparing the magnitudes of the slopes of the stress history between $A \rightarrow M^+$ (loading) and $M^+ \rightarrow A$ (unloading), one notices a greater rate of change in the unloading response. This is a consequence of the specimen surroundings (air and grips) and the endothermic $M^+ \rightarrow A$ transformation both cooling the specimen (parallel effects). By contrast, during loading, the specimen is cooled by the surroundings while being internally heated by the exothermic $A \rightarrow M^+$ transformation (opposing effects). Had we paused after loading to allow the specimen to return to ambient temperature before unloading (as was done in Chang *et. al.* [19] for experiments on straight wires), the effects would have been different. The surroundings and endothermic latent heat would have been counteracting effects on the specimen temperature during unloading and the rate of stress decrease would have been less. As seen in Fig. 5.9, the only parts of the specimen here that experienced sub-ambient temperatures during the experiment were the ends (outside the laser tags) near the end of unloading ($20 < t < 25$ s).

The DIC strain images of Fig. 5.10 show that many small fronts in individual wires nucleated at disparate points along the gage length, effectively distributing the temperature rise over the whole specimen. These fronts were relatively closely spaced and they immediately began to thermally interact right from the beginning of the $A \rightarrow M^+$ transformation, causing the specimen temperature and stress to continue rising throughout loading. Since the temperature field is rather uniform in Fig. 5.9, except near the grips (which act as heat sinks), and the temperature continually rises during loading, so the 7×7 axial load and torque rise nearly monotonically during $A \rightarrow M^+$ transformation at this moderately fast elongation rate. One can also see from image ⑦ of Fig. 5.10 that most wires on the outer surface of the cable did not finish transforming to martensite, so further transformation strain should be available in the cable.

Given that the core wire and core strand had load drops at $\dot{\delta}/L = \pm 1 \times 10^{-2}$ s^{-1} as new fronts nucleated, one might have expected the full cable to exhibit the same behavior. Close inspection of the strain field images in Fig. 5.10, however, show that $A \rightarrow M^+$ fronts originate from the crevices between the strands. Thus, the local contact stresses (stress risers) between the strands serve as initiation sites along the entire cable length. These allow local nucleation barriers to be easily overcome to initiate new fronts, so no sharp macroscopic load drops are measured. Thus, the different effects seen here between the 7×7 cable and its components are analogous to *heterogeneous nucleation* versus *homogeneous nucleation*, terminology commonly used in the materials science and thermodynamics literature for conventional liquid-solid phase transformations.

It is now possible to understand the non-monotonic trends in Fig. 5.8, where the 7×7
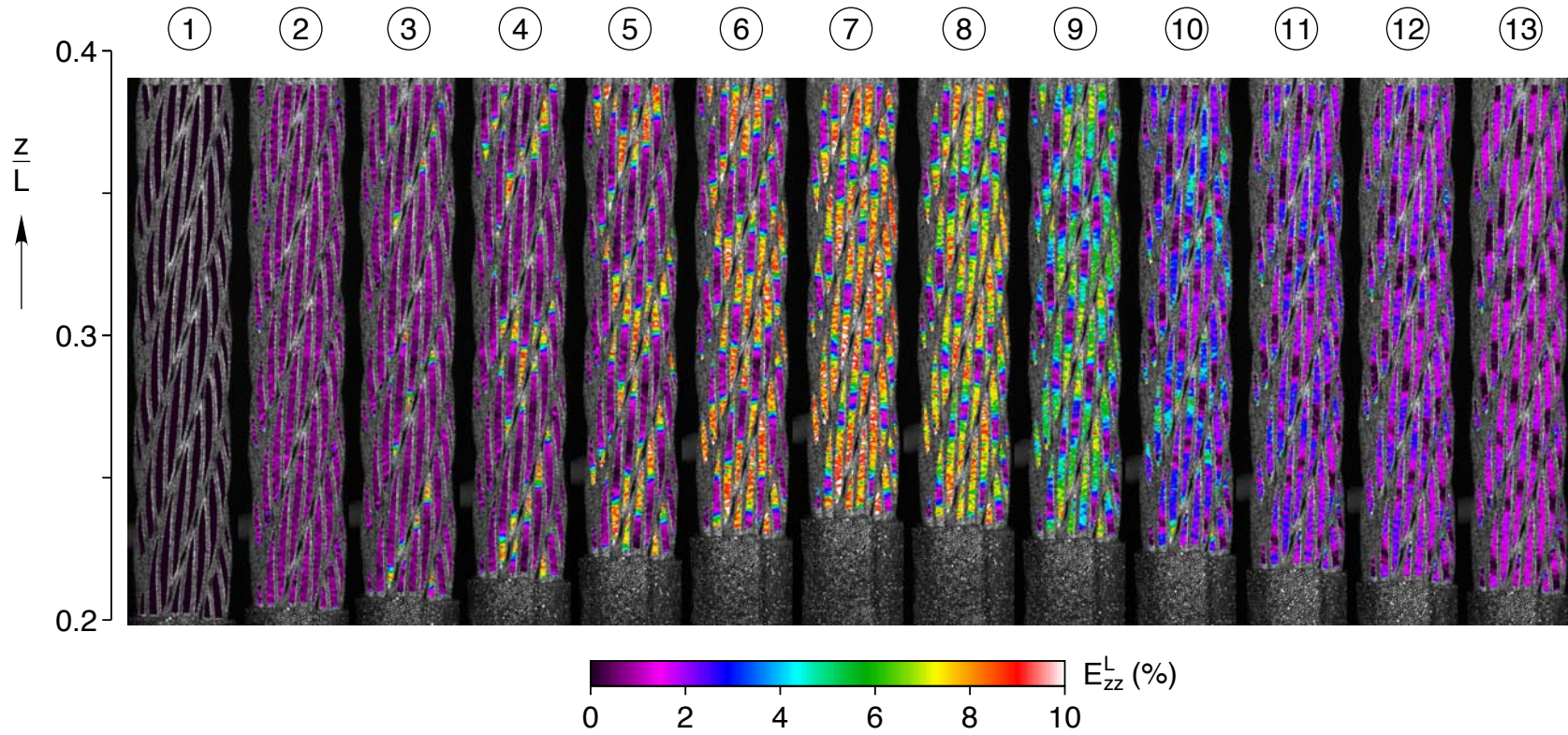
Figure 5.10 Experiment C1f. Selected axial strain field images of 7×7 cable at $\dot{\delta}/L = 1 \times 10^{-2}$ s^{-1}. Circled image labels images correspond to time labels in Fig. 5.9.

cable axial stress remains below that of the core wire and 1×7 core strand for much of the loading. One would have naturally (naively) expected the stress in the 7×7 to be generally larger than for the smaller components due to its larger thermal inertia and expected a greater amount of self-heating due to the larger internal heat source from $A \rightarrow M^+$ latent heat. However, since fronts nucleate at numerous contact points between the strands, the latent heat is distributed along the cable, instead of the intense local heating at the fronts seen in the core wire (Fig. 5.3a) and the core strand (Fig. 5.6a). This means the temperature of the cable rises more slowly, and the cable must be stretched as far as $\delta_e/L_e = 7$ % before the temperature catches up to that of the core wire and core strand. This again highlights the importance of recognizing local versus distributed transformation kinetics. It can dominate the rate-sensitivity of the SMA structures, despite thermal inertia differences that might suggest contrary behavior.

Another counterintuitive observation of the responses in Fig. 5.8, is that it would appear the onset of $A \rightarrow M^+$ transformation is significantly less for the 7×7 cable than for the core strand and core wire. Furthermore, examining again the rate-sensitivity of the responses of the core wire (Fig. 5.1) and core strand (Fig. 5.4) compared to that of the full cable (Fig. 5.7), one might conclude that the initiation stress for $A \rightarrow M^+$ transformation depends strongly on the elongation rate for the core wire and the core strand, but not for the cable. This supposed dependence is actually due to plotting the stress versus the LE strain δ_e/L_e instead of the grip strain δ/L (or better yet, time), which masks the true onset of $A \rightarrow M^+$ localization that occurs outside of the LE tags in the core wire and the core strand. Figure 5.5, for example, showed the stress history of the core strand at $\dot{\delta}/L = \pm 1 \times 10^{-3}$ s^{-1}. $A \rightarrow M^+$ fronts initiated at 509 MPa, which is the same as the stress required to initiate fronts at $\dot{\delta}/L = \pm 1 \times 10^{-5}$ s^{-1}. By the time the fronts in Fig. 5.5 have traveled inside the LE gage length, the temperature at the fronts has risen and the stress has reached its steady state plateau of 609 MPa. The cable, on the other hand, at $\dot{\delta}/L = \pm 1 \times 10^{-3}$ s^{-1} and 10^{-2} s^{-1} deforms more uniformly for the reasons stated above, so the onset of transformation is captured by the LE measurement. Thus, while global stress-strain responses are certainly useful, it is important not to suppress the important dependence on time when interpreting the results.

5.3   Experimental Results of 1×27 Components

We now turn to the elongation rate sensitivity of the 1×27×0.226 mm cable. Experimental results of three selected components of the 1×27×0.226 mm cable are presented below, progressing upward through the hierarchy from the 1×6 core strand, to the 1×15

(three-layer) multi-strand, to the full 1×27 cable (four-layer multi-strand). Each component was subjected to a single load-unload cycle at three global elongation rates, starting at the slow rate $\dot{\delta}/L = \pm 1 \times 10^{-4}$ s^{-1} and progressing to faster rates in 10 × intervals. We did not study the elongation rate dependence of the 1×27 core wire, since the 1×27 core wire is only 18 % less than the 7×7 core wire, should perform in a similar manner, and the behavior of straight wire is not the primary focus our study. Also, unlike the 7×7 cable, no experiments were performed at $\dot{\delta}/L = \pm 1 \times 10^{-5}$ s^{-1}, since $\dot{\delta}/L = \pm 1 \times 10^{-4}$ s^{-1} was sufficiently isothermal for the 1×27 components.

5.3.1   1×6 Core Strand

The 1×6×0.226 mm core strand from the 1×27 cable is similar in design to the 1×7-×0.275 mm core stand from the 7×7 cable, but the 1×6 core strand has larger helix angles and is made of one fewer and somewhat thinner wires. Figure 5.11 depicts the first and second cycle mechanical response of the 1×6 at three different elongation rates. The axial stress responses during loading, as expected for faster elongation rates, has larger stresses during $A \rightarrow M^+$ transformation. The magnitude of the torque response is also larger for the two highest rates than the slowest one, but although they are are quite close, the one at
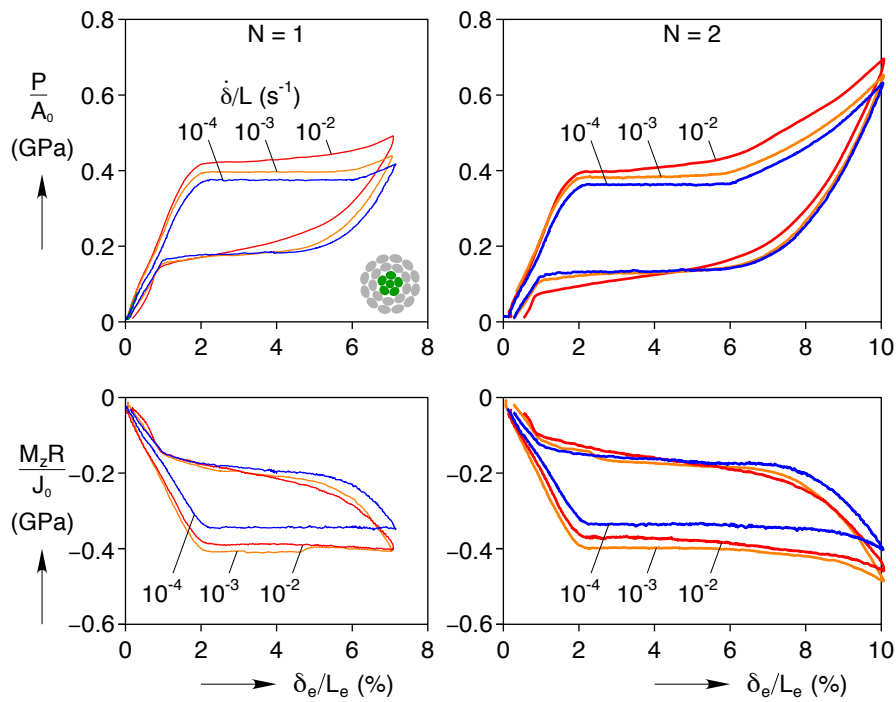
Figure 5.11   The first and second cycle mechanical response of the 1×6 at three different elongation rates (Experiments S2a, S2b, and S2c).

$\dot{\delta}/L = 1 \times 10^{-3}$ s^{-1} has a slightly larger magnitude than at $\dot{\delta}/L = 1 \times 10^{-2}$ s^{-1}. This could be due to some specimen-to-specimen variation or due to measurement uncertainty at these small torque values (the max torque measured was 16.8 N-mm, yet the torque cell capacity was 2824 N-mm). More importantly, comparing Fig. 5.11 to Fig. 5.4, the elongation rate sensitivity of the 1×6 strand is significantly less than that of the 1×7 strand. During loading at $\delta_e/L_e = 3$ %, the axial stress in 1×7 strand increased by 25 % when the elongation rate was changed from 10^{-4} s^{-1} to 10^{-2} s^{-1}, but the 1×6 axial strain only increased by 12 % between the same two elongation rates. Differences in thermal inertia (one less wire in the 1×6 and 18 % smaller wire diameter) certainly exist, but this does not fully account for the differences in rate sensitivity here. The temperature and strain field histories discussed below show additional factors at play.

The IR temperature field history for the 1×6 core strand at $\dot{\delta}/L = \pm 1 \times 10^{-4}$ s^{-1} was shown previously in Fig. 4.7b, which corresponds to the mechanical response during cycle 2 of Fig. 5.11. It showed temperature deviations generally less than ±1.5 °C from ambient, and pockets of transformation activity occurred at disparate locations along the specimen length with no clear macroscopic front. Thus, one can reasonably consider the response at this rate to be the isothermal, fundamental response.

Moving up in rate, the IR temperature history and strain field images of a 1×6 specimen at $\dot{\delta}/L = \pm 1 \times 10^{-3}$ s^{-1} are shown in Fig. 5.12, corresponding to the mechanical response of Fig. 5.11 during the second cycle, where the strand was stretched from $\delta_e/L_e = 0.07$ % to 10 % and back. Minimal shakedown occurred during the first cycle, and the loading plateaus of cycles 1 and 2 overlap closely. The IR temperature fields were also similar, so only cycle 2 is shown here. Figure 5.12a shows the IR contour plot and stress history, along with a magnified view of a selected region of the IR contour plot (Detail A). Figure 5.12b show a sequence of DIC strain field images, but here the normal strain component (E_{tt}^L) tangent to the outer wires is shown rather than E_{zz}^L. As discussed in Section 4.3, Vic-3D [30] uses a local coordinate system wrapped around the surface of the specimen by using the 3D surface geometry data generated in the stereo DIC analysis. The tangential strain provides a clearer view of transformation activity for the larger helix angles in the 1×6 construction.

The IR contour plot in Fig. 5.12a show scattered pockets of transformation activity, where the local temperature rises during loading are generally about 4 °C and the temperature drops during unloading are about -4 °C. The magnified view of IR Detail A shows a few of these brief and localized temperature blooms during $A \rightarrow M^+$ transformation between DIC images ③ and ⑤ (ignore the artificial streaks below $z/L = 0.25$ due to the thermocouple and LE tag). Every temperature bloom in Detail A has a counterpart strain bloom in images ②-⑤. They do not, however, propagate. Instead, isolated nucleations of this type occur
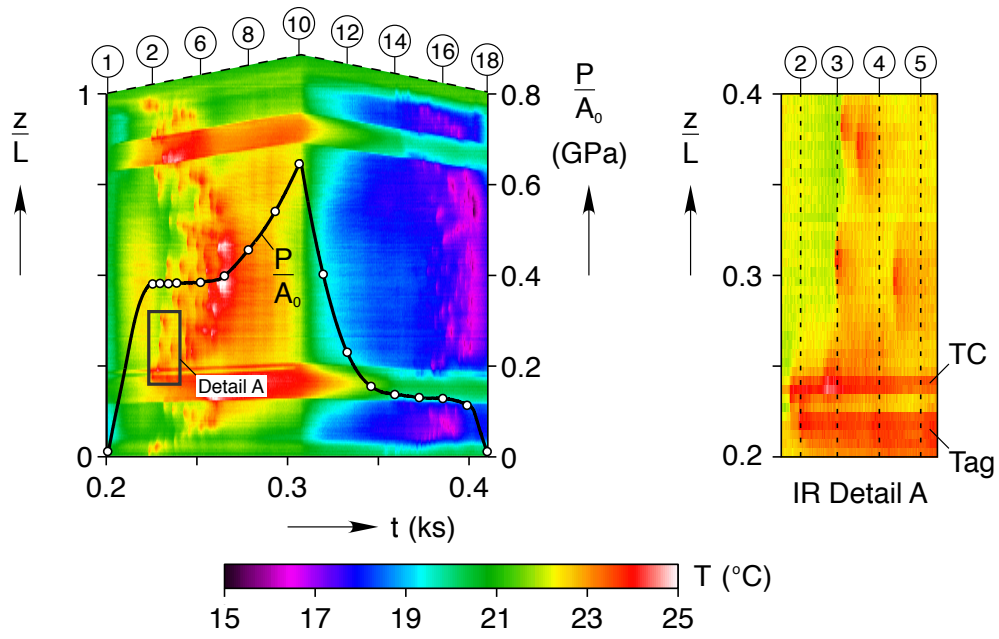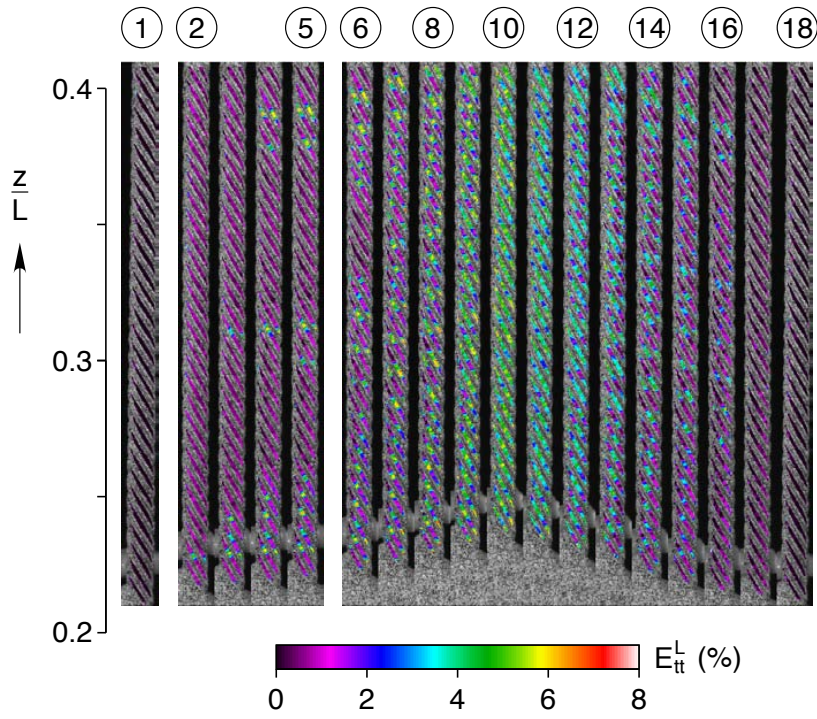
Figure 5.12 Experiment S2b on 1×6 core strand during second cycle at $\dot{\delta}/L = 1 \times 10^{-3} \ \mathrm{s}^{-1}$. (a) IR temperature field and overlaid stress history, (b) Tangential strain field images corresponding to labels in (a).

at numerous locations along the specimen during the load plateau. After the load plateau, the localized areas of strain slowly grow, causing more uniform temperature changes, until they eventually fill in the gage length of the specimen by DIC image ⑩. During unloading ($M^+ \rightarrow A$ transformation), these high strain regions slowly shrink between ⑩ and ⑮, while the specimen uniformly cools down. From ⑮ to ⑰ the high strain regions disappear in roughly the order in which they had been generated, causing the expected local drops in temperature.
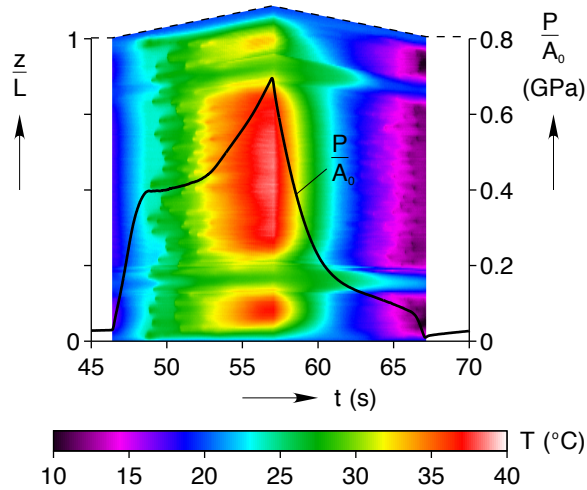
Figure 5.13 Experiment S2c. Temperature field history and stress history of the 1×6 during the 2nd cycle at $\dot{\delta}/L = 1 \times 10^{-2}$ s^{-1}.

The temperature field history (Fig. 5.13) of the 1×6 at $\dot{\delta}/L = \pm 1 \times 10^{-2}$ s^{-1} (Exp. S2c) continues in the trend set by the two slower rates. Faster rates create more temperature blooms, such that the temperature changes almost appear uniform at $\dot{\delta}/L = \pm 1 \times 10^{-2}$ s^{-1}. The DIC data for experiment S2c is not shown because the data was lost (along with the DIC data from experiment S2a), but the strain fields were qualitatively similar to Fig. 5.12b, as one might expect from the numerous temperature blooms. Let us compare the 1×6 strand at three different rates past the end of the plateau during loading. In this region, the temperature fields are relatively uniform and the strain localizations grow to fill in the remaining pockets of austenite. The approximate average temperature ranges from 20 °C to 23 °C to 37 °C as the elongation rate ranges from 10^{-4} s^{-1} to 10^{-3} s^{-1} to 10^{-2} s^{-1}. Only at the highest elongation rate is there a substantial temperature rise. We may also compare the 1×6 to the 1×7 strand. In the 1×7 strand (Fig. 5.6a) there are 18 propagating fronts during loading, but the 1×6 strand (Fig. 5.13) exhibits roughly 50 temperature blooms. Overall, this pattern of kinetics distributes any self-heating/self-cooling much more uniformly than if transformation had occurred by propagating fronts, and this is likely the primary reason the 1×6 is less rate sensitive than the previous 1×7 core strand.

The question then arises as to why localized strains develop without propagating fronts in the 1×6 core strand, so we offer the following explanation. Recall the scanning electron microscope images (see Fig. 4.8b) of the straight core wire and the 1×6 strand. The core wire had a helical line indent tracing the line of contact with the 5 layer B wires. The 1×6 had dimples and divots on its surface. During a tensile test of a 1×6, the layer B wires likely dig into the helical indent on the core wire, locking the two layers together. Upon further elongation, the onset of a front in the core wire is delayed because the layer B wires have not yet reached their transformation stress (due to their large helix angle). Eventually, however, the driving force to create a front in the core wire is strong enough to localize the strain in the layer B wires at the dimples and divots on the surface (② in Fig. 5.12b). The stored energy causes a quick nucleation and subsequent release of latent heat, leading to temperature blooms, even at $\dot{\delta}/L = 1 \times 10^{-4}$ s^{-1} (see Fig. 4.7b). Between ② and ⑦, further nucleations initiate at other defects until the end of the core wire plateau ($\delta_e/L_e = 6.0$ %). As the load rises (⑦ to ⑩), the core wire strains more or less uniformly, and the localizations in the layer B wires grow uniformly along the gage length as well (⑦ to ⑩). Thus, we believe the layer B wires do not develop a front because stress concentrations on their surfaces cause early transformation to accommodate the core wire.

5.3.2   1×15 Multi-Layer Strand and 1×27 Cable

For the remainder of the results section, we will discuss the elongation rate dependence of the 1×15 and 1×27 together since they are quite similar, as seen in Fig. 5.14. The axial load and torque for both components, during both cycles, exhibit the same trends. The higher rates all deviate from their fundamental responses most at the maximum strain for each cycle, but the deviation is much reduced compared to 7×7 components, which have propagating transformation fronts. The lack of propagating fronts in the 1×15 strand and 1×27 cable has been previously shown in their respective strain fields (Fig. 4.14b and Fig. 4.16b), so although DIC data was collected and analyzed for the higher rate experiments in Fig. 5.14, the strain fields are not displayed here because they are nearly identical. Similarly, temperature field histories at higher rates are not shown because the temperature field was spatially uniform (see Fig. 4.9b and Fig. 3.12b).

Instead of IR contour plots, the specimen thermocouple (T_s) history along with the stress history for the 2nd cycle (and the very end of the 1st cycle) are displayed in Fig. 5.15 for the 1×15 and 1×27. It is easier to read off specific temperatures from these plots than contour plots and they allow three different elongation rates to be directly compared on a single plot. Of course, the time required to load and unload is directly proportional to the elongation rate,
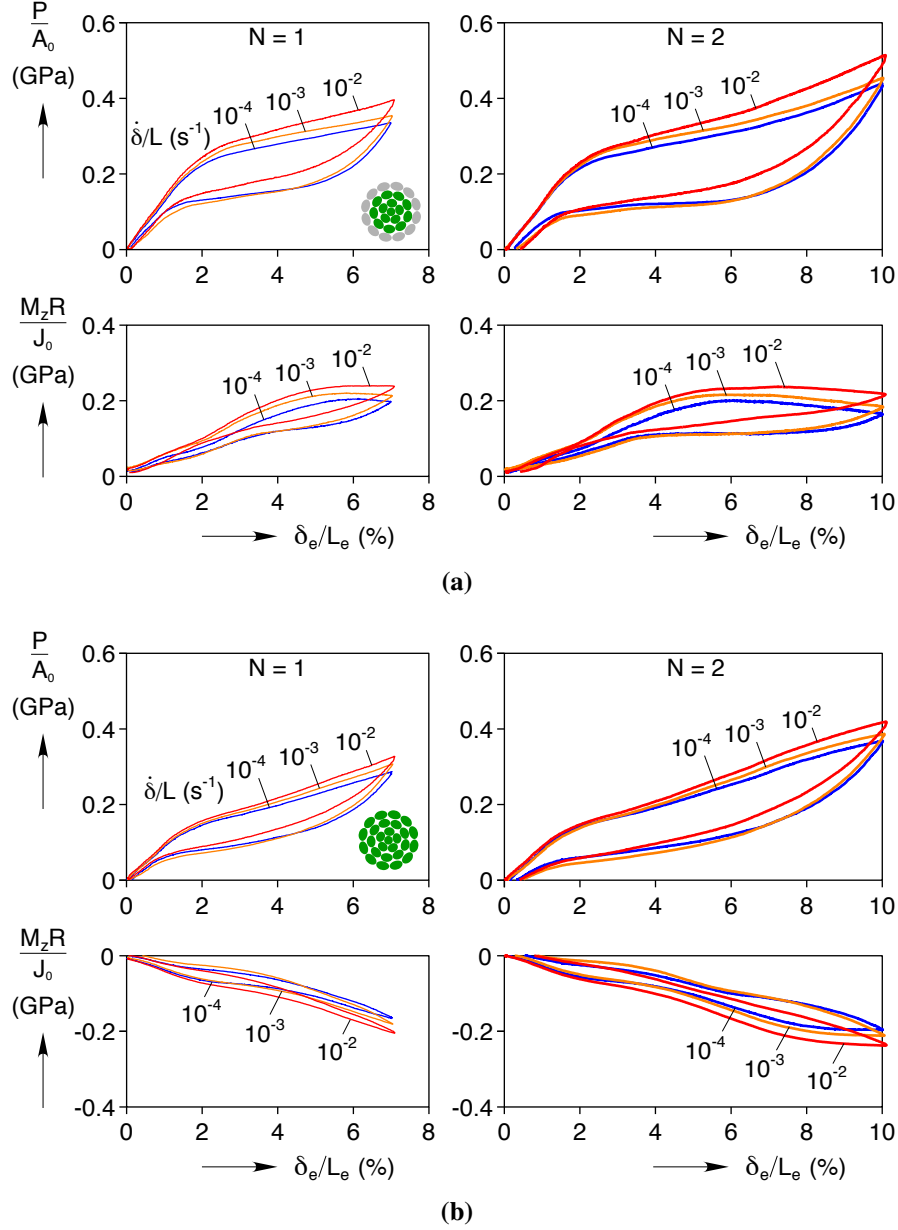
Figure 5.14 The first and second cycle mechanical response of (a) the 1×15 (Experiments M2a, M2b, and M2c) and (b) the 1×27 (Experiments C2d, C2e, and C2f) at three different elongation rates.

so to place all three experiments on the same plot, the time was normalized by the 2nd cycle time $t_2 - t_1$, where t_i is the time at the end of cycle i[a]. Note that the small drop in stress in Fig. 5.15a after the peak stress at $\dot{\delta}/L = \pm 1 \times 10^{-4}$ s^{-1} is just a small amount of stress relaxation when the load frame crosshead briefly stopped between loading and unloading.

[a]For reference, the second cycle times for the 1×15 were $t_2 - t_1$ =2164.7 s, 207.2 s, and 21.45 s for $\dot{\delta}/L = 10^{-4}$ s^{-1}, 10^{-3} s^{-1}, and 10^{-2} s^{-1}, respectively. The corresponding times for the 1×27 were 2143.8 s, 212.9 s, and 21.61 s.
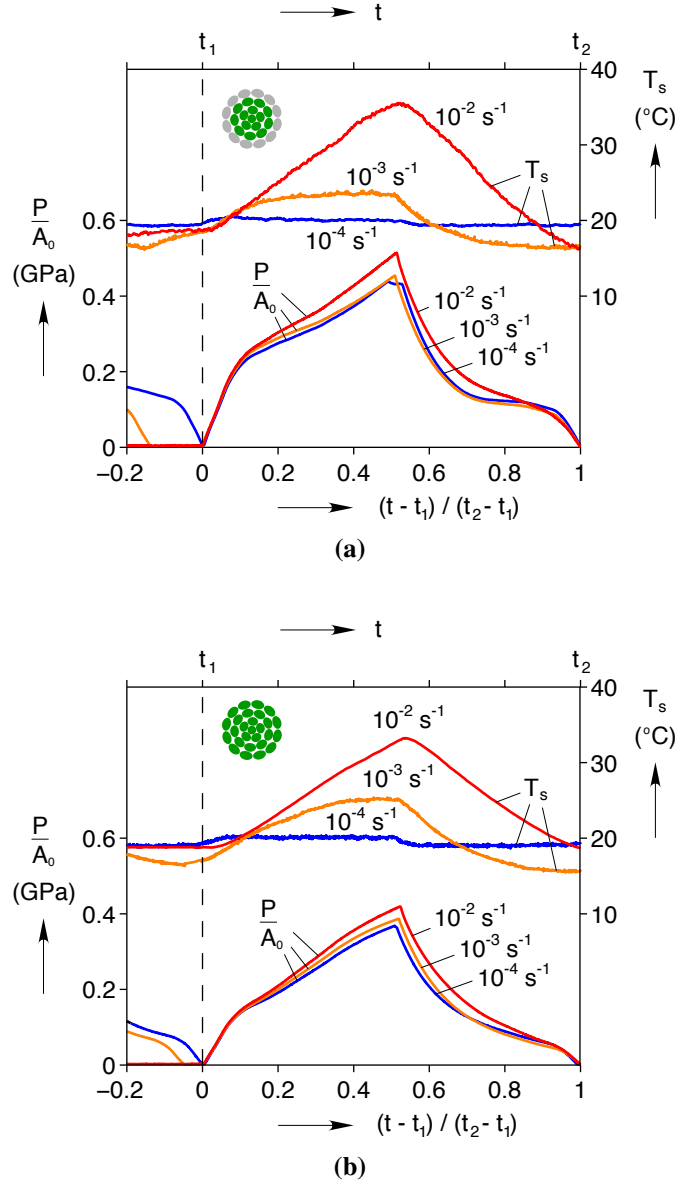
Figure 5.15 Stress and thermocouple history, during the 2nd cycle, at three different elongation rates for (a) the 1×15 (Exp. M2a, M2b, and M2c) and (b) the 1×27 (Exp. C2d, C2e, and C2f). Bottom time axis normalized by 2nd cycle time ($t_2 - t_1$).

Both the 1×6 and the 1×15 follow the trends that we would expect: higher elongation rates lead to higher axial forces and torques, and, again, the rate sensitivity is significantly reduced compared to the 7×7 components. Two reasons for this reduction in rate sensitivity have been previously mentioned: reduced thermal inertia and the absence of propagating transformation fronts. Nevertheless, comparing the rate sensitivity of the 1×6 (Fig. 5.11), 1×15 (Fig. 5.14a), and 1×27 (Fig. 5.14b) we can see that the rate dependence is also diminished as each layer of helical wires is added to the construction. That is, the rate dependence

of the 1×6 is less than the core wire (judging from the 7×7 core wire rate dependence), the 1×15 is less than the 1×6, and the 1×27 is less than the 1×15. Further inspection of the temperature field and thermocouple histories for each component (Fig. 4.7b, Fig. 5.12a, Fig. 5.13, and Fig. 5.15) reveals that the maximum temperatures attained for the 1×6, 1×15, and 1×27 are close to the same for each elongation rate. This trend does not fit the previous explanations. If all the components spatially distribute the latent heat, and the thermal inertia of the specimen increases each time a new layer is added, then one would expect significantly higher temperatures for the larger components. Recall that each new layer also has a larger helix angle α_0 and a larger helix radius r_0, causing each successive layer to begin transformation at a larger global strain. Referring back to the deduced outer layer responses in Chapter 4 (see Fig. 4.17b), layer B, layer C, and layer D begin to transform at δ_e/L_e =2.2 %, 6.0 %, and 8.8 %, respectively. Thus, a third reason that the 1×27 components have reduced rate sensitivity is the latent heat release is temporally spread out over the loading period by virtue of the construction of the 1×27 cable.

5.4   Summary & Conclusions

In Chapters 3 and 4, we motivated the study of SMA cables, described our experimental setup, and investigated the isothermal response of the superelastic 7×7 and 1×27 cable designs in tension. The 7×7 and its subcomponents performed similar to wires loaded in parallel, while the 1×27 and its subcomponents showed enhanced compliance.

In this chapter, the same two designs were probed for their sensitivity to various elongation rates. The 7×7 core strand and full cable both have small helix angles, which puts the wires predominately in tension. Thus, it was not surprising that the elongation rate sensitivity of the straight 7×7 core wire and 1×7 core strand were qualitatively similar for the elongation rates tested. Larger elongation rates caused the plateaus to offset further and further from their isothermal counterparts, until fronts thermally interacted causing the stress to rise toward the end of transformation. As higher elongation rates were applied to the 7×7 cable, however, its plateaus sloped further and further upward from the beginning. This is because transformation fronts nucleated at all the contact points between the 7×7 strands, distributing the latent heat exchanges along the cable, and causing fronts to thermally interact throughout transformation, instead of solely at the end. The 1×27 components, besides the core wire, all had minimal rate sensitivity compared to the 7×7 components. There are several reasons for this:

1. The 1×27 design has less thermal inertia, meaning its temperature tracks the ambient

air temperature more closely.

2. Propagating transformation fronts, which localize the latent heat of transformation, were not observed in the 1×27 components, besides the core wire. Instead, transformation was spread out along the 1×27 components' gage length.

3. As shown in Section 4.3, each layer of the 1×27 design starts to transform at a different global strain, causing the latent heat to be spread out in time as the cable is stretched.

The reduced sensitivity of the 1×27 cable could be useful to a designer who requires a tension element with large recoverable strains and hysteresis, but wishes to avoid the elongation rate effects inherent to SMA wires and rods.

Chapter 6

Tube Tension, Compression, and Bending Experiments

Chapters 3, 4, and 5 presented a thorough series of experiments on two SMA cable designs. Any effort to simulate the thermomechanical response of those designs, or other future cable designs, must start with a SMA constitutive model validated against careful experiments in fundamental deformation modes such as tension, compression, bending, and torsion. While many uniaxial tension experiments of shape memory alloys (SMAs) have been published in the literature, relatively few experimental studies address their behavior in compression or bending, despite the prevalence of this latter deformation mode in applications (see section 1.1.2).

In this chapter, superelastic NiTi tubes are characterized in tension, compression, and pure bending, in contrast to previous studies [10, 16, 98] that only performed tension and bending tests. (Torsion and other biaxial experiments are planned for future work.) The tubes studied here were also from a single lot of material, allowing direct comparisons between the deformation modes for the first time. Custom built fixtures are used to overcome some long-standing experimental difficulties with performing well-controlled loading and accurate measurements during uniaxial compression (avoiding buckling) and large-rotation bending. In all experiments, the isothermal, global, mechanical responses are measured, and stereo digital image correlation (DIC) is used, also for the first time, to measure the evolution of the strain fields on the tube's outer surface.

6.1   Materials and Specimen Preparation

The material studied was cold-drawn, slightly Ni-rich NiTi tube from Memry Corporation (P/N 10130W, Lot # 957152). The outer diameter and inner diameter were measured as $D = 2C = 3.176$ mm (0.125 inch) and 2.540 mm (0.100 inch), respectively, which corresponds to an outer diameter to thickness ratio of $D/H = 10$. Differential scanning calorimetry (DSC), using a Q2000 DSC (TA Instruments) at a scan rate of $\dot{T} = \pm 10$ °C/min,

120

was performed to characterize the material's transformation temperatures. The DSC specimen was prepared by diamond saw cutting six 0.75 mm thick half circles from the tubes (specimen mass of 35.4 mg) and placing them flat in the sample pan to ensure good thermal contact. The austenite (A_s and A_f), martensite (M_s and M_f) and rhombohedral (R_s and R_f) transformation temperatures, as well as the corresponding specific enthalpies of transformation, are indicated on the thermogram in Fig. 6.1a. Since $A_f = 19$ °C, the alloy is initially austenite at room temperature and is superelastic. During cooling, the material exhibits
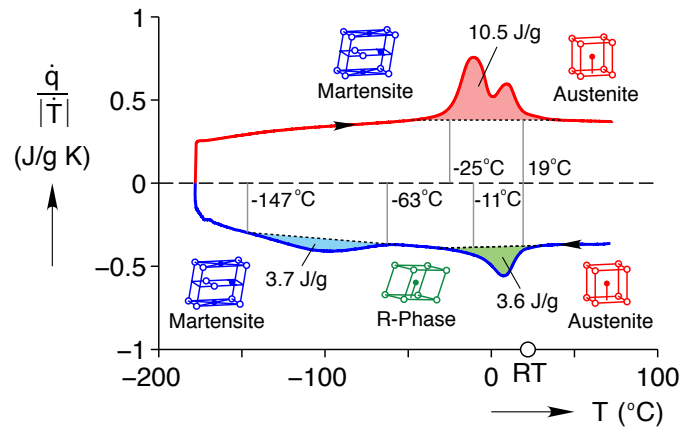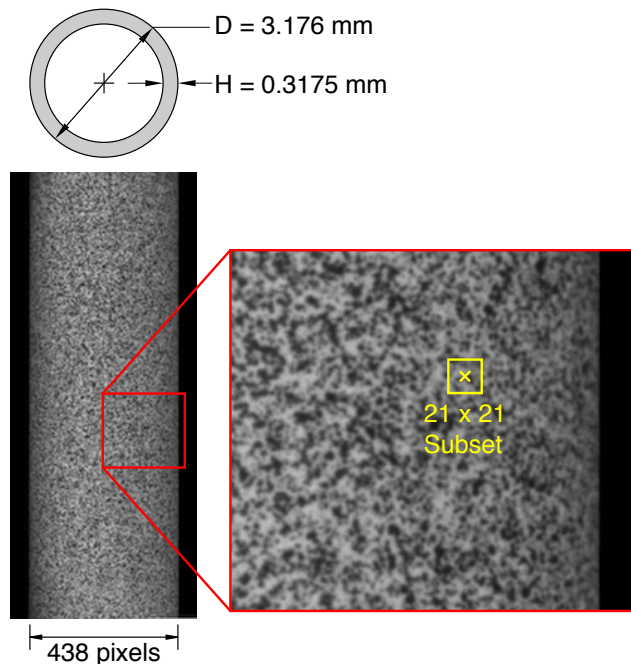
Figure 6.1 (a) Differential scanning calorimetry thermogram of NiTi tube material. (b) Cross-section dimensions and photograph of tube specimen showing the speckle pattern for tracking full field deformations.

121

a two step transformation first $A \rightarrow R$ and then $R \rightarrow M$, as is common for commercial superelastic Nitinol alloys. During heating, the $M \rightarrow R$ and $R \rightarrow A$ transformations overlap creating a double peak.

New, as-received, tube specimens were used for each tension, compression, and bending experiment. The strain distribution during the experiments was measured by DIC, which requires a high contrast specular pattern on the surface of the specimen. The specimen was first airbrushed with a background coat of Golden Airbrush Titanium White (#8380), followed by a speckle coat of Golden Airbrush Carbon Black (#8040). The resulting speckle pattern is shown in Fig. 6.1b. The magnified image is a portion of the actual image used for the DIC analysis and shows a typical 21×21 subset used in the correlation analysis. More details of the specimen airbrush procedure and subset selection can be found in Chapter 2. Segments of the specimen that were to be placed inside the tension and compression grips were not painted.

6.2 Experimental Setups

The following describes the setups for uniaxial tension, uniaxial compression, and pure-bending experiments, all performed in room temperature air. Six experiments, two of each type, will be presented in the following sections, and Table 6.1 provides a summary of specimen gage lengths and loading rates. Experiments are identified by T1, T2, C1, C2, B1, and B2, denoting the type of experiment by the letter and the number denoting the first or second experiment of that type. The reference length of the tube specimen is L and its elongation is δ. The viewable free length is L_f, and the DIC "extensometer" (gage) length chosen is L_e. The elongation rate (average strain rate) is $\dot{\delta}/L$ for the uniaxial experiments, and the estimated average outer-fiber strain rate during bending experiments is $\dot{\bar{E}}_{ZZ}^B(\pm D/2)$[a].

6.2.1 Tension and Compression Setups

The tension and compression setups shown respectively in Fig. 6.2a and 6.2b were similar, except for the grip designs. Both setups utilized a Test Resources 830L load frame with a linear servomotor actuator, operated in displacement control. A 5 kN load cell monitored the resultant axial force (P). A 2825 N·mm torque cell was also included in the tensile setup, but the torque was too small to obtain a reliable reading (as was also found by Feng and

---

[a]A bar over a quantity refers to an averaged quantity. As described later, E_{ZZ}^B denotes the component of the Biot strain along the length of the tube.

Table 6.1 Parameters for tension (T), compression (C), and bending (B) experiments

Parameter	Experiment					
	T1	T2	C1	C2	B1	B2
L (mm)	14.13	14.76	41.59	40.83	≥ 14.77	≥ 14.77
L_f (mm)	14.13	14.76	9.38	7.87	14.77	14.77
L_f/D	4.45	4.65	2.95	2.48	4.65	4.65
L_e (mm)	9.57	10.13	5.33	3.29	9.58	10.42
L_e/D	3.01	3.19	1.68	1.04	3.02	3.28
$\dot{\delta}/L$ (s^{-1})	2×10^{-5}	2×10^{-5}	2×10^{-5}	2×10^{-5}	–	–
$\dot{\bar{E}}^B_{ZZ}(\pm D/2)$ (s^{-1})	–	–	–	–	$\approx 2 \times 10^{-5}$	$\approx 4 \times 10^{-5}$

Sun [43]). The lower grip was fixed while the upper grip displacement (δ) was prescribed at a constant rate ($\dot{\delta} = d\delta/dt$) during loading and unloading. To maintain isothermal conditions, the prescribed global strain rate was quite slow, $\dot{\delta}/L = \pm 2 \times 10^{-5}$ s^{-1}, where L is the length of the specimen between grips. Isothermal conditions were verified with two type-K thermocouples, one measuring the air temperature (T_a) and one measuring the specimen temperature (T_s). A small amount of thermally conductive paste (Omegatherm 201) was applied to the specimen thermocouple and the tube outer surface to ensure good thermal contact. Measured deviations in specimen temperature due to latent heat effects during transformation were less than ± 0.3 °C from room temperature in both sets of experiments.

The tension specimens were held in 3.175 mm (1/8 inch) ER 16 steel sealed collets as shown in the section schematic of Fig. 6.2a. The collet holder was bolted directly to the load frame, and a Teckniks Power Coat nut was used to compress the collet. The unpainted (gripped) segments of the tension specimens were scored with a file to provide a higher friction gripping surface. In addition, steel dowel pins (2.515 mm diameter) were inserted into the ends of the tube specimen within the gripped region to increase the radial stiffness. Care was taken to ensure that the dowel pins did not protrude into the gage section between the grips.

Dowel pins were not used in the compression specimens, and the unpainted sections were coated with light oil to help the specimen slide freely in the compression grips. The compression grips shown in the section schematic of Fig. 6.2b were two 25.4 mm diameter steel cylinders, each with a 3.20 mm diameter by 15.9 mm deep hole. This design left a free length between the grips (L_f) for DIC measurements and permitted a relatively long specimen length L, while laterally supporting the specimen to avoid column buckling. Buckling was further prevented by the relatively stiff, short stackup (hardware between the crosshead and base in Fig. 6.2b) and careful alignment of the compression grips.
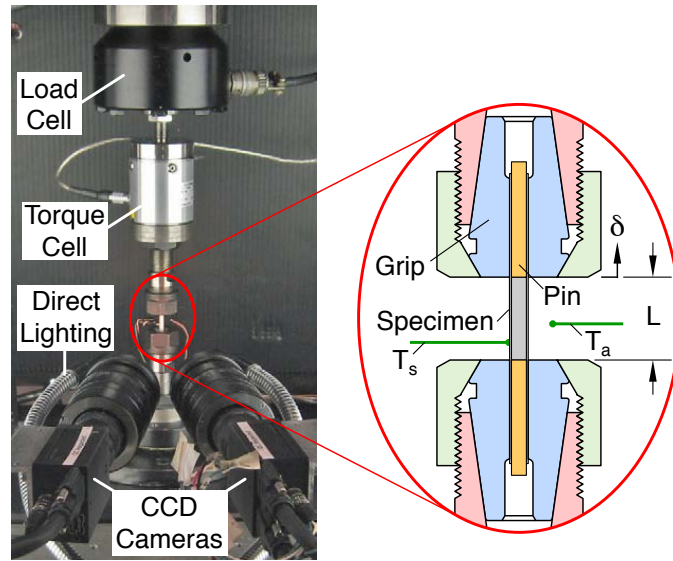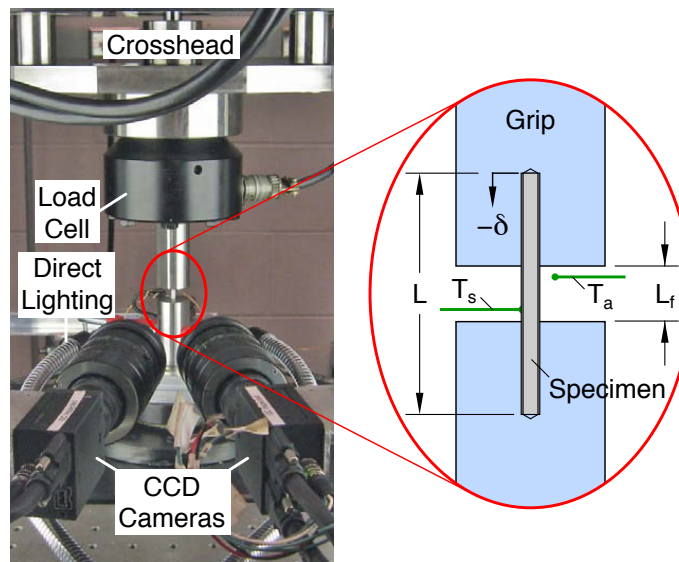
Figure 6.2 Photographs of uniaxial setups and schematics of grips (to scale): (a) tension setup, (b) compression setup.

6.2.2 Bending Setup

A photograph of the bending setup is shown in Fig. 6.3a, along with a magnified view of the 4-point bend fixture. The bending fixture design is similar to that used in Kyriakides *et. al.* [66] for pipe bending, except that our bending fixture was scaled down and integrated into an Instron 5585 lead-screw driven load frame. One can see the basic operation of the fixture by comparing the close-up photo of the fixture in Fig. 6.3a with an undeformed specimen, against the schematic in Fig. 6.3b with a deformed specimen. The four loading points are 4.80 mm diameter stainless steel rollers, machined with a semi-circular relief to capture the tube in the bending plane. Each roller was press-fit into a pair of miniature ball bearings such that the rollers could rotate freely, allowing the tube to slide to avoid any axial tension. Similar to the compression specimens, a thin coating of oil was carefully applied to the unpainted ends of the tube to further ensure that the tube would slide freely. Each pair of bearings was affixed to a D_w = 23.86 mm diameter aluminum loading wheel, each mounted to another center bearing. A single steel cable was wrapped around each wheel, one wheel at each end of the cable, and then pulled from above by the load frame operated under displacement control. A pair of pulleys above balanced the force between the wheels. A 500 N load cell, attached to the load frame crosshead, measured the vertical load P as the load frame crosshead was raised by an amount δ. The moment M applied to the tube was $P(D_w + D_c)/4$, where D_c = 1.19 mm was the diameter of the steel cable. The initial length of tube between the rollers was L = 14.77 mm, but since the axial load was essentially zero, the length of tube being bent became somewhat larger when end-rotations were large. The average curvature was measured over a fixed length L_e of material data points as described below in Section 6.2.3. Ambient temperature T_a was measured by a type-K thermocouple, but due to the large displacements, the temperature of the specimen was not directly measured. To ensure nearly isothermal conditions, the rotation rate was quite slow. In the single load-unload bending experiment (B1), the strain rate at the outer tensile fiber of the tube was about $\pm 2 \times 10^{-5}$ s^{-1} (11.5% strain over 87.9 min), similar to the average strain rate of the uniaxial experiments. A slightly faster strain rate of $\pm 4 \times 10^{-5}$ s^{-1} at the outer tensile fiber was used for the second bending experiment (B2).

6.2.3 DIC Setup and Post-processing

Stereo DIC was performed during all experiments presented below to measure the local surface displacement and surface strain fields on the viewable portion of the specimen. In the tension and compression experiments that follow, the mechanical responses are reported
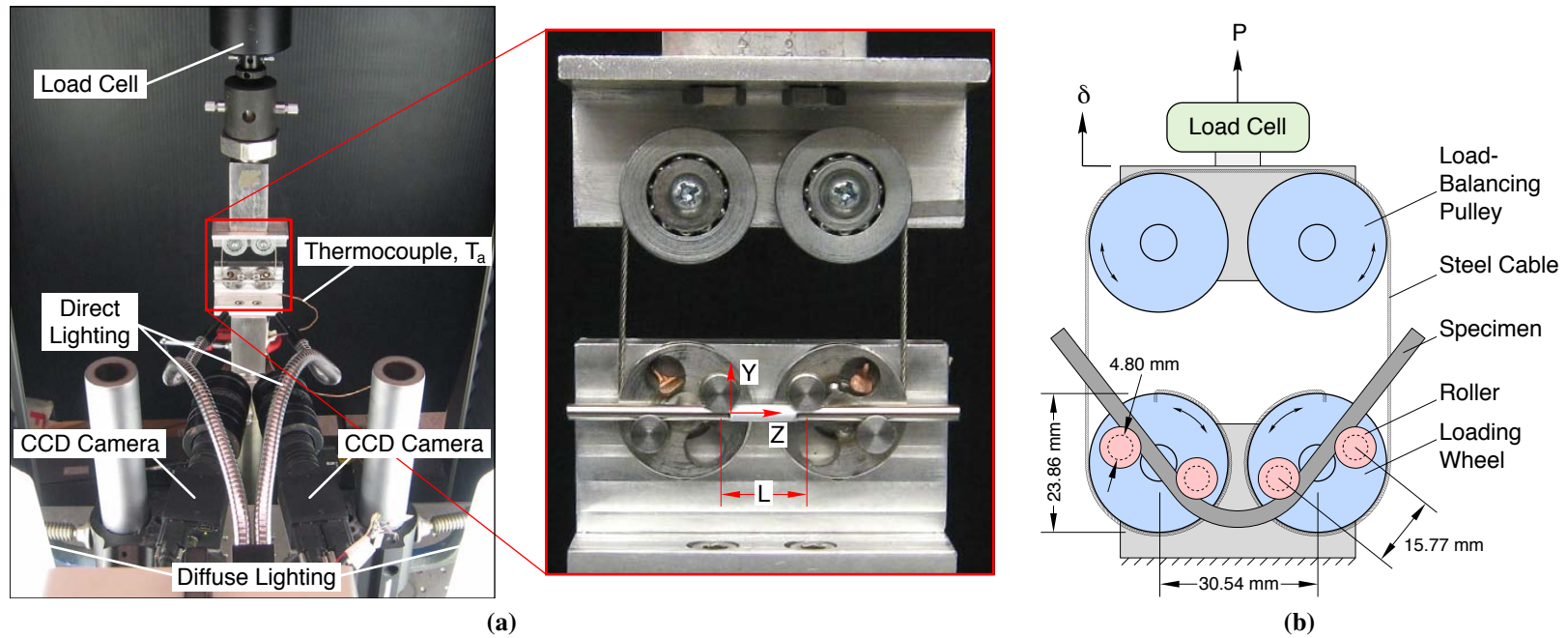
Figure 6.3 Bending setup: (a) photographs of overall setup and closeup of bending fixture with undeformed tube specimen, (b) schematic of pure-bending fixture with deformed specimen, (c) top view schematic, (d) front view schematics.

in terms of averaged strains ($\bar{E}_{ZZ}^{B}$) in a selected gage region (L_e) from the DIC analysis, rather than the global strain (δ/L), to eliminate any gripping artifacts. A sequence of simultaneous images was taken by the gray-scale CCD cameras shown in the foreground of the photographs in Fig. 6.2. The cameras were Pt. Grey Research Grasshoppers[b] (GRAS-50S5M-C), each with a 2048×2448 pixel array of square 3.45 μm pixels. For the uniaxial experiments the cameras had a stereo angle of 18° between them. The cameras were attached with Fujinon HF75SA 75 mm focal length lenses with either 32.5 mm or 35 mm extension tubes. The aperture diameter of each lens was set to 9.4 mm, which provided sufficient depth of field to keep both the crown and edge of the tube in focus. The exposure time ranged from 50.7 ms to 69.3 ms depending on the lighting. With the well known temperature sensitivity of NiTi, special care was taken to choose lighting sources that did not affect the temperature of the specimen. We used fluorescent lights behind frosted translucent plastic, similar to a photographer's light box, to produce a diffuse, flat light (just out of view in Fig. 6.2a and 6.2b, but just in view in Fig. 6.3a). Flexible fiber optic lights, as seen extending in from the bottom of the photos, with an adjustable light intensity were used to finely adjust the illumination and overcome shadows caused by the grips. Prior to the experiments, the DIC stereo system was calibrated using a 9×9 calibration grid with 1.34 mm spacing (Grid B, P/N AIG 045466 [30]). During the experiment, a function generator triggered the cameras every 10 seconds, and the signal was sent to the data acquisition system to synchronize all measurements, including load, thermocouple, and crosshead displacement.

After each experiment, the DIC images were analyzed using the commercially-available Vic-3D 2010 software [29] across a region of interest, centered on the tube axis (roughly 438 pixels across the outer diameter). We utilized a 21×21 subset, an analysis grid with 2×2 pixel spacing, and Vic-3D's default cross correlation function of the normalized sum of squared differences [119]. For the strain calculation at each analysis grid point, Vic-3D used a truncated Gaussian filter over a 31 pixel diameter circle with a weight of 1 at the center point and a weight of 0.1 at the circle edge.

The strain components from DIC analysis will be reported with respect to a referential Cartesian coordinate system (X, Y, Z) with Z along the tube axis, or a cylindrical coordinate system (R, Θ, Z)[c] aligned with the tube radius, circumference, and axis. In the results below, we chose to report the Biot strain, instead of Vic-3D's default strain measure of Green-Lagrange strain. In previous chapters, the Green-Lagrange Strain $\boldsymbol{E}^{L}$ was acceptable for

---

[b]The manufacturer reports the Grasshopper is capable of 14 bit grayscale resolution, but the effective (noise free) dynamic range was approximately 8 bits for our setup.

[c]For most variables, upper case coordinates refer to reference coordinates, while lower case coordinates refer to current coordinates. Where certain symbols have already been defined, a subscript or superscript '0' is added to indicate a reference quantity.

tracking localized transformation activity, but in this chapter the strain fields are analyzed quantitatively so it was important to chose a strain measure well suited to the experiments performed. The Biot strain tensor is defined as

$$\boldsymbol{E}^{\mathrm{B}} \equiv \boldsymbol{U} - \boldsymbol{I}, \tag{6.2.1}$$

where $\boldsymbol{U}$ is the right stretch tensor (from the polar decomposition of the deformation gradient $\boldsymbol{F} = \boldsymbol{R} \cdot \boldsymbol{U}$ with rigid rotation $\boldsymbol{R}$) and $\boldsymbol{I}$ is the identity tensor. The Biot strain ($\boldsymbol{E}^{\mathrm{B}}$) and its conjugate Biot stress ($\boldsymbol{\Pi}^{\mathrm{B}}$) are referential finite deformation measures that are convenient for large rotation bending of slender structures, where the local direction of uniaxial loading follows the material rotation during the loading process. Accordingly, the rotation $\boldsymbol{R}$ can be applied to the reference coordinate system (X, Y, Z) to define a new local, co-rotated, orthonormal frame (x, y, z), as shown in Fig. 6.4b. During bending, this local frame rotates about the X-axis to keep the z-axis aligned with the current beam axis and normal to the cross section (neglecting any shear deformation). Using our coordinates, the Biot strain E^{B}_{ZZ} coincides with the engineering strain in the co-rotated frame ($\mathrm{d}z/\mathrm{d}Z - 1$), even when local strains and rotations are large. Likewise, the Biot stress component Π^{B}_{ZZ} is just the engineering stress $\mathrm{d}P_z/\mathrm{d}A_0$ for an axial load P_z and reference cross-sectional area A_0 originally normal to the Z-direction. A more detailed justification of this choice and some further comments are provided in Appendix A.

The DIC setup for the bending experiment was similar to that of the tension and com-
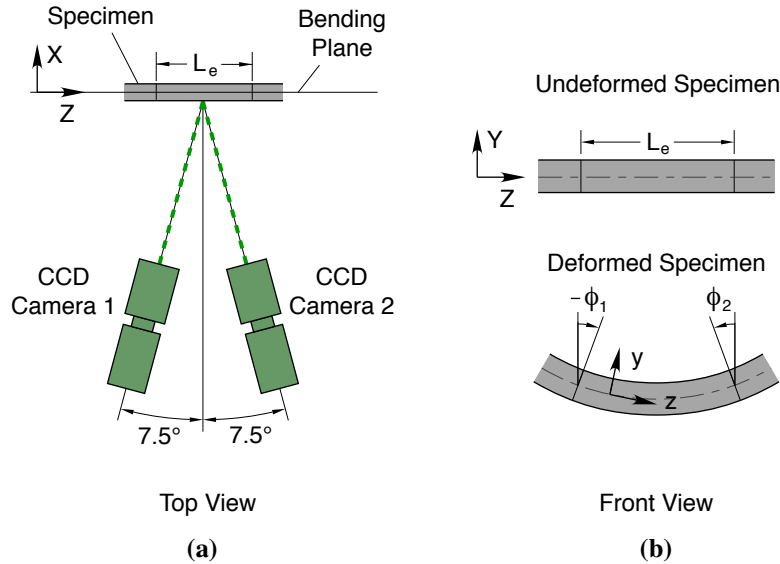
Figure 6.4 Bending setup: (a) top view schematic, (b) front view schematics.

pression experiments. Since the bending fixture oriented the tube horizontally instead of vertically, the cameras were rotated 90° about each of their optical axes and the stereo angle was reduced to 15° to keep the length of the tube in focus. The DIC processing parameters described previously were used, but some additional steps were taken. (1) The coordinate system was carefully aligned so that the X-axis was precisely perpendicular to the bending plane and the Z-axis was aligned with the centerline of the tube specimen (see Fig. 6.4a). (2) The material curvature for an initially straight beam is defined as $\kappa = \mathrm{d}\phi/\mathrm{d}Z$, where ϕ is rotation of the cross section about the $-X$-axis, and Z is the reference axial position. The average curvature $\bar{\kappa}$ over length L_e is $(\phi_2 - \phi_1)/L_\mathrm{e}$, where $L_\mathrm{e} = Z_2 - Z_1$ and ϕ_i are shown in Fig. 6.4b. To measure ϕ_i, we took two lines of constant Z_i, found their current positions (y_i, z_i) over 438 points across the diameter, and used the slope of a least squares fitted line. (3) The position of the neutral axis, defined as $E_{ZZ}^\mathrm{B} = 0$, was found for every set of data along L_e and then averaged over Z to calculate the average neutral axis offset $\overline{Y}_0$.

6.3 Tension and Compression Experiments

The mechanical responses of tube specimens were first characterized in uniaxial tension and compression at slow (quasistatic and nearly isothermal) elongation rates in room temperature air. Here, we present uniaxial experiments that will later be compared to the room temperature bending response of the tube. A more comprehensive set of experiments over various temperatures and rates on similar tubes of the same cross-section geometry can be found in [27].

The global mechanical responses of tube specimens in tension (experiment T1) and compression (experiment C1) are shown respectively in Figs. 6.5(a) and 6.5(b). The vertical axis is the Biot (engineering) stress $\bar{\Pi}_{ZZ}^\mathrm{B} = P/A_0$ averaged over the cross sectional area of the tube, and the horizontal axis $\bar{E}_{ZZ}^\mathrm{B}$ is the Biot strain along the tube axis, averaged over the points in the DIC "extensometer" gage length L_e. The responses show a significant tension-compression asymmetry, as is now well-known for textured NiTi. The tensile response exhibits flat transformation plateaus (see ②-⑥ in Fig. 6.5(a)), while the compressive response does not (see ④-⑥ in Fig. 6.5(b)). The magnitude of transformation strain in tension is larger than that for compression, and the magnitude of transformation stresses in tension are smaller than for compression.
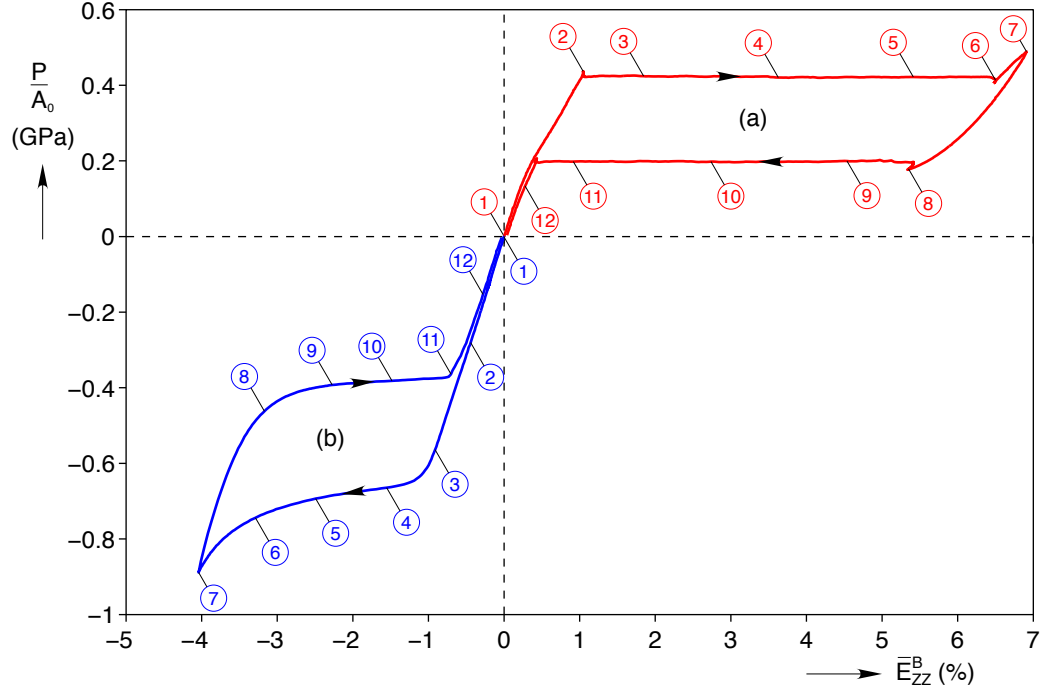
Figure 6.5 Mechanical responses of tube specimens during (a) tension experiment T1 and (b) compression experiment C1, showing significant tension-compression asymmetry.

6.3.1 Tension Results

Here we describe the tensile mechanical response shown in Fig. 6.5(a). The initial slight non-linearity from $\bar{E}_{ZZ}^{B} = 0.2\%$ to 0.6% is due to the rhombohedral phase [83], which is commonly present in Ni-rich NiTi in an intermediate range of temperatures and stresses. This is a relatively minor effect in the mechanical response, however, compared to the larger transformation to martensite. After the initially stiff segment, a distinct load plateau exists during loading (during $A \rightarrow M^{+}$ transformation), and another lower plateau exists during unloading (during reverse, $M^{+} \rightarrow A$ transformation)[d]. Each plateau is associated with a material instability, accompanied by propagating necks separating regions of high and low strain. (See Section 2.4 of Chang *et. al.* [19] for a discussion of why this is indeed a material instability and not just a structural instability.) Axial strain field (DIC) contours of the front half of the tube specimen are shown in Fig. 6.6, and the circled numbers correspond to labeled points in Fig. 6.5(a). Images ②-⑥ clearly show a single macroscopic $A \rightarrow M^{+}$ transformation front propagating from the lower grip to the upper grip during the loading plateau, and images ⑧-⑪ show a $M^{+} \rightarrow A$ transformation front propagating from the upper grip to the lower grip during the unloading plateau. Upon complete unloading, the average

---

[d]Using a macroscopic viewpoint, we denote stress-induced tensile martensite as M^{+} and stress-induced compressive martensite as M^{-}
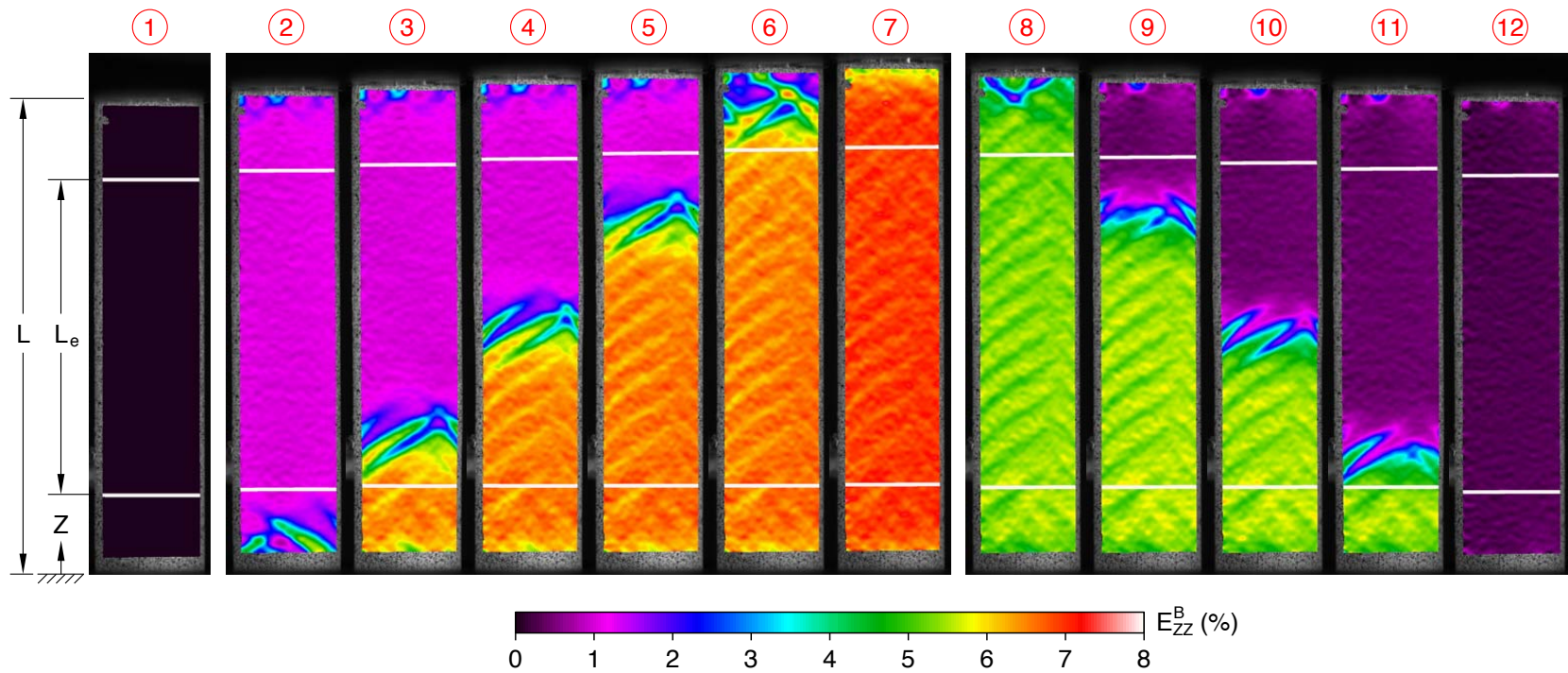
Figure 6.6 Experiment T1. Axial strain field images from DIC at times labeled in Fig. 6.5(a).

residual strain was quite small ($\bar{E}^{\mathrm{B}}_{ZZ} = 0.03$ %), indicating nearly perfect superelasticity.

Some details are worth mentioning. First, the small increases and drops in load at the beginning and end of the plateaus correspond to the front emerging from or entering the grips. Stress concentrations at the grips tend to suppress these load peaks, unless care is taken to suppress transformation at the grips [43, 58], but in this case gripping was uniform enough that small peaks were still evident. Second, close observation reveals that the region affected by the grip is about $D/4$ long in image ⑦ and ⑫ when the strain fields are mostly uniform. However, the boundary effect protrudes about $3D/4$ into the gage length when a front is near the grips, as seen in images ②, ⑥, and ⑧. Incidentally, DIC allows us to select our extensometer gage length after the experiment rather than before, so we selected the two white lines in image ① as the boundaries of L_{e} to avoid these grip effects. Third, consistent with the observations of Feng and Sun [43], each macroscopic front is actually made of fine "fingers" of high and low strain that convolute around the tube as the front propagates. The fingers appear slightly curved in Fig. 6.6, since they wrap around the curved surface of the tube. When the DIC data is "unwrapped" to a flat surface, as in Fig. 6.7a, the fingers are nearly straight and their angle can be accurately measured. In Fig. 6.7a the trailing edge angle and leading edge angle of one of the fingers is $\alpha_1 = 57.2^{\mathrm{o}}$ and $\alpha_2 = 64.1^{\mathrm{o}}$, respectively, to the Z-axis. The fingers in four other images (not shown) were also measured and α_1 ranged from 56.1^{o} to 58.5^{o}, while α_2 ranged from 64.1^{o} to 66.0^{o}. Only the tips of the fingers on the right side of the tube are visible, making it difficult to measure their leading and trailing edges. In image ③ the finger on the right side protruded a little further into the DIC FOV allowing us to measure its trailing edge angle $\alpha_3 = -59.6^{\mathrm{o}}$. Since the unwrapped tube is similar to a thin strip, a simple Mohr's circle analysis similar to that shown in Shaw and Kyriakides [112] gives an estimate for the ideal in-plane front angle α according to

$$\cos(2\alpha) = -\frac{1 - v_{Z\Theta}}{1 + v_{Z\Theta}}. \tag{6.3.1}$$

Using the DIC measured Poisson ratio $v_{Z\Theta} = -\bar{E}^{\mathrm{B}}_{\Theta\Theta}/\bar{E}^{\mathrm{B}}_{ZZ} = 0.45$ (discussed further in section 6.3.3) results in $\alpha = \pm 56.1^{\mathrm{o}}$, which is reasonably close to the angles measured.

Feng and Sun [43] explained that the branched finger morphology "helps to reduce the strain energy of the domain at the expense of increasing the total front length and therefore the total interfacial energy of the front." Put a different way, the material cannot suffer a jump discontinuity in lateral strain, so a macroscopic neck forms. Rather than a diffuse transition from low strain to high strain, fingers near the ideal angle form within the neck to minimize the strain energy associated with the incompatibility. Interestingly, Feng and Sun observed fingers that all pointed the same direction; whereas, the fingers on the left and right
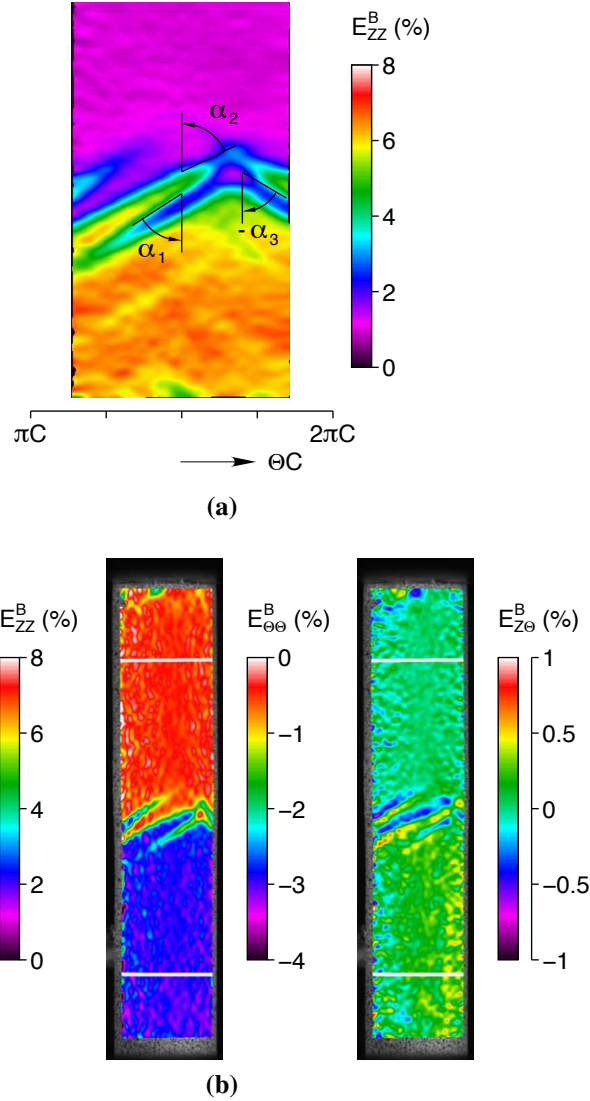
Figure 6.7 Experiment T1.(a) Magnified and unwrapped view of the "fingers" at time ③ of Fig. 6.6. (b) Surface strain fields (axial, hoop, and shear strain) from DIC at time ④.

side of our tube have positive and negative angles, respectively, resulting in a criss-cross pattern. While Feng and Sun's loading rate was similar to ours, the different observation may be due to different specimen shape (their dogbone versus our straight specimens), different onset of front propagation (their M first nucleated as a helix, then transformed into the finger morphology), different gage section dimensions (their $D/H = 13.3$ and $L/D = 23$, while our $D/H = 10$ and $L/D = 4.45$), different grips, and/or different load stack torsional rigidities. Other tension experiments on thin superelastic strips [111, 112] have also showed similar criss-crossing fingers before. They found that the occurrence of criss-crossing morphology was sensitive to the specimen length and the elongation rate, being more prevalent for short specimens (to minimize bending misalignment with the tensile axis caused by the small

axial kink across angled fronts) and very slow elongation rates (to minimize temperature gradients during exothermic/endothermic transformations). However, we performed another experiment (not shown here) on a longer tube specimen $L = 56.30$ mm ($L/D = 17.7$) which also resulted in similar finger crisscrossing. More data is necessary to determine exactly what scenarios cause or inhibit crisscrossing, but this is left for future work since it does not impact the current study.

Figure 6.7b shows a snapshot at time ④ of the tube surface strain field with respect to axial, hoop, and shear strain components (from left to right E_{ZZ}^B, $E_{\Theta\Theta}^B$, and $E_{Z\Theta}^B$). Note the change in color scale for each strain component. The hoop strain in the transformed M region (bottom half of the middle image) is like a reverse video image of the axial strain taken to negative strains. The shear strain field image shows a small positive shear strain of between 0.1 % to 0.4 % in the lower half (M region), as well as alternating stripes of about ±0.4 % across the fingers in the global transformation front.

6.3.2 Compression Results

Figure 6.5(b) shows the uniaxial compression response of a tube specimen, and the corresponding strain field contours are shown in Fig. 6.8. Again, $\bar{E}_{ZZ}^B$ is the axial strain from the DIC analysis averaged over the chosen gage length L_e, not the grip strain δ/L. High quality compression experiments of SMAs are quite difficult to achieve, and so, are much less prevalent in the literature than tension experiments. In this case DIC strain measurement was essential to successfully obtain accurate measurements. The grip strain measurement was contaminated by the specimen settling into the grips, the compliance of the grips, and the small friction between the specimen and the grips. In fact, even with careful alignment and attempts to avoid specimen settling by a pre-test elastic load-unload, the grip strain and $\bar{E}_{ZZ}^B$ differed by as much as 1.3% strain during some experiments.

While distinct transformation fronts in SMAs have been observed in tension using full field techniques, no such techniques have been used in compression to our knowledge. Due to the lack of a distinct stress plateau during isothermal $A \rightarrow M^-$ transformation, one expects that transformation fronts are not present in compression, and this is generally confirmed in the strain field images of Fig. 6.8, with one exception discussed below. The strain fields are nearly homogeneous during loading (images ①-⑦), aside from minor strain perturbations near the grips and minor axial strain fluctuations. The reason why tension exhibits strain localization, while compression does not, has been a long-standing open scientific question. Mao *et. al.* [75], however, recently provided a plausible explanation. Using electron backscatter diffraction on NiTi tubes, they found that grains favorably aligned for tension
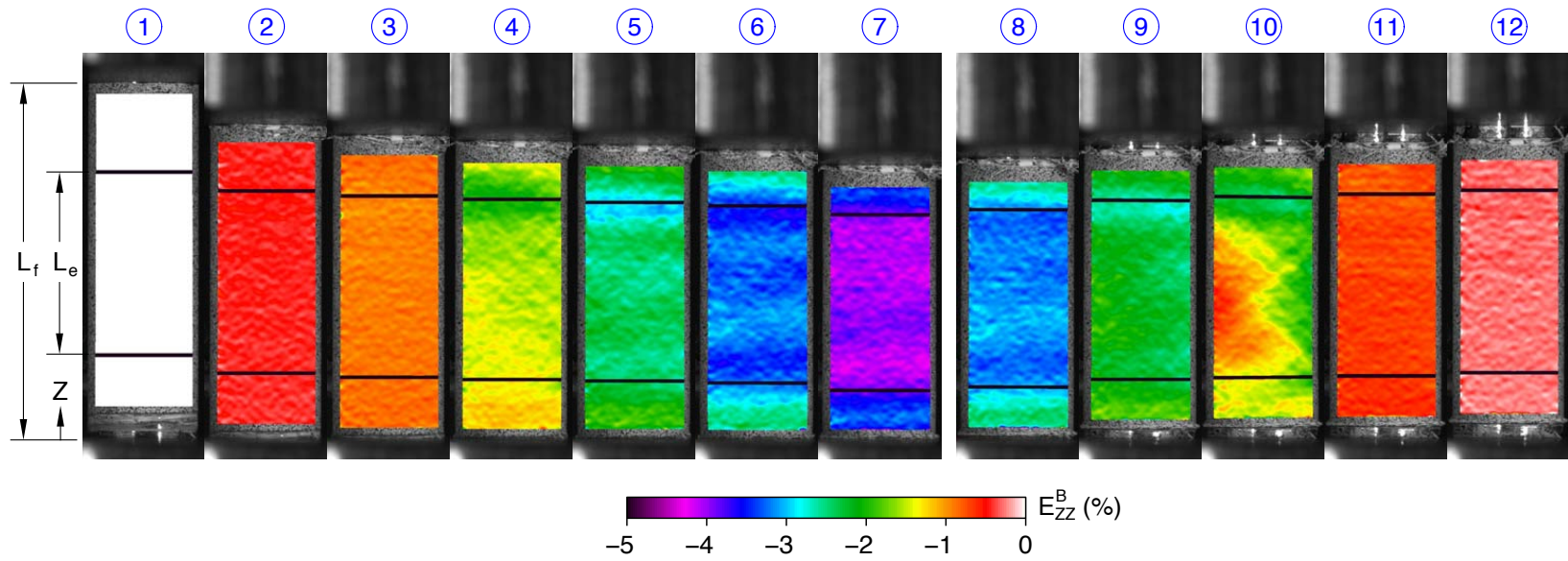
Figure 6.8   Experiment C1. Compressive axial strain field contours at times labeled in Fig. 6.5(b).

had a distribution of Schmid factors within ±8.7%, while the grains favorably aligned for compression varied by ±20%. They argued that a narrow distribution of Schmid factors leads to an auto-catalytic effect, where transformation in one grain causes neighboring grains to transform, leading to a macroscopic front. Conversely, a large distribution of Schmid factors means transformation is less likely to spread to neighboring grains without a large increase in stress, and this leads to more diffuse transformation involving non-adjacent grains.

Returning to our compression experiment, but now during unloading (images ⑧-⑫), the strain field is nearly homogeneous except for image ⑩ where the tube is slightly bent. The strain varies from −0.7% to −1.9% from the left to the right side of the specimen. Apparently, the tube buckled during mid $M^- \rightarrow A$ (reverse) transformation, which is an unexpected result and to our knowledge has never been reported before. The adjacent strain fields in images ⑨ and ⑪, however, are quite uniform, indicating that buckling is only a transient phenomenon. More precisely, we defined the tube as "buckled" when the difference in axial strain between left and right sides of the tube exceeded 0.375 % strain, using the full set of DIC data (not shown). Buckling occurred between $\bar{E}^B_{ZZ} = -2.2\%$ and −0.8%, which corresponded to when the average tangent modulus, $d\bar{\Pi}^B_{ZZ}/d\bar{E}^B_{ZZ}$, dropped below 2 GPa. At image ⑩ the average tangent modulus is only 1.1 GPa. The origin of this phenomenon is difficult to isolate, but we believe residual stresses induced during the $A \rightarrow M^-$ transformation (loading) delayed the onset of $M^- \rightarrow A$ transformation during unloading until the tangent modulus reached a sufficiently low value to trigger a structural instability. Nevertheless, the specimen reverted to a straight shape, and the final residual strain at zero load was quite small, $\bar{E}^B_{ZZ} = -0.03\%$.

6.3.3 Comparison of Tension & Compression Responses

The tension and compression behavior are directly compared in Fig. 6.9a, using absolute values of stress and strain. The lower portion of the plot shows two pairs of mechanical responses for tension and compression, respectively, with the previously presented tension/compression experiments (T1 and C1) shown by dotted lines and second tension/compression experiments (T2 and C2) shown by solid lines. The upper portion of the plot, using the vertical axis on the right, shows the magnitude of the average hoop strain, $\bar{E}^B_{\Theta\Theta}$, as a function of the average axial strain magnitude during the second set of experiments (T2 and C2 only). The second tension experiment and second compression experiment were performed (on separate new specimens) to characterize the behavior at larger strains, consistent with the bending experiments of the next section.
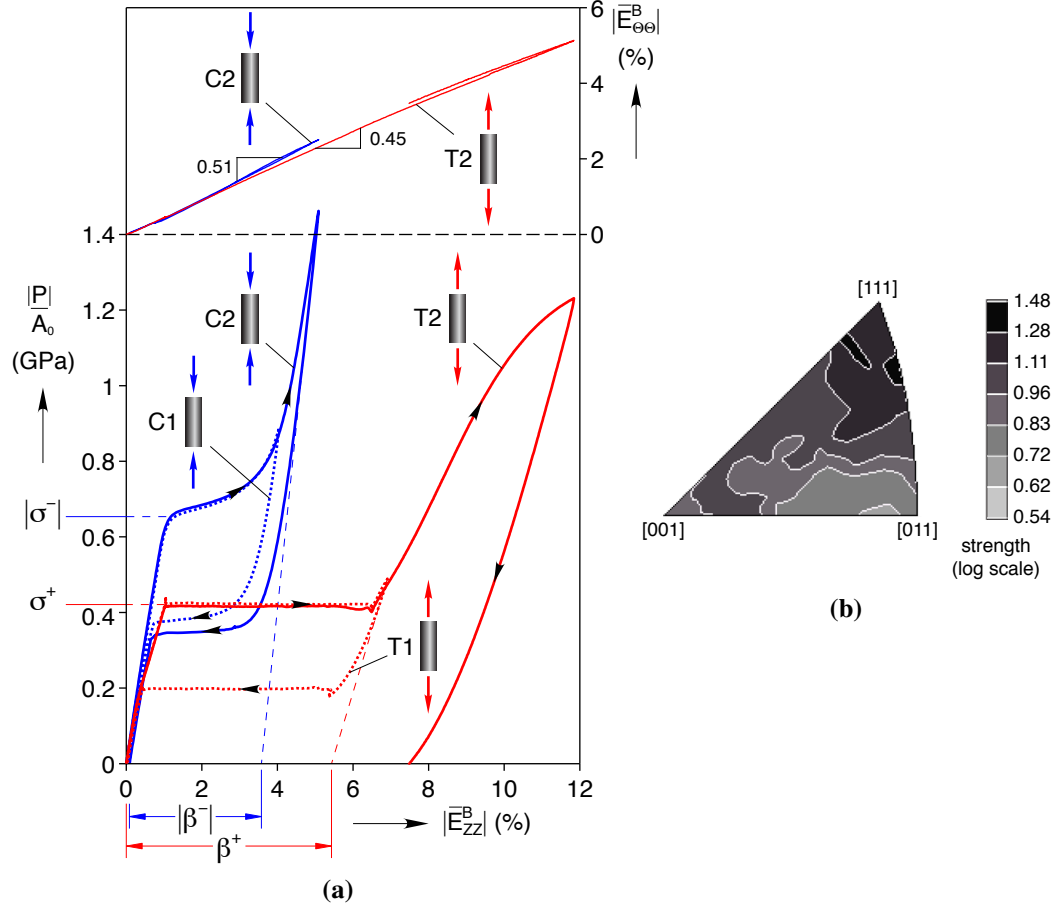
Figure 6.9 Comparison of tension and compression responses: (a) Lower plot shows four mechanical responses in tension (experiments T1 and T2) and compression (experiments C1 and C2) with magnitudes of transformation stresses and strains labeled. Upper plot shows the magnitude of the lateral (hoop) strain against the axial strain for tension experiment T2 and a compression experiment C2, with slopes indicating the measured Poisson ratios. (b) X-ray contour map, showing significant $\langle 111 \rangle_{B2}$ texture along the drawing axis of a similar tube (provided courtesy of K. Gall and J. Tyber, Georgia Institute of Technology).

One can see that the respective pairs of tension and compression responses agree quite well during the loading segments. There was one small deviation during the second tension experiment. Two fronts, rather than one, were observed during the $A \rightarrow M^+$ transformation, which caused the small dip in stress between $\bar{E}_{ZZ}^B = 5.5\%$ and 6.5% when the fronts neared one another and then coalesced. The first and second compression experiments, on the other hand, had similar uniform strain fields during loading.

The unloading responses of the second set of experiments are clearly different, since unloading commenced at much larger stresses. In the second tension experiment, the loop was not closed. A residual strain of 7.49% indicates the occurrence of significant plastic (slip) deformation and likely significant "locked-in" martensite (although we did not heat

the specimen to measure how much could be ultimately be recovered). The second compressive response, however, had only -0.09% residual strain after unloading, even after being subjected to a stress of -1.46 GPa! Nonetheless, comparing the unloading curve to the first compression experiment does show some signs of the extreme compressive stress during loading. First, the unloading $M^- \rightarrow A$ transformation stress was about 37 MPa lower (at -1.74% strain), indicating that a larger reverse driving force was needed to overcome locked-in martensite. Second, the transient buckling instability in the axial strain field was observed again when the tangent modulus dipped below 2 GPa, but this occurred between $\bar{E}_{ZZ}^{B} = -2.8\%$ and -1.0%, which is a 28% larger span than the first experiment. The increase supports our earlier hypothesis that the large compressive stresses during loading play a role in the buckling instability during unloading.

Since DIC provides all surface strain components, we also measured the lateral (hoop) strain $E_{\Theta\Theta}^{B}$. The upper plot of Fig. 6.9a provides the magnitude of the hoop strain averaged across the gage length L_e ($|\bar{E}_{\Theta\Theta}^{B}|$, right hand vertical axis) against the magnitude of the average axial strain $|\bar{E}_{ZZ}^{B}|$ (horizontal axis) for the second set of tension/compression experiments (T2 and C2). In the small strain limit, the ratio $v_{Z\Theta} \equiv -E_{\Theta\Theta}^{B}/E_{ZZ}^{B}$ is the Poisson's ratio, so the slope of the response curve $|\bar{E}_{\Theta\Theta}^{B}|$ versus $|\bar{E}_{ZZ}^{B}|$ gives an approximate Poisson's ratio, presuming the tube specimen is transversely isotropic about its centerline. The average lateral strain data from the two tension and compression experiments overlapped quite well, so only experiments T2 and C2 are shown here. The initial slope in experiment T2 is 0.45 up to about $\bar{E}_{ZZ}^{B} = 7.9\%$, where the slope changes to 0.39 as transformation is accompanied by plastic (slip) deformation. The compression experiment C2 has a slope of 0.45 until $|\bar{E}_{ZZ}^{B}| = 1.1\%$, where the slope changes to 0.51. A hysteresis in the Poisson's ratio exists between loading and unloading in both tension and compression (more noticeable in T2), probably since linear elastic deformation dominates the response during unloading, but the effect is rather small.

While the tension-compression asymmetry of drawn NiTi has been shown before, compression results are relatively rare in the published literature, so a quantitative comparison is worthwhile here. Initially the tensile and compressive linear elastic moduli match almost perfectly ($E_A = 65.3$ GPa), as one would expect from simple elastic deformation of the austenite lattice. After $|\bar{E}_{ZZ}^{B}| = 0.2$ % the tensile and compression responses start to deviate, since the small R-phase non-linearity in tension is absent in compression. As the strain exceeds $|\bar{E}_{ZZ}^{B}| = 1$ %, the tension/compression asymmetry becomes more pronounced. The $A \rightarrow M^+$ transformation (plateau) stress in tension is $\sigma^+ = 421$ MPa, and the $A \rightarrow M^-$ "plateau" in compression is $\sigma^- = -654$ MPa at its onset. Transformation strains were estimated by projecting a linear elastic tangent from the initial unloading response to the zero stress axis as

shown in Fig. 6.9a, and then subtracting the small amount of final residual strain. In tension the transformation strain is $\beta^+ = 5.43 - 0.03 = 5.40$ % (incidentally, quite close to the length of the plateau, 5.45 % strain) and in compression is about $\beta^- = -3.58 + 0.09 = -3.49$ %. Using a simple Gibbs free energy model (see Appendix B), the isothermal driving force for $A \rightarrow M$ transformation is linear in the quantity $\sigma\beta$. The model predicts transformation to occur at a constant stress, which is reasonable in light of our tension responses, but less so for our compression responses without true plateaus. Nevertheless, the model predicts that the ratio of tension to compression, $\sigma^+\beta^+/(\sigma^-\beta^-)$, should be near unity for experiments at the same temperature. Based on our measurements, the ratio is 0.996 which is consistent with basic thermodynamic theory.

The tension-compression asymmetry is generally attributed to the crystallographic asymmetry of the martensitic phase transformation. The tube drawing process textures the material such that the $\langle 111 \rangle_{B2}$ direction of the austenite lattice is well aligned with the longitudinal tube axis. Figure 6.9b is an X-ray map of a tube specimen[e] across the stereographic triangle that indeed shows a prevalent $\langle 111 \rangle_{B2}$ crystallographic texture aligned to the tube centerline. This texture allows us to approximate the tube as a single crystal to estimate the transformation strains in tension and compression. Many researchers use the set of observed 24 habit plane variants (HPV) of martensite [77] to model the superelastic behavior of SMAs (e.g. [47, 49, 87]). Using this theory and the experimental values of Matsumoto *et. al.* [77], we calculate the uniaxial Biot strains along $\langle 111 \rangle_{B2}$ to be 5.47 % in tension and -3.71 % in compression, which agree reasonably well with our measured values of 5.40 % and -3.49 %, respectively. Details of the calculation are provided in Appendix C.

6.4   Bending Experiments

In this section, we present two bending experiments (B1 and B2) in room temperature air, each performed on new superelastic tube specimens cut from the same lot as used in the previous tension and compression experiments. The setup used 4-point (pure) bending as previously described in Section 6.2.2, and specimen dimensions were given in Table 6.1. The end-rotations were controlled at constant, slow rates in both experiments.

Before presenting the experimental bending results and some analysis, a few preliminary

---

[e]The X-ray data was obtained on a tube specimen from the same manufacturer (Memry) of the same geometry, but from an older lot (# 358311) than the current lot (# 957152) used throughout this chapter. Some differences do exist in the mechanical responses between the two lots. In particular, tubes from lot # 358311 used in Churchill [27] had a 18 % shorter $A \rightarrow M^+$ plateau than the current lot # 957152. Based on this mechanical comparison, the strength of the $\langle 111 \rangle_{B2}$ texture may be, if anything, under-predicted by Fig. 6.9b for the current lot.

comments should be mentioned. Section 6.3 clearly showed that our NiTi tubes exhibit a significant degree of tension-compression asymmetry. Not only is the magnitude of the transformation stress larger in compression, but the strain localizes in tension, while in compression it does not. Both observations have implications for bending:

- *The neutral strain axis may deviate from the tube centerline.* As depicted in Fig. 6.10, we define the neutral axis (Y_0) as the location where the local axial strain is zero, $E_{ZZ}^B(X, Y_0, Z) = 0$. In pure bending the specimen has a zero net axial load. For conventional engineering materials that have symmetric tension-compression responses the neutral axis remains at the centroid of the cross section. However, for our NiTi tubes, the neutral axis must shift towards the compressive side to balance the distribution of tensile and compressive stresses in the cross section. This effect has been predicted by several SMA beam models (e.g. [33]). Experimentally, Rejzner *et. al.* [98] inferred the neutral axis position using strain gages on the top and bottom of a SMA beam, but here DIC allows Y_0 to be measured directly for the first time.

- *Plane-sections may not remain plane.* Under the classical Euler-Bernoulli beam theory assumption, the strain distribution across the diameter is $E_{ZZ}^B = -\kappa(Y - Y_0)$, where $\kappa \equiv d\phi/dZ$ is the referential beam curvature (as opposed to the strictly geometric curvature $d\phi/dz$), and Y is the distance from the centroid in the reference (straight) configuration. Note that the Biot strain gives a distribution that is strictly linear in Y, regardless of the magnitude of κ, unlike the Green-Lagrange strain that is quadratic [59]. This strain distribution is shown as the kinematically preferred strain profile in Fig. 6.10a. However, the fact that transformation tends to localize in tension suggests a different strain distribution, more like that of Fig. 6.10b. Intermediate tensile strains along the stress plateaus are associated with unstable material states (if otherwise unconstrained) which are largely absent in Fig. 6.6. The more compatible, kinematically preferred strain profile, however, requires strains in this unstable range. Thus, a competition exists between compatibility and local material stability, and one would expect an actual strain profile somewhere between the two extremes shown. Except for an isolated observation by Perry *et. al.* [89] where localized transformation was acknowledged during bending of a NiTi tube, the characteristics of NiTi localization in bending remains unexplored in the literature. Using DIC here, allowed bending strain profiles to be measured in NiTi for the first time and to observe how the material instability manifests in the presence of a significant lateral strain gradient.

In the following sub-sections, we first describe the single-cycle bend-unbend experiment (B1) taken to outer-fiber bending strains beyond the $A \to M^+$ and $A \to M^-$ uniaxial
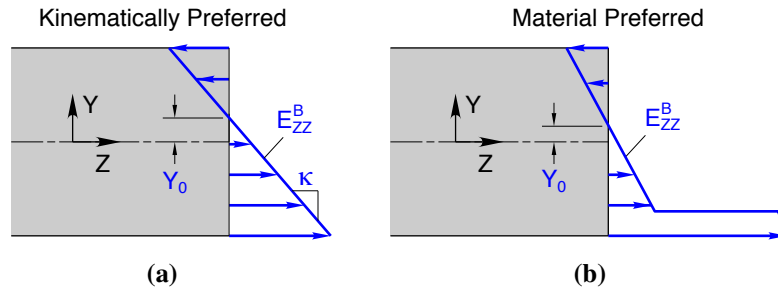
Figure 6.10 Schematics of two competing bending strain profiles.

plateaus. Comparisons are then made to this experiment of some potential simple bending models, based on the results of the previous tension and compression loading responses. This section ends with a description of the second bending experiment (B2), an incremental 5-cycle experiment with progressively larger rotation amplitudes within the range used for experiment B1.

6.4.1 Single-cycle Bending Experiment (B1)

The global bending response of the tube during a single load-unload cycle is shown in Fig. 6.11 (lower plot), along with the average position of the neutral axis (upper plot). The lower left vertical axis is the normalized moment MC/I, where M is the applied moment about the x-axis, I is the corresponding area moment of inertia of the cross section, and $C = D/2$ is the outer radius of the tube. The horizontal axis is the dimensionless curvature $C\overline{\kappa}$ averaged across the axial gage length (L_e = 9.58 mm) from the DIC data. The axes, MC/I and $C\overline{\kappa}$, where chosen as the classical formulas for the stress and strain at the outer fiber of a homogeneous, symmetric cross section, linear elastic beam with centroidal neutral axis. Berg [10] tested multiple wire diameters and found that these normalized quantities adequately removed the effect of geometry, despite the complex behavior of NiTi. The upper right vertical axis ($\overline{Y}_0/C$) in Fig. 6.11 is the normalized reference position of the neutral axis Y_0 averaged over L_e. The average neutral axis position at small curvatures is only lightly shaded, since the strains were too small to accurately measure $\overline{Y}_0$.

The circled labels in Fig. 6.11 correspond to the strain fields shown in Fig. 6.12 and 6.13 for bending (loading) and unbending (unloading), respectively. Note that the color scale is discontinuous at zero strain to clearly highlight the neutral axis in the strain field. The scallops in the strain field images at the top left and right (see Fig. 6.12) are dataless regions due to the rollers creating shadows on the specimen or obscuring the view of one of the DIC cameras. The thick black lines on the strain fields images of Fig. 6.12 and 6.13 are
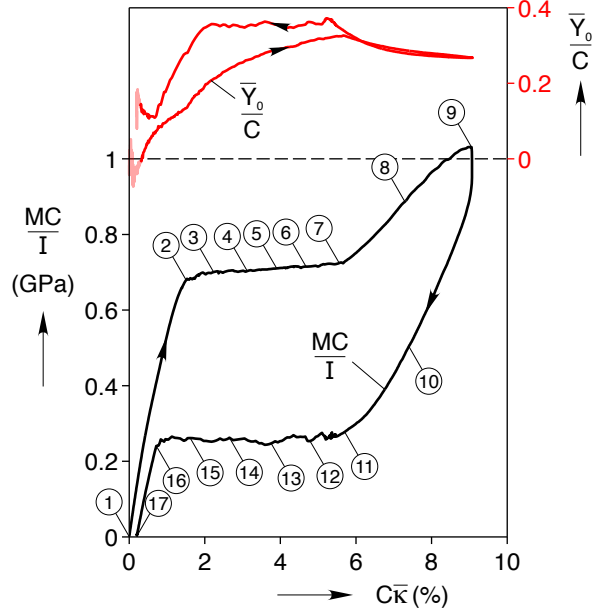
Figure 6.11 Experiment B1. Bending moment response (lower plot) and neutral axis (upper plot) versus average curvature for a single cycle.

the two positions (Z_1 and Z_2) where cross-section rotations (ϕ_1 and ϕ_2) were determined and then used to calculate the average curvature. The red and green lines on the strain field images in Fig. 6.12a correspond to the strain profiles shown in Fig. 6.12b. The black, red, and green lines appear curved because the strain fields and the lines were overlaid on images taken by camera 1 in Fig. 6.4a at 7.5° to the bending plane. Viewed normal to the bending plane, these lines are straight, as can be seen later, for example, in Fig. 6.14a. Note that the strain field images are overlaid on the deformed images of the tube by transforming to current coordinates (x, y, and z) in Fig. 6.12a, while the strain profiles are plotted with respect to reference coordinates (Y/C) in Fig. 6.12b. The strain profile predicted by classical Euler-Bernoulli beam theory is

$$E_{ZZ}^{\mathrm{B}}(Y) = -\bar{\kappa}(Y - \overline{Y}_0), \tag{6.4.1}$$

based on the measured average neutral axis ($\overline{Y}_0$) and average curvature ($\bar{\kappa}$). These are shown by blue, dashed lines in Fig. 6.12b for comparison to the measured local strain profiles.

Similar to the uniaxial responses, the moment-curvature response in Fig. 6.11 during loading has three regimes: an initially stiff segment (①-②), a more compliant ("plateau") region with a small positive tangent modulus (②-⑦), and a post-plateau stiff segment (⑦-⑨). Referring to Figs. 6.11 and 6.12 and stepping through the loading process in detail:

- ①-② The initial bending response is nearly linear, and as expected, the strain pro-

file is linear. The average neutral axis starts near the origin, but by ② has shifted upward (toward the compression side) to about $\overline{Y}_0 = 0.13C$, likely due to the R-phase nonlinearity on the tension side.

- ②-③ The global tangent modulus undergoes an abrupt reduction at ②, and six very small moment drops (upon close inspection) occur soon thereafter in the moment-curvature response that coincide with the six strain localizations seen in image ③. The green line intersects one of these fingers, so the green line's strain profile is non-linear on the tension side of the tube. Thus, plane sections clearly do not remain plane. The red line does not cut through one of the fingers, but it also deviates from $-\overline{\kappa}(Y - \overline{Y}_0)$, albeit in the opposite direction. This indicates a varying transformation rate at each axial location along the tension side. Close inspection at ② also reveals a kink in the evolution of the average neutral axis, after which it accelerates somewhat.

- ④-⑤ Further localizations appear, and two wedge-shaped regions develop on the tension side as localized strain regions coalesce. The average neutral axis position continues to shift upward, although the local neutral axis position has slight fluctuations near the apex of the wedge regions. Two, somewhat more diffuse, wedge shaped regions also appear on the compression side opposite the tension wedge regions. The green and red strain profiles deviate further from the blue, dashed line.

- ⑥ A third wedge forms on the tension side at the left, and the apex of the wedges have been driven nearly to the neutral axis. The red strain profile has a significant region of nearly constant 1.6 % strain ($-0.7 < Y/C < -0.1$), after which it begins to accelerate back towards the linear, blue, dashed line.

- ⑦ The tube nearly reaches the end of the compliant region in Fig. 6.11. Accordingly, only a small region of low strain remains at $Y = -C$, next to the righthand black line in image ⑦. At this point the average neutral axis is shifted upward to $\overline{Y}_0 = 0.32C$.

- ⑦-⑨ Soon after ⑦ the last region of low strain at $Y = -C$ disappears, and the moment response stiffens. By ⑧ the outer fiber strain on the tension side exceeds 8 %, and while the strain is still quite inhomogeneous, additional fingers have developed to fill in regions between the wedges. During ⑦ to ⑨ the average neutral axis has retreated somewhat toward the tube centerline. By ⑨ the average neutral axis reaches $\overline{Y}_0 = 0.27C$, and the green and red strain profiles have nearly converged to the blue, dashed line. One can also see that the tube gage length has shifted to the left in the strain field image ⑨, since the rollers allow additional tube length to be drawn in

(from the right in this case), but this does not adversely affect the quality of the data since DIC provides local strain and curvature measurement.

The response during unloading is similar to that of loading, but exhibits a large moment hysteresis and events generally occur in reverse order. The global moment-curvature response Fig. 6.11 also has three regions: a steep segment between ⑨ and ⑪, and serrated plateau between ⑪ and ⑯, and a final nearly linear unload segment after ⑯. Referring to Figs. 6.11 and 6.13 and stepping through the unloading process in detail:

- ⑨-⑪ Just after the end of loading, point ⑨, the end-rotations were briefly held fixed, and the normalized moment (MC/I) relaxes from 1.03 to 0.926 GPa as shown by the vertical segment in the moment-curvature response of Fig. 6.11. No change in the strain field was observed during this time. Soon after unloading commences, the moment-curvature response decreases in a monotonic manner with a shallowing tangent modulus. During ⑨-⑪, the strain field magnitudes decreases in a monotonic way, but otherwise the morphology remains relatively static. The average neutral axis position moves back upwards, retracing the path of the post-plateau loading response.

- ⑪-⑯ Shortly after ⑪ the unloading plateau begins in the moment-curvature response, and the average neutral axis position rises to a maximum (of the entire experiment) of $\overline{Y}_0 = 0.37C$. The moment plateau during unloading does not have a positive tangent modulus (as it generally did during loading), and it is accompanied by a more jagged response than occurred during loading (② to ⑦). The fluctuations in MC/I coincide with the disappearance of strain localizations in Fig. 6.13, and these happen in the reverse order that they were generated during loading. Although it may not be clear from the still images, a video of the DIC strain sequence shows that localizations vanish more abruptly during unloading than they had appeared during loading. The average neutral axis position remains relatively constant near $\overline{Y}_0 = 0.35C$ for most of the unloading plateau (unlike the monotonic increase during the loading plateau), at least until between ⑭ and ⑮ when it decreased steeply to $\overline{Y}_0 = 0.11C$ at ⑯. This time interval, from ⑭ to ⑯, corresponds to the disappearance of the final localized wedge regions in the strain field.

- ⑯-⑰ The final stage of unloading occurs as a steep linear segment of the moment-curvature response. The final residual curvature at zero moment is $C\overline{\kappa} = 0.19$ %. The fully unloaded strain image ⑰ shows a small residual lateral strain gradient with maximum outer fiber strains of about ±0.3 %.
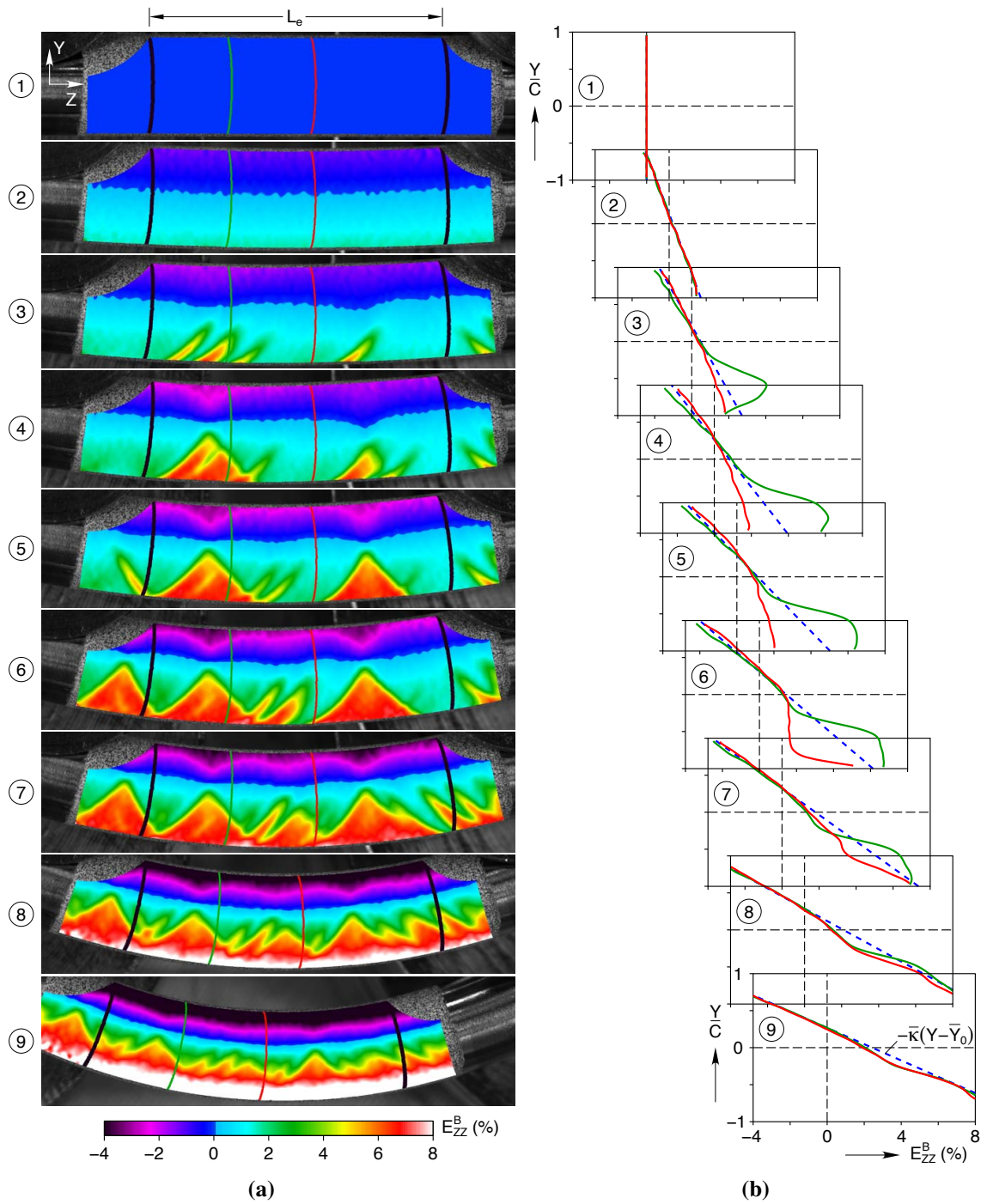
Figure 6.12 Experiment B1, loading. (a) Axial strain fields from DIC during loading corresponding to times labeled in Fig. 6.11, (b) Local axial strain profiles (solid lines) extracted from DIC compared against strain profiles predicted by beam theory (dashed lines), showing that locally plane sections do not remain plane.

145
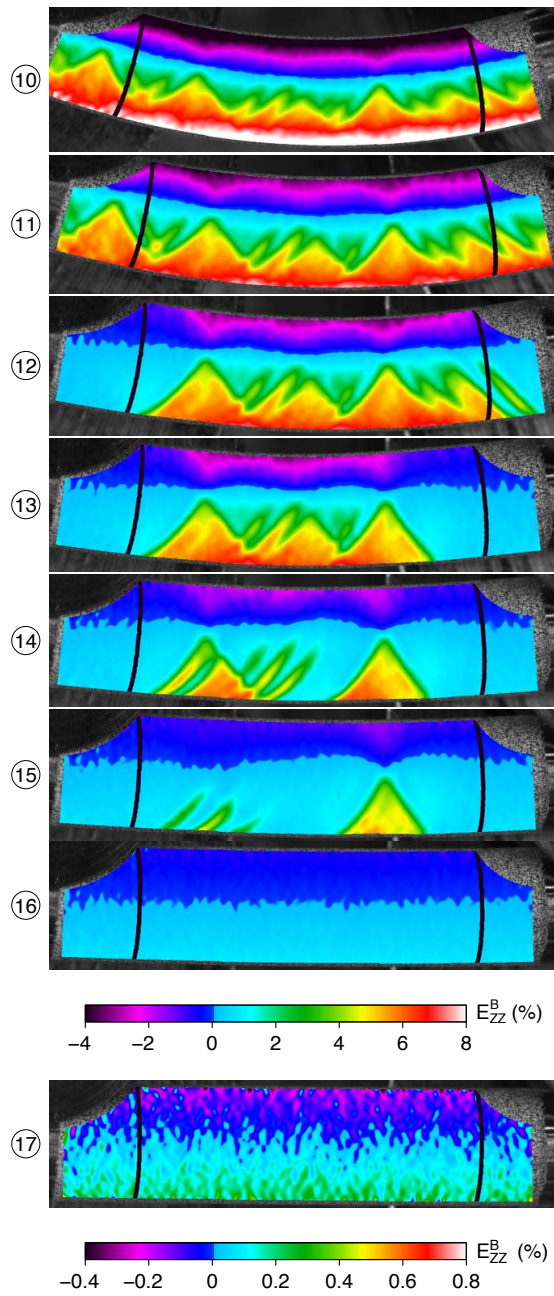
Figure 6.13 Experiment B1, unloading. Axial strain field images from DIC, corresponding to times labeled in Fig. 6.11, showing strain localizations disappearing in the reverse order that they were generated during loading. Note the magnified strain scale for the last image ⑰ after final unloading to zero applied moment.

Clearly, the strain localizations on the tension side and the absence of strain localization on the compression side are consistent with the unstable pure tension and stable (during loading) pure compression behavior shown in Fig. 6.6 and 6.8, respectively. The fingers look remarkably similar to those observed in uniaxial tension, and the wedges are an agglomeration of broadened fingers. Interestingly, the wedges on the tensile side bend the tube so far that it becomes kinematically necessary to form more diffuse wedges on the stable compression side as well. Close inspection of the raw images of the tube, as well as the three dimensional surface of the tube from the DIC analysis, however, did not reveal any localized wrinkling on the compression side.

While the localizations in tension and bending are qualitatively similar, there are quantitative differences. First, recall that finger angles in uniaxial tension ranged from 56.1º to 66º across 5 different images. For this bending experiment, using an unwrapped version of image ⑤, the low strain-high strain interfaces ranged from 44.5º to 70.5º to the tube axis. The center of this range is still close to our estimate of 56.1º for the ideal angle, but the spread is greater due to the more complex strain field during bending. Second, recall that in uniaxial tension the strain localizes at $\bar{E}_{ZZ}^{B} = 1$ %, yet in bending the strain profiles in ② reach 1.4% strain at $Y = -C$ prior to any strain localizations. Furthermore, the strain profile near the tube midspan (red line) shows little signs of localization even during ③-⑤. Instead, and the outer-fiber tensile strain at $Y = -C$ gets arrested at about $E_{ZZ}^{B} \approx 2$ %, while the average curvature of the tube continually increases (see lower end of the red strain profile in Fig. 6.12b). Later, this outer-fiber strain catches up to the one predicted by beam theory kinematics between ⑥-⑧.

The 2 % strain prior to localization is perhaps unexpected. The kinematically preferred strain gradient through the diameter of the tube likely suppressed the $A \rightarrow M^{+}$ instability, pushing the material to 2 % strain until there was sufficient driving force at that location to cause strain localization. One might conclude that austenite suffered 2% strain, meaning a stress at this location of roughly 65.3 GPa × 0.02 = 1.3 GPa (or about 1.05 GPa, if accounting for ≈ 0.4 % R-phase detwinning strain). This high tensile stress, however, is not reflected in the moment response between ② and ⑦. The discrepancy can be explained if $A \rightarrow M^{+}$ transformation can occur without localization in tension. It is known that some local pockets of $A \rightarrow M^{+}$ transformation do occur during tension prior to macroscopic strain localization. Brinson *et. al.* [15] observed martensite in isolated grains prior to localization using optical microscopy during tensile testing of thin NiTi strips, and Barney *et. al.* [7] found similar results by performing microdiffraction on samples cut from NiTi tubes. Accordingly, if isolated grains transformed prior to localization during our bending tests, the local strain could reach 2% without a huge increase in the local macroscopic stress.

This effect could have important implications for bending fatigue, where a material point might be forced to go through this process for millions of cycles in a bending application. Repeatedly suppressing the $A \rightarrow M^+$ instability in bending could cause a very different fatigue performance than what might be predicted from uniaxial data alone.

While the local strain profiles in Fig. 6.12b are certainly nonlinear, the average strain profile turns out to nearly linear if averaged over sufficient tube length. Figure 6.14a shows the axial strain field corresponding to instance ⑤ in Fig. 6.11. This is the same strain field as image ⑤ in Fig. 6.12a, except viewed normal to the bending plane and transformed back to the reference frame. Several straight vertical lines are overlaid on the axial strain field. The black line indicates the center of the gage length, while the other pairs of vertical lines indicate three averaging windows, whose widths are $\overline{L} = D$, $2D$, and $3D$. Figure 6.14b shows the strain profiles corresponding to the black vertical line (local strain profile) and the three averaging windows of Fig. 6.14a. Averaged over two diameters of length in the Z direction, the strain profile is nearly linear. Averaged over three diameters the average strain profile overlaps the beam theory prediction, $-\overline{\kappa}(Y - \overline{Y}_0)$, almost perfectly. In fact, a more judicious choice of averaging window is shown in Fig. 6.14c between the apexes of the wedge localizations, which has length of only $\overline{L} = 1.6D$. The corresponding average strain profile is shown in Fig. 6.14d, which matches the beam theory profile almost exactly, despite the fact that the local strain profile at the center of this window is very nonlinear since it intersects one of the protruding fingers. Thus, plane sections do not remain plane locally, but the average curvature $\overline{\kappa}$ correctly predicts the average strain gradient across the diameter of the tube. One should be aware, however, that the average curvature can over/under predict the local strain by as much as two-fold, as shown in the strain profiles of Fig. 6.12b.

Considering the overall evolution of bending strain fields, one might have expected the bending localizations to start at the rollers and propagate inward based on the front propagation in tension (see again Fig. 6.6). In fact, Kyriakides *et. al* [66] measured a flat moment-curvature response at the onset of plasticity in steel tubes with Lüders bands, and observed propagating regions of high curvature. In addition, several researchers [11, 17, 94] have postulated this sort of behavior for bending of SMAs, and have built models to simulate curvature propagation. In our case, the moment-curvature response is always at least slightly positive during loading, suggesting a structurally stable response, and curvature does not appear to propagate here. The stable bending response during loading is likely due to the stable compression response during loading, but it could also be caused by our short free length between the inner rollers, $L/D = 4.65$. (Note, the length of tube between the rollers is somewhat longer than it appears in Fig. 6.14a, since the cutouts in the strain field are not the actual roller locations. See instead ① in Fig. 6.12a where the rollers are outside the field of
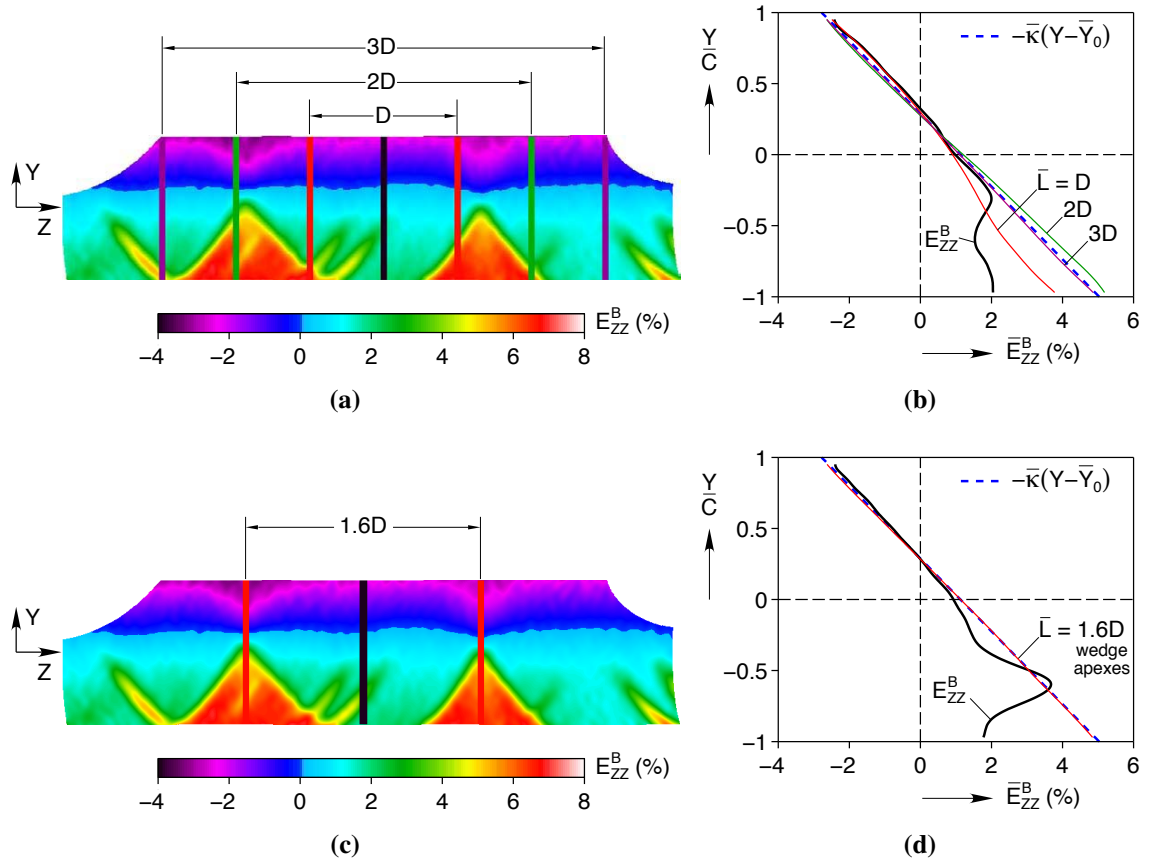
Figure 6.14 Experiment B1 at time ⑤: (a) Same axial strain field as image ⑤ in Fig. 6.12a, except shown normal to the bending plane and transformed to the reference frame. (b) Strain profiles at the gage length center (E_{ZZ}^B) and those averaged across $\overline{L}/D$ =1, 2, and 3 diameters of gage length corresponding to regions shown in (a). The dashed line is predicted by Euler-Bernoulli beam theory for comparison. (c) Same axial strain field ⑤, but showing an averaging region between apexes of wedge localizations. (d) Strain profile along the black line shown in (c) and the averaged strain profile in the region between wedge apexes.

view.) As shown in He and Sun [52], thin NiTi strips with large aspect ratios (length/width) exhibited front propagation in tension, but specimens with aspect ratios less than 1 had a stable global tensile response and no flat plateaus. It is possible that experiments using longer tube lengths than ours could exhibit propagating curvature.

While we did not observe curvature propagation during loading, there appears instead to be some axial periodicity to the more developed strain localizations. See, for example, the spacing between the two wedges in image ⑤ in Fig. 6.12 and the three wedges in image ②️ in Fig. 6.17b. The spacings are not the same due to the particular locations where localization began, but the size of the wedges do tend to set a characteristic length scale. This distributes the localizations somewhat evenly, which is why plane sections can be considered to remain

plane in a suitably average sense. Having said that, the bending response during unloading is reasonably flat between ⑪ and ⑯. Localizations disappear suddenly during this time, and the strain field sequence in Fig. 6.13 has some elements of curvature propagation in that strain localization disappears first near the two ends. Consistent with our earlier conjecture that the positive moment-curvature tangent modulus during loading is due to the stable loading response in pure compression, the faint evidence of curvature propagation during unloading may be connected to the flat $M^- \rightarrow A$ response during unloading in pure compression.

Another phenomenon that was observed during the bending of our tube was ovalization of the cross-section as shown in Fig. 6.15a. This is called the *Brazier effect*, which is the tendency of tubes, even those made of conventional materials, to ovalize in bending [14]. The cause can be explained with the help of Fig. 6.15b, using the co-rotated frame (x, y, z) introduced in Section 6.2.3. Under large bending deformations, the tensile/compressive normal force resultants on a cross section have a small, yet appreciable, component along the y-axis of nearby cross-sections. The force components on the tension (lower) and compression (upper) portions both point towards the neutral axis. Thus, they act to compresses the beam in the y-direction, causing thin-walled tube cross-sections to ovalize.

Figure 6.15a displays the ovalized shape of the tube outer diameter at ①, ⑦, and ⑨. Note, the shapes are not elliptical, due in part to anti-clastic curvature effects, but the tension-compression asymmetry may also have contributed here. These shapes were generated using the three dimensional DIC displacement data gathered on the $X < 0$ side of the tube. The x and y coordinates for each data point were averaged along the extensometer gage length L_e to generate the solid curves in Fig. 6.15a. Then the averaged DIC data was mirrored across the $X = 0$ plane and an 8-term Fourier series was fit in polar coordinates to each cross section to generate the dashed curves in Fig. 6.15a. This process was repeated for each DIC image during the experiment to find the current vertical deformed diameter (d) which was used to determine the evolution of the percent ovalization of Fig. 6.15c. Ovalization progressed right from the start of the experiment, but accelerated near ⑦ and reached a maximum value of $\left|\Delta d/D\right| = 8.2$ % at ⑨.

Some small error likely exists in the curves of Fig. 6.15a, since it was difficult to pinpoint the exact $x = 0$ location of the cross section. The tube moved small amounts, on the order of a few μm, in the X-direction during bending, and we did not have data around the full tube circumference to distinguish rigid body motion from deformation. We kept this error to a minimum, however, by extrapolating and integrating the hoop strain ($E^B_{\Theta\Theta}$) to fill in the missing surface coordinates at the top and bottom of the tube. This gave us a reasonable estimate for the rigid body motion of $x = 0$. Also, the uncertainty in the rigid body motion of
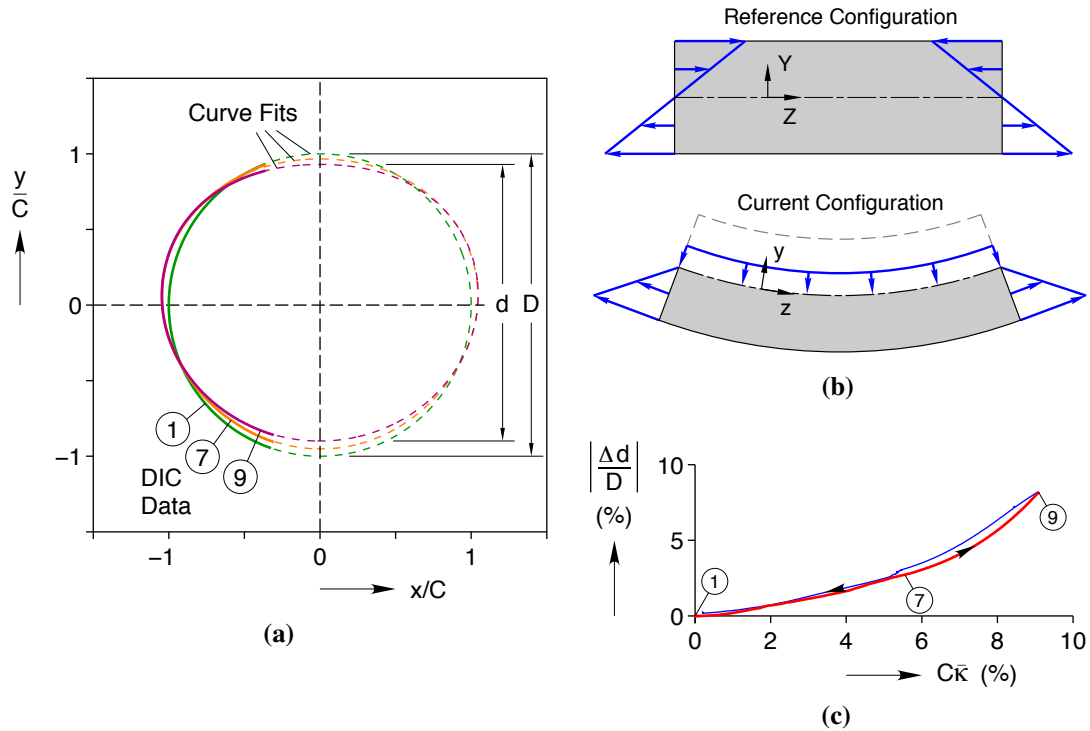
Figure 6.15 (a) Experiment B1. Measured (solid lines) ovalized cross-section at three times, ①, ⑦ and ⑨ of Fig. 6.11a, where $C\bar{\kappa}$ = 0 %, 5.56 %, and 9.04 %. Dotted lines are extrapolations of the DIC data. (b) Schematic of stresses (linear elastic behavior shown for simplicity) on an undeformed tube element, and on a deformed tube element with an additional cut along the neutral axis. (c) Evolution of percent ovalization versus average bending curvature calculated from the DIC data of Experiment B1.

$x = 0$ should have a minimal affect on the percent ovalization, since we defined ovalization as the change in diameter in the y-direction.

6.4.2   Bending Models

The question arises whether the previous uniaxial data can be used to predict the global bending response using simple bending theory, as is often done in engineering practice for SMA bending applications. The answer is yes, provided some care is taken, and in this sub-section we compare a few potential candidate models. This exercise also serves as consistency check between our pure-tension, pure-compression, and bending data sets.

Since plane sections remain plane when averaged over a few diameters of tube length, we investigated whether Euler-Bernoulli beam theory can predict the global bending response and the evolution of the average neutral axis based on our uniaxial data. For simplicity, we only attempted to capture the average moment-curvature response during loading, avoiding

for now unloading which would require a path-dependent constitutive model. Three bending models were generated from our uniaxial data:

(I) a symmetric model using only the tension data, mirrored for the compression side $(\Pi^- = -\Pi^+)$,

(II) an asymmetric model using the separate tension and compression data,

(III) an asymmetric pseudo-model that accounts for the Brazier effect on the bending moment. This last one is termed a "pseudo-model", since ovalization data from the bending experiment were used. It is not really a predictive model, but rather a consistency check on our data.

The assumed Biot strain distribution through the cross section was given in eq. (6.4.1). Treating the local bending stress as purely uniaxial,

$$\Pi_{ZZ}^B = \left\{ \begin{array}{llll} \Pi^+\left(E_{ZZ}^B\right) & = \widehat{\Pi}^+\left(Y;\overline{Y}_0,\overline{\kappa}\right) & : & E_{ZZ}^B \geq 0, \\ \Pi^-\left(E_{ZZ}^B\right) & = \widehat{\Pi}^-\left(Y;\overline{Y}_0,\overline{\kappa}\right) & : & E_{ZZ}^B < 0, \end{array} \right. \tag{6.4.2}$$

where functions Π^+ and Π^- use the respective averaged uniaxial loading responses from the high-strain tension and compression experiments of Section 6.3. The loading portions of T2 (895 data points) and C2 (255 data points) in Fig. 6.9 were linearly interpolated for Π^+ and Π^-, respectively. The small load drop at the end of the plateau of the solid red curve was ignored, since the drop is due to front coalescence and we neglect strain localization in these models.

Axial equilibrium is simply $P_z = 0$, and moment equilibrium is just a constant bending moment $M_x = M$, where M is the applied (external) moment and P_z and M_x are the respective force and moment resultants on a given cross-section of constant Z. This gives the following two equations that were used to solve for the two unknowns, $\overline{Y}_0$ and M, at each time in the loading process,

$$0 = \int_{A_0} \widehat{\Pi}\left(Y;\overline{Y}_0,\overline{\kappa}\right) \, \mathrm{d}A, \tag{6.4.3}$$

$$M = -\int_{A_0} Y\,\widehat{\Pi}\left(Y;\overline{Y}_0,\overline{\kappa}\right) \, \mathrm{d}A. \tag{6.4.4}$$

Integration was numerically calculated over the reference cross-sectional area with $\mathrm{d}A_0 = \mathrm{d}X\,\mathrm{d}Y$ by adaptive Simpson quadrature (quad function in Matlab 2010b [76]).

A comparison of the three models against the experimentally measured bending data (loading only) is shown in Fig. 6.16. Not surprisingly, the symmetric model (I) significantly
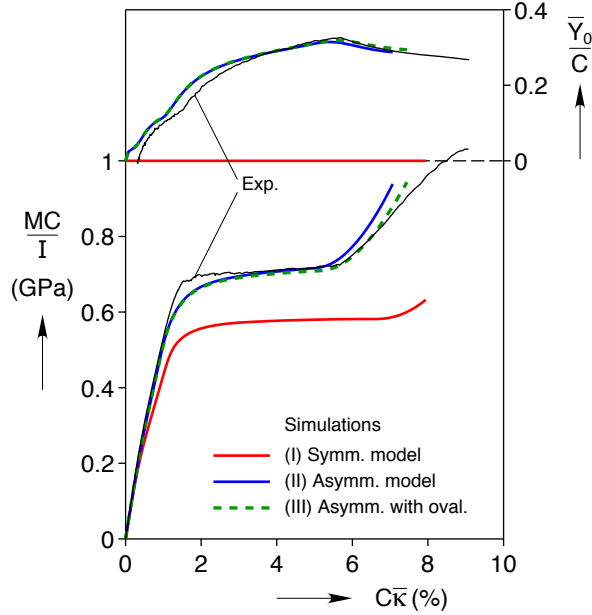
Figure 6.16 Comparison of measured bending response (Exp.) during loading to simulations using three bending models based on the uniaxial data (T2 and C3) of Fig. 6.9a. Model (I) assumes symmetric tension-compression behavior. Model (II) uses asymmetric tension-compression behavior. Pseudo-model (III) uses the asymmetric model but accounts for the measured average ovalization of the tube cross-section (see Fig. 6.15a).

under-predicts the overall moment response. This model predicts (1) a somewhat lower stiffness and a less linear response during the pre-plateau regime deviating from the experiment prior to $C\bar{\kappa} = 1.0\%$, (2) a normalized plateau moment of 577 MPa during $A \rightarrow M^+$ phase transformation, lower than the actual value of 712 MPa by about 19 %, and (3) a delayed termination of the moment plateau at $C\bar{\kappa} = 6.7$ %, compared to the measured value of 5.66 %. The only feature reasonably predicted by this model is perhaps the curvature value at the onset of the moment plateau ($C\bar{\kappa} = 1.4$ % predicted, versus 1.53 % actual). The symmetric model also predicts a neutral axis that remains at the tube centerline $Y_0 = 0$, which of course, is not the case in the experiment.

The asymmetric model (II), on the other hand, does match the experimental bending response rather well, both in terms of the average moment-curvature response and the evolution of the neutral axis. The initial pre-plateau response is matched very well up to an average curvature of about $C\bar{\kappa} = 1.0$ %. Thus, the slight R-phase tension-compression asymmetry at $\bar{E}^B_{ZZ} = 0.2\%$ in Fig. 6.9a is also confirmed in the bending data. The level of the moment plateau is matched almost exactly. Considering the very non-uniform strain fields in Fig. 6.12, the level of agreement (at least up to about $C\bar{\kappa} = 5.3\%$) is perhaps somewhat better than expected.

Certain details of the measured response are not captured, such as (1) the sharp onset of

the moment plateau which the model predicts a more gentle "knee" in the curve between $C\overline{\kappa}$ = 1.0 % and 3.1 %, (2) the modest over-prediction of the neutral axis location for average curvatures between 1.0 % and 3.1 %, and (3) the somewhat premature termination of the moment plateau at $C\overline{\kappa}$ = 5.3 % (compared to the measured value of 5.66 %). Regarding discrepancies (1) and (2), recall that the kinematically preferred linear strain gradient in the bending experiment delayed localization somewhat, which is not captured in the model. As a result, larger stresses were achieved on the tension side in the experiment before localization occurred, resulting in a sharper onset of the moment plateau and a delayed evolution of the neutral axis compared to the model predictions. As for why these discrepancies disappear beyond $C\overline{\kappa}$ = 3.1 %, we propose two possible reasons. First, the magnitude of the kinematically preferred strain gradient is larger and becomes more congruous with the strain profile preferred by the material. Second, once a localization has nucleated, it requires little additional stress to to grow, so the "overshoot" in the measured moment response becomes progressively reduced as the bending curvature becomes large and the model prediction catches up to the measured response.

Regarding discrepancy (3), the divergence of the moment prediction by model II above the measured one for $C\overline{\kappa}$ > 5.3 % appears to be due to the ovalization of the tube. As previously mentioned, the rate of ovalization gently starts to accelerate around $C\overline{\kappa}$ = 6 %, which is reasonably near $C\overline{\kappa}$ = 5.3 %. The pseudo-model (III) was created to take account for ovalization, and it validates our hypothesis as shown in Fig. 6.16. The DIC data (see again Fig. 6.15) was used to create a function $y = \hat{y}(Y)$ to link the current y position to the reference Y position. Then, equations (6.4.3) and (6.4.4) were modified as

$$0 = \int_{A_o} \widehat{\Pi}\left(\hat{y}(Y); \overline{y}_0, \overline{\kappa}\right) \, \mathrm{d}A, \tag{6.4.5}$$

$$M = -\int_{A_o} \hat{y}(Y) \, \widehat{\Pi}\left(\hat{y}(Y); \overline{y}_0, \overline{\kappa}\right) \, \mathrm{d}A, \tag{6.4.6}$$

to better account for the strain and moment arm at each point in the ovalized cross-section. We recognize that equations (6.4.5) and (6.4.6) involve both reference and current quantities, which is rather inelegant. This is done because we are using the measured ovalized cross section from experiment B1 in order to predict M and $\overline{Y}_0$ from the very same experiment, hence the name "pseudo-model". A true structural model would use equilibrium in the hoop direction to predict the ovalized shape of the cross section and use that to calculate M and $\overline{Y}_0$. In our case, material properties were not available in the hoop direction, which are likely quite different from those in the longitudinal direction due to the tube texture and would be difficult to obtain accurately. However, our pseudo-model satisfies our primary aim to verify

that our tension, compression, and bending data are consistent.

The pseudo-model quite nicely captures the termination of the moment plateau, as well as the initial stiffness of the post-plateau moment response. It does, however, start to diverge above the measured response when $C\bar{\kappa} > 6.6\%$. The cause is unclear, but the Brazier effect may again play a role as ovalization becomes extreme. The wall of the tube must locally bend and develop hoop stresses for the cross section to assume an ovalized shape. This more complex biaxial stress state could cause the material to soften in the axial direction, resulting in a lower than predicted moment. It should be mentioned, however, that many SMA bending applications use beams of solid cross-sections. If indeed the discrepancy is due to the Brazier effect, it is an issue only for hollow cross-section beams and would not be present for bending of solid cross-section beams. Furthermore, one should recognize this bending experiment is a rather extreme test of the material, considering that superelasticity is rarely used beyond strains of 6% in practice.

6.4.3 Incremental 5-cycle Bending Experiment (B2)

A second bending experiment (B2) was performed to characterize the incremental cyclic behavior. The moment-curvature response is shown in Fig. 6.17a for five successive cycles, each taken to progressively larger maximum curvatures. The five circled numbers correspond to the strain field images in Fig. 6.17b at the maximum curvature for each cycle. For convenience during this longer bending experiment, the average strain rate at the outermost tensile fiber was about $\pm 4 \times 10^{-5}$ s^{-1}, twice as fast as in experiment B1. The rate $\pm 4 \times 10^{-5}$ s^{-1} is still sufficiently slow to be considered a quasi-static, isothermal experiment. The strain rate sensitivity in bending is far less than in uniaxial tension, since in tension the latent heat is concentrated at the front, while in bending the latent heat exchanges are spread out along the length of the tube and only the outermost tensile fiber experiences the maximum global strain rate. This was verified by overlaying the outer envelope of this moment-curvature response (B2) and the response from experiment B1, which showed a negligible difference.

The moment-curvature data in Fig. 6.17a shows several cyclic shakedown features similar to that seen during cyclic loading of NiTi in unaxial tension:

- The stress at the onset of $A \rightarrow M^+$ transformation shifts downward with each cycle, i.e. exhibits (transformation) cyclic softening, with the largest changes seen during the first few cycles.

- Previous maximum strain points during $A \rightarrow M^+$ are "remembered". The $A \rightarrow M^+$ response in a subsequent cycle rises to meet these stress-strain points of the previous

cycle. (Although not done here, if reloading commenced before complete $M^+ \to A$ transformation, i.e., within the unloading plateau, these "turn-around" points would also be remembered and would affect the response of subsequent unload cycles.)

- The unloading plateau stresses during $M^+ \to A$ transformation decrease slightly with cycles when unloading begins from within the plateau region. The unloading plateau stresses are reduced more dramatically when unloading starts from points beyond the initial loading plateau.

These are all generally related to micro-plasticity that occurs predominantly during each high stress $A \to M^+$ transformation cycle which tends to create residual stress fields that "lock-in" martensite. Previous $A \to M^+$ cycles reduce the energy barriers for subsequent $A \to M^+$ transformations, allowing it to occur at progressively lower stresses (reduced thermodynamic driving force) during loading. Previous $A \to M^+$ cycles, however, increase energy barriers for reverse $M^+ \to A$ transformation, thereby requiring progressively lower stresses (larger reverse driving force) than before for the reverse transformation during unloading.

The strong strain gradient in bending causes material points at different Y locations to follow distinctly different stress-strain paths. Material points near the neutral axis, for example, only undergo partial transformations and some points nearest the neutral axis do not transform at all. For example, Atanackovic and Achenbach [5] used a model to show that the maximum stress magnitude in the cross section of an SMA beam during unloading can occur far from the outer fiber, similar to what can occur in reverse loading of a plastically bent bar of a conventional metal. Raniecki *et. al.* [96], in particular, modeled of the effect of SMA hysteresis in bending. Both studies predicted that the unloading moment "plateau" height is lower if the beam is bent to a greater maximum curvature. We see some evidence of that here, with the most prominent effect seen during cycles 4 and 5 where the outer fiber strains have been driven high/low off-scale in the strain images of Fig. 6.17b (well below -4% in compression and above 8% in tension). Thus, plasticity at the outer fibers likely contributes to a lower unloading moment plateau.

Under an incremental cyclic history, the shakedown response of bending is similar to the interesting staircase-like response found in tension of NiTi wires (see, for example, Fig. 17 of [105]). The loading plateau here is not truly flat so the effect is not as pronounced, but the same phenomenon is apparent in Fig. 6.17a. As seen in Fig. 6.17b, the wedges and fingers of high strain visible in one cycle appear in the same locations during the next cycle (and the sequence is even more obvious in a video of the full set of DIC strain images). The small moment drops associated with localization events also occur at nearly the same values of $C\bar{\kappa}$
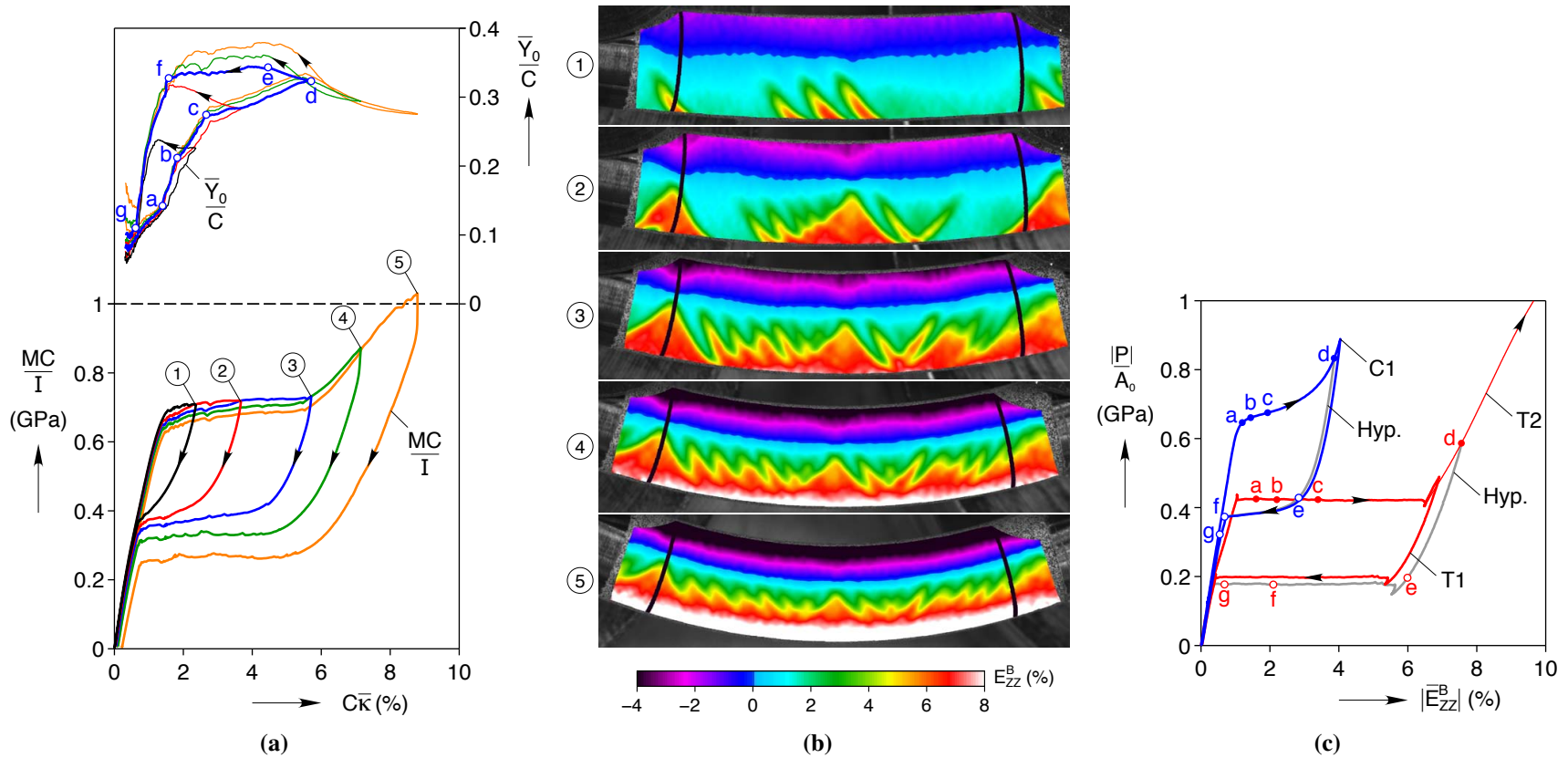
Figure 6.17 Experiment B2. (a) Bending moment (lower plot) and neutral axis position (upper plot) versus average curvature for incremental cycling, and (b) corresponding axial strain field images times labeled in (a). Each image was taken at the maximum curvature for that cycle. (c) Predicted outer fiber stress-strain states during cycle 3, showing corresponding points to those of the upper plot of (a).

each cycle during loading. In other words, if one were to bend a specimen repeatedly to the average curvature of point ②, only the material where the strain localizes in image ② would experience shake down and the moment at the onset of the plateau would decrease on each cycle. Subsequent bending to larger curvatures would require an increase in moment up to the original value to create localizations in other areas. Accordingly, each labeled point in Fig. 6.17a is a moment-curvature point that is crossed during the next cycle.

The movement of the neutral axis is also rather interesting in this cyclic experiment. Focusing first on loading only, the upper plots of Figs. 6.11 and 6.17a both show three stages of neutral axis movement corresponding to the three stages in the moment response. The neutral axis first moves up due to the R-phase non-linearity in tension. Once localization and the moment plateau begins, the neutral axis moves up more rapidly due to the $A \rightarrow M$ tension-compression asymmetry. When the moment response stiffens up again (post-plateau), the neutral axis moves back down since the tension-compression asymmetry is reduced as the tension side reaches high stresses in its post-plateau regime. Next, following the paths of $\overline{Y}_0$ during unloading in the upper plot of Fig. 6.17a, $\overline{Y}_0$ initially continues to move upward in all five cycles. For cycles 3, 4, and 5, $\overline{Y}_0$ reaches a relatively constant value during much of the moment plateau, but then drops steeply before the end of the moment plateau along a seemingly canonical line common to all unloading cycles. For cycles 1 and 2, no plateau exists in the $\overline{Y}_0$ movement, instead just reaching a local maximum then dropping steeply once it reaches this canonical line.

To explain the evolution of the neutral axis during a load-unload cycle, it helps to focus on just cycle 3 where the maximum curvature coincided with the end of the loading plateau, which should be relatively free of the significant plasticity effects inherent in the later cycles that were taken well into the post-plateau regime. The path of the neutral axis during cycle 3 is shown in the upper plot of 6.17a by the bold line and interesting points are labeled (*a* to *g*). Using the measured values ($\overline{Y}_0, \overline{\kappa}$) and eq. (6.4.1), the average outer fiber strains at $Y = \pm C$ can be estimated and mapped to stresses on the corresponding uniaxial responses. These points are shown on the uniaxial data in Fig. 6.17c. The maximum strains at *d* do

Table 6.2 Estimated stresses at selected points during cycle 3 of Experiment B2

		Stresses (MPa)						
		a	*b*	*c*	*d*	*e*	*f*	*g*
tension side	$Y = -C$	425	425	425	587	197	177	177
compression side	$Y = C$	-648	-661	-675	-833	-429	-374	-322
asymmetry ratio	$\lvert\Pi^-\rvert/\Pi^+$	1.52	1.56	1.59	1.42	2.18	2.11	1.82

not exactly correspond to the maximum strain for those uniaxial experiments, so estimated (hypothetical) unloading responses are shown by the gray lines. Table 6.2 provides the estimated values of outer fiber stresses at all these selected points during cycle 3 of Experiment B2, as well as the ratio of magnitudes of compression to tension stresses. While the neutral location depends on the integral of all material points in a cross-section, the extreme values do give a sense of the tension-compression asymmetry and the ratios indeed follow the trends of the neutral axis locations.

- (a to c) During loading, the neutral axis moves rapidly upward through points a, b, and c, which all correspond to $Y = -C$ states along the upper plateau of the tension response. Point a, when the neutral axis first accelerates upward, corresponds to the initial knee of the compression side ($Y = C$) uniaxial response. Point c, where the neutral axis slows its upward motion, corresponds to when the compression side reaches its minimum uniaxial tangent modulus.

- (d to e) Unloading begins at point d, and both the compression and tensile sides have reached stress states in their post-plateau responses. The neutral axis continues to move upward between points d and e, during which time $Y = \pm C$ points unload rapidly.

- (e to f) Point e, where the neutral axis stops moving upward, corresponds to the beginning of both compression and tension lower stress plateaus for the outer fiber locations. Between e and f the neutral axis remains relatively static.

- (f to g) Point f is where the neutral axis starts its rapid retreat downward, and this corresponds to the end of lower stress plateau on the compression side. The tension side is still on the lower stress plateau, and does not reach its end until about point g. During f to g, the tension side stress does not change while the compression side rapidly unloads along its final linear elastic response. The tension-compression asymmetry is quickly reduced during this time, which explains why the neutral axis moves back downward so rapidly.

Thus, the canonical line seems to exist whenever the tension side is still midway along its lower stress plateau and the compression side has already traversed its lower stress plateau and is unloading along its final unloading segment.

Finally, for cycles 4 and 5 during unloading it is interesting that the tube unloads to $C\overline{\kappa} = 6\%$ (near point d) before the hysteresis in $\overline{Y}_0$ becomes significant. This is because in the post-plateau regime the change in stress-strain tangent modulus from loading to

unloading is roughly the same for tension and compression. It is only when the outer fibers reach the $M \to A$ plateaus in tension and compression, that the unloading versus loading behavior is substantially different.

In closing, none of the SMA bending models in the literature capture the localizations shown in Fig. 6.17b, which is understandable since the tensile instability makes simulations significantly more difficult. However, if one wishes to understand the material response during multiple partial superelastic cycles, tracking strain localizations becomes important. We note that several studies have shown that even uniaxial cyclic behavior of SMAs is quite complex. For example, Iadicola and Shaw [57] cycled superelastic NiTi wires in tension between maximum and minimum strains within the $A \to M^+$ plateau, causing the stress to shake down and transformation fronts to sweep back and forth in the same region on the wire. Thus, even for simple tension histories, different material points experience different cyclic histories. Those in the propagating front region experience many transformation cycles, but those outside these regions see perhaps only one transformation cycle. If the elongation subsequently exceeds the previous maximum elongation, and a front must pass through relatively virgin material, the stress jumps back up to the virgin upper plateau level. In fact, during unloading beyond a previous minimum strain (turnaround) point, a significant energy barrier is encountered, current $M^+ \to A$ fronts are momentarily halted, and the stress drops abruptly and then jumps up again to join the virgin unload plateau as the material nucleates new $M^+ \to A$ fronts to continue the reverse transformation. Clearly, modeling of SMA cyclic behavior, even in the simplest context (uniaxial tension), is a challenging task. As we have shown, a simple change in the deformation mode (from uniaxial loading to bending) raises a number of new open scientific questions about the precise causes of (perhaps unexpected) phenomena in the structural response. It is fair to say, much work needs to be done to better understand the phenomena in deformation modes other than tension in order to develop modeling tools for designers and application engineers that can be used with confidence. Thus, a definite need exists for more high-fidelity experimental data on the various structural forms of SMA to help guide and validate these efforts. The few experiments presented herein are just a beginning attempt to fulfill that need, and further experiments are planned for the future.

6.5   Summary & Conclusions

Bending is a fundamental deformation mode of practical importance for superelastic SMAs, but there are few pure bending experiments in the literature and none that are directly

compared to pure tension and compression responses on the same material. We performed isothermal experiments on superelastic NiTi tubes in tension, compression, and large rotation, pure bending using custom-designed fixturing and stereo DIC to quantify the local strain field and eliminate grip effects. The important observations are as follows:

- Localized propagating transformation fronts were observed in uniaxial tension, but not in uniaxial compression. Strain fields in tension showed macroscopic transformation fronts that consisted of criss-crossing fingers of localized strain, largely consistent with previous observations by other researchers, but DIC provided some quantitative details not measured before. Strain fields in compression were largely uniform, except for some transient buckling during unloading (reverse transformation) which we have not seen reported before.

- The strain fields in bending contained localized strain on the tensile side, but no such localizations on the compression side of the tube. Localization regions started as fine angled fingers that eventually coalesced into wedge regions distributed along the tube length. Due to strain localizations, plane sections clearly did not remain plane locally, causing Euler-Bernoulli beam theory to under/over predict the local strain by as much as 2×. However, if the lateral strain profile is averaged over a few diameters of tube length, then Euler-Bernoulli assumptions are reasonable in an average sense.

- The strain on the tension side reached as high as 2 % in some areas along the tube prior to localizing. This is twice as high as the strain required to nucleate a transformation front in pure uniaxial tension.

- Using the uniaxial tension/compression data as inputs, Euler-Bernoulli beam theory successfully captured the measured moment-average curvature response and neutral axis evolution during loading up to the end of the moment plateau, provided tension-compression asymmetry was included. If additionally, the Brazier effect (tube ovalization) was accounted for, the agreement could be extended somewhat further beyond the moment plateau. Thus, despite the existence of strain localization and the local highly non-linear lateral strain profiles in bending, one can still achieve reasonable global moment-curvature predictions by suitable homogenization of the strain fields along the axial (fiber) direction.

These observations have several implications for further research and device applications.

(1) In many practical situations the moment is not constant along the length of a beam. A small moment gradient could lead to a region of high curvature propagating along the

length of the beam as the loading is increased. With localized self heating, three-point bending experiments, for example, could lead to interesting rate effects.

(2) The kinematic constraint of a constant strain gradient in bending is at odds with a localized strain distribution (non-linear strain gradient) created by the material instability. This results in an energetic competition between preferred bending kinematics and localized kinematics, and the material achieves a compromise through a complex morphology of localization (fingers and wedges). A solid cross section beam would strengthen the kinematic constraint and perhaps result in more diffuse localizations or a different morphology from the ones seen here.

(3) Strain localization likely has important implications in cyclic shakedown and fatigue, since local strain levels are relatively uncontrollable by remote boundary conditions. Furthermore, the constrained kinematics of bending delayed localization until tensile strains reached 2 %, a full 1 % strain beyond the onset of localization in pure tension. Such suppression of the $A \rightarrow M^+$ instability during bending could lead to very different fatigue performance than what might be predicted from uniaxial data alone. NiTi is frequently used in implanted medical devices where it must survive millions of superelastic sub-cycles. As such, NiTi fatigue has been heavily studied and several investigators have reported strangely non-monotonic constant life curves as a function of mean strain (Goodman diagram) in bending (see Adler *et. al.* [2] for a review). We suspect this strange behavior could be connected to the localizations found here in bending, although most bending-fatigue experiments are done on solid cross-section specimens that could exhibit a different localization morphology than the ones in our tubes.

Finally, we would like to again emphasize that transformational strain localization, now well known to occur in tension of NiTi, can also occur in bending. Strain localization may be ignored to predict the global mechanical behavior for many situations, but this should be done with caution. Localization plays an important role in the details of the strain field and the cyclic histories of various material points may be quite different. This will likely have a strong influence on shakedown evolution and eventual fatigue.

Chapter 7

Summary and Conclusions

7.1 Summary

This thesis presented a series of detailed experiments on two NiTi cable designs and NiTi tubes. The primary goals were to understand how NiTi performs in a hierarchical structure and how the material responds to some of the deformation modes in that structure. The two cable designs, a traditional 7×7 cable and a layered 1×27 cable, exhibited a wide range of nearly isothermal behaviors and rate dependent phenomena. Many of these behaviors were explained using simultaneous IR and DIC measurements, along with the responses of each cables' subcomponents. Also, NiTi tubes were characterized in tension, compression, and bending to guide future NiTi constitutive modeling efforts for the eventual simulation of SMA cables.

First, the simultaneous IR and DIC experimental setup was described and demonstrated on a superelastic (SE) wire in tension. After explaining the fundamentals of DIC, the details of specimen preparation, optical camera adjustment, lighting, and DIC post processing were reviewed. Along the way, a number of practical recommendations were provided to obtain accurate measurements. To demonstrate the setup, a SE wire was cycled 25 times in room temperature air, causing typical superelastic shakedown, while DIC and IR measurements tracked localized transformation fronts. As cycling progressed, changes in the wire's tensile stress were related back to features in the strain and temperature fields. Observations such as grip slippage, front nucleation, front speed, and front thermal interaction all played roles in the stress history. In general, the effects all correlated well with the well-known cyclic behavior of NiTi wires. Thus, the setup was confirmed to be operating properly in the simple case of a wire before moving on to the more complex cables.

Second, the nearly isothermal responses of the 7×7 and 1×27 cables were compared. The 7×7 cable performed similar to wires pulled in parallel due to the shallow helix angles of its construction, while the 1×27 was much more compliant, hardly resembling the uniaxial tensile response of its core wire. Dry and lubricated cables of each design were also tested,

163

showing that kinetic friction had a negligible effect, and permitting the focus to remain on dry cables for the remainder of the thesis. Two detailed, dry cable, experiments revealed further differences between the two designs. Global phase transformation fronts, made up of many little fronts in each of the wires, were detected in the strain and temperature fields of the 7×7 design. As these global fronts propagated along the specimen, sections of the cable rotated about the tensile (z) axis, despite being rigidly clamped at the grips. Restricting the rotation at the ends caused a reaction torque, which exhibited an interesting non-monotonic loading path. By contrast, the 1×27 design lacked transformation fronts and did not rotate appreciably. These observations were generally attributed to the larger helix angles in the 1×27 design, which cause a greater degree of torque and bending in the wires, thus stabilizing the response. The torque was also different: monotonically increasing in a stair step like fashion during loading. After later testing of the subcomponents of the 1×27, the stair steps were found to be caused by each layer of the 1×27 transforming at different global strains.

Third, subcomponents were harvested from the 7×7 and 1×27 tested individually at nearly isothermal elongation rates. As might be expected from the small helix angles, the core wire, core strand, and full 7×7 cable had qualitatively similar mechanical response curves, but small differences in plateau height and length did exist. The 1×27 subcomponents, on the other hand, were all significantly different. From the core wire to the full cable, each subcomponent consisted of a new layer of wires with a bigger helix diameter and bigger helix angle magnitude, meaning each subcomponent was more compliant than the one before it. Furthermore, the helix angle switched sign with each new layer, and accordingly, so did the reaction torque. Changes in the reaction torque gave a glimpse of the contribution of each individual layer, but subtracting the mechanical responses was shown to generate useful approximations of the response of each layer in isolation. The validity of this approach was confirmed by two observations. (1) After the subtractions, changes in the axial load and the reaction torque due to phase transformation occurred at the same laser extensometer strains, whereas before they did not. (2) Transformation activity in the DIC derived strain fields correlated well with the changes in the subtracted mechanical response, whereas the changes in the un-subtracted response did not. Thus, in the absence of direct measurements of a single helix wrapped around a rigid rod, the subtraction technique provided useful data to explain the observed behavior and likely guide future SMA cable design.

Fourth, motivated by the potential SMA cable applications of shock absorption and vibration damping, an elongation rate study was performed. The cables and their subcomponents were subjected to global strain rates ranging from 10^{-5} s^{-1} to 10^{-2} s^{-1}. While the isothermal

behaviors of the 7×7 cable and its subcomponents were similar, the non-isothermal, rate dependent, behaviors were significantly different. Most strikingly, the $A \rightarrow M^+$ loading plateau of the core wire became progressively higher at higher elongation rates, showing serrations at 10^{-2} s^{-1}, but the 7×7 cable axial load during transformation simply increased its slope at higher rates. This difference was traced back to front propagation in the two structures. At the elongation rates tested, the core wire fronts propagated with little thermal interaction between fronts for some length of time, causing the axial load to stay somewhat constant. The cable axial load continued to rise throughout because the fronts initiated at wire-to-wire contact points all along the cable and, being so close to one another, thermally interacted immediately upon propagation. Thus, even when the wires in a cable are predominately in tension, the strong thermomechanical coupling in SMAs can manifest itself in unexpected ways in a cable design. Conversely, the wires in the 1×27 and its subcomponents experienced torsion and bending in addition to tension, and they were shown to be far less rate sensitive than the 7×7 design. It was argued that the reduced rate sensitivity was due to the lack of transformation fronts, reduced thermal inertia, and a layered construction that temporally spread out the latent heat release. These results demonstrate that a cable's design can have an impact on not only its isothermal response, but also on its behavior at the moderately high strain rates likely to be seen in service.

Finally, any future effort to model SMA cables will require a material model that had been validated against tension, torsion, and bending experiments. Unfortunately, high quality experiments in strain states other than pure tension are rare in the published literature. To start filling this void, tension, compression, and bending experiments were performed on NiTi tubes. Tubes were selected instead of thin wires to avoid a number of experimental difficulties. Even with the larger diameter tubes, however, custom designed fixturing was necessary to suppress buckling in compression and to avoid undesirable axial loads in large rotation bending. As has been previously observed in textured NiTi, the tubes exhibited a significant degree of tension-compression asymmetry, with higher transformation stresses and lower transformation strains in compression than in tension. In addition, DIC revealed phase transformation fronts in tension, but no fronts were seen in compression. Consistent with our tension and compression results, bending resulted in a stiff-compliant-stiff response and caused the neutral axis to shift away from the centroid of the cross section by roughly a third of the tube outer radius. Furthermore, strain localizations were observed on the tension side, while mostly uniform strains were measured on the compression side. Detailed analysis of the localizations revealed that plane sections did not remain plane during the phase transformation, often over or under-predicting the strain by as much as two times. The kinematic assumptions of Euler-Bernoulli beam theory did hold, however, when the strain

was averaged over the gage length, and the tensile and compressive responses input into a simple model did capture the global mechanical bending response. It is expected that the tension, compression, and bending data will serve to inform, calibrate, and validate future NiTi constitutive models, which will ultimately be able to accurately simulate SMA cables.

7.2   Future Work

To this point, most of the effort has been focused on generating high quality experimental data on two superelastic SMA cable designs. Looking forward, there are many avenues for future work.

One wide open area, yet to be addressed, is actuation of cables in shape memory mode. There are many potential SMA cable actuator applications (see section 1.1.1), making this an important endeavor. The cables studied thus far would have required cooling to about -150°C to induce thermal-M, so we elected to carry out superelastic experiments at room temperature, but cables constructed of wires whose A_s temperature is above room temperature (shape memory wires) would make shape memory experiments significantly more tractable. With an experimental setup that controls the temperature, one could run a series of tests at constant loads to characterize each design's shape memory performance. From there, one could thermally cycle specimens to look into shakedown, or perhaps replace the dead load with a spring to better simulate practical applications. It could also be useful to compare how quickly the designs cool down after being heated above A_f. A SMA's maximum actuation frequency is determined almost entirely by the rate of cooling, and cables should cool somewhat faster than a monolithic rod of the same diameter due to a greater surface area to volume ratio.

As of now, the same design of SMA cable and traditional (steel) cable have not been directly compared. A few experiments might help to bring out the benefits of SMA cables and also help us further understand their behavior. (1) In uniaxial tension, traditional cables would likely plastically deform around 1 % global strain, superelastic cables would fully recover at least 6 % strain, and shape memory cables would recover similar strains upon heating. The stark differences between the three mechanical responses should assist in selling the idea of SMA cables, and provide an easily understood introduction to the topic for those who are not familiar with SMAs. (2) As previously discussed in Chapter 1, "birdcaging" is a bulbous-like deformation that can occur when a cable has experienced excessive compression. SMA cables would be able to survive far more severe birdcage deformations than cables made of conventional materials, either in superelastic mode or,

in shape memory mode, through heating. This could be experimentally quantified through compression tests on short gage length specimens, while taking digital images to record the birdcage deformation. SMA cables and traditional cables could be loaded and unloaded to progressively larger and larger compressive strains to monitor when the birdcage induced plastic deformation in the wires. (3) Cables are frequently selected in industrial applications for their bending flexibility. Bending tests could be as simple as monitoring the recovery after wrapping a cable around smaller and smaller rigid circles, or as involved as the experiments in section 6.4. An in depth analysis of cable bending may be difficult since they will likely ovalize as the wires move toward the neutral axis to minimize their uniaxial strain, but that does not stop one from making important comparisons between different cables. Bending tests could also feed into a study of the spooled cable actuators mentioned in section 1.1.1.

Now that a large volume of data has been gathered on the 7×7 and 1×27 designs, it would be sensible to perform the experiments mentioned above with those two designs, but there are a myriad of other designs that deserve attention as well. Clearly, one can modify helix angles, lays, and cable cross-sections to achieve different thermomechanical behaviors, but some more interesting designs (patents pending) modify the character of the wires themselves. For instance, SMA actuators often require a bias spring (see Fig. 1.1a), slightly complicating their elegant simplicity. Consider a SMA cable design similar to the 1×27, except the outer layer is made of steel wires with deep helix angles, while the inner layers are constructed from SMA wires with shallow helix angles (see Fig. 7.1a). The SMA wires could be Joule heated to actuate the cable, while the steel wires could serve as an integrated bias spring. In another example, accurate partial actuation of a monolithic SMA wire is not always straightforward due to difficulties in controlling the temperature within a narrow range. Each layer of a 1×27 style design could have a different A_f temperature (see Fig. 7.1b), allowing multi-stage actuation as the temperature is raised, or perhaps multiple A_f temperatures could be interspersed throughout a cable to effectively spread continuous actuation out over a wide temperature range. For a final example, consider the longstanding difficulty in quickly cooling SMA actuators to increase their actuation frequency capability. Elements that are capable of heating and cooling, such as a thermoelectric devices, could be placed inside a cable to actively cool the wires. Alternatively, the core wire in each strand of a 7×7 style design could be replaced with a SMA micro-tube (see Fig. 7.1c), permitting liquid or air to flow through the cable and rapidly change its temperature. The three examples given (and other innovative designs not yet dreamed of) are promising ideas, yet at this point they are only ideas, and many technical details must be solidified before commercial use is possible.
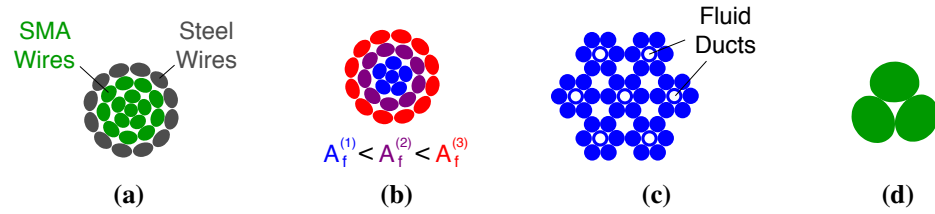
Figure 7.1 Potential SMA cable designs: (a) Actuator with integrated steel wire bias springs, (b) Multi-stage actuator, (c) Cable outfitted with micro-tubes for fluid flow, (d) 1×3 strand with no core wire

Another design worth studying for both practical and scientific reasons is a 1×3 strand. The core wires inside the strands of the 7×7 and 1×27 designs provide structural support to the helical wires surrounding them, but they also hinder the performance of the designs. In uniaxial tension, this construction causes the core wire to plastically deform long before the helical wires, significantly limiting the cable's recoverable global strain. A 1×3 strand has three wires that simply twist around one another, as shown in Fig. 7.1d, removing the need for a core wire. The same principle can be extended to a full cable by twisting three 1×3 strands together to create a 3×3 cable, which does not have a core strand. The lack of a core wire in a 1×3 strand not only increases its recoverable stroke, but also simplifies the thermomechanics of its behavior. In the course of the work documented by this thesis, several attempts were made to isolate the response of a single helical wire, each of which had its drawbacks. Instead, one can simply test a 1×3 strand and divide the response by 3 to receive the response of a single helical wire. Thus, a set mechanical responses from 1×3 strands with various helix angles would be ideal to start validating a SMA cable model.

Modeling of SMA cables is a challenging task, but a necessary one if we are to navigate the countless number of possible designs. One possible path to modeling the kinematics of a deforming cable is to treat each wire as a Cosserat rod [4]. This approach reduces the wire from a three-dimensional continuum down to a one-dimensional curvilinear description of the wire centerline, with six degrees of freedom at every point (three displacements, three rotations), or four if one ignores shear deformations (three displacements, one rotation). The Cosserat rod assumptions significantly simplify the analysis and may permit one to solve the problem of a helix wrapped around a rigid mandrel, for a simple material model, without having to resort to finite element (FE) calculations. Regardless, variants of Cosserat rod theory are implemented in commercial FE codes (B31 element in Abaqus [55], for example). These structural elements shorten computation time by orders of magnitude compared to a full three-dimensional continuum approach, making relatively involved design optimization studies possible. Computation time aside, either method will require an accurate mate-

rial model for SMA behavior in tension, torsion, and bending, which may be the bigger challenge.

The majority of three-dimensional polycrystalline SMA constitutive models can be classified into two groups: micromechanics-based models and phenomenological models. The micromechanics models start with some form of crystallographic information about the microstructure, such as the habit plane variants discussed in Appendix C, and perform a homogenization to bring such information up to the macroscopic scale within the context of continuum thermomechanics. The phenomenological models start with continuum thermomechanics from the beginning, using macroscopic experimental observations to inform the modeling choices. (See [67] for a more comprehensive review.) The micromechanics approach has greater scientific appeal, due to its ties to the microstructure, and can be useful in the absence of high quality macroscopic experiments. However, it is computationally expensive and the homogenization step frequently ignores interactions that become important on the macroscopic scale. Thus, in the interest of accurately simulating a complicated structure such as a cable, phenomenological models are likely a better choice.

Despite the preponderance of three-dimensional SMA models, their accuracy in loading scenarios other than pure tension, where they are often calibrated, is marginal. In most cases, modelers compare against a limited set of experiments that were not always carefully performed. Consequently there are either too few experiments to actually assess a model, or it is unclear whether the discrepancies are caused by the model or the experiment. This brings us to the direction initiated by the tube experiments in Chapter 6. There are a number of opportunities for further experiments to support constitutive model development.

As mentioned in section 1.1.2, the tubes were selected partly because it is relatively easy to flow fluid through the inner diameter and perform isothermal tests at temperatures above and below room temperature. This has been successfully performed by Churchill [27], where he showed that the Clausius-Clapeyron slope in compression was roughly double that of tension. These experiments were a good first attempt, but they should be repeated using DIC, because several assumptions were invoked in calculating the strain from the grips. (The experiments in Chapter 6 used similar fixturing and the DIC strain deviated from the grip strain by as much as 1.3 % strain.) There is also need to characterize the shape memory behavior of the tubes. For superelastic tubes, which are more readily available than shape memory tubes, this requires testing well below 0°C. If a tube below 0°C is exposed to room temperature air, water will condense on the tube, ruining optical strain measurements, such as DIC. Unless blowing dry nitrogen air across the specimen avoids condensation, it may be prudent to use strain gages or mechanical extensometers instead. If this is done, it is recommended to take close up digital images of the specimen in the

compression experiments to verify that it does not buckle, because the naked eye can easily miss small amounts of buckling that occur slowly.

Torsion was also mentioned in section 1.1.2 as a reason to study tubes, arguing that thin wall tubes provide a good approximation of pure shear if one neglects the strain gradient through the thickness. Several tension-torsion studies have been performed on NiTi tubes [50, 69, 71, 80, 117, 124], but they all suffer from some combination of the faults made in the bending studies (see section 1.1.2): no full field measurements, measuring the strain from the grips, and/or deforming the tube to only 3 % or 4 % axial/shear strain (likely due to limitations in their strain measurement technique). While some authors have made an effort to measure the initial $A \rightarrow M$ transformation surface or the initial M detwinning surface (analogous to a yield surface in plasticity) [69, 117], no one has attempted to measure when the material stiffens up after the $A \rightarrow M$ transformation or after M detwinning. These surfaces that define the completion of transformation/detwinning are likely path dependent, but radial paths in shear strain-axial strain space (proportional loading) would be a place to start, since many applications employ this style of loading. Regardless of the particular experimental program selected, incorporating DIC measurements into tension-torsion testing should remedy many of the faults of previous studies and dramatically improve the quality of the data used to calibrate constitutive models.

Hopefully it is now apparent that there are numerous paths to follow that have both engineering importance and scientific value. The key will be, of course, to select the paths that will bear the most fruit with the least number of potholes along the way.

Appendices

Appendix A

Comments on the Biot stress & strain measures

The Biot strain (E^B) and stress (Π^B) measures are rarely used for solving boundary value problems in finite deformation mechanics, due to the computational complexity arising from the need to decompose F into R and U (although proponents do exist). Accordingly, these measures may be somewhat unfamiliar, so the aim of this appendix is to justify our choice and to clarify (if only for the humble experimentalist, if not the grizzled theoretician) some implications of their use compared to other measures commonly used. In experiments, one can choose whatever self-consistent stress/strain measures he/she prefers, since the current configuration is not the solution being sought (like when solving a boundary value problem), but is the one actually being measured. We have found that the Biot strain and stress are convenient in certain structural mechanics applications, such as those in this thesis, where the loading is co-rotational, i.e. the applied traction vector on a surface element of interest follows the material rotation during the loading process. For example, Irschik and Gerstmayr [59] nicely showed that for finite deformation of a Euler-Bernoulli beam, the Biot strain leads to a linear strain distribution through the cross-section; whereas, the more commonly used Green-Lagrange strain leads to a quadratic strain distribution. Thus, the Biot strain is a more natural, and convenient, choice for bending of slender beams.

Recalling eq. (6.2.1), the Biot strain tensor definition is

$$E^B \equiv U - I. \tag{A.0.1}$$

The conjugate Biot stress tensor (Π^B) is defined such that the mechanical power per unit reference volume ($\hat{\mathcal{P}}_0$) is

$$\hat{\mathcal{P}}_0 = \Pi^B : \frac{\mathrm{d}E^B}{\mathrm{d}t} = \Pi^B : \dot{U}. \tag{A.0.2}$$

Obviously due to the symmetry of U, only the symmetric part of the Biot stress contributes to the mechanical power, so it is common to define a symmetrized Biot stress (or Jaumann

stress) as

$$\Pi^{\text{B}}_{\text{sym}} = \frac{1}{2}\left(N \cdot R + R^T \cdot N^T\right), \tag{A.0.3}$$

where N is the nominal stress tensor (related to the 1st Piola-Kirchhoff stress tensor by $N = P^T$). We prefer, however, to use the unsymmetrized Biot stress tensor definition[a] as

$$\Pi^{\text{B}} = N \cdot R, \tag{A.0.4}$$

which has a more physical interpretation as shown below. The nominal stress tensor is related to the Cauchy stress tensor (σ) by $N = JF^{-1} \cdot \sigma$ with $J \equiv \det F$. It is well known that eq. (A.0.2) is equivalent to the alternate forms $\hat{\mathcal{P}}_0 = J\sigma : D = N \cdot \cdot \dot{F} = S : \dot{E}^{\text{L}}$, where D is the rate of deformation tensor, S is the 2nd Piola-Kirchhoff stress tensor, and E^{L} is the Green-Lagrange strain tensor[b].

Continuum mechanics is typically concerned with reference (undeformed) and current (deformed) configurations, but it is sometimes convenient to consider the intermediate (rotationless, pure deformation) configuration (see configuration V^* in Fig. A.1). By the polar decomposition theorem $F = R \cdot U$, a general deformation F is uniquely decomposed into U, which stretches the body into the intermediate configuration, and R, which subsequently rotates the body into the current configuration. In this manner, a surface normal can be thought as being transformed from n_0 in the reference configuration (V_0), to n^* in the stretched configuration (V^*), and then to $n = R \cdot n^*$ in the current configuration (V). Forces, on the other hand, reside only in the current configuration, but in order to work with the other configurations one creates fictitious forces (often back-convected somehow). For a given material surface element dA in the current configuration, loaded by a contact force $\mathbf{d}f$, the current (Eulerian) traction vector is $t \equiv \mathbf{d}f/\mathrm{d}A$. As is commonly done, a pseudotraction per unit reference area (t_0) can be defined by $t\,\mathrm{d}A = t_0\,\mathrm{d}A_0$, which preserves both the magnitude and direction of the actual force. In certain circumstances it may be convenient (and possibly realistic for a particular time-dependent loading) to consider the co-rotated force vector ($\mathbf{d}f^*$), such that the force vector element is convected (by rotation only) from this intermediate configuration to the current configuration by $\mathbf{d}f = R \cdot \mathbf{d}f^*$, as was done for the surface normal n^*. One then defines an associated co-rotated (referential) pseudotraction vector (T^*) such that

$$\mathbf{d}f^* = T^*\,\mathrm{d}A_0. \tag{A.0.5}$$

---

[a]Note Irschik and Gerstmayr [59] define an alternate Biot stress tensor, which is the transpose of ours.

[b]The operation $C = A \cdot B$ between two 2nd order tensors (A and B) is the contraction resulting in a 2nd-order tensor with components $C_{ij} = A_{ik}B_{kj}$ with respect to a fixed cartesian frame. Double contraction operations are denoted $\phi = A \cdot \cdot B = A_{ij}B_{ji}$ and $\psi = A : B = A_{ij}B_{ij}$.
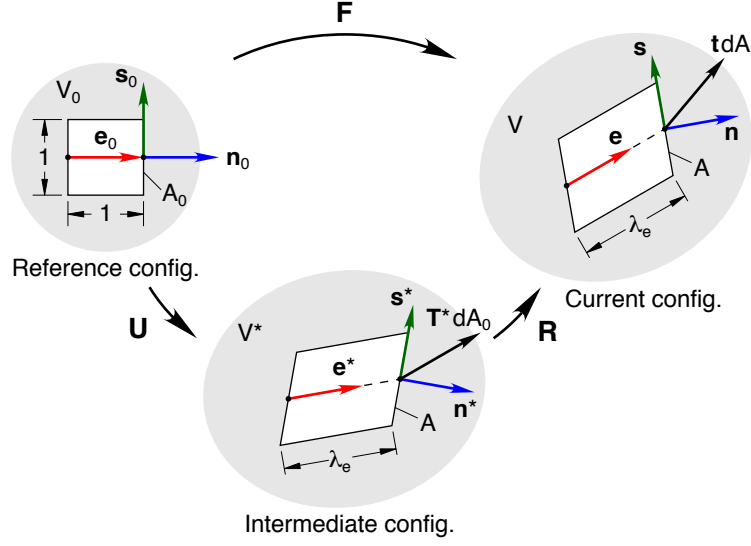
Figure A.1 Schematic of finite deformation, showing the various convected unit vectors e (line element), n, (surface normal) and s (surface tangent).

This gives the following relations between the different tractions,

$$\mathbf{d}f = t\,dA = t_0\,dA_0 = R \cdot T^*\,dA_0. \tag{A.0.6}$$

One should recognize that T^* is distinct from the pseudotraction vector $(T_0 \equiv d\hat{f}_0/dA_0)$ commonly used to define the 2$^{\text{nd}}$ Piola-Kirchhoff stress, where $\mathbf{d}f = F \cdot d\hat{f}_0$ and $T_0 = n_0 \cdot S$, which does not preserve the magnitude of the force. Substituting Cauchy's formula into eq. (A.0.6) gives the relations

$$n \cdot \sigma\,dA = n_0 \cdot N\,dA_0 = R \cdot T^*\,dA_0. \tag{A.0.7}$$

Premultiplying the second relation by R^T and rearranging, gives the result

$$T^* = n_0 \cdot (N \cdot R) = n_0 \cdot \Pi^{\text{B}}. \tag{A.0.8}$$

Thus, the quantity $\Pi^{\text{B}} \equiv N \cdot R$ plays the same role as N and σ in a Cauchy relation to its respective traction vector. Referring to the two-dimensional deformation in Fig. A.1, the normal (σ_n^0) and shear components (τ_n^0) of T^* can be calculated as

$$\sigma_n^0 = n_0 \cdot \Pi^{\text{B}} \cdot n^*, \tag{A.0.9}$$

$$\tau_n^0 = n_0 \cdot \Pi^{\text{B}} \cdot s^*. \tag{A.0.10}$$

It should be noted that a convected line element $U \cdot e_0 = \lambda_e e^*$, where λ_e is the stretch

ratio of that line element, may not be co-linear with the normal n^*. If, however, n^* is a principal axis of U, now thinking of elementary beam theory where shear deformation is neglected, then the axis remains co-linear with the surface normal, $e^* = n^* = n_0$, and in an orthogonal direction $s^* = s_0$. So in this special case, we have

$$\sigma_n^0 = n_0 \cdot \Pi^B \cdot n_0, \tag{A.0.11}$$

$$\tau_n^0 = n_0 \cdot \Pi^B \cdot s_0. \tag{A.0.12}$$

Besides bending, other situations may exist where the Biot stress/strain measures are useful, such as uniaxial loading of an anisotropic material as considered in C. In this case, the traction vector on surface element with current normal e is $t = \sigma e$ and the uniaxial Cauchy stress tensor is $\sigma = \sigma e \otimes e$ (see Fig. A.2). (This, of course, presumes that a suitable loading device can be constructed to achieve such a simple stress state – in practice, not a trivial task for experiments on anisotropic materials.) Thinking of our tension experiments on NiTi where transformation occurs at constant tension force, the current Cauchy stress (σ) is not constant during deformation. Instead, we seek to hold the force ($\sigma \, dA$) constant, which is more naturally done with one of the referential stress measures. Nanson's formula relates the oriented current area to the back-convected reference area as

$$n \, dA = J F^{-T} \cdot n_0 \, dA_0. \tag{A.0.13}$$

The reference pseudo-traction vector is $t_0 = \sigma_0 e$ such that eq. (A.0.6) is satisfied to give the correct force. Taking $e = n$ and using eq. (A.0.13) gives

$$\sigma_0 = J \sigma \lambda_e^{-1} e_0 \cdot n_0, \tag{A.0.14}$$

where $F^{-1} \cdot e = \lambda_e^{-1} e_0$ is the back-convected reference line element and λ_e is its stretch ratio. Again, it should be emphasized that in general $e_0 \neq n_0$, i.e. n_0 is not simply the back-convected unit vector of material line element, but instead depends on the cross product of two orthogonal vectors that define a surface element. This means that, in general, σ_0 is the normal force in the current configuration per unit reference area, not the force normal to the reference surface per unit reference area. Note, however, that $e_0 \cdot n_0$ is the projection of this reference area element onto an area element $e_0 \, dA_0^e$ that is in fact perpendicular to e_0 (see again Fig. A.2). Thus, if we define a new reference stress that actually acts like a normal stress as $\sigma_0^e \equiv J \sigma \lambda_e^{-1}$ the force magnitude is also preserved by $\sigma_0^e \, dA_0^e = \sigma_0 \, dA_0$.
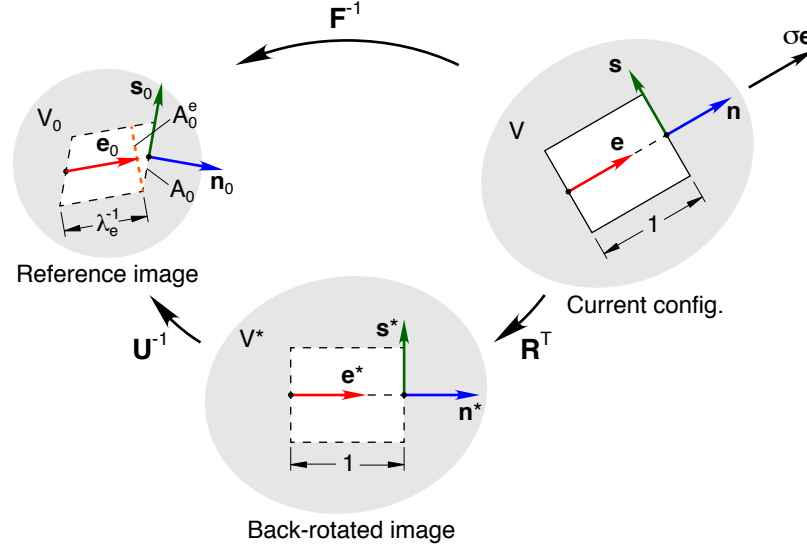
Figure A.2 Schematic of uniaxial Cauchy stress applied to an anisotropic material and its back-rotated and reference images.

With this definition, the nominal and Biot stress tensors take the simple forms

$$\boldsymbol{N} = \sigma_0^e \, \boldsymbol{e}_0 \otimes \boldsymbol{e}, \tag{A.0.15}$$

$$\boldsymbol{\Pi}^{\mathrm{B}} = \sigma_0^e \, \boldsymbol{e}_0 \otimes \boldsymbol{e}^*, \tag{A.0.16}$$

where $\boldsymbol{e}^* = \boldsymbol{R}^T \cdot \boldsymbol{e}$ is the unit vector of a back-rotated *line element* to the intermediate configuration (V*). This shows that both the nominal stress and Biot stress tensors are clearly two-point tensors, where the nominal stress has footing in configurations V_0 and V, while the Biot stress has footing in configurations V_0 and V^*. Certainly, the components of both tensors defy a simple physical interpretation in the most general case, and neither tensor is symmetric. While the Biot stress may be weirdly dependent on $\boldsymbol{U}$, its definition at least removes the dependence of its components on the rotation $\boldsymbol{R}$.

If, however, we consider uniaxial loading with force resultant P in the Z-direction and the material is at least *orthotropic* about this direction, then $\boldsymbol{e}_Z$ is a principal direction of $\boldsymbol{U}$, $\boldsymbol{R} = \boldsymbol{I}$, and $\boldsymbol{n}_0 = \boldsymbol{e}_Z$ remains fixed during loading. The only non-zero stress component is $\sigma_0 = \Pi_{ZZ}^{\mathrm{B}} = N_{ZZ}$, and when averaged over the cross-section, is the just engineering stress P/A_0. By contrast, the Green-Lagrange strain is non-linear in the displacement in uniaxial tension, and the conjugate 2$^{\mathrm{nd}}$ Piola-Kirchhoff stress ($\boldsymbol{S} = \boldsymbol{N} \cdot \boldsymbol{F}^{-T}$) has no simple physical interpretation. In particular, along the load plateau for uniaxial tension of NiTi where the force is constant with increasing elongation, $S_{ZZ} = \lambda_{ZZ}^{-1} P/A_0$ has a negative tangent modulus, since the global axial stretch ratio λ_{ZZ} is a monotonically increasing quantity. Thus, we

prefer the Biot stress and strain measures, since they are more easily interpreted in the context of experimentally measured quantities here.

Appendix B

A simple model based on a Gibb's mixure rule

A first-order, uniaxial superelastic model can be constructed from a simple Gibbs mixture rule,

$$g(\sigma, T, \xi) = (1 - \xi)\, g_A(\sigma, T) + \xi\, g_M(\sigma, T), \tag{B.0.1}$$

where g is the total specific (per unit mass) Gibbs free energy, σ is the uniaxial stress, T is the thermodynamic temperature, ξ is the mass fraction of martensite, and g_A, g_M are the specific Gibbs free energies of the two pure phases austenite and martensite. For the pure phases, the following forms are chosen,

$$-g_A = \frac{\sigma^2}{2\rho E} + s_0\,(T - T_0) + c_0\left[T \ln\left(\frac{T}{T_0}\right) - (T - T_0)\right], \tag{B.0.2}$$

$$-g_M = \beta\frac{\sigma}{\rho} + \frac{\sigma^2}{2\rho E} + (s_0 + \Delta s)\,(T - T_0) + c_0\left[T \ln\left(\frac{T}{T_0}\right) - (T - T_0)\right], \tag{B.0.3}$$

with material constants: elastic modulus (E), mass density (ρ), stress-free equilibrium transformation temperature (T_0), specific heat (c_0), $A \rightarrow M$ transformation strain (β), and $A \rightarrow M$ entropy difference ($\Delta s < 0$). This model neglects thermal expansion, some differences in A and M properties (i.e., elastic modulus, density, and specific heat), and any interfacial energy terms, all of which we accept as a first approximation. The specific driving force for $A \rightarrow M$ transformation ($\mu \equiv -\partial g/\partial \xi$) is calculated as

$$\mu = g_A - g_M = \beta\frac{\sigma}{\rho} - \frac{\Lambda}{T_0}\,(T - T_0), \tag{B.0.4}$$

where the specific entropy jump $-\Delta s \approx \Lambda/T_0$ has been substituted in terms of the latent heat of transformation ($\Lambda > 0$, a material constant). Assuming $A \rightarrow M$ transformation takes place when μ reaches a critical value μ_c (a material constant), the respective transformation

178

stresses for tension and compression are predicted to be,

$$\sigma^+ = \frac{\rho}{\beta^+}\left[\Lambda\left(\frac{T}{T_0} - 1\right) + \mu_c\right], \tag{B.0.5}$$

$$\sigma^- = \frac{\rho}{\beta^-}\left[\Lambda\left(\frac{T}{T_0} - 1\right) + \mu_c\right]. \tag{B.0.6}$$

Thus, $\sigma^+\beta^+ = \sigma^-\beta^-$ is a constant for isothermal transformation. Furthermore, eqs. B.0.5 and B.0.6 give the Clausius-Clapeyron relations for tension and compression, respectively, as

$$\frac{d\sigma^+}{dT} = \frac{\rho\Lambda}{T_0\beta^+}, \tag{B.0.7}$$

$$\frac{d\sigma^-}{dT} = \frac{\rho\Lambda}{T_0\beta^-}. \tag{B.0.8}$$

These equations predict a larger slope (magnitude) of the transformation stress with temperature for compression than for tension since $|\beta^-| < \beta^+$, which is consistent with experiments on similar tubes across various temperatures [27].

Appendix C

Transformation strains based on Habit Plane Variants

One can predict the transformation strains from micro-mechanics, so a quantitative comparison with our measurements is done here. The tension-compression asymmetry is generally attributed to the crystallographic asymmetry of the martensitic phase transformation, and many researchers use the set of 24 habit plane variants (HPV)[a] of martensite to model the superelastic behavior of SMAs (e.g. [47,49,87]). We should first mention that this view ignores any detwinning of the habit plane variants that likely occurs past the loading plateaus and is necessarily accompanied by plastic slip. Thus, one should expect the HPV model to apply only to the reversible portion of the superelastic behavior, e.g. excluding the post-plateau portion of the tensile $A \rightarrow M^+$ transformation. As noted in a HPV modeling paper [62], the tube drawing process textures the material such that the $\langle 111 \rangle_{B2}$ direction of the austenite lattice is well aligned with the longitudinal tube axis. Figure 6.9b showed an X-ray map of a tube specimen across the stereographic triangle that did indeed show a prevalent $\langle 111 \rangle_{B2}$ crystallographic texture aligned to the tube centerline. This texture allows us to approximate the tube as a single crystal to estimate the transformation strains in tension and compression. Using the HPV model, the deformation gradient for $A \rightarrow M$ transformation, relative to austenite, is

$$\boldsymbol{F}^{(k)} = \boldsymbol{I} + g\,\boldsymbol{m}^{(k)} \otimes \boldsymbol{n}^{(k)}, \quad k = 1, ..., 24, \tag{C.0.1}$$

where k is the index of a particular HPV, $\boldsymbol{I}$ is the identity tensor, g is the magnitude of the unit cell lattice displacement, $\boldsymbol{n}$ is the habit plane unit normal, $\boldsymbol{m}$ is the unit direction of lattice displacement, and $\otimes$ denotes the outer tensor product of two vectors. We chose the experimental values from Matsumoto *et. al.* [77] with respect to the B2 frame: $g = 0.140$,

---

[a]Also called correspondent variant pairs (CVPs) by others, since each HPV consists of pairs of twin-related lattice correspondence variants (LCVs) of specific volume fractions, about 27% and 73% by theory, to achieve an approximately compatible habit plane between austenite and martensite.

$n_j^{(1)} = (-0.8684, -0.4138, 0.26878)$, and $m_k^{(1)} = (0.4580, 0.7706, 0.4432)$. The other variants are found by permutations of the components, and we adopted the ordering found in Gall *et. al.* [47][b]. The driving force for $A \rightarrow M$ transformation (per unit reference volume) for each HPV is

$$\rho_0 \mu^{(k)} = J \boldsymbol{\sigma} : \boldsymbol{\varepsilon}_T^{(k)} = \boldsymbol{N} \cdot \cdot \boldsymbol{H}^{(k)}, \qquad (C.0.2)$$

where $J = \det \boldsymbol{F}$ (close to unity for NiTi), and the following are the respective conjugate transformation strains to the Cauchy stress and Nominal stress tensors: $\boldsymbol{\varepsilon}_T = \frac{1}{2}\left(\nabla_{\boldsymbol{x}} \boldsymbol{u} + (\nabla_{\boldsymbol{x}} \boldsymbol{u})^T\right)$ is the symmetrized (Eulerian) displacement gradient, and $\boldsymbol{H} = \nabla_{\boldsymbol{X}} \boldsymbol{u} = \boldsymbol{F} - \boldsymbol{I}$ is the (referential) displacement gradient.

Assuming the applied stress is purely uniaxial and using the form of the nominal stress of eq. (A.0.15), the thermodynamic driving force for each variant becomes

$$\rho_0 \mu^{(k)} = \boldsymbol{N} \cdot \cdot \boldsymbol{H}^{(k)} = \mathrm{tr}\left(\boldsymbol{N} \cdot \boldsymbol{H}^{(k)}\right) = \sigma_0^e \left(\boldsymbol{e} \cdot \boldsymbol{H}^{(k)} \cdot \boldsymbol{e}_0\right). \qquad (C.0.3)$$

Thus, for a given value of σ_0^e the quantity in parentheses plays the role of the conjugate transformation strain β as shown in eq. (B.0.4),

$$\beta^{(k)} = \boldsymbol{e} \cdot \boldsymbol{H}^{(k)} \cdot \boldsymbol{e}_0 = e_i H_{ij}^{(k)} e_j^0, \qquad (C.0.4)$$

where the usual summation convention applies for i and j in the Cartesian coordinate system of the austenite frame. The preferred HPV (l) is just selected as the maximum of the set of driving forces

$$\mu^{(l)} = \max_{k \in [1,\dots,24]} \left\{\mu^{(k)}\right\}, \qquad (C.0.5)$$

and this could be done for each loading direction in the austenite frame to find $l = l(\boldsymbol{e}_0)$, say across the stereographic triangle (but see our comment at the end of this appendix). In the $\langle 111 \rangle_{B2}$ direction with $\hat{\boldsymbol{e}}_0 = \{1, 1, 1\} / \sqrt{3}$, $\beta^{(l+)} = 0.06639$ for tension and $\beta^{(l-)} = -0.03152$ for compression. These are somewhat different from the transformation strains we measured. However, there are in fact six equally preferred HPV's in tension and another six in compression, since $\langle 111 \rangle$ is a relatively high symmetry axis for the crystal. This means that several HPV's may be generated with equal probability and be activated simultaneously. Choosing instead the average (homogenized) deformation gradient $\bar{\boldsymbol{F}}$ of the six preferred HPVs, one finds that, unlike the individual HPVs, the ensemble (both for tension and compression) is a rotationless pure deformation, $\bar{\boldsymbol{F}} = \bar{\boldsymbol{U}}$, and $\langle 111 \rangle_{B2}$ is a principal axis of the deformation.

---

[b]Note, however, [47] used the theoretical values instead of experimental values from Matsumoto *et. al.* [77].

Now, $e = e_0$ and the relevant strain measure on average is $\bar{U} - I$ (the Biot strain), so

$$\beta_{\langle 111 \rangle} = \hat{e}_0 \cdot \left(\bar{U} - I \right) \cdot \hat{e}_0. \tag{C.0.6}$$

This calculation gives $\beta_{\langle 111 \rangle}^+ = 0.05470$ for tension and $\beta_{\langle 111 \rangle}^- = -0.03714$ for compression. These values agree rather well with our uniaxial data (0.0540 and -0.0349), especially considering the fact that the tube specimen is not truly a single crystal.

Finally, the impetus to use finite deformation measures was our desire to be as precise as possible in the interpretation of our data. One might argue, however, that infinitesimal strain theory would have been sufficiently accurate, considering the moderate transformation strains of NiTi (of order 5 %). In fact, eq. (C.0.6) is numerically equivalent to $\hat{e}_0 \cdot H^{(l)} \cdot \hat{e}_0$ calculated from an individual preferred variant, seemingly the same as infinitesimal theory. However, this equivalence stems from our choice to use the average of the six preferred HPVs, which have zero *average* rotation, and the fact that the stress state is purely uniaxial which extracts only the symmetric part of $H^{(l)}$. We showed above that the effect of finite rotation of a *single* variant is not that small (a 20 % difference in transformation strain in tension), so the effect warrants careful consideration. Furthermore, the thermodynamic driving force used here to extract the transformation strain was derived from a potential function (the Gibb's free energy), so finite rotations (whether they are included or not) have implications on how one calculates the correct potential energy of the external loading device. We see some pitfalls here. Additionally, it is not obvious how one should calculate the transformation strain, at least in a simple way, for other loading axes. A slight change in loading direction off the $\langle 111 \rangle$ axis would lead to a single preferred variant, according to the simplistic prescription of eq. (C.0.5), which would give a jump in the transformation strain values from those strictly along $\langle 111 \rangle$. Such a discontinuity would be rather unexpected, and one would need to consider how compatibility enforces constraints on neighboring material domains to give a more continuous dependence of the macroscopic transformation strain on loading direction. How this homogenization should be properly done, without resorting to extremely detailed calculations, is probably open for debate.

Bibliography

[1] Y. Adachi, S. Unjoh, and M. Kondoh. Development of a shape memory alloy damper for intelligent bridge systems. *Mater. Sci. Forum (Switzerland)*, 327-328:31 – 4, 2000.

[2] P. H. Adler, J. Allen, Lessar J., and R. Francis. Martensite transformations and fatigue behavior of nitinol. *Journal of ASTM International*, 4(7), 2007.

[3] B. Andrawes and R. DesRoches. Unseating prevention for multiple frame bridges using superelastic devices. *Smart materials and structures*, 14:S60, 2005.

[4] S.S. Antman. *Nonlinear problems of elasticity*, volume 107. Springer Verlag, 2005.

[5] T. Atanacković and M. Achenbach. Moment-curvature relations for a pseudoelastic beam. *Continuum Mechanics and Thermodynamics*, 1(1):73–80, 1989.

[6] F. Auricchio and E. Sacco. A superelastic shape-memory-alloy beam model. *Journal of intelligent material systems and structures*, 8(6):489–501, 1997.

[7] MM Barney, D. Xu, SW Robertson, V. Schroeder, RO Ritchie, AR Pelton, and A. Mehta. Impact of thermomechanical texture on the superelastic response of nitinol implants. *Journal of the Mechanical Behavior of Biomedical Materials*, 2011.

[8] P. Barooah and N. Rey. Closed-loop control of a shape memory alloy actuation system for variable area fan nozzle. In Vittal S. Rao, editor, *Proceedings of SPIE*, volume 4693 of *Smart Structures and Materials 2002: Modeling, Signal Processing, and Control*, pages 384–395, 2002.

[9] B. Bay, T. Smith, D. Fyhrie, and M. Saad. Digital volume correlation: Three-dimensional strain mapping using X-ray tomography. *Experimental Mechanics*, 39:217–226, 1999. 10.1007/BF02323555.

[10] BT Berg. Bending of superelastic wires, Part I: Experimental aspects. *Journal of Applied Mechanics*, 62:459, 1995.

[11] BT Berg. Bending of superelastic wires, Part II: Application to three-point bending. *Journal of Applied Mechanics*, 62:466, 1995.

[12] Kaushik Bhattacharya. *Microstructure of Martensite: Why it forms and how it gives rise to the shape-memory effect*. Oxford Series on Materials Modelling. Oxford University Press, NY, first edition, 2003.

[13] Zhonghe Bo and Dimitris Lagoudas. Thermomechanical modeling of polycrystalline SMAs under cyclic loading, Part III: evolution of plastic strains and two-way shape memory effect. *International Journal of Engineering Science*, 37(9):1175–1203, 1999.

[14] LG Brazier. On the flexure of thin cylindrical shells and other" thin" sections. *Proceedings of the Royal Society of London. Series A*, 116(773):104, 1927.

[15] L. C. Brinson, I. Schmidt, and R. Lammering. Stress-induced transformation behavior of a polycrystalline NiTi shape memory alloy: micro and macromechanical investigations via in situ optical microscopy. *Journal of the Mechanics and Physics of Solids*, 52(7):1549–1571, 2004.

[16] B. Bundara, M. Tokuda, B. Kuselj, B. Ule, and J. Tuma. Superelastic tension and bending characteristics of shape memory alloys. *Metals and Materials International*, 6:293–299, 2000. 10.1007/BF03028074.

[17] G. Buratti. Stresses and deflections in a pseudo-elastic beam under cyclic loads. *Continuum Mechanics and Thermodynamics*, 17(2):149–157, 2005.

[18] F. Casciati, L. Faravelli, and C. Fuggini. Cable vibration mitigation by added sma wires. *Acta Mechanica*, 195(1-4):141–155, January 2008.

[19] B.-C. Chang, J. A. Shaw, and M. A. Iadicola. Thermodynamics of shape memory alloy wire: Modeling, experiments, and application. *Continuum Mechanics and Thermodynamics*, 18(1-2):83–118, 2006.

[20] E. Choi, D.H. Lee, and NY Choei. Shape memory alloy bending bars as seismic restrainers for bridges in seismic areas. *Int. J. Steel Struct*, 9(4):261–273, 2009.

[21] T. C. Chu, W. F. Ranson, and M. A. Sutton. Applications of digital-image-correlation techniques to experimental mechanics. *Experimental Mechanics*, 25(3):232–244, Sep. 1985.

[22] C. B. Churchill and J. A. Shaw. Thermo-electro-mechanical shakedown response of conditioned shape memory alloy wires. In *Proceedings of the ASME 2009 Conference on Smart Materials, Adaptive Structures and Intelligent Systems (SMASIS 2009)*, volume 1, pages 137–148. ASME, Sep. 2009.

[23] C. B. Churchill, J. A. Shaw, and M. A. Iadicola. Tips and tricks for characterizing shape memory alloy wire: Part 2 – fundamental isothermal responses. *Experimental Techniques*, 33(1):51–62, Jan-Feb 2009.

[24] C. B. Churchill, J. A. Shaw, and M. A. Iadicola. Tips and tricks for characterizing shape memory alloy wire: Part 3 – localization and propagation phenomena. *Experimental Techniques*, 33(5):70–78, Sept/Oct 2009.

[25] C. B. Churchill, J. A. Shaw, and M. A. Iadicola. Tips and tricks for characterizing shape memory alloy wire: Part 4 – thermo-mechanical coupling. *Experimental Techniques*, 34(2):63–80, Mar/Apr 2010.

[26] Chris B. Churchill and John A. Shaw. Shakedown response of conditioned shape memory alloy wire. In *Behavior and Mechanics of Multifunctional and Composite Materials, Proceedings of the SPIE 15th Annual International Symposium on Smart Structures and Materials*, volume 6928, 2008.

[27] Christopher B. Churchill. *Experimental Techniques for Characterizing the Thermo-Electro-Mechanical Shakedown Response of SMA Wires and Tubes*. PhD dissertation, The University of Michigan, Department of Aerospace Engineering, Dec. 2010.

[28] Correlated Solutions. *Vic-Snap Manual*. Correlated Solutions, Inc., Columbia, SC, 2009.

[29] Correlated Solutions. *Vic-3D Manual*. Correlated Solutions, Inc., Columbia, SC, 2010.

[30] Correlated Solutions. *Vic-3D Testing Guide*. Correlated Solutions, Inc., Columbia, SC, 2010.

[31] G. Costello. *Theory of Wire Rope*. Springer, New York, NY, 2nd edition, 1998.

[32] S. Daly. Digital image correlation in experimental mechanics for aerospace materials and structures. In R. Blockley and W. Shyy, editors, *Encyclopedia of Aerospace Engineering*. Wiley and Sons, 2010.

[33] S. De la Flor, C. Urbina, and F. Ferrando. Asymmetrical bending model for NiTi shape memory wires: Numerical simulations and experimental analysis. *Strain*, pages 1475–1305, 2010.

[34] Reginald DesRoches and Jason McCormick. Properties of large diameter shape memory alloys under cyclical loading. *Proceedings of SPIE - The International Society for Optical Engineering*, 5057:187 – 196, 2003.

[35] M. Dolce and D. Cardone. Mechanical behaviour of shape memory alloys for seismic applications 1. martensite and austenite NiTi bars subjected to torsion. *International Journal of Mechanical Sciences*, 43(11):2631 – 2656, 2001.

[36] M. Dolce and D. Cardone. Mechanical behaviour of shape memory alloys for seismic applications 2. austenite NiTi wires subjected to tension. *International Journal of Mechanical Sciences*, 43(11):2657 – 2677, 2001.

[37] M. Dolce and D. Cardone. Fatigue resistance of SMA-martensite bars subjected to flexural bending. *International Journal of Mechanical Sciences*, 47(11):1693–1717, 2005.

[38] Mauro Dolce and Donatello Cardone. Theoretical and experimental studies for the application of shape memory alloys in civil engineering. *Journal of Engineering Materials and Technology, Transactions of the ASME*, 128(3):302 – 311, 2006.

[39] Duerig, T. W. and Pelton, A. and Stöckel, D. An overview of nitinol medical applications. *Materials Science and Engineering A*, 273-275:149–160, 1999.

[40] Dynalloy, Inc. www.dynalloy.com, 2011.

[41] G Eggeler, E Hornbogen, A Yawny, A Heckmann, and M Wagner. Structural and functional fatigue of niti shape memory alloys. *Mat Sci Eng A-Struct*, 378(1-2):24–33, Jan 2004.

[42] O. Faugeras. *Three-dimensional computer vision: a geometric viewpoint*. MIT Press, 1993.

[43] P. Feng and Q. P. Sun. Experimental investigation on macroscopic domain formation and evolution in polycrystalline niti microtubing under mechanical force. *Journal of the Mechanics and Physics of Solids*, 54:1568–1603, May 2006.

[44] C. Franck, S. Hong, S. Maskarinec, D. Tirrell, and G. Ravichandran. Three-dimensional full-field measurements of large deformations in soft materials using confocal microscopy and digital volume correlation. *Experimental Mechanics*, 47:427–438, 2007. 10.1007/s11340-007-9037-9.

[45] Carl P. Frick, Alicia M. Ortega, Jeffrey Tyber, A. El. M. Maksound, Hans J. Maier, Yinong Liu, and Ken Gall. Thermal processing of polycrystalline NiTi shape memory alloys. *Materials Science and Engineering: A*, 405(1-2):34–49, 2005.

[46] Ft. Wayne Metals. http://www.fwmetals.com/strands.php, 2010.

[47] K. Gall, H. Sehitoglu, Y. Chumlyakov, and I. Kireeva. Tension-compression asymmetry of the stress-strain response in aged single crystal and polycrystalline NiTi. *Acta Materialia*, 47(4):1203–1217, 1999.

[48] K. Gall, J. Tyber, V. Brice, C. Frick, H. Maier, and H. Morgan. Tensile deformation of NiTi wire. *Journal of Biomedical Materials Research A*, pages 810–823, 2005.

[49] Xiujie Gao, Miinshiou Huang, and L. Catherine Brinson. A multivariant micromechanical model for smas part 1. crystallographic issues for single crystal model. *International Journal of Plasticity*, 16(10-11):1345–1369, 2000.

[50] C. Grabe and O.T. Bruhns. Path dependence and multiaxial behavior of a polycrystalline NiTi alloy within the pseudoelastic and pseudoplastic temperature regimes. *International Journal of Plasticity*, 25:513–545, 2009.

[51] D.S. Grummon, J.A. Shaw, and J. Foltz. Fabrication of cellular shape memory alloy materials by reactive eutectic brazing using niobium. *Materials Science and Engineering, A*, 438-440:1113–1118, Nov. 2006.

[52] YJ He and QP Sun. Macroscopic equilibrium domain structure and geometric compatibility in elastic phase transition of thin plates. *International Journal of Mechanical Sciences*, 52(2):198–211, 2010.

[53] L. Heller, P. Šittner, J. Pilch, and M. Landa. Factors controlling superelastic damping capacity of SMAs. *Journal of materials engineering and performance*, 18(5):603–611, 2009.

[54] J. D. Helm, S. R. McNeill, and M. A. Sutton. Improved three-dimensional image correlation for surface displacement measurement. *Optical Engineering*, 35:1911–1920, 1996.

[55] HKS. *ABAQUS Manual*. HKS, 6.9 edition, 2009.

[56] Jan Van Humbeeck. Non-medical applications of shape memory alloys. *Materials Science and Engineering A*, 273-275:134–148, 1999.

[57] M. A. Iadicola and J. A. Shaw. The effect of uniaxial cyclic deformation on the evolution of phase transformation fronts in pseudoelastic NiTi wire. *Journal of Intelligent Material Systems and Structures*, 13(2):143–156, 2002.

[58] M. A. Iadicola and J. A. Shaw. An experimental setup for measuring unstable thermo–mechanical behavior of shape memory alloy wire. *Journal of Intelligent Material Systems and Structures*, 13(2):157–166, 2002.

[59] H. Irschik and J. Gerstmayr. A continuum mechanics based derivation of reissner's large-displacement finite-strain beam theory: the case of plane deformations of originally straight bernoulli–euler beams. *Acta Mechanica*, 206(1):1–21, 2009.

[60] AD Johnson and J. Kramer. State-of-the-art of shape memory actuators. In *Proc. 6th Int. Conf. on New Actuators (Bremen, Germany, June 1998)*, 1998.

[61] Rita Johnson, Jamie E Padgett, M Emmanuel Maragakis, Reginald DesRoches, and M Saiid Saiidi. Large scale testing of nitinol shape memory alloy devices for retrofitting of bridges. *Smart Materials and Structures*, 17(3):035018 (10pp), 2008.

[62] Youngjean Jung, Panayiotis Papadopoulos, and R. O. Ritchie. Constitutive modelling and numerical simulation of multivariant phase transformation in superelastic shape-memory alloys. *International Journal for Numerical Methods in Engineering*, 60:429–460, 2004.

[63] Q. Kan and G. Kang. Constitutive model for uniaxial transformation ratchetting of super-elastic niti shape memory alloy at room temperature. *International Journal of Plasticity*, 26(3):441–465, 2010.

[64] W. G. Knauss, I. Chasiotis, and Y. Huang. Mechanical measurements at the micron and nanometer scales. *Mechanics of Materials*, 35:217–231, 2003.

[65] P. Krulevitch, A.P. Lee, P.B. Ramsey, J.C. Trevino, J. Hamilton, and M.A. Northrup. Thin film shape memory alloy microactuators. *Journal of Microelectromechanical Systems*, 5(4):270–282, Dec 1996.

[66] Stelios Kyriakides, Ali Ok, and Edmundo Corona. Localization and propagation of curvature under pure bending in steel tubes with Lüders bands. *International Journal of Solids and Structures*, 45:3074–3087, 2008.

[67] D.C. Lagoudas, P.B. Entchev, P. Popov, E. Patoor, L.C. Brinson, and X. Gao. Shape memory alloys, part ii: Modeling of polycrystals. *Mechanics of Materials*, 38(5-6):430–462, 2006.

[68] Dimitris C. Lagoudas, editor. *Shape Memory Alloys: Modeling and Engineering Applications*. Springer, July 2008.

[69] K. Lavernhe-Taillard, S. Calloch, S. Arbab-Chirani, and C. Lexcellent. Multiaxial shape memory effect and superelasticity. *Strain*, 45(1):77–84, 2009.

[70] KM Liew, J. Ren, and S. Kitipornchai. Analysis of the pseudoelastic behavior of a sma beam by the element-free galerkin method. *Engineering analysis with boundary elements*, 28(5):497–507, 2004.

[71] T.J. Lim and D.L. McDowell. Mechanical behavior of an Ni-Ti shape memory alloy under axial-torsional proportional and nonproportional loading. *Journal of Engineering Materials and Technology*, 121:9, 1999.

[72] M. Liu, H. Li, G. Song, and J. Ou. Investigation of vibration mitigation of stay cables incorporated with superelastic shape memory alloy dampers. *Smart Materials and Structures*, 16:2202, 2007.

[73] Y. Liu, Y. Liu, and J. Van Humbeeck. Lüders-like deformation associated with martensite reorientation in NiTi. *Scripta Materialia*, 39(8):1047–1055, 1998.

[74] P. Luo, Y. Chao, M. Sutton, and W. Peters. Accurate measurement of three-dimensional deformations in deformable and rigid bodies using computer vision. *Experimental Mechanics*, 33(2):123–132, June 1993.

[75] SC Mao, JF Luo, Z. Zhang, MH Wu, Y. Liu, and XD Han. EBSD studies of the stress-induced B2-B19'martensitic transformation in NiTi tubes under uniaxial tension and compression. *Acta Materialia*, 58(9):3357–3366, 2010.

[76] Matlab R2010b. *Matlab Documentation*. MathWorks, Natick, MA, 2010.

[77] O. Matsumoto, S. Miyazaki, K. Otsuka, and H. Tamura. Crystallography of martensitic transformation in Ti-Ni single crystals. *Acta Metallurgica*, 35(8):2137 – 2144, 1987.

[78] J. McCormick, R. DesRoches, D. Fugazza, and F. Auricchio. Seismic vibration control using superelastic shape memory alloys. *Trans. ASME, J. Eng. Mater. Technol. (USA)*, 128(3):294 – 301, July 2006.

[79] H. A. McKenna, John W. S. Hearle, and N. O'Hear. *Handbook of Fibre Rope Technology*. CRC Press LLC, 2004.

[80] J.M. McNaney, V. Imbeni, Y. Jung, Panayiotis Papadopoulos, and R.O. Ritchie. An experimental study of the superelastic effect in a shape-memory nitinol alloy under biaxial loading. *Mechanics of Materials*, 35:969–986, 2003.

[81] Barry Meier. http://www.nytimes.com/2007/10/16/business/16device.html, 2007.

[82] S. Miyazaki, T. Imai, Y. Igo, and K. Otsuka. Effect of cyclic deformation on the pseudoelasticity characteristics of Ti-Ni alloy. *Metallurgical Transactions*, 17A:115–120, Jan. 1986.

[83] S. Miyazaki and K. Otsuka. Deformation and transition behavior associated with the R-phase in Ti-Ni alloys. *Metallurgical and Materials Transactions A*, 17(1):53–63, 1986.

[84] NB Morgan. Medical shape memory alloy applications—the market and its products. *Materials Science & Engineering A*, 378(1-2):16–23, 2004.

[85] A.M. Ortega, J. Tyber, C.P. Frick, K. Gall, and H.J. Maier. Cast NiTi shape-memory alloys. *Adv. Eng. Mater. (Germany)*, 7(6):492 – 507, June 2005.

[86] J.E. Padgett, R. DesRoches, and R. Ehlinger. Experimental response modification of a four-span bridge retrofit with shape memory alloys. *Structural Control and Health Monitoring*, 17(6):694–708, 2010.

[87] E. Patoor, A. Eberhardt, and M. Berveiller. Micromechanical modelling of superelasticity in shape memory alloys. *Journal de Physique(France) IV(France)*, 6(1):277–292, 1996.

[88] AR Pelton, N. Rebelo, TW Duerig, and A. Wick. Experimental and FEM analysis of the bending behavior of superelastic tubing. In *SMST-94: Proceedings of the First International Conference on Shape Memory and Superelastic Technologies,(AR Pelton, D. Hodgson and TW Duerig eds.) Pacific Grove, California, USA*, page 353, 1994.

[89] KE Perry, PE Labossiere, and E. Steffler. Measurement of deformation and strain in Nitinol. *Experimental mechanics*, 47(3):373–380, 2007.

[90] W. H. Peters and W. F. Ranson. Digital imaging techniques in experimental stress analysis. *Optical Engineering*, 21(3):427–432, 1982.

[91] W. H. Peters, W. F. Ranson, M. A. Sutton, T. C. Chu, and J. Anderson. Application of digital correlation methods to rigid body mechanics. *Optical Engineering*, 22:738–742, 1983.

[92] R. Plietsch, C. Bourauel, D. Drescher, and B. Nellen. Analytical description of the bending behaviour of NiTi shape-memory alloys. *Journal of materials science*, 29(22):5892–5902, 1994.

[93] J. Poissant and F. Barthelat. A novel "subset splitting" procedure for digital image correlation on discontinuous displacement fields. *Experimental Mechanics*, 50:353–364, 2010. 10.1007/s11340-009-9220-2.

[94] P.K. Purohit and K. Bhattacharya. On beams made of a phase-transforming material. *International journal of solids and structures*, 39(13-14):3907–3929, 2002.

[95] K. Rajagopal and A. Srinivasa. On the bending of shape memory wires. *Mechanics of Advanced Materials and Structures*, 12(5):319–330, 2005.

[96] B. Raniecki, J. Rejzner, and C. Lexcellent. Anatomization of hysteresis loops in pure bending of ideal pseudoelastic SMA beams. *International journal of mechanical sciences*, 43(5):1339–1368, 2001.

[97] John A. Redmond, Diann Brei, Jonathan Luntz, Alan L. Browne, and Nancy L. Johnson. Behavioral model and experimental validation for a spool-packaged shape memory alloy actuator. In L. Porter Davis, Benjamin K. Henderson, and M. Brett McMickell, editors, *In: Proceedings of SPIE, Industrial and Commercial Applications of Smart Structures Technologies 2008*, volume 6930, pages 693004–69004–13. SPIE, 2008.

[98] J. Rejzner, C. Lexcellent, and B. Raniecki. Pseudoelastic behaviour of shape memory alloy beams under pure bending: experiments and modelling. *International journal of mechanical sciences*, 44(4):665–686, 2002.

[99] Julien Réthoré, François Hild, and Stéphane Roux. Extended digital image correlation with crack shape optimization. *International Journal for Numerical Methods in Engineering*, 73:248–272, 2008.

[100] N. M. Rey, G. Tillman, R. M. Miller, T. Wynosky, M. J. Larkin, J. D. Flamm, and L. S. Bangert. Shape memory alloy actuation for a variable area fan nozzle. In A.-M. R. McGowan, editor, *Society of Photo-Optical Instrumentation Engineers (SPIE) Conference Series*, volume 4332, pages 371–382, June 2001.

[101] S. Saadat, J. Salichs, M. Noori, Z. Hou, H. Davoodi, I. Bar-on, Y. Suzuki, and A. Masuda. An overview of vibration and seismic applications of NiTi shape memory alloy. *Smart Mater. Struct. (UK)*, 11(2):218 – 29, 2002/04/.

[102] H. W. Schreier, J. R. Braasch, and M. A. Sutton. Systematic errors in digital image correlation caused by intensity interpolation. *Optical Engineering*, 39(11):2915–2921, November 2000.

[103] H. W. Schreier, D. Garcia, and M. A. Sutton. Advances in light microscope stereo vision. *Experimental Mechanics*, 44:278–288, 2004.

[104] M. Schwartz. *Encyclopedia of Smart Materials*, volume 1. John Wiley and Sons, New York, NY, 2002.

[105] J. A. Shaw. *Material Instabilities in a Nickel-Titanium Shape Memory Alloy*. PhD dissertation, The University of Texas at Austin, Department of Aerospace Engineering, Jan. 1997.

[106] J. A. Shaw. Simulations of localized thermo–mechanical behavior in a NiTi shape memory alloy. *International Journal of Plasticity*, 16(5):541–562, 2000.

[107] J. A. Shaw. A thermomechanical model for a 1–D shape memory alloy with propagating instabilities. *International Journal of Solids and Structures*, 39(5):1275–1305, 2002.

[108] J. A. Shaw, C. B. Churchill, and M. A. Iadicola. Tips and tricks for characterizing shape memory alloy wire: Part 1 – differential scanning calorimetry & basic phenomena. *Experimental Techniques*, pages 55–62, Sep-Oct 2008.

[109] J. A. Shaw, D. S. Grummon, and J. Foltz. Superelastic NiTi honeycombs: Fabrication and experiments. *Smart Materials and Structures*, 16:S170–S178, 2007.

[110] J. A. Shaw and S. Kyriakides. Thermomechanical aspects of NiTi. *Journal of the Mechanics and Physics of Solids*, 43(8):1243–1281, 1995.

[111] J. A. Shaw and S. Kyriakides. On the nucleation and propagation of phase transformation fronts in a NiTi alloy. *Acta Materialia*, 45(2):683–700, 1997.

[112] J. A. Shaw and S. Kyriakides. Initiation and propagation of localized deformation in elasto–plastic strips under uniaxial tension. *International Journal of Plasticity*, 13(10):837–871, 1998.

[113] John A. Shaw and Christopher B. Churchill. A reduced-order thermomechanical model and analytical solution for uniaxial shape memory alloy wire actuators. *Smart Materials and Structures*, 18(6):065001 (21pp), 2009.

[114] G. Song, Y. L. Mo, K. Otero, and H. Gu. Health monitoring and rehabilatation of a concrete structure using intelligent materials. *Smart Materials and Structures*, 15:309–314, 2006.

[115] Helen Sun, Anupam Pathak, Jonathan Luntz, Diann Brei, Paul W. Alexander, and Nancy L. Johnson. Stabilizing shape memory alloy actuator performance through cyclic shakedown: an empirical study. In L. Porter Davis, Benjamin K. Henderson, and M. Brett McMickell, editors, *In: Proceedings of SPIE, Industrial and Commercial Applications of Smart Structures Technologies 2008*, volume 6930, page 69300Q. SPIE, 2008.

[116] Q. P. Sun, Z. Q. Li, and K. K. Tse. On superelastic deformation of NiTi shape memory alloy micro–tubes and wires — band nucleation and propagation. *Proceedings of IUTAM Symposium on Smart Structures and Structronic Systems, Magdeburg Germany*, Sept. 26-29 2000.

[117] Qing-Ping Sun and Zhi-Qi Li. Phase transformation in superelastic NiTi polycrystalline micro-tubes under tension and torsion–from localization to homogeneous deformation. *International Journal of Solids and Structures*, 39(13-14):3797–3809, 2002.

[118] M. A. Sutton, S. R. McNeill, J. D. Helm, and Y. J. Chao. Advances in two-dimensional and three-dimensional computer vision. In P.K. Rastogi, editor, *Photomechanics, Topics Applied Physics*, volume 77, pages 323–372. Springer Verlag, 2000.

[119] M. A. Sutton, J. J. Orteu, and H. W. Schreier. *Image Correlation for Shape, Motion, and Deformation Measurements: Basic Concepts, Theory, and Applications.* Springer, New York, 2009.

[120] M. A. Sutton, W. J. Wolters, W. H. Peters, W. F. Ranson, and S. R. McNeill. Determination of displacements using an improved digital correlation method. *Image and Vision Computing*, 1(3):133–139, August 1983.

[121] M. A. Sutton, J. H. Yan, V. Tiwari, H. W. Schreier, and J. J. Orteu. The effect of out-of-plane motion on 2D and 3D digital image correlation measurements. *Optics and Lasers in Engineering*, 46(10):746–757, October 2008.

[122] M. Thier, A. Mick, D. Drescher, and C. Bourauel. Deformation behaviour of niti shape memory alloys in bending. *Journal of Materials Science*, 26(23):6473–6478, 1991.

[123] J. Van Humbeeck. Damping capacity of thermoelastic martensite in shape memory alloys. *J. Alloys Compd. (Switzerland)*, 355:58 – 64, June 2003.

[124] YF Wang, ZF Yue, and J Wang. Experimental and numerical study of the superelastic behaviour on niti thin-walled tube under biaxial loading. *Computational Materials Science*, 40(2):246–254, 2007.

[125] John C. Wilson and Michael J. Wesolowsky. Shape memory alloys for seismic response modification: A state-of-the-art review. *Earthquake Spectra*, 21(2):569 – 601, 2005.

[126] P. D. Zavattieri, V. Savic, L. G. Hector Jr., J. R. Fekete, W. Tong, and Y. Xuan. Spatio-temporal characteristics of the Portevin–Le Châtelier effect in austenitic steel with twinning induced plasticity. *International Journal of Plasticity*, 25:2298–2330, 2009.

[127] X.B. Zuo, A.Q. Li, et al. Optimal design of shape memory alloy damper for cable vibration control. *Journal of Vibration and Control*, 15(6):897, 2009.